CHARACTERIZING NEUTRAL TRANS-NEPTUNIAN OBJECTS

A DISSERTATION SUBMITTED TO THE GRADUATE DIVISION OF THE UNIVERSITY OF HAWAIʻI AT MĀNOA IN PARTIAL FULFILLMENT OF THE REQUIREMENTS FOR THE DEGREE OF

DOCTOR OF PHILOSOPHY

IN

ASTRONOMY

August 2013

By
Sarah Sonnett

Dissertation Committee:

Karen J. Meech, Chairperson
Robert Jedicke
Schelte Bus
Norbert Schorghofer
Michael Mottl

We certify that we have read this dissertation and that, in our opinion, it is satisfactory in scope and quality as a dissertation for the degree of Doctor of Philosophy in Astronomy.

DISSERTATION COMMITTEE

_____

Chairperson

_____

_____

_____

_____

To Brandon, for his astounding patience; and to Mom, Dad, Caitlin, Erin, Jim, Nancy, Peggy, and Ryan who have always supported my endeavors, scientific and beyond.

Acknowledgements

First, I wish to thank my dissertation committee for their time and dedication in guiding my education over the past $\sim$ 4.5 years. Especially to Karen Meech - your extremely valuable experience and knowledge base has been fundamental in this work. Thank you for sharing that, helping tailor my scientific thought processes and writing style, and opening up several stimulating professional opportunities. I also want to specifically thank Rob Jedicke, who was the research advisor on my Masters project, for initially prompting me to develop the professional skills that have partially and directly led to my success (learning IDL, statistics, work with survey data, and advice on building a professional network).

Thank you also to the many postdocs at the University of Hawaii for numerous helpful discussions, statistics lessons, and practical instruction, notably Gal Sarid, Henry Hsieh, Jan Kleyna, Timm Riesen, and Bin Yang. My observing and data handling knowledge is mostly based on helpful instruction from Jana Pittichova. I also really need to thank the network of graduate students (far too many to convey) that have come through the Institute for Astronomy over the years for their assistance and friendship on this long, difficult journey to a Ph.D. I would have been difficult to keep my sanity in tact without having such amazing academic companions! I also wish to thank the IfA graduate students come and gone that developed the macros that made assembling this document in LaTeX much easier.

I am also very grateful to Steve Desch, who has helped support my career immensely in the past couple of years through scientific discussions, letter writing, editing, and professional encouragement. I have Keith Noll's benchmark work to thank for motivating

me to focus on studies of small body binaries, which are the basis of a large part of my dissertation and planned postdoctoral work. Thank you as well to Susan Benecchi for sharing some of her data with me so that I may better explore the rotation properties of my survey targets. Brian Carcich was absolutely invaluable in the development of the lightcurve simulation software. I have learned a lot from scientific conversations with Steve Freeland and thank him for helping me keep a broad scope on astrobiology, which I will continue to prioritize during my next professional phase. My interactions with Giovanni Strazzulla via his work on properties of radiated regolith were key in interpreting the results of the rotationally phased colors of my targets. I would like to thank Olivier Hainaut, Pierre Vernazza, and Colin Snodgrass for inviting me to visit their facilities and serving as my primary in-person science contacts while I worked in Germany. My collaboration with Olivier Hainaut was directly responsible for the dataset that made the photometry experiments and subsequent paper possible.

In addition to the friends I've made through professional avenues (some listed above), I also wish to thank the friends I've made outside of the astronomy program – especially my fellow artists and performers, bandmates, and both groups of scotch enthusiasts that have helped me maintain a much-needed and (reasonably) good balance in my work-home life.

My mainland-based family were a major direct and indirect help in my finishing this program. Specifically, my mom, dad, stepmom, sisters, and my Uncle Luke were all responsible for immense amounts of necessary support and perspective. To my in-laws, it takes very special people to offer to proofread large portions of this nearly 300 page document; thank you so much for actively supporting me and giving me more time to write!

Most importantly, to my amazing husband, Brandon - I truly cannot thank you enough for the listening, commenting, editing, moral support, understanding, and patience that have been absolutely integral to making this work a success, and for uprooting your professional life to join me in the next step of mine.

Abstract

Trans-Neptunian Objects (TNOs) are small bodies with orbits beyond Neptune (3050 AU). TNOs are cold and small enough to have remained relatively well-preserved, therefore providing our best observable proxy to the early solar system. Roughly 1/3 of TNOs possess neutral colors indicative of fresh surfaces. Three different mechanisms may explain the neutral colors: (i) collisional resurfacing, which only re-coats a fraction of the surface, producing heterogeneous colors; (ii) compositional differences, producing homogeneous colors; and (iii) cometary outgassing, through which either jets produce a heterogeneous object or a global outgassing event produces a homogeneous object.

We conducted two surveys to search for homogeneity on the surfaces of neutral TNOs in order to help discern between these resurfacing theories a brightness variation survey (BVS) in which we sparsely sampled lightcurves of 38 neutral TNOs to select follow-up targets, and a color variation survey (CVS) of the 9 follow-up targets to densely sample their rotational lightcurves.

Through the BVS, we found that the amplitude distributions of red and neutral TNOs are similar, suggesting a similar collisional histories and refuting the collisional resurfacing mechanism. We detected no close/contact binaries but placed upper limits to the binary fraction of $\sim 12 - 20\%$ at angular component separations of $0.02^{+0.03}_{-0.02}''$, which supports the existence of a turnover in the binary fraction as a function of component separation.

From our CVS results, updated spin distributions also reveal similarity between red and neutral TNOs, supporting the BVS findings. We constrained the spin periods of seven objects, one of which (collisional family member 2003 OP_{32}) was found to have the fastest

measured rotation period of any outer solar system object at ~ 2.4 or 2.6 hours. We found evidence for companions to four of our CVS targets, giving a binary fraction of $> 24\%$ for separations $0.04 \pm 0.02''$. Combined with the BVS and other surveys, these limits suggest that two binary formation mechanisms not involving collisions were simultaneously at work in the Trans-Neptunian belt, one of which was likely the Goldreich et al. (2002) model of dynamical friction.

Table of Contents

List of Tables

List of Figures

Chapter 1

Introduction

The discovery and study of Trans-Neptunian objects (TNOs), small bodies beyond Neptune ($\gtrsim$ 30 AU), have drastically reshaped our understanding of the solar system formation and evolution by offering a glimpse of the early solar system (*e.g.*, Stephens & Noll 2006; Levison et al. 2008; Morbidelli et al. 2008). Although crucial to constraining formation and evolution models, this epoch is difficult to study because almost all observable solar system bodies have since been significantly thermally- and/or dynamically-altered, leaving little to no evidence as to their initial chemical, physical, and dynamical conditions. However, TNOs are cold and typically small enough (having insignificant self-gravity to alter the surface, retaining primordial shape) to have preserved key information about early solar system processes and environments (*e.g.*, Luu & Jewitt 2002; Lykawka & Mukai 2008). Because of the low masses compared to planets, TNOs also have generally easily perturbed orbits that leave a record of the solar system's dynamical history. TNO studies give critical information on interrelations between small solar system bodies and may eventually be applicable to extrasolar planetary systems, allowing dynamical models to be compared to the current planetary architecture, chemical disk models, and disk observations (Jiménez-Torres et al. 2011).

Some key TNO observational findings have delivered a wealth of information about solar system evolution. Stephens & Noll (2006) found a relatively high Trans-Neptunian binary fraction compared to other small solar system bodies ($\gtrsim$ 10% in the Trans-Neptunian belt

with separations $< 1.00''$). The binary frequency distribution with respect to component separation is diagnostic of several different types of dynamical environments (Goldreich et al. 2002; Weidenschilling 2002; Kern & Elliot 2006; Perets & Naoz 2009). TNO solar phase curves (brightening as an object approaches smaller Sun-Target-Earth angles) have also revealed information about TNO surfaces, including fluffy textures(Shkuratov et al. 2002; Rabinowitz et al. 2007; Belskaya et al. 2008). The discovery of the Haumea family (the only known collisional family in the outer solar system) has provided a unique testbed for models exploring the dynamical nature of the outer solar system, past and present. Likewise, uncovering a rich TNO orbital substructure - now divided into dynamical classes - has led to better knowledge of the migration patterns of the gas giants and other planetesimal populations, scattering of ejected rogue planets, and influence of passing stars (*e.g.*, Malhotra 1993; Ida et al. 2000; Gladman & Chan 2006; Lykawka & Mukai 2008).

One of the most intensely debated and yet poorly understood observational discoveries is the most diverse color distribution for any small body population in the solar system. Hydrocarbon ices and organics thought to be common to TNOs and abundant on their surfaces (Brown 2012) are supposed to become darker and slightly redder with time due to irradiation by solar wind, cosmic rays, and high energy EM radiation (Cruikshank et al. 1998; Baragiola 2003; Strazzulla 2012). However, the current surface color distribution (Fig. 1.1) shows that $\sim 32\%$ of these targets have very neutral colors suggestive of fresh surfaces with $V - R$ colors < 0.52 (*e.g.*, Hainaut & Delsanti 2002; Romanishin & Tegler 2007). We consider neutral objects those that fall within the two TNO taxonomies BB and BR, rather than the two TNO taxonomies IR and RR which correspond to much redder objects (Barucci et al. 2005). The diverse TNO color distribution takes on a different shape depending on dynamical population.

Three dynamical classes of TNOs have been identified: (i) resonators - those in mean motion orbital resonance with Neptune; (ii) classicals - those between $\sim 42 - 48$ AU with low to moderate eccentricities; and (iii) scattered disk objects - those with relatively close perihelia ($\sim 25 - 35$ AU) and high eccentricities (Fig. 1.2). Resonators, which have a

range of eccentricities and semimajor axes, show different bulk colors depending on the resonance, with the 5:3 and 7:4 resonances having ultra-red colors, the 4:3 and 5:2 having moderately red colors, and the 2:1 and 3:2 populations displaying a wide variety of colors (Sheppard 2012). The low- to moderate- eccentricity class between $42 - 48$ AU are known as classicals, and are further divided into two distinct groups based on their colors. The dynamically "hot" classicals have higher inclinations ($i > 12°$) and neutral colors whereas the "cold" classicals ($i < 12°$) are ultra-red in color (Peixinho et al. 2004, 2008). Although a darker, ultra-red surface would imply long-term irradiation for the simple hydrocarbons detected on TNOs, some cold classicals have high albedos suggesting a rejuvenated surface (Moroz et al. 2004; Brunetto et al. 2006; Noll et al. 2008; Brucker et al. 2009). Lastly, scattered disk objects show a binomial color distribution similar to Centaurs (which have perihelia > 5.2 AU and semimajor axes < 30.1 AU; Tegler et al. 2008).

There are three leading theories that address the cause of unusually neutral TNO colors: (i) collisional resurfacing, in which impactors excavate and expose the icy, pristine, spectrally-blue subsurface; (ii) intrinsic compositional differences, in which some TNOs formed within different ice condensation lines as others (thereby showing different long-term radiation patterns) and were later scattered outward by Neptune when Jupiter and Saturn reached $2 : 1$ orbital resonance (Brown et al. 2011); and/or (iii) comet-like outgassing, which could be explained by solar radiation gradually penetrating the regolith and reaching subsurface water ice, then excess energy causing structural rearrangement (annealing), releasing gases trapped since TNO formation (Meech et al. 2009).

Cometary-like outgassing and intrinsic compositional differences can occur globally, thereby leaving a homogeneous surface. Simulations of collisions, however, show that for a $\sim$ 100-km sized body, the collisional timescale with a 1-km impactor is 0.07-0.4 Gyr, meaning no more than $\sim 1/3$ of a TNO's surface can be globally coated in ejecta blankets (Durda & Stern 2000). This collisional resurfacing may be comparable to the irradiation reddening timescale of 0.1 Gyr, depending on the exact collisional resurfacing circumstances of the parent body (*e.g.*, size and location; Brunetto et al. 2006; Hudson et al. 2008).

Therefore, collisions likely only produce patches of neutral material, leaving a heterogeneous surface. As a diagnostic toward understanding which resurfacing mechanism dominates, we carried out a survey of surface color variation by observationally searching for color variations with rotation in a sample of 10 TNOs. If we find significant color variation on our targets, then our results would indicate that intrinsic compositional differences were not the source of the color diversity. On the other hand, if we find only evidence of homogeneous surfaces, then the collisional resurfacing mechanism is not the likely cause of the diverse TNO colors. As a by-product of this search, we used the rotational lightcurves to infer information on shape, structure, and density properties, and used the solar phase curves to compare surface properties (such as texture and porosity) of our sample to other types of TNOs and small bodies.

Since this study is founded on photometry of survey targets, choosing a photometry technique that reports the most accurate and precise magnitudes for our datasets was essential, so Chapter 2 presents an exhaustive investigation into this matter. Chapter 3 details (i) sample selection, (ii) the observational setup, and (iii) the conditions during each of the 76 observing runs. A description of the brightness variation survey and its limits on the close/contact binary fraction and neutral TNO shapes are presented in Chapter 4. Surface textures from the solar phase curves that were obtained as part of both the brightness variation survey and the subsequent color variation survey are given in Chapter 5. Constraints on shape, structure, surface homogeneity, and collisional history are presented in Chapter 6 regarding rotational light curves. Lastly, the information gathered about TNO surfaces from each of these studies is compiled in Chapter 7 and used to paint a comprehensive picture of neutral TNO surfaces, to draw implications on the surfaces of redder objects, and to discuss which resurfacing processes may be dominant in the outer solar system.

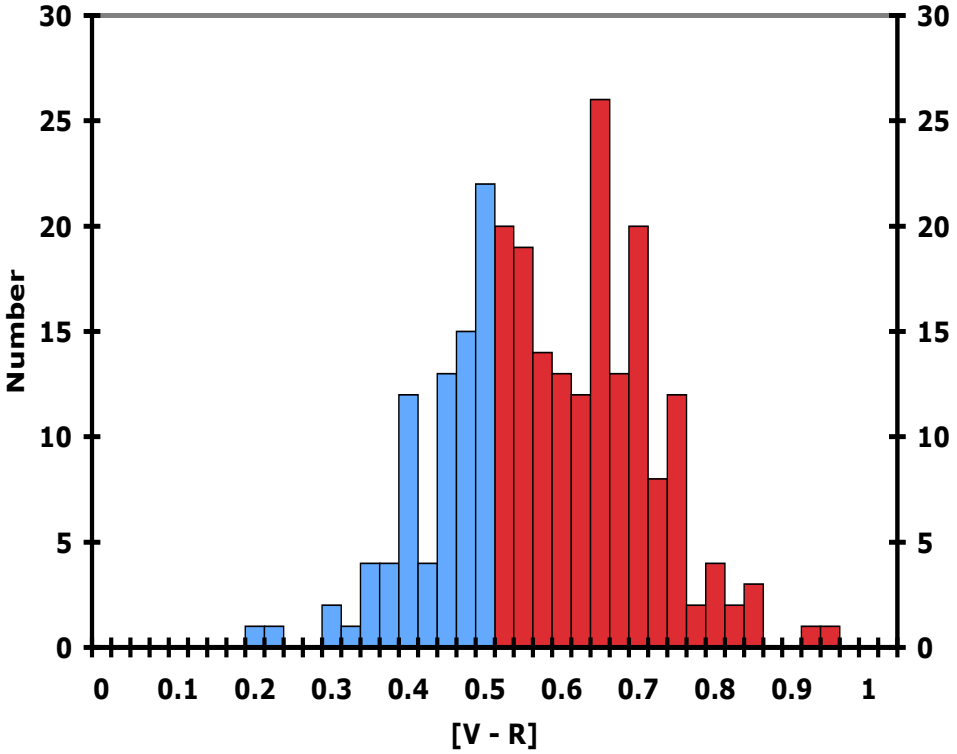

Figure 1.1 TNO $V - R$ color distribution. The data span a wider range of color space than expected for objects thought to become darker and redder as they evolve. The blue group at $V - R < 0.52$ divides neutral from red objects based on the Barucci et al. (2005) taxonomy.

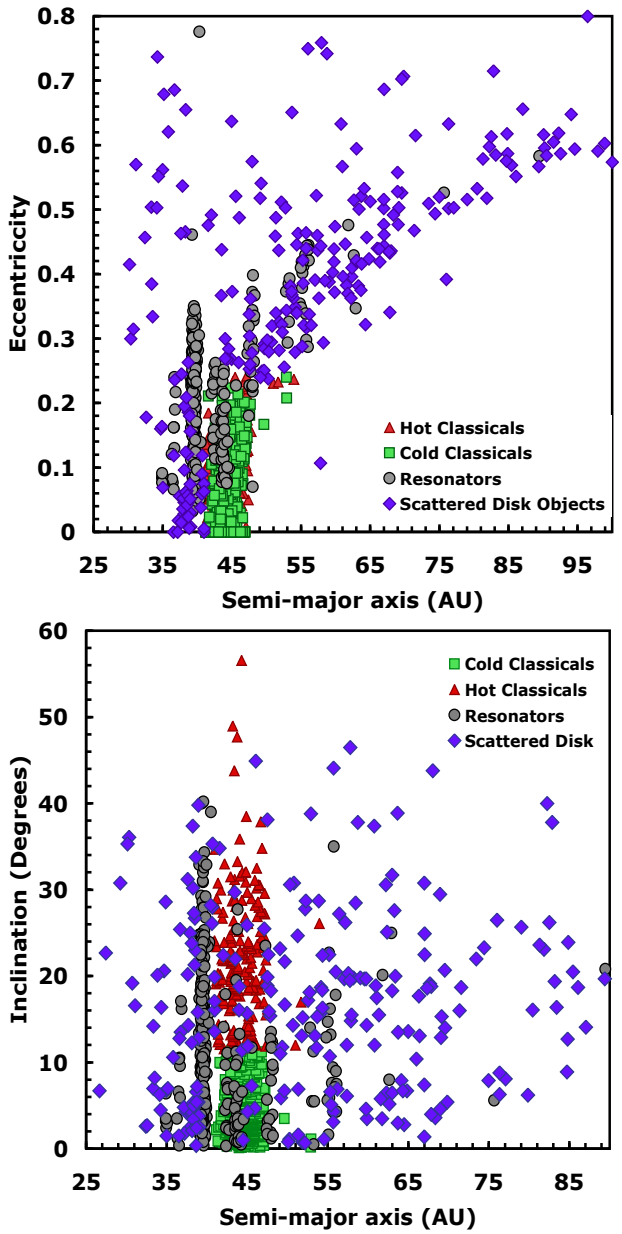

Figure 1.2 Orbital Distribution of Trans-Neptunian objects (TNOs), categorized by dynamical class. Top: Eccentricity vs. semi-major axis, showing the dynamical separation between the low-perihelia, high-eccentricity scattered disk (purple diamonds) and the low- to moderate eccentricity resonators (gray circles) and hot and cold classicals (red triangles and green squares, respectively). Bottom: Inclination (i) vs. semi-major axis, showing the separation between the hot classicals ($i \gtrsim 12°$; red triangles) and cold classicals ($i \lesssim 12°$; green squares).

References

Baragiola, R. A. 2003, Planet. Space Sci., 51, 953

Barucci, M. A., Belskaya, I. N., Fulchignoni, M., & Birlan, M. 2005, AJ, 130, 1291

Belskaya, I. N., Levasseur-Regourd, A.-C., Shkuratov, Y. G., & Muinonen, K. 2008, Surface Properties of Kuiper Belt Objects and Centaurs from Photometry and Polarimetry, ed. M. A. Barucci, H. Boehnhardt, D. P. Cruikshank, A. Morbidelli, & R. Dotson, 115–127

Brown, M. E. 2012, Annual Review of Earth and Planetary Sciences, 40, 467

Brown, M. E., Schaller, E. L., & Fraser, W. C. 2011, ApJ, 739, L60

Brucker, M. J., Grundy, W. M., Stansberry, J. A., Spencer, J. R., Sheppard, S. S., Chiang, E. I., & Buie, M. W. 2009, *Icarus*, 201, 284

Brunetto, R., Barucci, M. A., Dotto, E., & Strazzulla, G. 2006, ApJ, 644, 646

Cruikshank, D. P., Roush, T. L., Bartholomew, M. J., Geballe, T. R., Pendleton, Y. J., White, S. M., Bell, J. F., Davies, J. K., Owen, T. C., de Bergh, C., Tholen, D. J., Bernstein, M. P., Brown, R. H., Tryka, K. A., & Dalle Ore, C. M. 1998, *Icarus*, 135, 389

Durda, D. D. & Stern, S. A. 2000, *Icarus*, 145, 220

Gladman, B. & Chan, C. 2006, ApJ, 643, L135

Goldreich, P., Lithwick, Y., & Sari, R. 2002, Nature, 420, 643

Hainaut, O. R. & Delsanti, A. C. 2002, A&A, 389, 641

Hudson, R. L., Palumbo, M. E., Strazzulla, G., Moore, M. H., Cooper, J. F., & Sturner, S. J. 2008, Laboratory Studies of the Chemistry of Transneptunian Object Surface Materials, ed. M. A. Barucci, H. Boehnhardt, D. P. Cruikshank, A. Morbidelli, & R. Dotson, 507–523

Ida, S., Larwood, J., & Burkert, A. 2000, ApJ, 528, 351

Jiménez-Torres, J. J., Pichardo, B., Lake, G., & Throop, H. 2011, MNRAS, 418, 1272

Kern, S. D. & Elliot, J. L. 2006, ApJ, 643, L57

Levison, H. F., Morbidelli, A., Vokrouhlický, D., & Bottke, W. F. 2008, AJ, 136, 1079

Luu, J. X. & Jewitt, D. C. 2002, ARA&A, 40, 63

Lykawka, P. S. & Mukai, T. 2008, AJ, 135, 1161

Malhotra, R. 1993, Nature, 365, 819

Meech, K. J., Pittichová, J., Bar-Nun, A., Notesco, G., Laufer, D., Hainaut, O. R., Lowry, S. C., Yeomans, D. K., & Pitts, M. 2009, *Icarus*, 201, 719

Morbidelli, A., Levison, H. F., & Gomes, R. 2008, The Dynamical Structure of the Kuiper Belt and Its Primordial Origin, ed. M. A. Barucci, H. Boehnhardt, D. P. Cruikshank, A. Morbidelli, & R. Dotson, 275–292

Moroz, L., Baratta, G., Strazzulla, G., Starukhina, L., Dotto, E., Barucci, M. A., Arnold, G., & Distefano, E. 2004, *Icarus*, 170, 214

Noll, K. S., Grundy, W. M., Stephens, D. C., Levison, H. F., & Kern, S. D. 2008, *Icarus*, 194, 758

Peixinho, N., Boehnhardt, H., Belskaya, I., Doressoundiram, A., Barucci, M. A., & Delsanti, A. 2004, *Icarus*, 170, 153

Peixinho, N., Lacerda, P., & Jewitt, D. 2008, AJ, 136, 1837

Perets, H. B. & Naoz, S. 2009, ApJ, 699, L17

Rabinowitz, D. L., Schaefer, B. E., & Tourtellotte, S. W. 2007, AJ, 133, 26

Romanishin, W. & Tegler, S. C. 2007, in Astronomical Society of the Pacific Conference Series, Vol. 371, Statistical Challenges in Modern Astronomy IV, ed. G. J. Babu & E. D. Feigelson, 210

Sheppard, S. S. 2012, AJ, 144, 169

Shkuratov, Y., Ovcharenko, A., Zubko, E., Miloslavskaya, O., Muinonen, K., Piironen, J., Nelson, R., Smythe, W., Rosenbush, V., & Helfenstein, P. 2002, *Icarus*, 159, 396

Stephens, D. C. & Noll, K. S. 2006, AJ, 131, 1142

Strazzulla, G. 2012, in EAS Publications Series, Vol. 58, EAS Publications Series, 187–194

Tegler, S. C., Bauer, J. M., Romanishin, W., & Peixinho, N. 2008, Colors of Centaurs, ed. M. A. Barucci, H. Boehnhardt, D. P. Cruikshank, A. Morbidelli, & R. Dotson, 105–114

Weidenschilling, S. J. 2002, *Icarus*, 160, 212

Chapter 2

Photometry Experiments

2.1 Introduction

This chapter addresses the treatment of the data once acquired. A justification of the sample selection and description of the targets and observing circumstances is given in Chapter 3. Photometry is the practice of measuring the flux and corresponding uncertainty of astronomical objects. Many different photometry approaches have been developed, each of them optimized for a particular set of goals, and choosing which approach to adopt is a difficult task. The science goals, intrinsic nature of the target(s), and instrumental properties dictate which of the dozens of available photometry algorithms might be most effective. Some scientists, such as those with high-volume computing needs like the Sloan Digital Sky Survey group, develop their own codes, comparing them to popular algorithms (*e.g.*, Ivezić et al. 2004; Lupton et al. 2002; Alard 2000). Other groups try to optimize existing software for a specific task. For example, Becker et al. (2007) tested several algorithms for meeting LSST science requirements, and Ferrarese et al. (2000) assessed the performance of two algorithms in crowded fields.

Photometry packages currently distributed for public use can be roughly divided into three groups: those that perform aperture photometry, those that construct a model point-spread function (PSF) from field objects, and those that blend the two. It is now generally accepted that low signal-to-noise (S/N) object magnitudes are most accurately recovered

through PSF-fitting since the errors are dominated by background uncertainty (*e.g.*, Handler 2003; Becker et al. 2007). Conversely, high-S/N objects are best represented by aperture photometry, which are more forgiving than PSF-fitting techniques of out-of-focus frames and intrinsic morphological complexities (which may be time variable) in the PSF.

In addition to accurately measuring flux, a second challenge to photometry is absolute calibration, which converts the flux measured in instrumental units (or instrumental magnitudes) into true apparent magnitudes. Absolute calibration takes into account the zeropoint (the scaling factor in magnitude units), the atmospheric extinction, and the color conversion from those of the filters used to the standard color system. We shall not discuss calibration of this dataset in this paper, which focuses only on the initial flux measurements.

Moving targets are typically comets and asteroids, which by virtue of their size, distance, and low reflectivity, are very faint; thus, observations of the primary science targets are typically low S/N, making optimal sky determination critical. Unless imperfections in the optics distort the field, fixed point sources in the field should have exactly the same PSF that can most likely be described by a fitting function. Moving targets, however, will produce a trailed PSF that may not be approximated by a function, with the amount of trailing dependent on the object's proper motion. No publicly available photometry software was designed to handle trailed PSFs. We conducted the first study that quantitatively determines which available photometry algorithm optimizes accuracy and precision for faint moving targets. We familiarized ourselves with 15 different aperture or PSF-fitting algorithms and tested which one most accurately and precisely reproduced the true light curve of a moving object with a known rotational light curve.

2.2 Observations

One way of testing a technique's accuracy is to use it on data with a known trend and measure the root-mean-square (RMS) of the residuals against a model. We acquired data for the Trans-Neptunian object 1996 TO_{66} as part of a campaign to determine the object's light

curve. As the purpose of this paper is simply to use this dataset to explore methodology, we will not comment on the campaign itself, nature of the target, or the details of the model and instead defer that information to an upcoming publication (Hainaut *et al.*, *private comm.*).

The data were obtained on September 22, 2011 using the University of Hawai'i (UH) 2.2-m telescope with the Kron-Cousins R-band filter and the Tek (2048×2048) CCD camera, which has a pixel scale of $0.219''$/pixel. The sky was not photometric due to occasional cirrus clouds. We measured a median seeing of $0.95''$ FWHM, which varied by $\sim 20\%$ over the course of the 1996 TO_{66} observations. The focus was checked before beginning the 1996 TO_{66} observations, but we could not change the focus later as the night progressed due to technical difficulties. Consequently, a slightly triangular-shaped PSF indicative of poor focus was present in two of our images (Fig. 2.1). Exposure times varied between 900 and 1100 seconds (the median being $945s$) to achieve our S/N goal of ~ 30, which is still too faint to have well-defined PSF wings. This was done in an attempt to achieve a constant S/N under changing transparency and seeing conditions.

Non-sidereal guiding was used so that the target was not trailed. The target's motion averaged -2.7$''$/hr in R.A. and -0.8$''$/hr in Dec., corresponding to $\sim 0.72''$ of trailing per frame for stars, or a theoretical PSF length-to-width ratio (or trailing aspect) of ~ 1.8 for field stars and 1.0 for the target. The best-fit models using the tphot PSF-fitting algorithm, however, give trailing aspects of 1.5 for the field stars and 1.1 for the target; the difference between the theoretical and actual trailing aspect is likely attributable to telescope guiding problems (Fig. 2.2). We stress that this amount of trailing is considered minimal compared to typical rates of inner solar system objects (Vereš et al. 2012). The medians of the peak and background counts were ~ 3350 and ~ 2550, respectively, and the median flux within a 7-pixel aperture was 23000 ± 600 counts. We calculate a medan S/N of ~ 35 using the tphot algorithm (discussed in Section 2.4.3).

Figure 2.1 shows both 1996 TO_{66}'s track along the sky and the target-centered subsections of the ten 1996 TO_{66} images. The observations interleaved 1996 TO_{66} with another target over 8.12 hours, until 1996 TO_{66} reached airmass 2.0. Preliminary results from

Hainaut *et al.* (private comm.) give a light curve amplitude of ~ 0.14 magnitudes and a rotation period of 7.94 ± 0.33 hours. The model light curve reproduces all data obtained as part of a multi-year, multi-telescope, multi-solar phase angle observational campaign to determine the light curve of 1996 TO_{66}. Our observations correspond to rotation phases (ϕ) of $0.114 - 0.989$, or 87.5% of the full rotational light curve. One data point was consistently fainter than the model by $\gtrsim 0.1$ magnitudes regardless of the technique used, likely due to a bad pixel that was not identified during construction of a bad pixel mask, so we excluded it from analysis (Fig. 2.1).

2.3 Initial Image Processing

We prepared the images for analysis using IRAF's "CCDPROC" package (Tody 1986), applying bad pixel, bias, and overscan corrections and flat-fielding with dithered twilight sky frames. To exclude field stars from the bad pixel mask construction, we median-combined the brightest twilight flats to produce a stacked bright flat, then repeated that process for a stacked faint flat in the same filter. We fed the ratio of the stacked bright to the stacked faint flat to the IRAF "CCDMASK" task, which computes a bad pixel mask from a ratio image, then used the "fixpix" task within CCDPROC to interpolate over bad pixels. We noted that in two images, a bad pixel was relatively close to the target – 8 pixels from the target centroid in Frame 3 (Fig. 2.1), and 9 pixels from the target centroid in the Frame that was excluded from analysis (See Section 2.2). The bad pixel regions were visually and quantitatively comparable to the local sky after correction (as it should be), so their proximity to the target was of no consequence to our photometry. Afterward, we fit a polynomial to the overscan for line by line bias subtraction and trimmed the data. We then combined 20 bias frames taken at the beginning and end of the night to produce a stacked bias frame for subtraction.

We acquired seven R-band twilight sky flats at the beginning of the night and six at the end, all below the limit of the linearity regime for the chip. However, because the dust

pattern changed multiple times within the 1996 TO_{66} observation window, the twilight flats were not always representative of the field. Consequently in the flattened images, residuals from improperly-corrected dust donuts can be seen in a third of our images, possibly influencing background determination for field stars in affected areas. The residual dust donuts were not close enough to the target to affect the target photometry from any of the algorithms. Lastly, we corrected for cosmic rays using the "COSMICRAY" task within IRAF's "CRUTIL" package. We found that a threshold of 3.8σ relative to noise in R-band images effectively removed most cosmic rays without falsely flagging real sources. The entire reduction procedure from bad pixel to cosmic ray correction did not differ between photometry algorithms.

After reduction, we measured the effective gain and read noise by doing a linear least squares fit to the square of the sky noise over the sky, all in units of ADU. The slope of the fit is the inverse of the gain, and the y-intercept is the square of the read noise in ADU. We measured a gain and read noise of ~ 1.31 e^-/ADU and ~ 21 e^-, respectively.

2.3.1 Detection, Differential Photometry, and Systematic Errors

Field source detection for all photometry algorithms was done using Source Extractor (SExtractor), which identifies point sources as a user-defined minimum number of adjacent pixels (sharing either a border or a corner) that are above a specified detection threshold (Bertin & Arnouts 1996). If the intensity distribution of a cluster of source pixels shows a distinct saddle point, the surrounding peaks are considered to belong to two separate objects. SExtractor then measures the shape and centroid of each object, eliminates bright object artifacts, and further cleans the source list. Because we find this rigorous detection method very effective at identifying, de-blending, and broadly classifying all field sources, we used it to produce a coordinate list for field stars.

We restricted field stars for further analysis to those that had S/N >10 within an aperture diameter of $4\times$FWHM, as preliminarily determined by SExtractor's "MAG_BEST" routine. To correct for extinction and occasional clouds for each algorithm, we applied an

offset correction for each frame to bring the field stars brightnesses to the same level. This correction was computed by removing the median offset in bright field star magnitudes between frames.

We recognize that systematic errors - a bias in the way the photometry was performed, not in the data itself - may be present due to over- or under-sampling of the background, non-optimal criteria for rejecting contaminants, and/or source flux threshold being too low or high. To test and correct for systematic errors, after removing the shift between frames for cloud correction, we subtracted each star's median magnitude for the night and fit a gaussian to the distribution of differential star magnitudes in that frame. The HWHM of the gaussian fit (σ_g) is the same as the total error (σ_{total}) and should be a sum in quadrature of the statistical and median systematic error for each target (σ_{stat} and σ_{sys}, respectively). Therefore, $\sigma_{sys}^2 = \sigma_g^2 - \sigma_{stat}^2$. If $\sigma_g \lesssim \sigma_{stat}$, then we considered $\sigma_{sys} = 0$. We note that this is the systematic error for field stars, not the untrailed target. Because the trailed field stars cover a larger number of pixels, the probability of contamination and erroneous background sampling is higher than for the target. Therefore, these systematic errors may be overestimated for the target. Figure 2.3 shows a typical gaussian fit to the differential magnitude distribution. We performed Monte Carlo simulations of random gaussian distributions with different sample sizes and found that fitting greater than 30 field stars gave a $> 95\%$ chance of getting a real and reasonable solution. We found that σ_g varied depending on the absolute magnitude range of the stars used, with brighter stars giving a smaller σ_g than fainter stars. Therefore, to determine the systematic error most representative of the target, we considered only the $\gtrsim 30$ field stars closest in magnitude to the target (R-magnitude ~ 21.3). Lastly, to fit the data to the model, we tested relative offsets in increments of 0.0001 magnitudes within 0.1 magnitudes of the median-subtracted target magnitudes and used the offset that gave the lowest RMS residuals against the model.

2.4 Aperture Photometry Algorithms

Aperture photometry packages usually differ in their definition of aperture size and shape and/or in the way the background is determined, but they are popular largely because they are not sensitive to irregular PSF shapes. Determining the background correctly is one of the fundamental challenges of photometry. Howell (1989) found that the flux measured within an aperture radius is extremely sensitive to correct background measurement and subtraction. If the sky is overestimated, then too much background is subtracted, and as the aperture size is increased, the sum of counts within the aperture decreases rather than yielding a constant flux. This effect is less prevalent for brighter objects, whose PSF wings are more distinct from the noise out to larger radii. It is therefore recommended not to use a bright star alone to determine which aperture radius captures a large percentage of the source flux ($\gtrsim$ 95%) because a faint object's flux at that radius may already be significantly contaminated by background. Howell (1989) also found that different background measurement methods (*e.g.*, median vs. mean, etc.) yield different accuracies. They found that a weighted mean is more accurate for fainter objects but underestimated uncertainties for brighter objects.

In addition to proper background subtraction, variation in the PSF across the frame caused by optical aberrations is an important consideration with aperture photometry. Most aperture photometry algorithms, save SExtractor, do not allow for variation in aperture size across a chip, leaving it difficult to choose the best constant aperture radius for the entire frame. In a detailed study using the HST WFPC-2 CCD camera, Tanvir et al. (1995) found that radial variation in the images was significant ($\sim$ 3%), and Ivezić et al. (2004) found up to a 15% difference in FWHM across the CCD cameras for the Sloan Digital Sky Survey (SDSS). Although these are extreme examples of wide field imagers with large distortions, it is important to check for spatial variations. We saw no such distortion in our images to a fraction of a percent, so no spatially-variant aperture was necessary.

Popular aperture photometry algorithms that were compared include the PHOT task within the IRAF/APPHOT package and Source Extractor (SExtractor). We also implement the tphot aperture photometry technique, optimized in centroiding and reducing background contamination. Ours is the first publication of the tphot software. Lastly, the Aperture Photometry Tool (APT) was developed as an educational tool, and because of its ease of use, possible similarity in quality to SExtractor, and application to a wider populace, we include it in our study (Laher et al. 2012b).

2.4.1 The IRAF/APPHOT PHOT task

The PHOT task is widely used for traditional aperture photometry (Tody 1986). An identical task can be found within the DAOPHOT package. Depending on the sky in the vicinity of the target, there are several opportunities to change the way the background is measured within PHOT, four of which are tested here (each on all 10 images) with IRAF version 2.14.1. PHOT gives the option of rejecting sky annulus pixels that are above or below a user-defined sigma-threshold, which we chose to be 2.5. Photometry for both the target and the field stars were done with these settings.

To determine the aperture radius, we measured a curve-of-growth on several stars of different magnitudes spread over the chip and identified the aperture radius that contained 99.5% of the light, with weighting given to brighter stars. In general, we found that this aperture only varied by $\lesssim 4\%$ between bright unsaturated stars and fainter stars at S/N ~ 30, indicating that the background was measured accurately. We repeated this process for all 10 images used and took the largest frame-specific aperture (18 pixels, or $\sim 3.9''$) as the fixed, unweighted aperture radius for all images. The aperture chosen was used for both the trailed stars and the target.

One concern in choosing a photometric aperture radius for moving targets is that the target PSF should be narrower than trailed field stars. Consequently, the aperture chosen from field star curves of growth may be larger than the target's 99.5% flux radius, causing an increased contribution from sky noise and potential faint background source contamination.

Centered sky annulus

If the target moves along a track free of significant background contaminants within the sky annulus (see Fig. 2.1), then a target-centered sky annulus best represents the sky in the photometric aperture. For fainter point sources, the PSF wings are indistinguishable from random noise beyond the aperture containing 99.5% of the target flux (assuming the CCD is flat), so the choice of inner radius of the sky annulus is somewhat arbitrary, so long as it is outside the aperture. For bright point sources, however, a small amount of noticeable source flux may be in the region outside the aperture, affecting the magnitude uncertainty. To be sure we were clear of the PSF wings of these bright stars, we defined the inner radius of the annulus at $6''$, or 28 pixels (10 pixels greater than the aperture). We chose the outer bounds of the sky annulus to be $11''$ (50 pixels) to ensure good background sampling.

Off-center, manual sky measurement

If the sky annulus centered on the target contains a significant amount of unavoidable contamination from background sources, one can manually measure the sky background away from the target. A manually-defined sky annulus would also be necessary for active comets to avoid dust trails. We used a sky aperture of the same area as the centered sky annulus in Section 2.4.1 and measured the sky 10-15 times in a radially-isotropic distribution within $\sim 17.5''$ (80 pixels) of the target for every frame, avoiding overlap with the photometric aperture or contaminants. The final sky and sky noise levels used in the photometry for each frame were the average of the individual measurements in that frame. Manually measuring the background at several locations off-center from the photometric aperture is too time-intensive to execute for every field star in every frame. Thus, for field stars only, we used PHOT's non-interactive centered sky annulus technique described in Section 2.4.1. Since the systematic error is empirically determined from the dispersion in differential field star magnitudes, the systematic error per frame was the same as determined in the centered sky annulus method.

Small aperture + aperture correction

Decreasing the photometric aperture excludes some sky noise and nearby contamination but may also exclude source flux. We used bright field stars with well-defined PSF wings to estimate the aperture correction, or amount of source flux lost by using a smaller aperture. We then added back the residual magnitude estimated from our aperture correction to the magnitudes measured with the smaller aperture for the target. With moving targets, we risk that the untrailed target may not be accurately represented by the aperture correction given by trailed field stars, which have a wider PSF than the target.

The choice of the small aperture size is somewhat arbitrary, so long as it is consistent from frame to frame, so we chose a small aperture radius of $\sim 2.2''$ (10 pixels) to avoid the cosmic ray hit seen in Frame 1 (Fig. 2.1). We measured the aperture correction between the small aperture and a large aperture at $\sim 3.9''$ (18 pixels), using only field stars with $\sigma_{total} \leq 0.02$, to ensure good flux sampling in the PSF wings. Field stars that gave aperture corrections more than 2 standard deviations from the mean for that frame were excluded from the computation, leaving on average 16 field stars per frame to determine the aperture correction. The standard deviation of these stars' aperture corrections (σ_{ap}) was used as the error on the frame's aperture correction, which was added in quadrature to σ_{stat} and σ_{sys} to compute σ_{total} ($i.e. {\sigma_{total}}^2 = {\sigma_{stat}}^2 + {\sigma_{sys}}^2 + \sigma_{ap}^2$). To measure the sky, we used the sky annulus settings described in Section 2.4.1.

Small aperture + aperture correction photometry on sky-subtracted images made with IMARITH

There are sometimes faint background contaminants close to the target that render inaccurate sky determination or add to the target flux. These background sources may not be obvious in individual frames, but can be seen in a stacked image. To correct for these contaminants, we constructed a median-combined sky composite (to remove the moving target), scaled the sky composite to match the mode of an individual frame's background, and subtracted the scaled, aligned composite from each frame using the IRAF "IMARITH"

task. The sky composite was made from 8 of the 10 science frames, with frames 8 and 9 excluded because the target's location did not change enough relative to other frames to remove all target flux from the median sky composite. The subtracted images should be free of faint sources, but residuals from subtraction close to the centroid of brighter sources are often apparent, caused by inaccurate alignment before subtraction and/or the changes in seeing/image quality or non-linear regime of the detector. We also found that inaccurate alignment before subtraction led to substantial inaccuracies in background measurement, so we used dozens of bright field stars to compute a shift as accurately as possible. Figure 2.4b shows one of the individual frames used in our analysis after IMARITH sky subtraction.

Sky subtraction takes place *before* performing photometry, so to assess the improvement to the results, we apply the same photometry technique used on frames without sky subtraction and compare the outcomes. We chose to implement the aperture correction photometry method (Section 2.4.1) because it is believed to produce more accurate results than the centered and off-center sky annulus methods described in Sections 2.4.1 and 2.4.1. Field star photometry was performed on the frames before sky subtraction, and photometry on the target as performed after the subtraction.

Small aperture + aperture correction photometry on sky-subtracted images made with ISIS

Section 2.4.1 describes how sky subtraction can improve photometry by removing background contaminants, but constructing a sky composite is a sensitive function of determining the correct sub-pixel shift between stars in different frames and scaling the composite to match each frame. The ISIS software package (Alard 2000), which internally determines shifts, median-combines frames, and subtracts the composite from individual images, was designed to do the best possible job of sky composite construction and subtraction. The main differences between using IMARITH and using ISIS to build a sky composite are that: (1) the ISIS composite must be built from frames with the best seeing, and (2) before subtracting the composite, ISIS convolves it with a kernel solution

for the individual frame, matching the FWHM of the sources in the composite to the same sources in the individual frame. We made the ISIS sky composite from the five frames with the best seeing, with a mean seeing of $\sim 0.99''$ compared to the remaining five frames' mean seeing of $\sim 1.08''$.

ISIS can also perform differential photometry after sky subtraction. Although Irwin et al. (2006) found that using ISIS instead of traditional aperture photometry did not improve photometry results for star clusters, Alard (2000) noted an improvement by up to a factor of 20 in ISIS photometry over DoPHOT. However, we were not able to fully adapt the ISIS software for moving objects, even when shifted stamps showing the object at the same position were manually constructed and fed into the algorithm. Therefore, we could not make use of ISIS's photometry capabilities for our moving target; instead, we only used it for sky subtraction. Figure 2.4 shows that ISIS offers considerable improvement over IMARITH in removing background sources. The standard deviation within an aperture radius of $\sim 4''$ (or 18 pixels) at the location of subtracted field stars was reduced by a factor of ~ 1.7 by using ISIS rather than IMARITH to perform sky subtraction.

2.4.2 Source Extractor

Source Extractor (hereafter SExtractor) is a photometry algorithm that was designed to quickly identify and classify field objects and to perform aperture photometry on both extended and point sources. We used SExtractor 2.5.0 (Bertin & Arnouts 1996).

One of the main differences between SExtractor and other aperture photometry algorithms is that SExtractor constructs a background map for the entire image rather than measure the background within a defined annulus for each object. The background map is locally determined over a defined mesh size, and pixels above a 3σ threshold within the mesh are iteratively discarded from the background computation until no pixels above this threshold remain. If the field is considered crowded (*i.e.*the sky noise drops less than 20% per iteration), then the final background within the mesh is computed in a different way from an uncrowded background (Holwerda 2005). The final background map is a bi-cubic-

spline interpolation over all regions. By visual comparison between the background map and an individual frame, we found that a mesh size of 64×64 pixels and a smoothing-region size of 3 gave the most accurate background map.

SExtractor also offers flexibility in the aperture shape. There are five types of apertures available within SExtractor, all of which were tested in this study: MAG_APER, MAG_AUTO, MAG_ISO, MAG_ISOCOR, and MAG_BEST. The MAG_APER option lets the user define a fixed circular aperture to place over all identified sources in a frame. We chose an aperture radius at 4×HWHM (which theoretically encompasses 99.994% of the object's flux) for each frame. Using the MAG_AUTO aperture choice will internally determine an aperture at the Kron radius, defined as the radius that contains 90% of a source's flux, for each identified field source (Kron 1980). The aperture's ellipticity and position angle with respect to a row is then computed via the second order moment on each object. MAG_ISO draws an aperture around all adjacent pixels above a defined detection threshold, making it highly flexible for irregularly-shaped PSFs and extended sources. We chose a recommended detection threshold of 1.5σ above the background (Holwerda 2005). The MAG_ISOCOR aperture type is a crude method of determining an aperture correction to the MAG_ISO magnitudes, assuming the object's PSF is an axisymmetric Gaussian (Holwerda 2005). Lastly, MAG_BEST is a combination of MAG_AUTO and MAG_ISOCOR; when the neighboring source contamination reaches 10%, MAG_ISOCOR measurements are returned, otherwise MAG_AUTO measurements are returned.

2.4.3 The tphot aperture photometry technique

The tphot routine has three basic components: (1) triggering on a potential object, (2) aperture photometry, and (3) PSF fitting photometry. The trigger function identifies all pixels that are a local maximum out to a specified radius (nominally 5 pixels) and that exceed a threshold level (specified as an absolute level or as a S/N above sky level and noise).

Tphot performs photometry on all triggered objects, but this these calculations may be rejected according to a number of tests, including inadequate S/N, a fitted centroid that moves from the brightest pixel, a profile that is too broad or narrow, etc. Tphot offers the option of using an external file of object positions.

The uncertainty in the photometry is based on a noise model that is implemented using two parameters, a gain (e^-/ADU) and a bias level. The "bias" level is subtracted from the image and the noise is then taken to be the square root of the number of electrons. The "bias" level can be negative if the image preprocessing has already subtracted a sky level, and it can be augmented according to read noise variance.

The aperture photometry function of tphot performs a fit for the sky level near an object, and then calculates the total flux within a specified aperture, less the sky contribution. For maximum accuracy the aperture should be 1.5 FWHM in radius (Tonry 2011). For robustness in the presence of neighboring objects, tphot starts by calculating the median flux in annular rings around the object of interest. The sky level is determined by fitting the outermost rings beyond a specified radius with a constant plus r^{-3} object profile. The object flux is calculated as the sum of pixels within the aperture radius, less the sky level. This algorithm has proven to be very accurate and robust for bright objects and fields that may be somewhat crowded.

2.4.4 APT

The Aperture Photometry Tool (version 2.1.9, hereafter APT) is a relatively new algorithm intended as both a professional and an educational tool capable of performing straightforward and accurate photometry (Laher et al. 2012a). Its main feature is its graphical user interface, encouraging visualization of the process and visual checks on aperture and sky annulus choices. Because of its simplicity, APT was not designed for or tested on crowded fields. The user defines the sky annulus and the radius, ellipticity, and position angle of the photometric aperture. There are also options to remove the median or mean background, perform photometry in batch mode, define an aperture correction, and include/exclude

manually-selected pixels from the aperture radius. APT only accepts integer input pixels, then upon the user's request, it internally recomputes the centroid to 0.01 pixel resolution. The APT help manual states that this sub-pixel centroiding may perform poorly, especially in more crowded fields. The user can also define rejection limits (in counts) above and/or below which sky annulus pixels are excluded from background determination.

Performing photometry manually for every field source was impractical because we had over 100 objects in our target list, so we chose to operate in batch mode, which meant using the same aperture and sky annulus settings across the entire frame. We chose a fixed circular photometric aperture of 18 pixels, inner-sky radius at 28 pixels, and outer-sky radius at 50 pixels (the same settings used in Section 2.4.1). We also chose to perform median background subtraction and make use of the pixel exclusion feature to remove the cosmic ray hit in Frame 1 (Fig. 2.1). We used the APT-computed sky level and sky sigma in the target's sky annulus to determine the 2.5σ rejection threshold for background determination in each frame.

2.5 PSF-fitting Algorithms

PSF-fitting algorithms differ amongst themselves primarily in the way the model is stored for later use (Stetson 1992). Some fit an analytic function (Gaussian, Lorentzian, or a combination thereof) while others determine an empirical PSF model through numerical interpolation. Some PSF-fitting algorithms also offer a spatially-variable solution in case the PSF varies across the chip. Because PSF-fitting routines theoretically exclude more background contamination from the source flux than an aperture, they offer a potential advantage in accuracy and precision of faint objects (Handler 2003).

A few comparison studies of PSF-fitting algorithms have been published. Becker et al. (2007) found that DAOPHOT outperforms DoPHOT by a factor of 1.5-4 in accuracy for fixed targets, but Friel & Geisler (1991) and Schechter et al. (1993) noted that DAOPHOT can be susceptible to background source contamination. However, the usefulness of these

algorithms for moving target photometry has not been explored. The fact that trailed field stars are used as templates for the PSF model presents a problem to moving targets in that the model will not exactly represent the untrailed target. We investigate the accuracy and precision of the popular PSF-fitting algorithms DAOPHOT and DoPHOT and the profile-fitting capabilities of the new tphot algorithm.

2.5.1 DAOPHOT

DAOPHOT is one of the most popular photometry algorithms. This software package operates within IRAF and exploits the strengths of both analytic and empirical approaches to PSF-fitting. First, an analytic function is fit to manually-inspected template stars without overlapping PSFs, and errant pixels in the source PSF (either cosmic ray hits or bad pixels) are down-weighted and local background is determined. Six different types of analytic functions can be fit - Gaussian, Lorentzian, 2 modified Lorentzians, and 2 Gaussian + Lorentzians (Stetson 1992). The model that returns the lowest scatter is subtracted from each template star, and the average residuals are stored in a two-dimensional lookup table to account for any flux lost in the analytic model. The user can specify whether or not the PSF varied across the chip, in which case DAOPHOT will compute additional lookup tables representing the linear or quadratic change in flux across the frame. To ensure that flux is not artificially enhanced or decreased due to spatially-variant lookup tables, the net volume of the higher-order tables is forced to be zero. The option for a spatially-variable model solution have sometimes been implemented with difficulty, even failing altogether as they did for us (Irwin et al. 2006). For each field source, the model is scaled down to the flux within a defined fit radius (usually the FWHM), and the PSF model is iteratively fit to field sources.

We altered the many input free parameters as recommended by the DAOPHOT reference guide, using the DAOEDIT task to determine and define each image's FWHM, background, and sky noise (Davis 1994). We defined the inner-sky radius as 4×FWHM, the outer-sky radius as 8×FWHM, and the radius within which the model computed for template stars

is computed as $(4\times\text{FWHM})+1$, following the Davis (1994) suggestions. Because the target was moving and we were comparing photometry for individual frames, we were unable to use DAOPHOT's ALLFRAME task, which performs photometry on a stacked image (Becker et al. 2007; Ferrarese et al. 2000).

2.5.2 DoPHOT

DoPHOT (Mateo & Schechter 1989; Schechter et al. 1993) was developed as an alternative fitting algorithm to DAOPHOT, because determining the appropriate settings for each image and computing the model PSF for DAOPHOT is very time-consuming. DoPHOT requires minimal user interaction and optimizes speed; we used version 4.1. The user inputs estimates for the background, seeing, gain and read noise, which are used by the algorithm to identify sources above a defined threshold. These sources are fit with an analytical power-law function to determine a best-fit model, which is then subtracted from the frame. Noise is added back to the black sky patches left after star subtraction to ensure that the patches resemble the sky noise. The detection threshold is then lowered to fit a model to fainter sources, which are then subtracted. The brighter sources already identified are added back into the frame and refit, now without possible contamination from faint sources. The improved model parameters are saved, and the magnitude, background, and poisson noise close to the source is recorded. These iterations continue for lower and lower thresholds (*i.e.*fainter objects) until no additional stars are detected. A final model weighted by S/N is computed from all objects that are unambiguously identified as point sources, then all of the objects detected in the image are refit with the improved model. We used DAOEDIT's background and FWHM measurements (see Section 2.5.1) for the DoPHOT input background and seeing estimates, respectively. Otherwise, we preserved the default setting as recommended by the DoPHOT manual (Mateo & Schechter 1989).

2.5.3 The tphot PSF-fitting technique

After performing an aperture photometry calculation (Section 2.4.3), tphot also performs a PSF fit to each potential object. Using the position and crude FWHM from the aperture fit, tphot does a least-squares fit of an elliptical "Waussian" (Gaussian truncated at the r^6 term) profile. Tphot can be requested to perform profile fits of two parameters (flux and sky), four parameters (plus position), or seven parameters (plus PSF shape). It also can fit a trailed profile, substituting trail length for major axis. The resulting major axis a, minor axis b, and peak value P can be multiplied to obtain a value $a\,b\,P$ that is proportional to the total flux of the Waussian.

Depending on the application, tphot may be run multiple times. It is most commonly run once at a relatively high S/N threshold to obtain aperture photometry and PSF profile shape parameters for bright stars. It is then rerun at a low S/N threshold and a four parameter fit, forcing all stars to a common PSF profile. The $a\,b\,P$ value provides accurate, relative photometry for faint objects as well as bright ones, and the aperture photometry of bright stars from the previous iteration provides net fluxes.

In this image there are a comparable number of galaxies and stars; a different galactic latitude or magnitude limit would be different. We did not attempt any automatic star-galaxy classification for this application. Instead, we chose the objects whose major axis a falls below the median, and then use the median values of those objects for a, b, and θ as representative of stellar PSFs. A mode of all values less than the median a, b, and θ would have also been suitable. Measuring the change in aperture photometry of stars between different frames then correcting for the change put all images on the same photometric scale. The RMS for these comparisons was less than 0.01 magnitude.

Although the target was trailed, its trailing amount was small enough relative to the seeing that we did not bother to use the trailed profile function of tphot.

2.6 Photometry Algorithms not Explored here

We were not able to test all existing photometry algorithms. Becker et al. (2007) find that the Photo software used on the Sloan Digital Sky Survey performs high-quality photometry on both extended sources and field stars, but it is not portable or flexible and was thus not available to install. Three other prominent photometry packages, ISIS, MOMF, and DIA, could not be modified for use on data for a moving target, though they did offer promising improvements to our photometry results (Kjeldsen & Frandsen 1992; Alard 2000; Wozniak 2000; Lee et al. 2010). These packages all perform photometry on fixed objects in median-sky subtracted images, identifying low-level deviations from the nightly median. The main advantage of these methods over traditional sky-subtraction is the process of convolving a "best-seeing" sky composite with the FWHM of individual frames before subtraction, so that the PSFs match and no residual background source flux remains on the chip after subtraction, with the exception of saturated pixels (see Fig. 2.4 and Section 2.4.1). Because the change in magnitude is measured from sky-subtracted images, no absolute magnitude calibration is offered in any of these methods. These difference-image techniques may also present a challenge to moving targets in that the FWHM would not be the same for the target as the trailed stars, so the convolution would be incorrect and residual flux would always be present. Section 2.4.1 details how we were unable to adapt the promising ISIS software for our moving target. We assumed we would experience the same difficulties implementing the other difference image techniques, so we did not attempt to run them. The potential of these difference-frame algorithms to optimize accuracy and precision begs that they be made adaptable to moving objects.

2.7 Results

For each algorithm, we use the RMS of the residuals against the light curve model as a diagnostic for magnitude accuracy, and the χ^2_ν statistic as a measure of how reasonable the magnitude uncertainties are. Section 2 explains the model's origin. Figure 2.5 plots the

results of all algorithms against the model light curve, shown in order of least to greatest RMS of the residuals. We also report σ_{sys} to determine how much systematic bias is incurred in each algorithm and σ_{total} (calculated using the σ_{sys} determined for each frame and the target-specific σ_{stat} reported by each algorithm), which assesses the precision of the results. If the magnitudes themselves are accurate and all systematic errors have been accounted for, then $\chi^2_\nu \sim 1.0$. If $\chi^2_\nu \lesssim 1.0$, then the errors (including systematics) are overestimated, but if $\chi^2_\nu \gtrsim 1.0$, either the magnitudes are inaccurate or σ_{total} is still underestimated. Table 2.1 lists the RMS of the residuals, the χ^2_ν, σ_{total}, and σ_{sys} for each implementation.

2.7.1 PHOT algorithms

Figure 2.5 and Table 2.1 show that the widely-used aperture photometry algorithm PHOT generally performed poorest of all other algorithms tested, with or without subtracting a sky composite with IMARITH. We saw no change in the results by using a manually-placed, off-center sky aperture as opposed to a centered sky annulus, presumably as long as the sky measurements were made relatively close to the target (Fig. 2.5m vs. Fig. 2.5n). Aperture correction gave an improvement in RMS by a factor of 2.5 over using an aperture that encompassed 99.5% of the flux, making it comparable to SExtractor results. Since the sky was measured in PHOT in the same way before or after sky subtraction, the improvement in RMS must be caused by a more accurate accounting of source flux.

The two PHOT algorithms that involved subtracting a sky composite to remove faint background contamination before performing photometry (Sections 2.4.1 and 2.4.1) generally rendered a larger light curve amplitude than the model, which increased the RMS of the residuals and χ^2_ν (Fig. 2.5f and Fig. 2.5o). Visual inspection shows that the ISIS-processed images contain one exceptionally deviant data point at $\phi = 0.332$. This data point corresponds to Frame 1 in Figure 2.1, where a cosmic ray hit that was missed in initial cosmic ray correction is seen close to the target. It may be that the cosmic ray hit compromised the photometry more so in the ISIS-treated frames than in results from other realizations of PHOT, though there is no clear explanation for why this would be the case.

Also, the cosmic ray removal routine that we used obviously did not correct for all hits because it was designed to flag point source cosmic ray hits (*e.g.*, single pixels) rather than grazing hits such as the one in Fig. 2.1. Thus, the routine may have left additional faint contaminants near the target PSF and affected the accuracy of the photometry. Only after removing the anomalous data point at $\phi = 0.332$ from analysis did ISIS sky-subtraction render a RMS comparable to the other PHOT aperture correction algorithms. Subtracting the sky with IMARITH before applying an aperture correction offered no improvement in RMS, likely because contaminants were already sufficiently removed from source flux measurements by using a smaller aperture. We speculate that if the background within the sky annulus contained more faint sources, then performing IMARITH sky subtraction would offer further improvement in accuracy before using aperture correction.

The $\chi^2_\nu \gtrsim 1.0$ for all PHOT algorithms, especially the two algorithms involving sky subtraction (Table 2.1), comes from incorrect magnitude measurement, background determination, and/or noise models. To test whether or not the background was correctly determined and subtracted, we repeated the centered sky annulus method (Section 2.4.1) with successively larger apertures; if the background was overestimated, then the magnitude measured would become steadily fainter toward larger radii, and vice versa (Howell 1989). We found that the magnitude stayed the same, only the magnitude uncertainty changed using larger aperture radii, implying that background subtraction was done correctly.

PHOT calculates the magnitude uncertainty from the photon noise within the aperture and the standard deviation within the sky annulus, and it includes a term to account for uncertainty in the background level. Since we find that background subtraction was done properly, we assume that the standard deviation measurement within the sky annulus is also correct. With sky subtraction, we found that the standard deviation of the background was reduced by a factor of 2, which consequently gave a smaller magnitude uncertainty and even larger χ^2_ν. If the aperture contained contamination from background sources, however, then both the source flux and aperture's photon noise would be inaccurate, the magnitude more so. Such an effect would manifest as slightly large σ_{total} and even larger RMS, which

is what we see in the PHOT results. The factor of ~ 2.5 improvement in RMS by using a smaller photometric aperture but measuring the background in the same way provides further evidence that background contamination within the aperture is significant.

2.7.2 APT

Laher et al. (2012b) compared APT to SExtractor's MAG_APER, noting overall agreement between the two algorithms. We do not find the same result here, possibly indicative of APT's limitations toward fainter objects. Table 2.1 shows that APT's residual RMS is roughly twice that of MAG_APER, though the χ^2_ν is slightly larger due to the slightly smaller σ_{total} and much larger RMS. To investigate the cause of the large RMS, we tested for correct background determination by checking that the source flux stayed constant in several aperture radii beyond the original 18-pixel radius. We saw that as we increased the aperture size, the source flux continued to decrease, indicating that the background was overestimated. Incorrect background determination can lead to inaccurate measurement of source flux and background uncertainty, which then increase the RMS and χ^2_ν. Some photometry inaccuracy may stem from incorrect sub-pixel shifts, as noted in the APT manual (Laher et al. 2012a). Like PHOT, APT also appears to do a poor job of systematically excluding faint background contamination from the aperture. We found that APT measured the largest target flux within a 10-pixel radius of all aperture photometry algorithms, even with the background overestimated, implying background contamination.

2.7.3 DoPHOT

The DoPHOT results are given in Figure 2.5l and Table 2.1. The comparably large RMS shows that DoPHOT did not do a good job of reproducing the model, performing worst of the PSF-fitting algorithms but slightly better than PHOT's non-aperture correction algorithms. Magnitude uncertainties are also relatively large compared to the algorithms tested here. We suspect that the main sources of error for both magnitudes and uncertainties are that (1) DoPHOT PSF-fitting fails at accurately modeling the PSF of a trailed field

star, and (2) DoPHOT is too inclusive in PSF model computation. If a field contains many irregularly-shaped, compromised, and/or extended sources, then the final model may be significantly affected. Due to DoPHOT's limited user interaction, we could not further explore the role of potentially incorrect background determination, insufficient uncertainty estimates, and/or contamination in increasing the RMS and χ^2_ν. The σ_{sys} was also the largest of all algorithms tested, indicating that a substantial amount of systematic bias was incurred.

2.7.4 SExtractor

Table 2.1 shows that SExtractor improved the RMS by a factor of ~ 2.5 over PHOT (except for the aperture correction algorithm) and ~ 2.0 over APT and DoPHOT, implying better magnitude accuracy. Of the SExtractor aperture choices, MAG_ISOCOR delivered the lowest RMS but relatively unchanged σ_{total}, meaning it offered an improvement in accuracy but not in precision. MAG_ISOCOR determines an aperture correction to the MAG_ISO magnitude measurements (Fig. 2.5h), and the aperture correction technique was already shown in Section 2.7.1 to be more accurate than using a large aperture to add up source photons, so it is unsurprising that MAG_ISOCOR provided an improvement in RMS and χ^2_ν over MAG_ISO (Table 2.1). Becker et al. (2007) noted that in isophotal mode, the position and shape of sources detected in SExtractor may be systematically inaccurate toward fainter magnitudes, but given the success of MAG_ISO and MAG_ISOCOR here, our target must not have been faint enough to be affected.

The MAG_APER choice (Fig. 2.5j) gave the smallest χ^2_ν, owing to it having a relatively large σ_{total} and a minimally different RMS. This finding suggests that a fixed circular aperture can include significant amounts of background, adding more background uncertainty to the final error. The MAG_AUTO aperture option (Fig. 2.5g) offered essentially no improvement in accuracy but improvement in precision by a factor of ~ 2 over MAG_APER, implying that it was more effective at excluding pixels that do not contain

source flux. The MAG_BEST results were almost identical to the MAG_AUTO results, meaning that the field was relatively uncrowded (Table 2.1).

Despite SExtractor's general success over other aperture photometry algorithms (except tphot) at accurately reproducing the model light curve, the χ^2_ν was comparably large. A smaller RMS but larger χ^2_ν suggests that the magnitude uncertainties are underestimated. Bertin & Arnouts (1996) pointed out that the uncertainty in the local background estimate (which is notably complex) was not included in the final reported magnitude. We therefore assume that this exclusion made the magnitude uncertainties in our experiments artificially and significantly small. Because the degree to which the magnitude uncertainties are artificially small is unknown, it is difficult to determine whether or not inaccuracy of the SExtractor magnitudes also contribute to the large χ^2_ν value.

2.7.5 DAOPHOT

The DAOPHOT results are given in Figure 2.5c and Table 2.1, which shows that DAOPHOT is the third-most accurate algorithm tested, behind the two tphot algorithms. The σ_{total} is comparably small, indicating good isolation of source flux, though the small χ^2_ν value may indicate that the magnitude uncertainty is still overestimated. Becker et al. (2007) noted that systematic errors stem from inadequate correction factors in the wings of the model PSF, and that DAOPHOT consistently underestimated the uncertainties by $\sim 20\%$, which is inconsistent with our results. We suspect that the underestimation they noted was for brighter objects, where the intricacies of the true PSF may be poorly reproduced by the model. The σ_{sys} in our results was relatively small, suggesting minimal systematic bias compared to other algorithms.

The somewhat small amount of trailing in the template stars did not seem to affect the accuracy of the PSF model's fit to the target. We hypothesize that because the trailing was within the expected seeing disc, DAOPHOT's analytic functions had no difficulty computing a model that was applicable to both the trailed template stars and the untrailed target. We tried using DAOPHOT to build a model from moving-object frames where the stars

showed more pronounced trailing ($\sim 3.7''$, or trailing aspect of ~ 5), but the χ^2_ν fit of the model to the untrailed target was $\sim 6 - 20$ per frame, clearly indicating that the template stars were too trailed to reasonably match the target's PSF. In contrast, the average χ^2_ν of DAOPHOT fits to the 1996 TO_{66} data was 1.84.

Becker et al. (2007) found that performing aperture photometry within DAOPHOT (the same as aperture photometry with PHOT described in Section 2.4.1) rendered more accurate results than DAOPHOT's PSF-fitting routine because the flux of faint objects is increasingly underestimated toward fainter magnitudes. Because our results do not reflect this flux inaccuracy, we assume that 1996 TO_{66} was bright enough (S/N $\sim$ 25 from DAOPHOT) for this not to be a factor.

2.7.6 tphot

Results from the tphot PSF-fitting and aperture photometry algorithms are shown in Figures 2.5a and 2.5b, respectively, and in Table 2.1. The low RMS value shows that tphot produced the most accurate results of any algorithm tested.

The tphot PSF-fitting algorithm returned the lowest σ_{total} of all algorithms tested, implying excellent precision, but $\chi^2_\nu > 1.0$ suggests that the errors may be very slightly underestimated. Visual inspection of the results in Fig. 2.5a shows that the uncertainties on magnitudes are consistent with the model, except for one data point at $\phi = 0.587$ (corresponding to Frame 3 in Fig. 2.1), which is the likely cause of the large χ^2_ν. We can find no reason to exclude this point from analysis unless the model is poorly constrained at this particular rotation phase or the target PSF contains unavoidable deviant pixels. Removing this point gives $\chi^2_\nu = 0.99$, exactly what it should be if the data accurately represent the model, so either the questionable data point is compromised in some way or tphot is reporting inaccurately. Given the success of tphot at reproducing the model at all other phases, we assume the problem is not with the algorithm itself and rather with the data, possibly due to a bad pixel missed during bad pixel mask construction. Despite the target PSF not appearing especially radially-isotropic in the images (*e.g.*, some frames were

out of focus; Fig. 2.1), tphot did not exclude asymmetric flux within the circular aperture annuli by computing the median.

Tphot's aperture photometry gave a $\chi^2_\nu \sim 1.4$ for all data and $\chi^2_\nu \sim 1.0$ if we exclude the data point at $\phi = 0.587$, despite a relatively small σ_{total}, meaning the magnitudes and uncertainties are a good representation of the model. We also note that the low σ_{sys} implies that the tphot aperture photometry technique incurs little systematic bias compared to all algorithms explored (except DAOPHOT, which has a similarly low mean σ_{sys}). For these reasons, we have no reason to suspect any errors in the tphot aperture photometry routine.

2.8 Summary and Discussion

The tphot algorithm produces the best photometry results for our faint moving target, improving RMS very minimally over DAOPHOT, and by a factor of $\sim 1.9 - 2.3$ over SExtractor, ~ 4.3 over APT, ~ 4.7 over DoPHOT, and $\sim 2.0 - 8.5$ over IRAF's PHOT. Tphot's success is likely thanks to its careful treatment of the centroid, exclusion of contamination within the photometric aperture, and use of an iteratively-refined Waussian function. An updated version of tphot is currently under construction to better handle significantly trailed objects. DAOPHOT produced the next-best results, giving the same accuracy as tphot's aperture photometry algorithm (largely due to careful accounting of source flux) but overestimated errors. While offering a distinct advantage in speed, SExtractor generally underestimates magnitude uncertainties, likely because of exclusion of error in the background determination. The MAG_ISOCOR aperture technique renders the most accurate and precise magnitude measurements amongst the SExtractor options because as an aperture correction technique, it more carefully isolates target flux and excludes contaminants. IRAF's PHOT algorithm can only accurately measure magnitudes of a moving target if an aperture correction technique is used (without sky subtraction), though it returns median uncertainties ~ 4 times larger than what could be achieved with tphot. Although the background was measured correctly, PHOT did not exclude

background contaminants from within the aperture, giving inaccurate photometry. The APT algorithm, while fairly flexible and excellent as a visualization and educational tool, was outperformed by all other software except DoPHOT and a few PHOT algorithms. APT struggles with both accurately measuring the background and with systematically excluding contaminants from within the photometric aperture. We suggest that APT is better suited for photometry on brighter objects. DoPHOT performed slightly worse in both accuracy and precision compared to APT. We deduce that its fitting routine was not able to as accurately produce a PSF model possibly because it included too many field sources in its construction of a model PSF and/or it was very sensitive to trailed PSFs.

At some point, trailing will be significant enough for the PSF peak to be two-dimensional (*i.e.*a line rather than a point). In these cases, the ideal aperture would be the same shape of the target PSF to exclude as much background contamination as possible. Techniques that only allow a circular aperture such as tphot, SExtractor's MAG_APER, and PHOT will incorporate large amounts of background contamination with an aperture that encompasses the extent of the trailed PSF. The elliptical aperture allowed by APT and SExtractor's MAG_AUTO and MAG_BEST may be a good approximation to the target shape if trailing is minimal (*e.g.*, our data), but at some point, trailing may be significant enough for an ellipse's axes to extend well beyond the PSF. The only aperture photometry technique that we tested that places no restrictions on target shape are SExtractor's MAG_ISOCOR and MAG_ISO, which we consequently predict will be most suitable of the techniques tested here for aperture photometry of significantly trailed objects.

These findings could be more statistically robust if we had more images of 1996 TO_{66}, which would eliminate the dependency on a relatively small sample size of N = 10. As such, our results are only applicable to data sets similar to ours – for slow-moving objects with S/N $\sim$ 35 (according to uncertainties given by our most precise algorithm), mostly because no other images for a moving object with a well-determined light curve described by a shape model were available to us at the time. It would be useful to test these algorithms on other objects with (1) brighter targets to determine at what point aperture photometry starts to

outperform PSF-fitting because of more well-defined intricacies in the PSF morphology that are not reproduced by analytic functions, and (2) a range of trailing aspects to determine the aspect beyond which photometric accuracy becomes significantly compromised. Vereš et al. (2012) tested the latter for a 2-dimensional symmetric gaussian function and a square aperture 3×FWHM, finding a ~ 1.0 and 0.5 magnitude loss, respectively, at a trailing length of 3×FWHM, but this experiment should be repeated for popular algorithms.

PSF-fitting routines suffer similar challenges to accurately representing the target PSF as aperture photometry. Techniques that fit a radially-isotropic function to the data will fail in recovering the true PSF shape, but no profile-fitting technique that we tested makes this assumption of radial isotropy. Allowing for an elliptical analytic function is a first-order approximation to representing the true PSF shape of minimally-trailed data, and all of the PSF-fitting techniques we tested have this feature. However, rather than a single function calculated at the centroid, a trailed PSF might be best represented by the sum of a series of analytic functions calculated at different increments along the direction of motion, such as a trailed Gaussian given in its analytic form by Vereš et al. (2012). However, this technique has not yet been adapted into software available to the public. Existing PSF-fitting algorithms cannot calculate a series of different functions for a single trailed source, so we suspect that in the event that an ellipse is no longer a good approximation to the PSF shape and until trail-fitting algorithms are made available, all PSF-fitting packages will fail at accurately representing the PSF. Therefore, of all the techniques tested here, SExtractor's MAG_ISO and MAG_ISOCOR are likely the only ones capable of performing accurate photometry on significantly trailed PSFs.

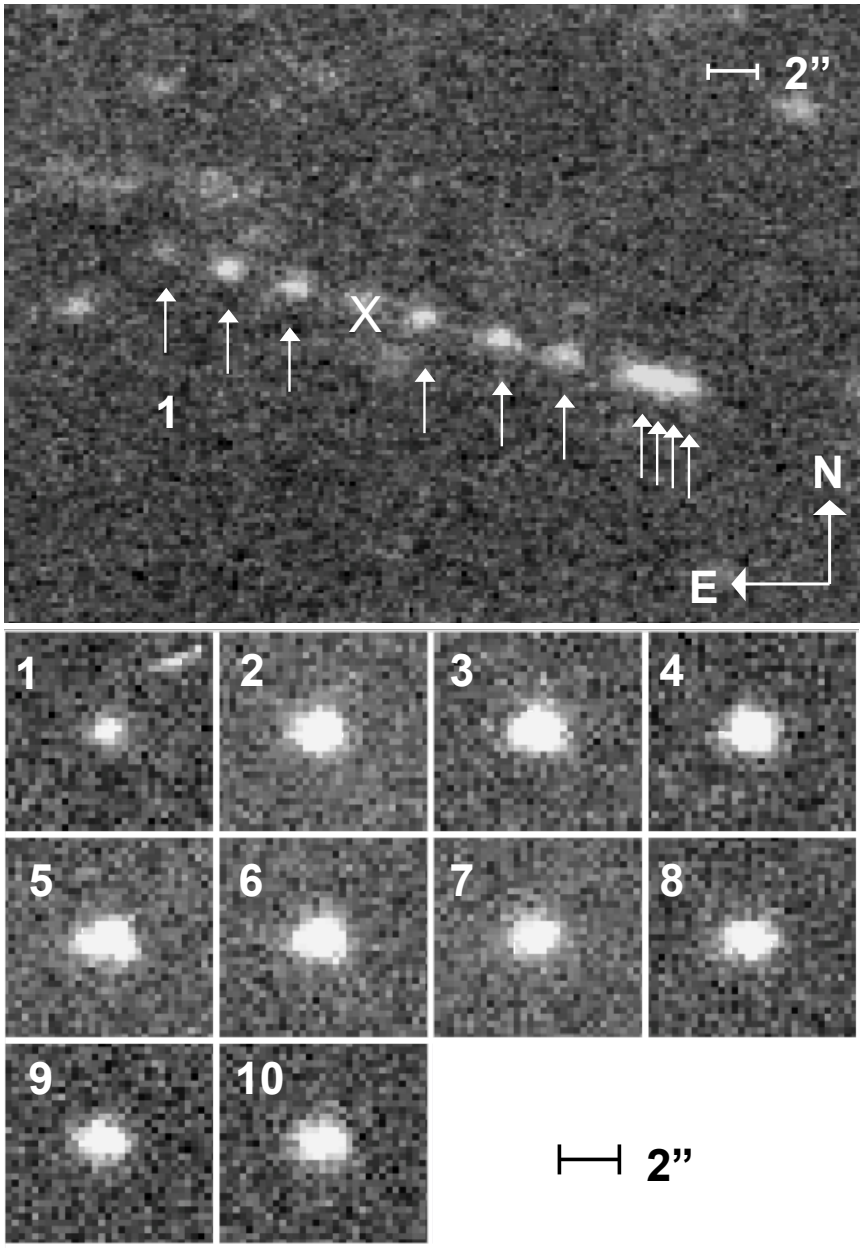

Figure 2.1 Images used in analysis. The top panel is the sky composite showing 1996 TO_{66}'s motion across the sky (indicated by arrows, with the first image indicated by a “1”), showing the background in the target's vicinity. The composite was made by shifting, mode-scaling, and summing all frames. The data point indicated by an “X” was excluded because it was likely contaminated by a bad pixel. The bottom panel shows postage stamps of the target in the individual frames used in analysis (ordered chronologically $1 - 10$) in order to show the PSF morphology. The stamps have the same brightness scale. A cosmic ray hit $\sim 3.1''$ from the target's centroid in Frame 1 may have compromised some of the photometry, and minor focus problems manifested as slightly triangular PSFs are seen in Frames 5 and 6.

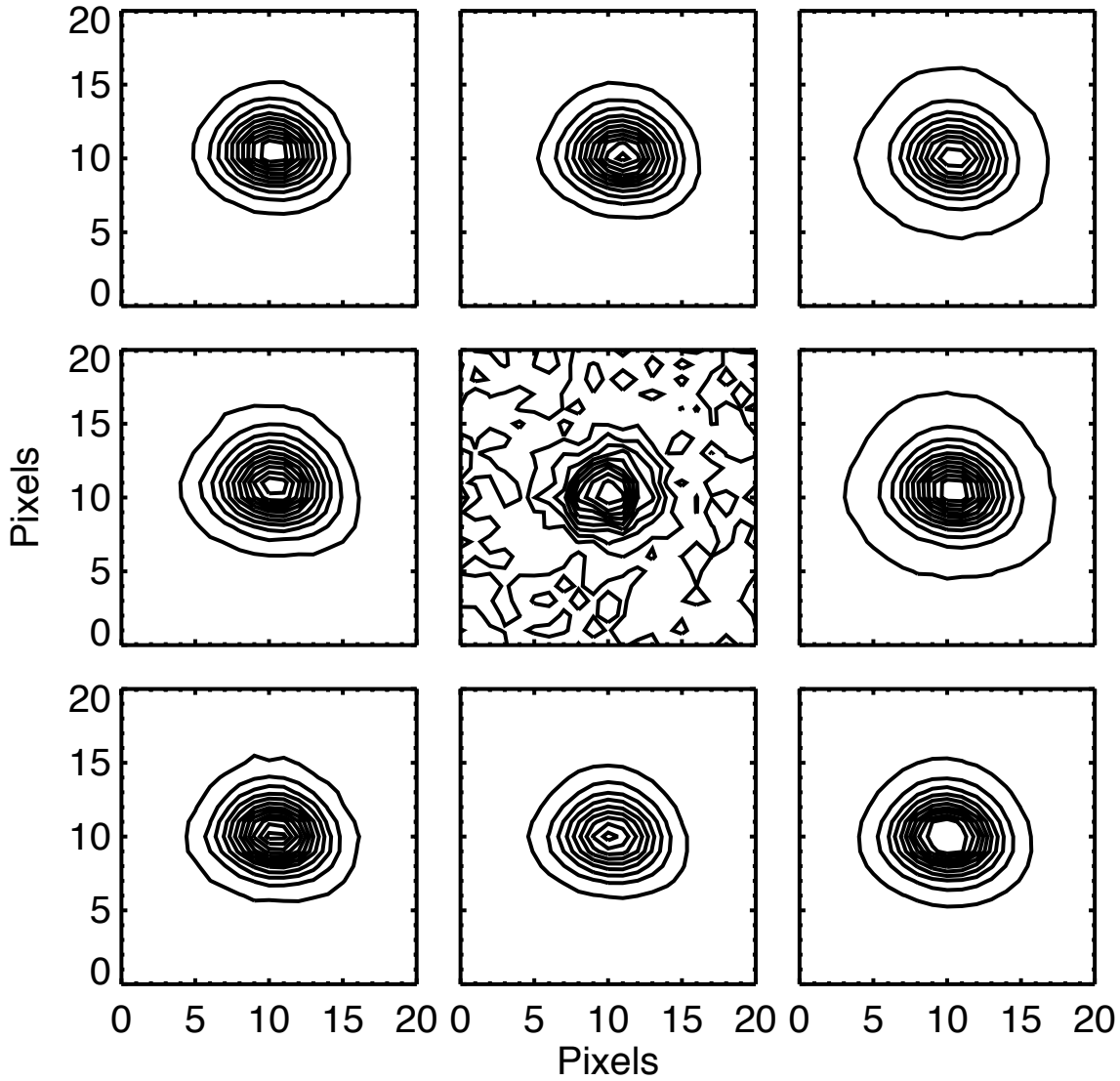

Figure 2.2 Contour plots of the target (center panel) and surrounding bright field stars for Frame 5. Based on tphot's best-fit PSF models, the trailing aspect is 1.5 for field stars and 1.1 for the target. The PSF shapes are consistent across the image, indicating no spatial variation to a fraction of a percent.

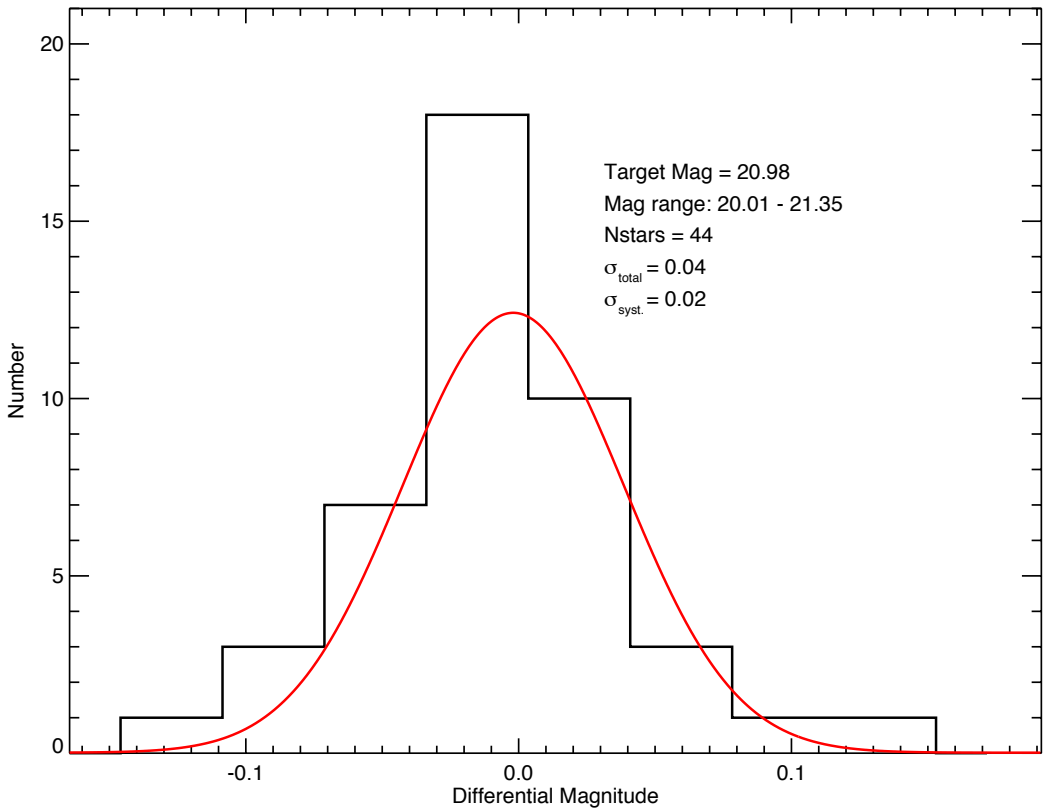

Figure 2.3 Distribution of differential magnitudes relative to the night's median for field stars in Frame 5 comparable in magnitude to the target (histogram). The smooth curve shows a gaussian fit to the distribution. The gaussian sigma (σ_g) is given as σ_{total} in the upper right corner, along with the target's magnitude, range of magnitudes of the comparison stars, number of comparison stars within this range, and computed systematic error (σ_{sys}). The systematic error calculation is described in more detail in Section 2.3. The differential field star magnitudes are well fit by a gaussian, rendering reasonable systematic error computations.

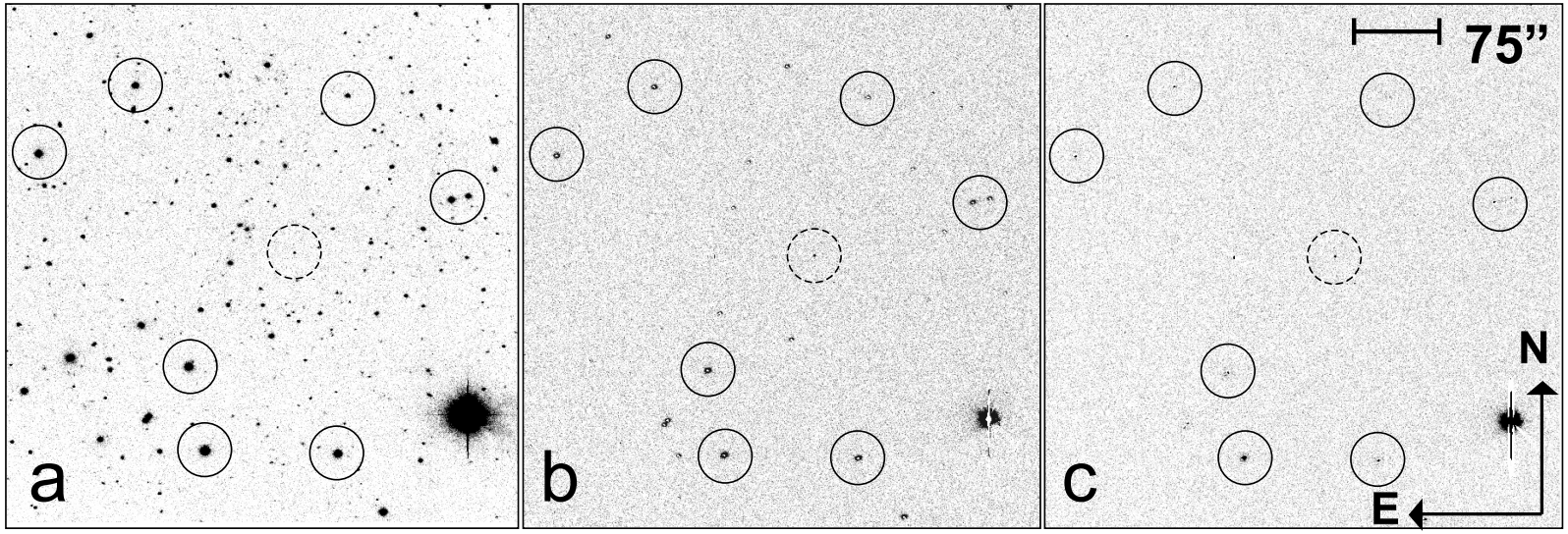

Figure 2.4 A comparison between sky composite subtraction results for a full frame (Frame 7), with a circle placed around several relatively bright field stars visible in the raw images (Sections 2.4.1 and 2.4.1). The moving target has a dashed circle placed around it in each panel. The size and orientation is the same for all panels. a) The original frame before sky subtraction. b) The residuals of composite subtraction performed with IRAF's IMARITH task, which subtracted a median-combined reference sky image from individual frames. The negative spots are residuals left from field stars after subtraction and are likely caused by inadequate alignment and/or composite scaling before subtraction. c) Sky subtraction residuals using ISIS software, which convolves a “best-seeing” sky composite with a spatially-variable kernel representative of the individual frame's FWHM in order to match the image quality before subtraction. ISIS subtraction shows a noticeable improvement over IMARITH subtraction in fully removing background sources.

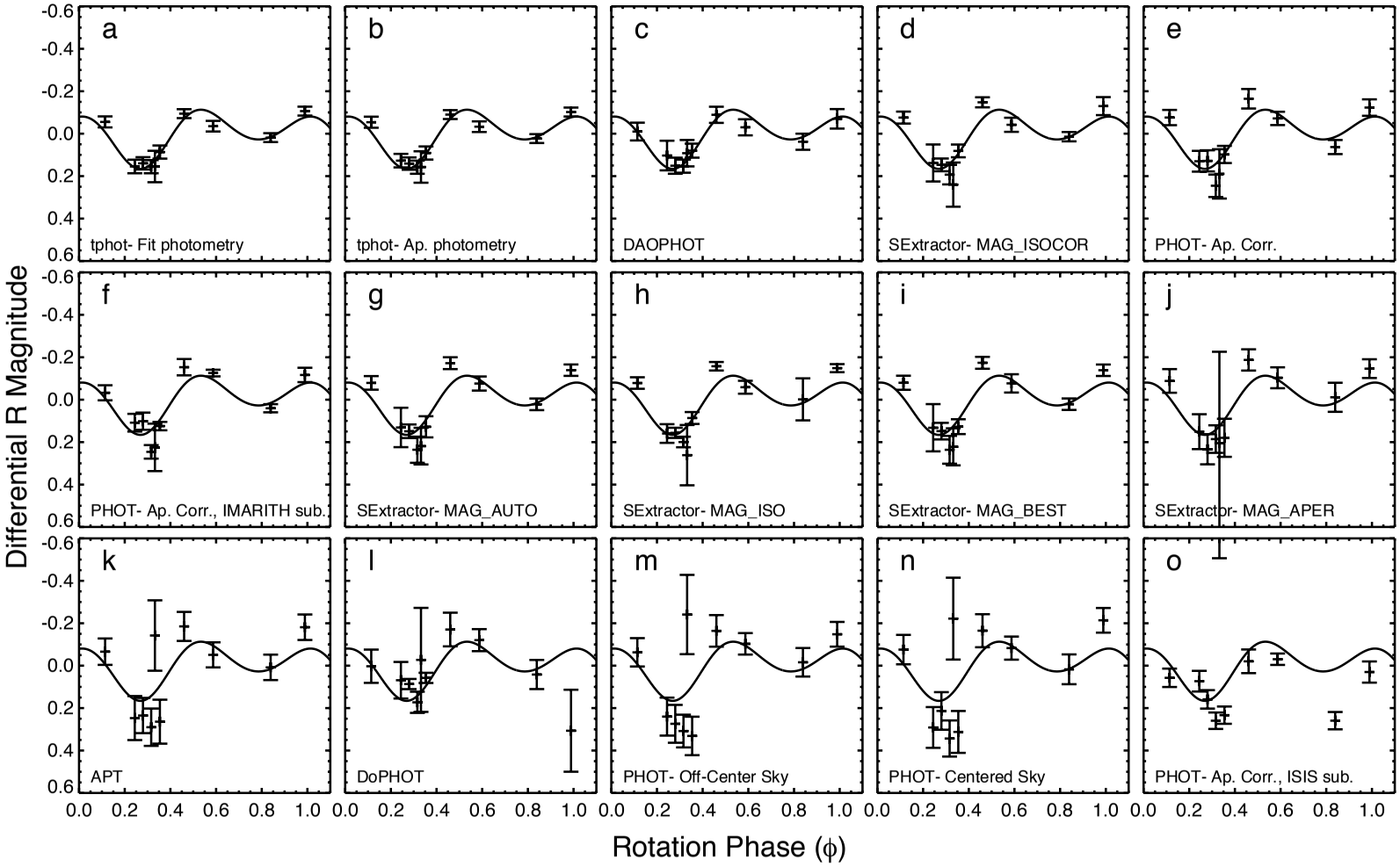

Figure 2.5 1996 TO_{66} photometry from different algorithms. The panels are arranged in left-to-right, top-to-bottom order of smallest to largest RMS of the residuals against the model, which we use as a diagnostic for accuracy. The algorithm name is given at the bottom of each panel, and pertinent statistics are given in Table 2.1.

Table 2.1 Statistics for each photometry algorithm. We give RMS residuals against the model, the reduced chi-squared (χ^2_ν), the mean total photometric uncertainty (σ_{total}), and the mean systematic error (σ_{sys}). The results are ordered by increasing RMS.

Technique	Panel in Fig. 2.5	RMS[a]	χ^2_ν	Mean σ_{total}	Mean σ_{sys}
tphot, Fit photometry	a	0.030	1.436	0.031	0.012
tphot, Ap. photometry	b	0.031	1.488	0.032	0.008
DAOPHOT	c	0.031	0.561	0.044	0.010
SExtractor, MAG_ISOCOR	d	0.058	2.501	0.045	0.027
PHOT, Ap. Corr.	e	0.060	1.855	0.049	0.021
PHOT, Ap. Corr., IMARITH Subtraction	f	0.062	3.296	0.039	0.018
SExtractor, MAG_AUTO	g	0.063	2.985	0.047	0.023
SExtractor, MAG_ISO	h	0.064	5.062	0.046	0.032
SExtractor, MAG_BEST	i	0.064	3.008	0.050	0.028
SExtractor, MAG_APER	j	0.068	1.342	0.101	0.066
APT	k	0.125	1.858	0.085	0.026
DoPHOT	l	0.141	2.145	0.090	0.082
PHOT, Off-Center Sky Annulus	m	0.159	2.413	0.085	0.048
PHOT, Centered Sky Annulus	n	0.161	2.655	0.089	0.048
PHOT, Ap. Corr., ISIS subtraction	o	0.255	14.840	0.048	0.025

[a] The RMS of the residuals against the model.

References

Alard, C. 2000, in Astronomical Society of the Pacific Conference Series, Vol. 203, IAU Colloq. 176: The Impact of Large-Scale Surveys on Pulsating Star Research, ed. L. Szabados & D. Kurtz, 50–55

Becker, A. C., Silvestri, N. M., Owen, R. E., Ivezić, Ž., & Lupton, R. H. 2007, PASP, 119, 1462

Bertin, E. & Arnouts, S. 1996, A&AS, 117, 393

Davis, L. 1994

Ferrarese, L., Silbermann, N. A., Mould, J. R., Stetson, P. B., Saha, A., Freedman, W. L., & Kennicutt, Jr., R. C. 2000, PASP, 112, 177

Friel, E. D. & Geisler, D. 1991, AJ, 101, 1338

Handler, G. 2003, Baltic Astronomy, 12, 243

Holwerda, B. W. 2005, ArXiv Astrophysics e-prints

Howell, S. B. 1989, PASP, 101, 616

Irwin, J., Aigrain, S., Hodgkin, S., Irwin, M., Bouvier, J., Clarke, C., Hebb, L., & Moraux, E. 2006, MNRAS, 370, 954

Ivezić, Ž., Lupton, R. H., Schlegel, D., Boroski, B., Adelman-McCarthy, J., Yanny, B., Kent, S., Stoughton, C., Finkbeiner, D., Padmanabhan, N., Rockosi, C. M., Gunn, J. E.,

Knapp, G. R., Strauss, M. A., Richards, G. T., Eisenstein, D., Nicinski, T., Kleinman, S. J., Krzesinski, J., Newman, P. R., Snedden, S., Thakar, A. R., Szalay, A., Munn, J. A., Smith, J. A., Tucker, D., & Lee, B. C. 2004, Astronomische Nachrichten, 325, 583

Kjeldsen, H. & Frandsen, S. 1992, PASP, 104, 413

Kron, R. G. 1980, ApJS, 43, 305

Laher, R. R., Gorjian, V., Rebull, L. M., Masci, F. J., Fowler, J. W., Helou, G., Kulkarni, S. R., & Law, N. M. 2012a, PASP, 124, 737

Laher, R. R., Rebull, L. M., Gorjian, V., Masci, F. J., Fowler, J. W., Grillmair, C., Surace, J., Mattingly, S., Jackson, E., Hacopeans, E., Hamam, N., Groom, S., Teplitz, H., Mi, W., Helou, G., van Eyken, J. C., Law, N. M., Dekany, R. G., Rahmer, G., Hale, D., Smith, R., Quimby, R. M., Ofek, E. O., Kasliwal, M. M., Zolkower, J., Velur, V., Walters, R., Henning, J., Bui, K., McKenna, D., & Kulkarni, S. R. 2012b, PASP, 124, 764

Lee, C.-U., Koo, J.-R., Kim, S.-L., Lee, J. W., Park, B.-G., & Han, C. 2010, Journal of Astronomy and Space Sciences, 27, 289

Lupton, R. H., Ivezic, Z., Gunn, J. E., Knapp, G., Strauss, M. A., & Yasuda, N. 2002, in Society of Photo-Optical Instrumentation Engineers (SPIE) Conference Series, Vol. 4836, Society of Photo-Optical Instrumentation Engineers (SPIE) Conference Series, ed. J. A. Tyson & S. Wolff, 350–356

Mateo, M. & Schechter, P. L. 1989, in European Southern Observatory Conference and Workshop Proceedings, Vol. 31, ESO/ST-ECF Data Analysis Workshop, ed. P. J. Grosbøl, F. Murtagh, & R. H. Warmels, 69–83

Schechter, P. L., Mateo, M., & Saha, A. 1993, PASP, 105, 1342

Stetson, P. B. 1992, in Astronomical Society of the Pacific Conference Series, Vol. 25, Astronomical Data Analysis Software and Systems I, ed. D. M. Worrall, C. Biemesderfer, & J. Barnes, 297

Tanvir, N. R., Robinson, D. R. T., & von Hippel, T. 1995, ArXiv Astrophysics e-prints

Tody, D. 1986, in Society of Photo-Optical Instrumentation Engineers (SPIE) Conference Series, Vol. 627, Society of Photo-Optical Instrumentation Engineers (SPIE) Conference Series, ed. D. L. Crawford, 733

Tonry, J. L. 2011, PASP, 123, 58

Vereš, P., Jedicke, R., Denneau, L., Wainscoat, R., Holman, M. J., & Lin, H.-W. 2012, PASP, 124, 1197

Wozniak, P. R. 2000, Acta Astron., 50, 421

Chapter 3

Observations

3.1 Survey design and sample

Our first consideration in designing observations to constrain color variation on neutral TNOs was choosing the most efficient way to determine color variation for the least amount of targets necessary to make the data scientifically meaningful. If color variation is present on the surface of an object, then brightness variation must be present in at least one of the broad-band filters used to compute the colors, so detecting color variation requires detecting brightness variation. Searching for brightness variation is less observationally expensive than searching for color variation since it only requires observations in one filter for the same temporal resolution, and only sparse light curve sampling is needed (*e.g.*, Mann et al. 2007). Therefore, building a sample for the color variation survey first required obtaining "initial-pass" photometry in the R-band (which can achieve the best S/N for our targets). The brightest and most neutral targets with significant magnitude changes in this Brightness Variation Survey (hereafter, BVS) comprised the Color Variation Survey (hereafter, CVS) sample. Brighter objects were favored to ensure the best possible signal-to-noise (S/N) in the least amount time, affording relatively low errors, dense lightcurve sampling, and efficient use of telescope time. The most neutral colors were also favored to focus on the most extreme cases within the color distribution, thereby maximizing our

likelihood of observing a fresh surface. Thus, the observational campaign was two-part, with the BVS used to determine the CVS targets.

We next considered what sample size was needed. To extrapolate from the CVS to the entire neutral population (~ 80 objects with $V-R < 0.52$ to date), a statistically significant sample size was necessary. There are only two outcomes of the color variation survey if all we are interested in is homogeneity: either an object shows color variation or it does not. A survey with two possible outcomes can be described by binomial statistics, which can then be used to estimate the minimum sample size. The following presents the sample size estimation in the context of our survey and using binomial statistics.

If f is the fraction of neutral TNOs which exhibit color variation and C is the fraction of objects with color variation that are oriented such that the variation can be detected, then the expected number of objects with color variation (N_v) out of all observed neutral objects (N) is:

$$N_v = fC\ N\ . \tag{3.1}$$

Eq. 3.1 can be rewritten to solve for f:

$$f = \frac{N_v}{C\ N}$$

and

$$\sigma_f = \frac{\sigma_{N_v}}{C\ N}\ , \tag{3.2}$$

where σ_f and σ_{N_v} denote the uncertainty in f and N_v, respectively. Properties of binomial statistics dictate that Eq. 3.2 can be rewritten as:

$$\sigma_f = \frac{\sqrt{N\ fC\ (1-fC)}}{C\ N}\ ,$$

or

$$N = \frac{f\,(1 - fC)}{C\,\sigma_f^2} \tag{3.3}$$

A statistically significant (3σ) detection of $(1-f)$ requires that $(1-f)/\sigma_f > 3$. Substituting this expression into Eq. 3.3, we obtain:

$$N > \frac{9\,f\,(1 - fC)}{C\,(1 - f)^2} \tag{3.4}$$

In this circumstance, we must assume a probability of successfully detecting color variation, which we take to be 50% (*i.e.*, $f = 0.5$). Using Eq. 3.4, a total of ~ 45 objects must be observed as part of the BVS survey in order to detect enough CVS targets to make a statistically significant claim on the fraction of neutral objects with heterogeneous surfaces. The number of CVS targets needed was determined by repeating the above exercise but for $C = 1$ (since all targets will have detectable variation because they have been selected based on detectable variation), giving that a CVS sample size greater than 9 was needed.

The BVS sample was chosen from the TNO color catalogs of Hainaut & Delsanti (2002), Romanishin & Tegler (2007), and Neese (2008), which listed all known TNO colors (56 objects at the start of this work). We selected objects with neutral colors ($V - R \leq 0.52$; Barucci et al. 2005) and apparent magnitudes bright enough to achieve magnitude errors of 0.03 (corresponding to a color error of 0.05 after adding the two magnitude errors in quadrature) on the University of Hawai‘i 2.2-meter telescope. With uncertainties in color of 0.05, we can significantly detect color variation of 0.1.

It is difficult to convey the difference in age of the material observed indicated by a change in color for several reasons. First, the reddening and darkening timescales differ between ice species, with simple hydrocarbons producing a much more pronounced change in spectral slope (*i.e.*, color) than more complex hydrocarbons over the same amount of time (Moroz et al. 2004; Brunetto et al. 2006). Second, mathematically, the flux difference that corresponds to a color difference is not just dependent on the change in color, but also on the initial color value itself. For example, if an object showed $V - R$ between $0.3 - 0.4$, that

would correspond to a difference in flux of 7%, while $V - R$ between $0.4 - 0.5$ corresponds to a flux difference of 6%. Lastly, there are few ice species with model spectra at different ages available, especially at outer solar system temperatures, so quantifying color variation will not specify exactly which species and at what ages exist across the surface, rather the variation can be used to qualitatively assess surface heterogeneity. Therefore, unless one is trying to detect specifically different ages of a particular material with available optical constants at temperatures relevant in the Trans-Neptunian region, choosing the amount of color variation to detect is somewhat arbitrary. We chose to tailor our observations for detecting 10% color variation in order to ascertain which portions of the target's surface would technically belong to a different taxonomy as statistically defined by Barucci et al. (2005). This sensitivity in color variation requires that the magnitude uncertainty be ~ 0.03, which is comparable to the lowest rotational lightcurve amplitudes previously detected for TNOs (discussed in detail in Chapter 4).

We then excluded objects that had already been sufficiently examined for color and/or spectral variation (only 2 fit this description), leaving 54 TNOs for the BVS sample (listed in Section 4). The BVS targets were observed in order of closest to farthest from opposition (to ensure adequate light curve sampling) until 10 targets with detectable variation and belonging to a range of dynamical classes were identified for follow-up with the CVS (listed in Section 6). Further discussion of the targets within the individual BVS and CVS survey samples is provided in Sections 4 and 6, respectively.

Conducting a survey of this size and design should provide the following for neutral TNOs:

- $\sim 30 - 50$ sparsely-sampled light curves
- ~ 10 phase curves
- ~ 10 rotational light curves
- ~ 10 color curves

3.2 Observing runs

The data were obtained on 76 nights between August 2009 and November 2012, 56.5 of which were originally allocated to this program and 50 of which were usable, on the University of Hawai'i (UH) 2.2-m telescope. Both the Tek (2048×2048) CCD camera, with a pixel scale of $0.219''$/pixel and Kron-Cousins filters, and the imaging capabilities of the Wide Field Grism Spectrograph 2 (WFGS2), with a pixel scale of $0.345''$/pixel and Sloan filters were used. The Kron-Cousins V filter has a central wavelength of $\lambda_c = 540$ nm and a bandwidth of $\Delta\lambda = 90$nm, while the R filter has $\lambda_c = 647$nm and $\Delta\lambda = 125$nm. The sloan g' filter has $\lambda_c = 465$nm and the r' filter has $\lambda_c = 625$nm, though their bandwidths are not listed for the WFGS2 instrument which required the Sloan filters. A summary of the observing conditions is provided in Table 3.1. Sky conditions varied between photometric, non-photometric due to passing cirrus clouds (causing the seeing to sometimes change within a night) but still observable, and non-observable due to thick clouds or poor weather (*e.g.*, high winds, high humidity, fog/ice). Occasional instrumental problems (*e.g.*, broken filter wheel, stuck dome) also rendered some nights unusable.

The focus was checked before each night and changed as needed if field star radial profiles began to show increased scatter around the median. We were not able to change the focus on some nights due to technical difficulties, leaving a slightly triangular-shaped PSF characteristic of the UH 2.2m mirror support system. This caused our chosen photometry algorithm to fail when trying to fit a PSF model to such an irregularly shaped PSF, giving no useful magnitudes for those images. Exposure times were modified as needed for all data to achieve a constant magnitude error goal of 0.03 under changing transparency and seeing conditions. We sampled the light curves of 38 TNOs (the most possible with the number of usable nights) between 3-12 times over a night as part of the BVS, using only the Kron-Cousins R filter and the Tek camera (Table 3.1). The original cadence used for the CVS was simply alternating V and R images to compute the $V - R$ color over as small a time resolution as possible while still achieving S/N ~ 30 in each filter (typically one $V - R$ pair

per $\sim$ 40 minutes). However, difficulties determining the rotation period for phasing the color data prompted us to adopt a R-V-R or r'-g'-r' cadence during and after April 2012, giving 33% more data in one filter (for better constraints on the rotation period). When available, non-sidereal guiding was used so that the target was not trailed. The absolute magnitude of the targets' motions averaged $\sim 3.0''$/hr in R.A. and $1.0''$/hr in Declination, among the slowest-moving rates of motion for small bodies and thus providing very minimal trailing.

All images were prepared using IRAF's "CCDPROC" package (Tody 1986), as described in Section 2.3. Each night, we acquired $20-30$ bias frames for a nightly stacked bias frame and $5-9$ twilight sky flats in each filter at both the beginning and end of each full night, all below the limit of the linearity regime for the chip. In some cases, changing dust patterns caused residual dust "donuts" in flattened images, but none were close enough to the target to affect photometry. We also removed cosmic ray artifacts using typically, a $3-6\sigma$ rejection threshold relative to noise. This was effective at removing most cosmic rays without falsely flagging real sources, although visual inspection showed that this procedure was not able to remove all cosmic rays, perhaps because a different threshold was needed for different regions within the field. Thus, aperture photometry for a small fraction of field stars (which was used for determining parameters of the refined PSF-modeling photometry algorithm; see Section 2.5.3) may have been contaminated.

Both the Tek and WFGS2 instruments use the same chip, but instrumental deterioration and various technical difficulties (including a lightning strike in June 2011) have caused the chip's fundamental properties to change over the course of this work. Therefore, the gain (g) and read noise (σ_{rn}) needed to be measured for each night. This was done by a linear least squares fit to the square of the sky noise (σ^2_{sky}) over the sky (s) for images of a range of exposure times:

$$s = \frac{1}{g}\left(\sigma^2_{sky}\right) + \sigma^2_{rn} \quad , \tag{3.5}$$

where s, σ^2_{sky}, and σ^2_{rn} are all in atomic data units (ADU). The gain and read noise measured for each night are recorded in Table 3.1. For nights on which we could not compute the gain and read noise (*e.g.*, the images did not possess a large enough range of sky values so as to compute a reasonable g and σ_{rn} solution), we assumed the most recently measured values.

Field source detection and photometry were done using the profile-fitting function of the "tphot" algorithm. A description and justification of the use of this algorithm was provided in Section 2.5.3. The median frame-to-frame magnitude offset was determined using field stars that were visually inspected for contaminants (cosmic ray hits and faint background sources) close to the source centroid, and with errors within 1.5 that of the target. Systematic errors were calculated as described in Section 2.3.1.

Magnitude

calibration was done using Sloan Digital Sky Survey (SDSS) absolute photometry for field stars, when available. For our fields that were observed in Kron-Cousins filters (Table 3.1), SDSS field star photometry was converted to the Kron-Cousins photometric system using transformations at http://www.sdss3.org/dr8/algorithms/sdssUBVRITransform.php. When the science field was not SDSS calibrated, we observed both the science field (again) and Landolt standard stars on photometric nights (Landolt 1992). Several Landolt V and R images were taken on these nights at a range of airmasses (between 1.0 and 2.5) to determine the extinction coefficient, absolute zeropoint, and color term, then the science field was calibrated with these terms.

Table 3.1. Summary of all observing runs on the University of Hawaii 2.2-m telescope.

UT date	# Nights	Instrument	Filters[a]	Conditions[b]	Seeing ($''$)[c]	Survey	Objects Observed	# Images[d]	Moon[e]	Gain	σ_{rn}
Aug 21, 2009	1.0	Tek	R	0	0.83	BVS	2000 OU_{69}, 2000 PE_{30}, 2001 QB_{243}, 2001 QC_{298}, 2001 QF_{298}, 2001 QY_{297}, 2002 MS_4	23	2	1.41	10
Aug 23, 2009	1.0	Tek	R	1	0.77	BVS	1993 SB, 1995 QY_9, 1995 SM_{55}, 1995 TL_8, 1998 SN_{165}, 2001 KB_{77}, 2002 GP_{32}	23	12	1.52	21
Aug 24, 2009	1.0	Tek	R	0	0.70	BVS	2002 GP_{32}, 2005 RR_{43}	5	20	1.47	17
Aug 28, 2009	0.5	Tek	...	-1	...	...	...	...	58	...	...
Aug 29, 2009	0.5	Tek	...	-1	...	...	...	...	68	...	...
Sep 07, 2009	0.5	Tek	...	-1	...	...	...	...	92	...	...
Oct 20, 2009	1.0	Tek	R	0	0.7	BVS	1996 TL_{66}, 1996 TS_{66}, 1999 RY_{215}, 1999 TD_{10}, 2002 XV_{93}, 2003 AZ_{84}, 2003 UB_{313}, 2003 UZ_{117}	20	5	1.29	6
Oct 22, 2009	1.0	Tek	V, R	0	0.8	CVS	1995 SM_{55}	33	18		
Dec 23, 2009	1.0	Tek	R	0	0.8	BVS	1999 CD_{158}, 1999 CL_{158}, 1999 TD_{10}, 2000 YW_{134}, 2002 XV_{93}, 2003 AZ_{84}, 2003 UZ_{117}, 2005 RR_{43}	50	37	1.19	18
Dec 24, 2009	1.0	Tek	V, R	1	0.6	BVS, CVS	2003 AZ_{84}, 2003 UZ_{117},	33	46		

Table 3.1—Continued

UT date	# Nights	Instrument	Filters[a]	Conditions[b]	Seeing ($''$)[c]	Survey	Objects Observed	# Images[d]	Moon[e]	Gain	σ_{rn}
							2005 RR_{43}				
Jan 09, 2010	1.0	WFGS2	r', i'	1	0.6	CVS	1996 TL_{66}, 2000 YW_{134}, 2002 XV_{93}	16	29		
Jan 10, 2010	1.0	WFGS2	r', i'	1	0.6	CVS	1996 TL_{66}	15	20		
Jan 11, 2010	1.0	WFGS2	...	-1	...	...	...	...	13		
Feb 14, 2010	1.0	Tek	R	1	0.65	BVS	1998 HB_{12}, 1998 UR_{43}, 2000 CQ_{105}, 2000 EE_{173}, 2000 GP_{183}, 2001 CZ_{31}, 2001 FP_{185}, 2004 EW_{95}, 2005 FY_9	25	0	1.60	32
Feb 15, 2010[f]	1.0	Tek	V, R	1	0.78	BVS, CVS	2000 EE_{173}, 2000 GP_{183}, 2000 YW_{134}, 2001 FP_{185}	39	2	1.60	32
Apr 20, 2010	1.0	Tek	V, R	1	0.8	BVS, CVS	1999 CL_{119}, 2002 GP_{32}, 2002 MS_4	22	34	1.46	21
Apr 21, 2010	1.0	Tek	V, R	0	0.8	CVS	2000 GP_{183}, 2002 MS_4	26	45		
Apr 23, 2010	1.0	Tek	...	-1	...	...	...	...	68	...	...
Apr 24, 2010	1.0	Tek	V, R	1	0.8	CVS	2000 GP_{183}, 2002 MS_4	18	78		
Apr 25, 2010	1.0	Tek	V, R	1	0.6	CVS	2000 GP_{183}, 2002 MS_4	25	87		
May 18, 2010	1.0	Tek	...	-1	...	...	...	...	22	...	...
May 20, 2010	1.0	Tek	...	-1	...	...	...	...	43	...	...
Sep 03, 2010	0.5	Tek	...	-1	...	...	...	...	31	...	...
Sep 04, 2010	1.0	Tek	V, R	1	0.45	CVS	2001 QF_{298}, 2002 TX_{300},	33	22		

Table 3.1—Continued

UT date	# Nights	Instrument	Filters[a]	Conditions[b]	Seeing ($''$)[c]	Survey	Objects Observed	# Images[d]	Moon[e]	Gain	σ_{rn}
							2003 OP_{32}				
Sep 05, 2010	1.0	Tek	V, R	1	0.4	CVS	2001 QF_{298}, 2002 TX_{300}, 2003 OP_{32}	59	13		
Sep 06, 2010	1.0	Tek	V, R	1	0.5	CVS	2001 QF_{298}, 2002 TX_{300}, 2003 OP_{32}	54	6		
Sep 07, 2010	1.0	Tek	V, R	1	0.5	CVS	2001 QF_{298}, 2002 TX_{300}, 2003 OP_{32}	55	2		
Oct 29, 2010	1.0	Tek	V, R	0	0.5	CVS	1995 SM_{55}, 2001 QF_{298}, 2002 TX_{300}	36	61		
Oct 30, 2010	1.0	Tek	V, R	1	0.73	CVS	1995 SM_{55}, 2001 QF_{298}	32	50		
Nov 03, 2010	0.5	Tek	V, R	0	0.74	CVS	1995 SM_{55}, 2003 UZ_{117}	16	10		
Nov 04, 2010	0.5	Tek	V, R	0	0.6	CVS	1995 SM_{55}, 2003 UZ_{117}	11	4		
Nov 06, 2010	1.0	Tek	...	-1	...	...	...	...	0	...	...
Nov 07, 2010	1.0	Tek	V, R	1	0.78	CVS	1995 SM_{55}, 2000 YW_{134}	33	2		
							2003 UZ_{117}				
Dec 01, 2010	1.0	Tek	...	-1	...	...	...	...	22	...	...
Dec 02, 2010	1.0	Tek	V, R	0	0.6	CVS	2002 XV_{93}, 2003 UZ_{117}	21	13		
Dec 04, 2010	1.0	Tek	V, R	0	0.63	CVS	2002 XV_{93}, 2003 UZ_{117}	38	2		
Mar 01, 2011	1.0	Tek	V, R	1	0.5	CVS	2000 YW_{134}, 2002 XV_{93}, 2004 EW_{95}	30	10		
Mar 02, 2011	1.0	Tek	V, R	0	0.66	CVS	2000 YW_{134}, 2004 EW_{95}	32	5		
Mar 03, 2011	0.5	Tek	V, R	0	0.85	CVS	2000 YW_{134}	13	2		

Table 3.1—Continued

UT date	# Nights	Instrument	Filters[a]	Conditions[b]	Seeing ($''$)[c]	Survey	Objects Observed	# Images[d]	Moon[e]	Gain	σ_{rn}
Mar 05, 2011	1.0	Tek	···	-1	···	···	···	···	0	···	···
Apr 01, 2011	1.0	Tek	V, R	1	0.7	CVS	2004 EW_{95}	47	4		
Apr 23, 2011	1.0	Tek	V, R	0	0.7	CVS	2004 EW_{95}	8	66		
Apr 25, 2011	1.0	Tek	···	-1	···	···	···	···	46	···	···
Apr 26, 2011	1.0	Tek	V, R	0	0.5	CVS	2000 YW_{134}, 2004 EW_{95}	21	37		
May 13, 2011	1.0	Tek	···	-1	···	···	···	···	77	···	···
Jun 11, 2011	1.0	Tek	···	-1	···	···	···	···	75	···	···
Aug 08, 2011	1.0	Tek	V, R	0	0.4	CVS	2001 QF_{298}	11	71		
Aug 18, 2011	1.0	Tek	V, R	1	0.6	···	calibration frames	8	81		
Sep 18, 2011	1.0	Tek	V, R	0	0.65	CVS	2001 QF_{298}	11	70		
Sep 23, 2011	1.0	Tek	V, R	0	0.6	CVS	2001 QF_{298}	14	21		
Dec 14, 2011	1.0	Tek	···	-1	···	···	···	···	85	···	···
Dec 24, 2011	1.0	Tek	···	-1	···	···	···	···	0	···	···
Dec 25, 2011	1.0	Tek	···	-1	···	···	···	···	1	···	···
Feb 16, 2012	0.5	WFGS2	g', r'	0	1.0	CVS	2003 AZ_{84}	15	31		
Feb 22, 2012	1.0	WFGS2	···	-1	···	···	···	···	0	···	···
Feb 24, 2012	1.0	WFGS2	g', r'	1	0.7	CVS	2003 AZ_{84}, 2004 EW_{95}	32	6		
Feb 25, 2012	1.0	WFGS2	···	-1	···	···	···	···	11	···	···
Feb 26, 2012	1.0	WFGS2	g', r'	0	0.7	CVS	2003 AZ_{84}, 2004 EW_{95}	26	18		
Feb 27, 2012	0.5	WFGS2	g', r'	0	0.6	CVS	2003 AZ_{84}	7	25		
Feb 28, 2012	0.5	WFGS2	g', r'	0	0.5	CVS	2003 AZ_{84}	19	34		
Feb 29, 2012	0.5	WFGS2	···	-1	···	···	···	···	43	···	···

Table 3.1—Continued

UT date	# Nights	Instrument	Filters[a]	Conditions[b]	Seeing ($''$)[c]	Survey	Objects Observed	# Images[d]	Moon[e]	Gain	σ_{rn}
Apr 17, 2012	1.0	WFGS2	g', r'	0	1.5	CVS	2003 AZ_{84}, 2004 EW_{95} 2002 MS_4	27	13		
Apr 18, 2012	1.0	WFGS2	g', r'	0	1.4	CVS	2003 AZ_{84}, 2004 EW_{95} 2002 MS_4	28	8		
Apr 27, 2012	1.0	WFGS2	g', r'	1	0.5	CVS	2004 EW_{95}	21	30		
Apr 28, 2012	1.0	WFGS2	g', r'	0	0.8	CVS	2004 EW_{95}	15	39		
Jun 14, 2012	1.0	WFGS2	g', r'	0	0.5	CVS	2002 MS_4	16	22		
Jun 16, 2012	1.0	WFGS2	g', r'	0	0.7	CVS	2002 MS_4	18	9		
Oct 14, 2012	1.0	Tek	V, R	1	0.8	CVS	2002 TX_{300}, 2003 UZ_{117}	28	2		
Oct 15, 2012	1.0	Tek	V, R	0	0.9	CVS	2002 TX_{300}, 2003 UZ_{117}	30	0		
Oct 19, 2012	1.0	Tek	V, R	0	0.8	CVS	2002 TX_{300}, 2003 UZ_{117}	24	20		
Oct 20, 2012	1.0	Tek	V, R	0	0.7	CVS	2002 TX_{300}, 2003 UZ_{117}	42	30		
Nov 18, 2012	1.0	Tek	···	-1	···	···	···	···	26	···	···
Nov 19, 2012	1.0	Tek	···	-1	···	···	···	···	36	···	···
Nov 21, 2012	1.0	Tek	···	-1	···	···	···	···	58	···	···
Nov 23, 2012	1.0	Tek	···	-1	···	···	···	···	77	···	···
Nov 24, 2012	1.0	Tek	···	-1	···	···	···	···	84	···	···

[a] V and R filters refer to the Kron-Cousins photometric system, and g' and r' refer to the Sloan Digital Sky Survey filters.

[b] Key: -1 = night lost due to poor weather or instrument problems; 0 = conditions were observable but not photometric or only partially photometric due to passing cirrus clouds; 1 = photometric

[c] approximated from the CFHT WX Tower (http://wx.ifa.hawaii.edu/current/seeing/) when available and by my best-focus frames otherwise

[d] Number of science images excluding those with poor tracking or other instrumental errors rendering the data unusable

[e] Moon's illumination (%)

[f] The dispersion in sky background for images taken on this night was very small, providing a poor determination of the linear fit in Eq. 3.5, so the previous night's gain and read noise measurements were used in photometry.

Note. —

References

Barucci, M. A., Belskaya, I. N., Fulchignoni, M., & Birlan, M. 2005, AJ, 130, 1291

Brunetto, R., Barucci, M. A., Dotto, E., & Strazzulla, G. 2006, ApJ, 644, 646

Hainaut, O. R. & Delsanti, A. C. 2002, A&A, 389, 641

Landolt, A. U. 1992, AJ, 104, 340

Mann, R. K., Jewitt, D., & Lacerda, P. 2007, AJ, 134, 1133

Moroz, L., Baratta, G., Strazzulla, G., Starukhina, L., Dotto, E., Barucci, M. A., Arnold, G., & Distefano, E. 2004, *Icarus*, 170, 214

Neese, C. 2008, NASA Planetary Data System, 103

Romanishin, W. & Tegler, S. C. 2007, in Astronomical Society of the Pacific Conference Series, Vol. 371, Statistical Challenges in Modern Astronomy IV, ed. G. J. Babu & E. D. Feigelson, 210

Tody, D. 1986, in Society of Photo-Optical Instrumentation Engineers (SPIE) Conference Series, Vol. 627, Society of Photo-Optical Instrumentation Engineers (SPIE) Conference Series, ed. D. L. Crawford, 733

Chapter 4

Brightness Variation Survey

4.1 Introduction

A major goal of this dissertation work was to rotationally-resolve $V - R$ colors for neutral TNOs. Achieving this goal required choosing targets with detectable brightness variation because: (i) color variation, if present, can only be detected if variation in one of the broadband filters used in the color computation was significant, and (ii) rotation periods can only be determined from objects with significant brightness variation, and determining the rotation period is necessary to allow the color data to be rotationally-phased. We conducted the Brightness Variation Survey (BVS) for the primary purpose of compiling a sample of neutral TNOs that exhibit detectable brightness variation in one broadband filter.

A change in brightness can be attributed to surface heterogeneity. Portions of the surface may have a different "freshness" or radiation exposure age and/or composition than others, changing the spectral slope and/or overall albedo (Moroz et al. 2004; Brunetto et al. 2006; Kaňuchová et al. 2012). Heterogeneity is expected to have a more subtle effect on light curve amplitudes compared to other mechanisms (like shape or binarity), causing a photometric range up to 0.25 magnitudes but more typically less than 10-20% (Magnusson 1991; Sheppard & Jewitt 2004).

Brightness variation can also be caused by rotation of objects with elongated shapes, with light curve maxima corresponding to the largest projected cross-section. Light curve

amplitudes explained by shape convey information about an object's projected axis ratios (discussed further in Chapter 6). The shape distribution contains information on the nature of past collisions. In a collisionally evolved population, objects smaller than 100 km in diameter are expected to be irregularly shaped fragments of parent bodies, while larger objects (greater than 200km in diameter) are collisionally fractured rubble piles which are subsequently tidally elongated through rotation (Catullo et al. 1984; Farinella & Davis 1996). In contrast, *large* objects that are not collisionally evolved should take on roughly spherical shapes over time, so by constraining the shapes of neutral TNOs, we can infer the role of collisions in their evolution. Upper limit estimates of the diameters of BVS targets show that most of them are relatively large (diameters > 100 km).

Constraining the amplitude distribution gives clues to the shape or albedo distribution and frequency of binaries, and comparing shapes between small body populations assesses the similarities in collisional history. For example, Binzel & Sauter (1992) found that Jupiter Trojans (hereafter, Trojans) and Hilda asteroids have similar shape distributions, implying a common origin and collisional rate. The same group also found that only large Trojans (diameters > 90km) have more elongated shapes than main belt asteroids of comparable size, implying that large Trojans have a different formation and/or collisional history than small Trojans.

Some of the major and competing solar system formation models predict different dynamical and collisional similarities between small bodies. The widely cited "Nice" model of solar system formation suggests that the giant planets underwent significant migration, scattering planetesimals violently and chaotically (*e.g.* Morbidelli et al. 2005; Levison et al. 2011). In the Nice model, Trojans were injected into their present orbits from the TNO region, so Trojans and TNOs should have similar shape distributions. However, earlier models of minimal planetary migration necessitate that Trojans were dynamically captured from the giant planet region of the solar system, meaning they should not share bulk physical properties with TNOs (Shoemaker et al. 1989; Marzari & Scholl 1998). Using our amplitude measurements from the BVS, we explored similarities amongst the amplitude

distributions of TNOs, TNO subsets, and other major small body populations like Trojans (whose amplitudes are available in the literature).

Highly elongated objects (with axis ratios $a : b \gtrsim 2.3$) are not stable against rotational disruption, so only photometric ranges less than 0.9 magnitudes can be explained by an object's shape (*e.g.*, Leone et al. 1984). Above this range, the only mechanism possible to explain observed amplitudes is a fully or partially eclipsing binary system. For binaries, minima correspond to the orbital configuration that renders the smallest projected cross-section of the system (*e.g.*, one component directly behind another), and vice versa. Brightness changes due to orbiting binaries are distinguishable by large light curve amplitudes, sharp light curve minima, and broad maxima (*e.g.*, Sheppard & Jewitt 2004).

Binary systems are important as diagnostics for several types of dynamical environments during both their formation and subsequent dynamical evolution. Several binary formation models exist, each predicting different observational outcomes. For example, in the Goldreich et al. (2002) model for binary formation, two objects become gravitational bound to one another when a third object passes within their mutual sphere of gravitational influence (the Hill sphere), removing energy from the system, effectively slowing down their speeds enough to for gravitational capture to occur between the interacting pair. This dynamical friction model predicts that later gravitational encounters with other passers-by will further reduce the separation between the two components, causing the overall distribution of binaries to be higher toward smaller separations. Astakhov et al. (2005) later refined the Goldreich et al. (2002) model by providing a mechanism by which the bound pair initially started interacting - via chaotic assistance (specifically mentioning solar tides) in the primordial, more densely populated Trans-Neptunian belt. This theory was further developed by Lee et al. (2007).

Weidenschilling (2002) describes a binary formation model by which two bodies physically collide within the Hill sphere of a third, more massive body, forming a debris disk and eventually a companion around the more massive object. This model calls for a

much more spatially dense outer solar system environment (about two orders of magnitude more than predicted in size distributions; Kenyon & Bromley 2004; Astakhov et al. 2005). Contrary to the Goldreich et al. (2002) and Astakhov et al. (2005) models, Weidenschilling (2002) predicts that the binary fraction should increase with component separation because the outer shells of the primary's Hill sphere contain more volume than inner shells of the same width, increasing the probability of gravitationally capturing a collision.

Funato et al. (2004) present a binary formation model whereby collisions of low mass objects onto higher mass bodies create a binary system with a low mass ratio (similar to binary formation in the main asteroid belt), but then a more massive body passes within the binary Hill sphere, ejecting the smaller companion and becoming bound to the primary in a wider, elliptical orbit. This formation scenario predicts highly eccentric systems with nearly equal mass components. Canup (2005) successfully reproduced the Pluto-Charon system by modeling a low-velocity collision between high mass objects, but this collisional formation scenario is generally regarded as exceptional for the Trans-Neptunian region, presumably since very large pre-collisional bodies are required, of which there were few during the TNO formative years. Lastly, Nesvorný et al. (2010) explore binary formation via gravitational collapse, which would naturally form wider, equal-mass, and eccentric binary systems.

Subsequent dynamical evolution after primordial binary formation must also be considered in explaining the currently observed binary fraction as a function of component separation. Petit & Mousis (2004) examined the effect of impacts on formed pairs, finding that impacts tended to disrupt wide binaries, which were more easily unbound than tight binaries. Parker & Kavelaars (2010) found that gravitational scattering of an already-formed system by a Neptune encounter also disrupted wide binaries. Other models show that tidal friction (which slowly leeches energy from a binary due to tidal forces between the two components) in addition to Kozai cycles (orbital oscillations produced by solar torque which slowly add energy to a binary system) result in close binaries (Perets & Naoz 2009; Porter & Grundy 2012). Collisional grinding may also be present, which is another mechanism by which wide binaries are disrupted.

Determining the difference between frequencies of wide versus tight binary systems therefore offers a way to discern between these competing formation theories. Perets (2011) also suggest that binaries may play an important role in planetary formation by catalyzing collisions and helping induce planetary growth. Observational efforts to determine binary frequency have been heavily focused on widely-separated systems, which can be directly detected (*e.g.*, Stephens & Noll 2006). Five direct-detection surveys have imaged nearly 900 TNOs in search of wide binaries, each having a different spatial resolution and thus a different binary separation detection limit (Noll et al. 2003; Stephens & Noll 2006; Kern & Elliot 2006b; Kern 2006).

Current results for TNOs show that the fraction of binaries toward smaller mutual separations may increase until a certain point, then turnover (Fig. 4.1). This turnover is only suggested by one data point (HST:NIC2), and most of the small-separation end of the distribution remains unexplored. The Goldreich et al. (2002) model, which was converted into an form easily compared to observations by Kern & Elliot (2006b), is plotted with the data in Fig. 4.1 and seems to reproduce the observed trend apart from the turnover. Unfortunately, other models have not yet been presented in a comparably quantitative form. Surveys like the BVS are capable of exploring the frequency of tight binaries in the region of the supposed turnover, further constraining the binary fraction as a function of mutual separation. Figure 4.2 summarizes the amplitude and period domains of each brightness variation mechanism. Objects with photometric ranges less than 25% can be explained by either surface variegation, elongated shape, or binarity, while objects with ranges of $0.25 \leq \Delta m \leq 0.9$ could have variation attributable to shape or binarity, and $\Delta m > 0.9$ can only be explained by a tight binary.

Several studies have investigated TNO brightness variation, all of which are summarized in Table 4.1 (compiled using the Asteroid Lightcurve Database; Warner et al. 2009). The combined results from previous work indicate that 65% of all TNOs with well-constrained variability (a sample of 63 objects) exhibit photometric ranges greater than 0.15, 43% have ranges greater than 0.4, and 5% have amplitudes greater than 0.9 magnitudes attributable

to binarity. In the remainder of this chapter, we explore the amplitude distribution for the neutral compared to red TNOs and the similarities in the inferred shape distribution and binary fraction using new data from our BVS.

Table 4.1. Results from previous brightness variation studies.

Designation	Diam. (km)	H	V-R	σ_{V-R}	V-R Ref.	Period (h)	Δm	Period/ Δm Ref.
Pluto	2700	-0.92	···	···	···	153.29	0.3	23
1993 SC	148	7.26	0.8	0.07	7	···	< 0.04	24
1994 TB	102	8.07	0.78	0.06	14	6.5	0.3	24
1994 VK_8	131	7.53	0.67	0.03	1	9	0.42	24
1995 QY_9	97	8.18	0.46	0.06	2	7	0.6	24
1995 SM_{55}	519	4.54	0.39	0.01	3	8.08	0.19	25
1996 GQ_{21}	383	5.2	0.69	0.03	4	···	< 0.1	26
1996 PW	6	14.1	···	···	···	35.44	0.44	27
1996 TL_{66}	350	5.4	0.35	0.01	5	12	0.07	28
1996 TO_{66}	575	4.32	0.38	0.02	6	7.92	0.26	25
1996 TP_{66}	140	7.39	0.68	0.03	5	···	< 0.12	24
1996 TQ_{66}	122	7.69	0.6	0.06	16	···	< 0.22	24
1996 TS_{66}	194	6.48	0.69	0.05	7	···	< 0.16	24
1997 CS_{29}	331	5.17	0.66	0.02	8	300.24	< 0.17	49
1997 CV_{29}	121	7.71	0.65	0.02	3	15.8	> 0.3	29
1998 BU_{48}	153	7.2	0.68	0.04	4	12.6	0.68	26
1998 HK_{151}	127	7.6	0.52	0.04	9	···	< 0.15	26
1998 SG_{35}	24	11.23	0.48	0.01	3	9.72	0.4	30,28
1998 SN_{165}	319	5.6	0.4	0.04	7	8.84	0.16	31
1998 VG_{44}	211	6.5	0.58	0.04	10	···	< 0.1	26
1998 WH_{24}	432	4.94	0.63	0.03	10	···	< 0.1	26

Table 4.1—Continued

Designation	Diam. (km)	H	V-R	σ_{V-R}	V-R Ref.	Period (h)	Δm	Period/ Δm Ref.
1998 WT_{31}	153	7.2	0.44	0.07	11	···	> 0.05	32
1999 CD_{158}	401	5.1	0.54	0.03	9	···	0.6	32
1999 DE_{9}	383	5.2	0.62	0.02	12	24	< 0.1	26
1999 DF_{9}	253	6.1	0.71	0.05	9	6.65	0.4	31
1999 KR_{16}	235	6.26	0.74	0.03	7	11.7	0.18	26
1999 OX_{3}	146	7.3	0.69	0.01	1	9.26	0.11	33
1999 OY_{3}	183	6.8	0.37	0.02	1	···	< 0.05	32
1999 RY_{215}	160	7.1	0.48	0.05	13	···	< 0.05	32
1999 RZ_{253}	278	5.9	0.65	0.06	14	···	< 0.05	31
1999 TC_{36}	295	5.33	0.69	0.01	15	6.21	0.06	34,35
1999 TD_{10}	65	9.06	0.47	0.01	3	15.382	0.65	36,35,37
2000 CG_{105}	211	6.5	0.4	0.2	17	···	0.45	32
2000 CM_{105}	192	6.7	0.8	0.3	17	···	< 0.14	31
2000 EB_{173}	411	5.05	0.53	0.01	13	13.5	< 0.06	26,35
2000 FV_{53}	96	8.2	0.45	0.09	11	7.58	0.07	38
2000 GN_{171}	265	6	0.63	0.03	4	8.329	0.64	39
2000 WR_{106}	600	3.96	0.63	0.02	3,18	6.3436	0.5	40,35,41
2000 YW_{134}	474	4.74	0.39	0.02	10	···	< 0.1	25
2001 CZ_{31}	265	6	0.5	0.1	4	4.71	0.21	31
2001 FP_{185}	223	6.38	0.58	0.01	15	···	< 0.06	25
2001 FZ_{173}	239	6.23	0.55	0.01	15	···	< 0.06	26

Table 4.1—Continued

Designation	Diam. (km)	H	V-R	σ_{V-R}	V-R Ref.	Period (h)	Δm	Period/ Δm Ref.
2001 KD_{77}	291	5.8	0.65	0.04	9	···	< 0.07	25
2001 KX_{76}	919	3.3	0.61	0.03	10	···	< 0.15	35
2001 QC_{298}	231	6.3	0.49	0.03	18	12	0.4	32
2001 QF_{298}	401	5.1	0.6	0.04	10	···	< 0.12	25
2001 QG_{298}	121	7.71	0.6	0.02	19	13.774	1.14	42
2001 QY_{297}	319	5.6	0.43	0.09	10	11.68	0.49	33
2001 UQ_{18}	200	6.55	0.74	0.08	20	···	< 0.3	43
2001 UR_{163}	532	4.49	0.84	0.03	10	···	< 0.08	25
2001 YH_{140}	350	5.4	···	···	···	13.25	0.21	43
2002 AW_{197}	701	3.57	0.58	0.02	18	8.86	0.08	47
2002 GH_{32}	334	5.5	0.57	0.07	21	···	0.75	32
2002 GO_{9}	62	9.17	0.76	0.01	15	13.94	0.14	35
2002 KW_{14}	420	5	···	···	···	6.63	0.25	49
2002 KX_{14}	562	4.5	···	···	···	···	< 0.05	49
2002 LM_{60}	908	2.74	0.64	0.01	15	17.679	0.13	44,39
2002 PN_{34}	78	8.66	0.52	0.02	10	8.45	0.18	35
2002 TC_{302}	730	3.8	0.64	0.02	6	5.41	0.04	33
2002 TX_{300}	286	3.47	0.36	0.01	15	8.12	0.09	25,46
2002 UX_{25}	688	3.93	0.54	0.03	18	14.382	0.21	45
2002 VE_{95}	298	5.75	···	···	···	6.76	0.08	47
2002 WC_{19}	440	4.9	···	···	···	···	< 0.05	43

Table 4.1—Continued

Designation	Diam. (km)	H	V-R	σ_{V-R}	V-R Ref.	Period (h)	Δm	Period/ Δm Ref.
2003 AZ_{84}	737	3.78	0.4	0.03	12	13.42	0.14	25
2003 BF_{91}	19	11.7	···	···	···	18.2	1.09	38
2003 BG_{91}	30	10.7	···	···	···	8.4	0.18	38
2003 BH_{91}	18	11.9	···	···	···	···	> 0.15	38
2003 EL_{61}	1303	0.43	0.37	0.02	18	3.9154	0.3	48
2003 FY_{128}	440	4.9	0.6	0.02	6	8.54	0.15	28
2003 MW_{12}	878	3.4	···	···	···	5.9	0.06	28
2003 OP_{32}	801	3.6	···	···	···	4.854	0.18	50
2003 QY_{90}	221	6.4	···	···	···	3.4	0.34	51
2003 SQ_{317}	253	6.1	···	···	···	7.5	1	32
2003 TH_{58}	127	7.6	···	···	···	···	< 0.05	32
2003 UZ_{117}	371	5.27	0.35	0.02	18	···	> 0.1	52
2003 UZ_{413}	607	4.2	···	···	···	4.14	0.1	52
2003 VS_2	636	4.1	···	···	···	7.42	0.6	34,28
2004 DW	1526	2.2	···	···	···	13.188	0.18	39
2004 GV_9	666	4	0.74	0.1	16	5.86	0.16	53
2004 NT_{33}	554	4.4	···	···	···	7.87	0.04	33
2004 PT_{107}	265	6	···	···	···	20	0.05	32
2004 SB_{60}	607	4.2	···	···	···	6.09	0.2	28,32
2004 TY_{364}	546	4.43	···	···	···	11.7	0.22	43
2004 UX_{10}	529	4.5	0.58	0.03	22	5.68	0.1	52,28

Table 4.1—Continued

Designation	Diam. (km)	H	V-R	σ_{V-R}	V-R Ref.	Period (h)	Δm	Period/ Δm Ref.
2004 XA_{192}	666	4	···	···	···	7.88	0.07	33
2005 CB_{79}	483	4.7	···	···	···	6.76	0.13	28
2005 EF_{298}	277	6.02	···	···	···	4.82	0.31	49
2005 FY_{9}	1524	0.09	0.46	0.02	18	22.48	0.03	54
2005 GE_{187}	160	7.1	···	···	···	12.2	0.5	32
2005 PR_{21}	253	6.1	···	···	···	···	< 0.28	49
2005 QU_{182}	416	3.5	···	···	···	9.61	0.12	49
2005 RM_{43}	554	4.4	···	···	···	6.71	0.05	52,28
2005 RN_{43}	697	3.9	···	···	···	6.95	0.06	49
2005 RR_{43}	666	4	···	···	···	7.87	0.06	28
2005 TB_{190}	483	4.7	0.56	0.03	6	12.68	0.12	33
2005 UQ_{513}	878	3.4	···	···	···	7.03	0.3	32,33
2006 HJ_{123}	283	5.7	···	···	···	···	< 0.13	49
2007 JF_{43}	336	5.6	···	···	···	4.76	0.22	49
2007 JH_{43}	505	4.7	···	···	···	···	< 0.08	49
2007 JJ_{43}	694	3.9	···	···	···	6.04	0.13	49
2007 OR_{10}	1200	2	···	···	···	···	< 0.09	49
2007 TY_{430}	183	6.8	···	···	···	23050	···	55
2008 QY_{40}	336	5.2	···	···	···	···	< 0.15	49
2009 YE_{7}	200	4.25	···	···	···	···	< 0.2	49
2010 EK_{139}	470	3.8	···	···	···	3.53	0.12	49

4.2 Data and Photometry

The BVS sample selection and observing conditions are described in Chapter 3, Sections 3.2 and 3.1, respectively. Orbital parameters and known surface properties of the final BVS targets are provided in Table 4.2. We chose the R filter to assess the brightness variation because the combination of typical TNO colors, detector quantum efficiency, and filter transmission would give the highest signal-to-noise (S/N). We also obtained V measurements for color. Our target list was comprised of the brightest objects of the ~ 50 known neutral TNOs at the start of this project. We started observing the brightest of the neutral targets first and intended to cease BVS observations once the necessary sample size of follow-up objects (*i.e.*, those with detectable variation) was found. However, because of accuracies in our photometry which rendered falsely low amplitude photometric ranges at first (and was later corrected after the photometry experiments in Chapter 2 were performed), we ended up observing far more BVS targets than were actually needed for determination of follow-up targets - 38 neutral TNOs, each $\sim 3 - 12$ times per night.

The tphot algorithm extensively explored in Chapter 2 was used to perform differential photometry, including systematic error. The photometric range was computed as the maximum observed change in brightness. To determine candidates for the follow-up CVS, we computed the statistical variance in magnitude for each point source in the field and plotted them as a function of median apparent magnitude. Targets that showed variance greater than field stars of comparable magnitude were considered for follow-up. Figure 4.3 provides the magnitude-variance for each BVS target, and the photometric ranges are reported in Table 4.2.

Table 4.1—Continued

Designation	Diam. (km)	H	V-R	σ_{V-R}	V-R Ref.	Period (h)	Δm	Period/ Δm Ref.
2010 EL_{139}	423	5.1	···	···	···	3.16	0.15	49
2010 EP_{65}	352	5.5	···	···	···	7.48	0.17	49
2010 ER_{65}	368	5.4	···	···	···	···	< 0.16	49
2010 ET_{65}	404	5.2	···	···	···	3.94	0.13	49
2010 FX_{86}	612	4.3	···	···	···	7.9	0.26	49
2010 HE_{79}	402	5.21	···	···	···	9.75	0.11	49
2010 KZ_{39}	702	4	···	···	···	···	< 0.17	49
2010 PU_{75}	336	5.6	···	···	···	6.19	0.27	49
2010 RF_{43}	671	4.1	···	···	···	···	< 0.08	49
2010 RO_{64}	386	5.3	···	···	···	···	< 0.16	49
2010 TY_{53}	404	5.2	···	···	···	···	< 0.14	49
2010 VK_{201}	534	4.6	···	···	···	3.79	0.3	49
2010 VZ_{98}	443	5	···	···	···	···	< 0.18	49

Note. — Reference Key: 1: Tegler & Romanishin (2000); 2: Luu & Jewitt (2002); 3: Tegler & Romanishin (2003); 4: Sheppard & Jewitt (2002); 5: Tegler & Romanishin (1998); 6: Sheppard (2010); 7: Jewitt & Luu (2001); 8: Barucci et al. (2000); 9: Doressoundiram et al. (2002); 10: Doressoundiram et al. (2007); 11: Peixinho et al. (2004); 12: DeMeo et al. (2009); 13: Doressoundiram et al. (2001); 14: Delsanti et al. (2001); 15: Tegler et al. (2003); 16: Gil-Hutton & Licandro (2001); 17: Trujillo & Brown (2002); 18: Jewitt et al. (2007); 19: Sheppard & Jewitt (2004); 20: Doressoundiram et al. (2005); 21: Santos-Sanz et al. (2009); 22: Romanishin et al. (2010); 23: Tholen & Buie (1997); 24: Romanishin & Tegler (1999); 25: Sheppard & Jewitt (2003); 26: Sheppard & Jewitt (2002); 27: Davies et al. (1998); 28: Thirouin et al. (2010); 29: Chorney & Kavelaars (2004); 30: Bauer et al. (2003); 31: Lacerda & Luu (2006); 32: Snodgrass et al. (2010); 33: Thirouin et al. (2012); 34: Ivanova et al. (2005); 35: Ortiz et al. (2003a); 36: Rousselot et al. (2003); 37: Mueller et al. (2004); 38: Trilling & Bernstein (2006); 39: Rabinowitz et al. (2007); 40: Farnham (2001); 41: Hicks et al. (2005); 42: Sheppard & Jewitt (2004); 43: Sheppard (2007); 44: Ortiz et al. (2003b); 45: Rousselot et al. (2005); 46: Ortiz et al. (2004); 47: Ortiz et al. (2006); 48: Rabinowitz et al. (2006); 49: Benecchi & Sheppard (2013); 50: Rabinowitz et al. (2008); 51: Kern & Elliot (2006a); 52: Perna et al. (2008); 53: Dotto et al. (2008); 54: Ortiz et al. (2007); 55: Sheppard et al. (2012)

Table 4.2. BVS photometry results and basic dynamical and physical properties for our 38 neutral TNOs. Orbital elements include semimajor axis (a in AU), eccentricity (e), and inclination (i in degrees).

Designation	a	e	i	Dyn. Class[a]	Diameter (km)	Diam. Ref.[c]	$V-R$[b]	σ_{V-R}	H	Obs. UT date	# images	Δm	$\sigma_{\Delta m}$	Comments
1993 SB	39.64	0.33	1.94	P	130	1	0.51	0.08	7.7	8/23/09	3	0.15	0.08	
1995 QY_9	39.85	0.27	4.84	P	140	1	0.5	0.1	7.5	8/23/09	4	0.18	0.07	
1995 SM_{55}	42.03	0.11	27.03	C	250	2	0.39	0.05	4.8	8/23/09	4	0.1	0.1	Haumea family member
1995 TL_8	52.75	0.24	0.24	C	430	1	0.40	0.06	5.3	8/23/09	3	0.24	0.02	Binary, $\sim 0.01''$separation
1996 TL_{66}	84.72	0.59	23.95	S	360	3	0.38	0.07	5.4	10/20/09	2	0.00	0.02	
1996 TS_{66}	44.19	0.13	7.33	C	230	1	0.43	0.02	6.4	10/20/09	3	0.21	0.06	
1998 SN_{165}	38.01	0.05	4.60	S	460	4	0.44	0.08	5.8	8/23/09	4	0.03	0.03	
1998 UR_{43}	39.78	0.23	8.75	P	100	1	0.5	0.1	8.3	2/14/10	2	0.3	0.1	
1999 CD_{158}	43.81	0.14	25.42	R	300	2	0.48	0.08	5.1	12/23/09	10	0.60	0.09	
1999 CL_{119}	47.07	0.01	23.25	C	300	1	0.5	0.1	5.9	4/21/10	4	0.0	0.1	
1999 CL_{158}	41.65	0.21	10.02	C	190	1	0.39	0.05	6.9	12/23/09	7	0.1	0.2	
1998 HB_{12}	55.42	0.41	13.15	R	160	1	0.50	0.06	7.2	2/14/10	3	0.05	0.05	
1999 RY_{215}	45.34	0.24	22.20	C	300	1	0.48	0.09	7.1	10/20/09	3	0.09	0.08	
1999 TD_{10}	98.85	0.88	5.96	S	80	1	0.51	0.03	8.8	12/23/09	5	0.24	0.05	
2000 CQ_{105}	57.14	0.39	19.66	S	290	1	0.4	0.2	5.9	2/14/10	3	0.0	0.1	
2000 EE_{173}	49.34	0.54	5.95	S	90	1	0.49	0.01	8.5	2/15/10	3	0.14	0.08	
2000 GP_{183}	39.70	0.07	4.92	P	230	1	0.44	0.09	6.4	4/21/10	3	0.12	0.03	
2000 OU_{69}	43.09	0.05	4.42	C	260	1	0.5	0.2	6.1	8/21/09	3	0.1	0.2	
2000 PE_{30}	54.21	0.34	18.44	S	260	1	0.4	0.1	6.2	8/21/09	3	0.00	0.07	
2001 QB_{243}	34.87	0.56	6.79	S	100	1	0.42	0.09	8.3	8/21/09	3	0.12	0.07	

Table 4.2—Continued

Designation	a	e	i	Dyn. Class[a]	Diameter (km)	Diam. Ref.[c]	$V-R$[b]	σ_{V-R}	H	Obs. UT date	# images	Δm	$\sigma_{\Delta m}$	Comments
2000 YW_{134}	58.26	0.29	19.78	S	430	1	0.39	0.03	4.8	12/23/09	7	0.22	0.03	Binary, $\sim 0.06''$separation
2001 CZ_{31}	45.35	0.12	10.21	C	360	1	0.5	0.1	5.4	2/14/10	3	0.12	0.06	
2001 FP_{185}	216.42	0.84	30.80	S	270	1	0.52	0.06	6.1	2/15/10	3	0.12	0.04	
2001 KB_{77}	39.43	0.28	17.54	P	180	1	0.44	0.08	7	8/23/09	2	0.07	0.09	
2001 QC_{298}	46.33	0.12	30.60	C	280	1	0.49	0.04	6.1	8/21/09	4	0.06	0.07	Binary, $\sim 0.13''$separation
2001 QF_{298}	39.41	0.11	22.36	P	440	5	0.42	0.06	4.7	8/21/09	3	0.07	0.03	
2001 QY_{297}	43.76	0.08	1.55	C	340	1	0.4	0.1	5.6	8/21/09	3	0.03	0.08	Binary, $\sim 0.09''$separation
2002 GP_{32}	55.11	0.42	1.56	R	230	1	0.47	0.05	6.4	8/24/09	2	0.08	0.06	
2002 MS_4	41.61	0.15	17.71	C	1360	6	0.38	0.03	3.8	4/21/10	3	0.03	0.03	
2002 TX_{300}	43.41	0.12	25.87	C	340	2,7	0.36	0.04	3.1	9/4/10	12	0.14	0.03	Haumea family member
2002 XV_{93}	39.55	0.12	13.27	P	860	5	0.37	0.03	4.9	10/20/09	3	0.08	0.05	
2003 AZ_{84}	39.64	0.17	13.54	P	350	5	0.45	0.05	4	12/23/09	6	0.22	0.02	Binary, $\sim 0.22''$separation
2003 OP_{32}	43.13	0.10	27.15	C	320	2	0.39	0.06	4.2	9/5/10	11	0.2	0.1	Haumea family member
2003 UB_{313}	67.96	0.44	43.89	S	4780	8	0.39	0.03	-1.2	10/20/09	3	0.016	0.004	Binary, $\sim 0.53''$separation
2003 UZ_{117}	44.51	0.14	27.40	C	430	2	0.36	0.03	5.3	10/20/09	2	0.14	0.03	Haumea family member
2004 EW_{95}	39.32	0.31	29.30	P	190	1	0.38	0.03	6.7	2/14/10	3	0.03	0.02	
2005 FY_9	45.56	0.16	29.01	C	4980	9,10	0.46	0.03	-0.4	2/14/10	3	0.013	0.006	
2005 RR_{43}	43.46	0.14	28.46	C	300	2	0.41	0.04	4	12/23/09	5	0.08	0.01	Haumea family member

[a]Key to the dynamical class: C = classical, S = scattered disk objects, P = plutinos, R = resonant objects not in 3:2 resonance (occupied by plutinos)

[b]Colors reported here are compiled from the literature compiled in the latest version (8 at the time of writing) of the catalog initially presented in Neese (2008).

[c]Reference key: 1: Assumed albedo of 0.09, the mean measured albedo for TNOs (Warner et al. 2009); 2: Stansberry et al. (2011); 3: Santos-Sanz et al. (2012); 4: Stansberry et al. (2008); 5: Mommert et al. (2012); 6: Vilenius et al. (2012); 7: Elliot et al. (2010); 8: Sicardy et al. (2011); 9: Ortiz et al. (2012); 10: Lim et al. (2010)

4.3 Amplitude distributions

We constructed updated amplitude distributions by merging our data with previous work (Table 4.1). In instances of duplication between the BVS data and previous studies, the largest maximum amplitude measurement superseded all others (10 objects fit this description). We provided new amplitude constraints for 17 additional TNOs, increasing the number of objects with measured amplitudes by 24% to a total of 89. To investigate trending amongst TNO sub-populations as well as between TNOs and other small body populations, we calculated the Kolmogorov-Smirnov (KS) probability that two samples are statistically similar for many combinations of small body subsets (Table 4.3). A low KS probability of $\lesssim 0.002$ indicates that the samples being considered have a low probability of coming from the same distribution.

Our calculations suggest that the amplitude distribution of neutral TNOs ($V - R \leq 0.52$) is not intrinsically different from that of red TNO, although only 20 red TNOs have meaningful amplitude measurements. Small TNO amplitudes may also be similar to large TNO amplitudes, but more small TNO amplitude measurements are needed to better assess this relationship. The greatest similarity between different TNO dynamical classes is between Classicals and Resonant objects while Classicals and Scattered/Detached objects show the least amplitude similarity, though very few amplitude measurements exist for SDOs/Detached objects and Resonators. TNOs do appear to have different amplitude distributions from Trojans, MBAs, and potentially Centaurs based on statistically significant sample sizes and regardless of the size regime explored. Figure 4.4 gives the cumulative fraction distributions for samples that showed significant dissimilarity and $> 50\%$ probability of similarity. We plotted the cumulative fractions for samples of comparable sizes and the fractional number distribution for samples of very different sizes.

Table 4.3 Comparison between amplitude distributions of various subsets of TNOs and between TNO subsets and other populations, including Centaurs, Trojans, and Main belt asteroids (MBAs). A low KS probability of ≤ 0.002 indicates that the samples being considered are statistically different.

Sample 1	Sample 2	Sample Size 1	Sample Size 2	KS probability
TNOs: neutral	TNOs: red	69	20	0.3270
TNOs $\leq$ 200km	TNOs $>$ 200km	17	72	0.2447
TNOs: Classicals	TNOs: SDOs & Detached	45	16	0.4110
TNOs: Classicals	TNOs: Resonators	45	28	0.9331
TNOs: Resonators	TNOs: SDOs & Detached	28	16	0.5826
TNOs	Centaurs	89	27	0.0911
TNOs	Trojans	89	124	0.0003
TNOs	MBAs	89	2629	$<$ 0.0001
TNOs	Outer MBAs	89	1380	$<$ 0.0001
TNOs: SDOs & Detached	Centaurs	16	27	0.0796
TNOs: SDOs & Detached	Trojans	16	124	0.0043
TNOs: Classicals	Trojans	45	124	0.0047
TNOs $>$ 100km	Centaurs $>$ 100km	83	10	0.6845
TNOs $>$ 100km	Trojans $>$ 100km	83	19	0.0099
TNOs $>$ 100km	MBAs $>$ 100km	83	184	$<$ 0.0001
TNOs $>$ 100km	Outer MBAs $>$ 100km	83	147	$<$ 0.0001

4.4 Calculating the neutral tight binary fraction at BVS separation sensitivities

4.4.1 Determining the BVS separation sensitivity

Out of 89 TNOs with known lightcurve ranges, 3 (or 3.4%) have ranges > 0.9 magnitudes, the upper limit for brightness variations caused by shape. The range of mutual separations which we could detect was dependent on the maximum mutual separation of the system relative to the primary's size, the size of the components themselves, and the geocentric distance at the time the data were taken. The seeing was not a factor in detecting binaries (other than affecting the uncertainties in the magnitudes) because we were not trying to resolve the two components separately, but rather infer the presence of a companion from by the effect it has on the rotational lightcurve. Equation 2 from Noll et al. (2008) gives the simplified trigonometric formula for the angular separation in arcseconds between two components (θ'') of a binary as

$$\theta'' = \frac{4s}{2900\Delta} \quad , \tag{4.1}$$

where s is the physical separation (in km) between the binary components and Δ is the geocentric distance in AU. Leone et al. (1984) give the unitless parameter D such that

$$D = \frac{r_s + r_p}{s} \quad , \tag{4.2}$$

where r_s and r_p are the radii of the secondary and primary, respectively, in kilometers. We combine Eqs. 4.1 and 4.2 to compute

$$\theta'' = \frac{4\,(r_p + r_s)}{2900\,\Delta\,D} \quad . \tag{4.3}$$

Determining the sensitivity limits in separation for each object meant determining the maximum r_p and r_s and minimum D, since Δ is essentially fixed for the observations. Leone

et al. (1984) found that binary systems with $\Delta m \geq 0.9$ correspond to mutual separations greater than ~ 1.4 times the sum of the components' largest axis length, or $D \gtrsim 0.7$. In the limiting case where $r_s = r_p$, Equation 6.8 becomes:

$$\theta''_{lim} = \frac{4\ (2r_p)}{2030\ \Delta} \quad . \tag{4.4}$$

Using diameter estimates from Table 4.2 and Δ from each target's ephemeris on the night it was observed, we compute θ''_{lim} for each target. The average for all θ''_{lim} estimates gives a typical separation sensitivity for the BVS of $\sim 0.02''$, and the standard deviation of the individual θ''_{lim} calculations for all targets gives the uncertainty on that sensitivity of $\sim 0.03''$.

4.4.2 Determining the tight binary fraction

The debiased binary fraction in neutral TNOs ($f_{neutral}$) can be expressed as:

$$f_{neutral} = f_{obs}\ /\ (f_{0.9} \times f_{night} \times f_{orient} \times f_{cadence}) \quad , \tag{4.5}$$

where f_{obs} is the fraction of the sample observed to have brightness variation (Δm) greater than 0.9 magnitudes, $f_{0.9}$ is the fraction of tight binaries that are elongated such that $\Delta m \geq 0.9$, f_{night} is the fraction of those objects with rotation periods fast enough to produce $\Delta m \geq 0.9$ within a typical BVS observing night of length 10 hours, f_{orient} is the fraction of tight binaries oriented such that a large amplitude can be observed (*i.e.*, with the binary orbital plane perpendicular or parallel to the line-of-sight), and $f_{cadence}$ is likelihood that we will detect large variation given the observing cadence.

We must use the observed range of variation in magnitude to diagnose binarity when an object's period is unknown. The amplitude of a tight binary system is dependent on its separation and mass ratio (Chandrasekhar 1969). Those with lower mass ratios between the primary and secondary components are less tidally distorted into elongated shapes and have small photometric ranges due to the relatively smaller change in projected surface area.

Even if we assume a uniform range of separations within the tight binary range ($\leq 5\times$ the Hill radius), an unbiased mass ratio distribution has not yet been constrained for outer solar system objects. Thus, we were not able to meaningfully constrain $f_{0.9}$, which necessitated modifying Equation 4.5 to:

$$f_{neutral} = f_{obs} \ / \ (f_{night} \times f_{orient} \times f_{cadence}) \quad . \tag{4.6}$$

Removing the $f_{0.9}$ term meant that our results only applied to systems with mass ratios that give $\Delta m > 0.9$. We know from Leone et al. (1984) that only mass ratios $\gtrsim 0.6$ give $\Delta m \geq 0.9$ regardless of the density and/or separation. Our results therefore carry the caveat that our calculated binary fraction only applies to mass ratios $\gtrsim 0.6$.

We determined f_{obs} through the BVS survey. Because we detected no objects with $\Delta m \geq 0.9$ of the 34 objects sampled that are not known binaries, we found $f_{obs} < 1/34$, or $f_{obs} < 0.029$. The f_{night} term was determined using numerical solutions to Roche binary equilibrium models based on Chandrasekhar (1969) and calculated in Leone et al. (1984). They found that Roche binaries with low densities (typical of the outer solar system) must have fast orbital periods (< 15 hours) so that they do not merge. Therefore, all tight binaries will have orbital periods < 15 hours (consistent with observational findings Sheppard & Jewitt 2004), so the full photometric range (corresponding to 1/4 of the rotation) will occur within 3.75 hours, giving $f_{night} = 1$.

Mann et al. (2007) found that f_{orient} depends on the shape of the binary components. They calculated that for an extreme case where the two components most closely resemble rectangular solids (*e.g.*, two shoeboxes connected on their ends) and assuming random pole orientation, the probability that the viewing geometry would allow $\Delta m > 0.9$ to be observed is 0.17. For ellipsoidal components, the probability becomes 0.29.

Lastly, the $f_{cadence}$ term is dependent on the signal-to-noise of the photometry, the rotation period amplitude, the number of data points, and the rotation phases sampled. We performed Monte Carlo simulations of the rotation phase sampling for each dataset

to determine the likelihood of sampling $> 15\%$ variation for a typical TNO, . For each simulation, we took the photometric error on each data point and the number of data points from the true dataset, then distributed the points randomly (with the random factor chosen from a Gaussian distribution)about a light curve that had the same photometric range as the average TNO light curve (~ 0.29 Warner et al. 2009). We also required that the minimum rotation phase range be greater than 0.08 to reflect the minimum sampling rate ($\sim$ 170 minutes) relative to the slowest known TNO rotation period of 35.44 hours (excluding Pluto, which is locked in synchronous orbit with its relatively large companion). We found that 100,000 realizations per target dataset were sufficient to produce a well-defined distribution of simulated photometric ranges. The probability of detecting variation greater than 15% is the fraction of simulated photometric ranges greater than 15% for each dataset. We took the average of the individual datasets' probabilities to compute an 86% probability of detecting $> 15\%$ variation in the entire sample (*i.e.*, $f_{cadence} = 0.86$).

Feeding these terms into Equation 4.6, we found a tight binary fraction for neutral TNOs of $f_{neutral} < 12 - 20\%$ for separations of $\sim 0.02^{+0.03}_{-0.02}{}''$. Our result falls in between the HST:NIC2 results (at $\theta = 0.013''$) and the HST:STIS results (at $\theta = 0.1''$), the region where the overturn in the binary fraction as a function of separation is suggested to exist (Fig. 4.1).

4.5 Discussion & Conclusions

Results from the BVS indicate that TNOs likely have a uniquely low amplitude distribution relative to other small body populations except possibly Centaurs, whose amplitudes are only minimally sampled. This finding suggests that compared to other small body populations, TNOs underwent minimal collisional processing. If TNOs had a different collisional history than other populations they may not be the parent population of Jupiter Trojans, which does not support the NICE model (Morbidelli et al. 2005). However, little is known about the difference between *subsequent* collisional processing of these small bodies

compared to TNOs. TNOs may have been subject to a much gentler collisional history after the chaotic scattering event described in the NICE model if there was significant depletion of the TNO region through dynamical ejection into other parts of the solar system.

Our updated amplitude distributions also show evidence that Classicals and Resonant TNOs have similar shape distributions, suggesting that Resonators were captured from the Classical region. Trilling & Bernstein (2006) found evidence for a size-amplitude correlation based on their observations of a small sample size, which we did not see in our data. The absence of this correlation is not consistent with small objects being irregularly shaped collisional fragments, again suggesting a relatively gentle collisional history. It could be, however, that some of our size estimates (namely those that come from assumed and not measured albedos) are wrong, so obtaining additional albedo measurements would assist in accurately determining this correlation.

Neutral TNOs did not appear to have different amplitudes from red TNOs, suggesting a common history. If neutral and red TNOs share the same shape distribution, implying that they are equally likely to be tidally elongated collisional by-products, then it is unlikely that neutral colors are produced by a higher instance of collisions. In this way, the collisional resurfacing scenario for neutral colors was not supported by our findings.

We found that 36% of our targets had $\Delta m > 0.15$, which is consistent with Sheppard & Jewitt (2003) and Lacerda & Luu (2006). We found no objects with $\Delta m > 0.9$, allowing us to place upper limits on the tight binary fraction within the neutral population. We then computed a debiased neutral tight binary fraction of $< 12 - 20\%$ for separations $\sim 0.02^{+0.03}_{-0.02}''$ and mass ratios greater than 0.6. If the neutral and red TNO binary fractions at small separations are similar, then our finding suggests a turnover between $\sim 0.02 - 0.1''$ in the binary frequency as a function of separation. The turnover could exist if the binary fraction observed is the product of two different formation mechanisms, one preferentially forming wide systems (*i.e.*, Weidenschilling 2002; Funato et al. 2004; Nesvorný et al. 2010), and another more commonly producing systems with small separations (*i.e.*, Goldreich et al. 2002; Astakhov et al. 2005). Another explanation for the observed binary fractions

is a binary formation model that produces a greater number of small separation systems (Goldreich et al. 2002), accompanied by a subsequent dynamical evolution mechanism that either preferentially disrupts tight binaries or adds energy to the system, increasing the separation between the two components. Because such a physical mechanism of depleting the tight binary population, we find it more likely that two formation mechanisms were at work simultaneously in the Trans-Neptunian belt.

In summary, evidence from the updated amplitude distributions suggests that TNOs generally experienced a gentle collisional history, which is not consistent with them being a dynamically excited population. We also find no evidence that TNOs have similar amplitude/shape distributions to other small body populations, indicating that they either do not have common origins with any other population or underwent significant depletion which lowered the subsequent collisional rate. However, more data are needed, especially albedo measurements for TNOs with amplitude constraints, and amplitude measurements for red TNOs, SDOs, Detached objects, in order to adequately investigate trending within the Trans-Neptunian region. Our results also support the existence of a turnover in the binary fraction as a function of component separation, which we attribute to two binary formation mechanisms dominant during binary formation in the Trans-Neptunian belt, one of which is likely to be the dynamical friction model first described by Goldreich et al. (2002) since it is one of the only mechanisms that preferentially forms tight binaries and fits the data very well at larger separations.

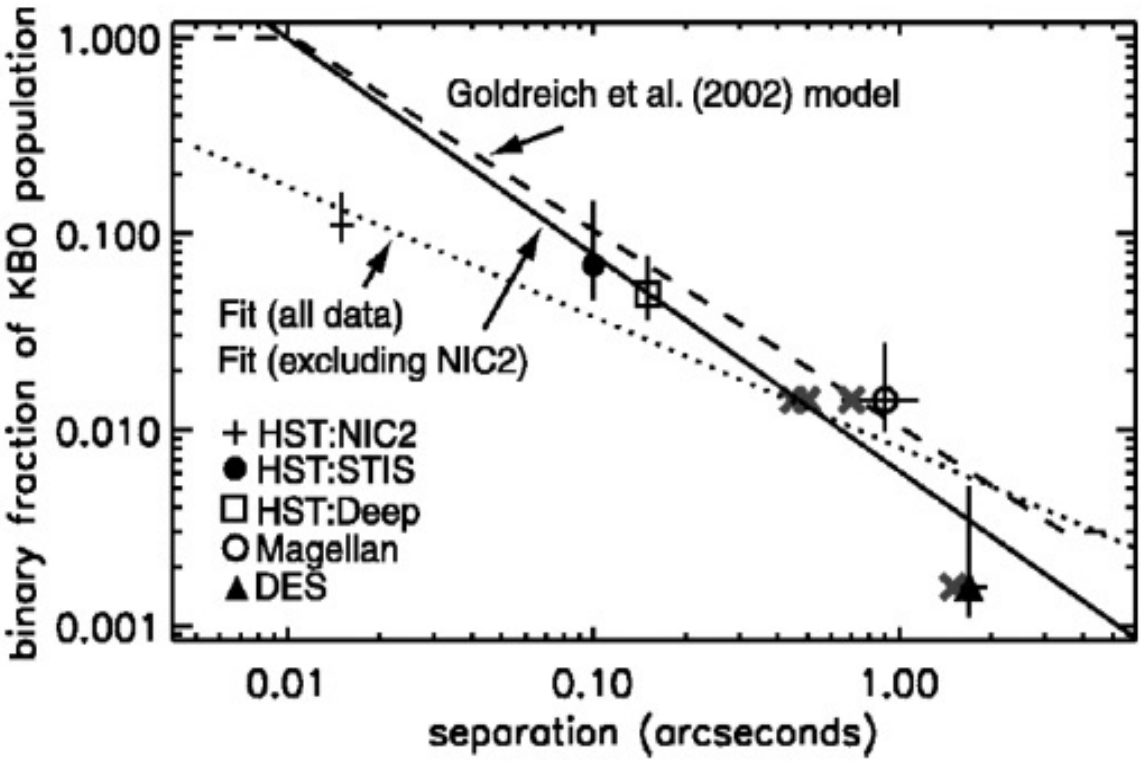

Figure 4.1 The TNO binary fraction as a function of mutual separation determined from different surveys (taken from Kern & Elliot 2006b). The solid line shows the linear fit to all datasets except the HST:NIC2 survey by Stephens & Noll (2006), which imaged 81 targets. The dotted line shows the linear fit including the HST:NIC2 data, and the dashed line shows the trend predicted by the Goldreich et al. (2002) model. The data show a potential turnover. Results from the BVS offers constraints toward small separations ($\leq 0.06''$) in order to investigate this turnover.

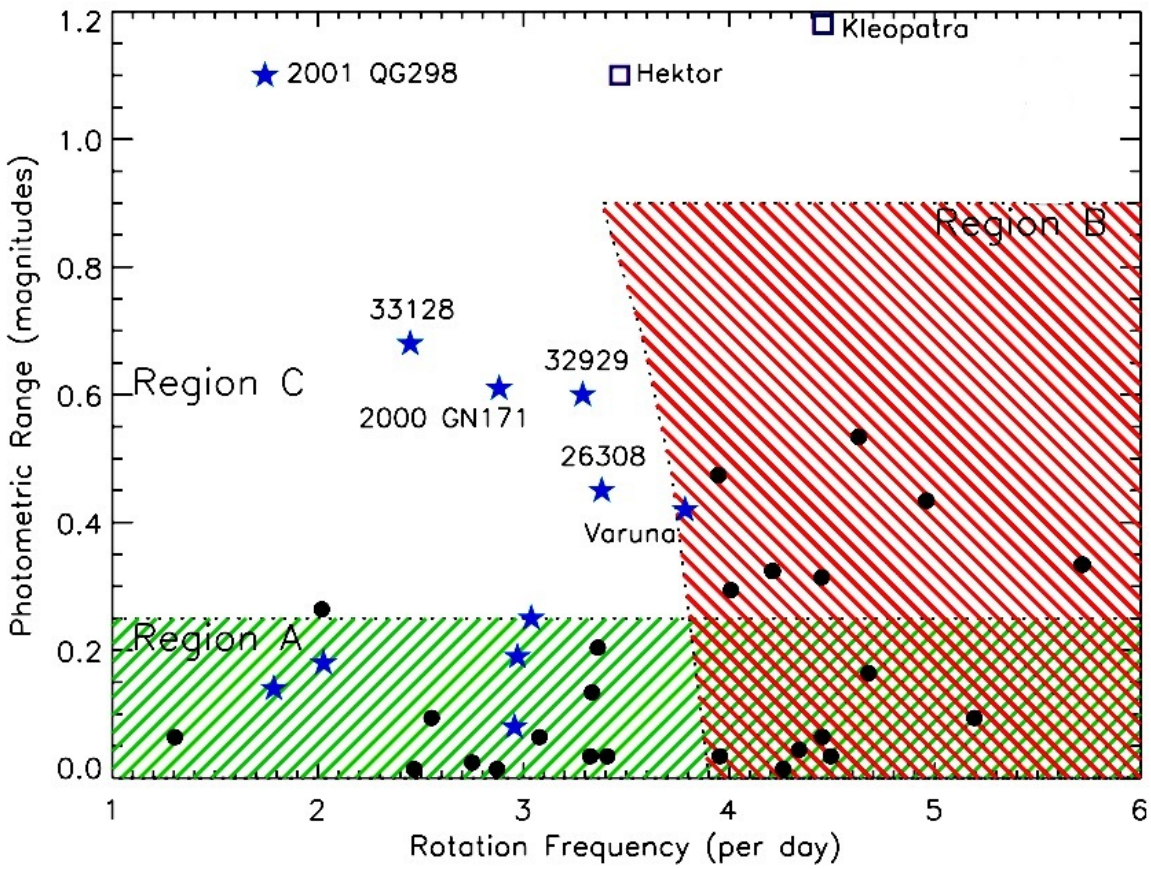

Figure 4.2 Lightcurve amplitudes vs. frequency for selected Trans-Neptunian binaries (stars), main belt asteroids (circles), one trailing Trojan contact binary, and one main belt contact binary (squares; taken from Sheppard & Jewitt 2004). The objects plotted were some of the only ones to have well-constrained periods and photometric ranges at the time of the Sheppard & Jewitt (2004) publication. Objects within region A (green) are equally likely to exhibit binarity, surface variations, and/or elongated shape. Objects within region B (red) are most likely rotationally elongated, and objects within region C (white) are most likely binaries. The regions are defined by both the shapes allowed by equilibrium ellipsoidal models (Regions A and B) and the photometric ranges that can be reasonably reproduced by albedo changes (limited to Region A)

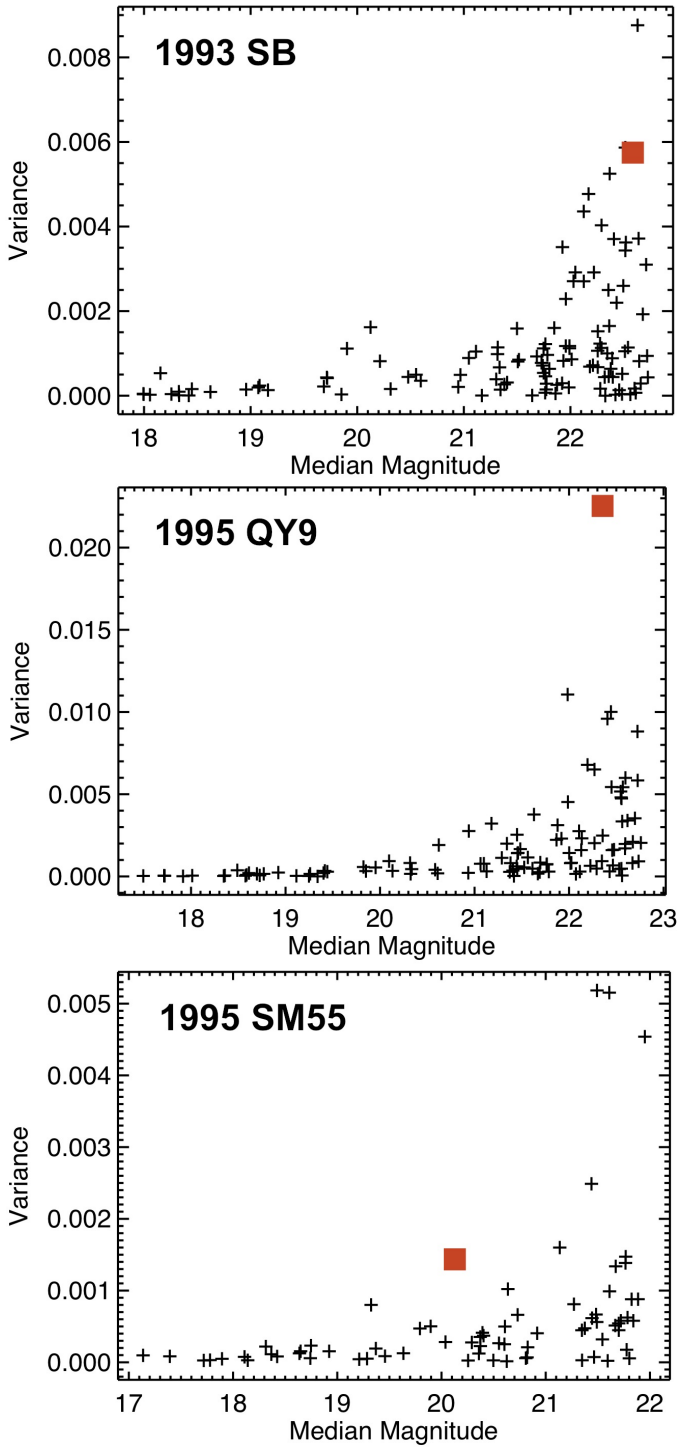

Figure 4.3 The variance in field stars (black crosses) compared to each BVS target (red square). Targets that show higher variance than field stars of comparable brightness (± 1 magnitude) were considered significantly variable.

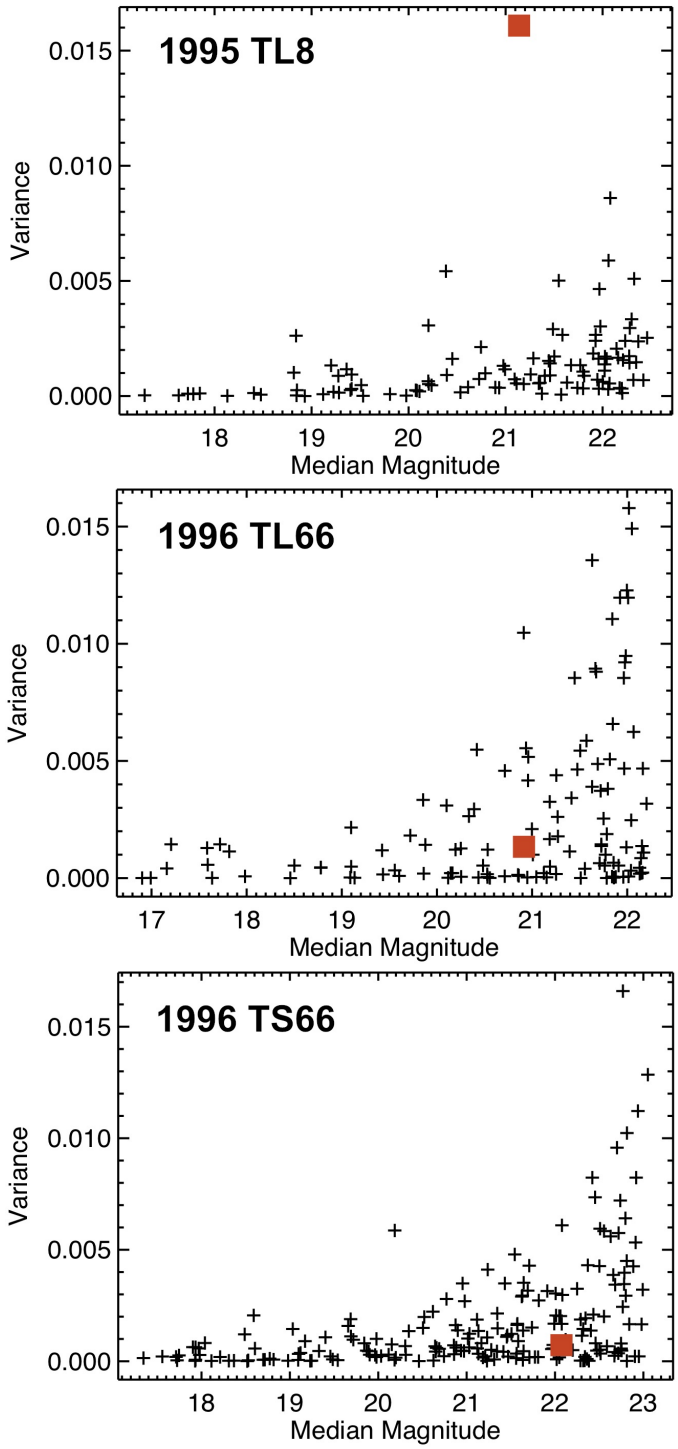

Figure 4.3 Continued

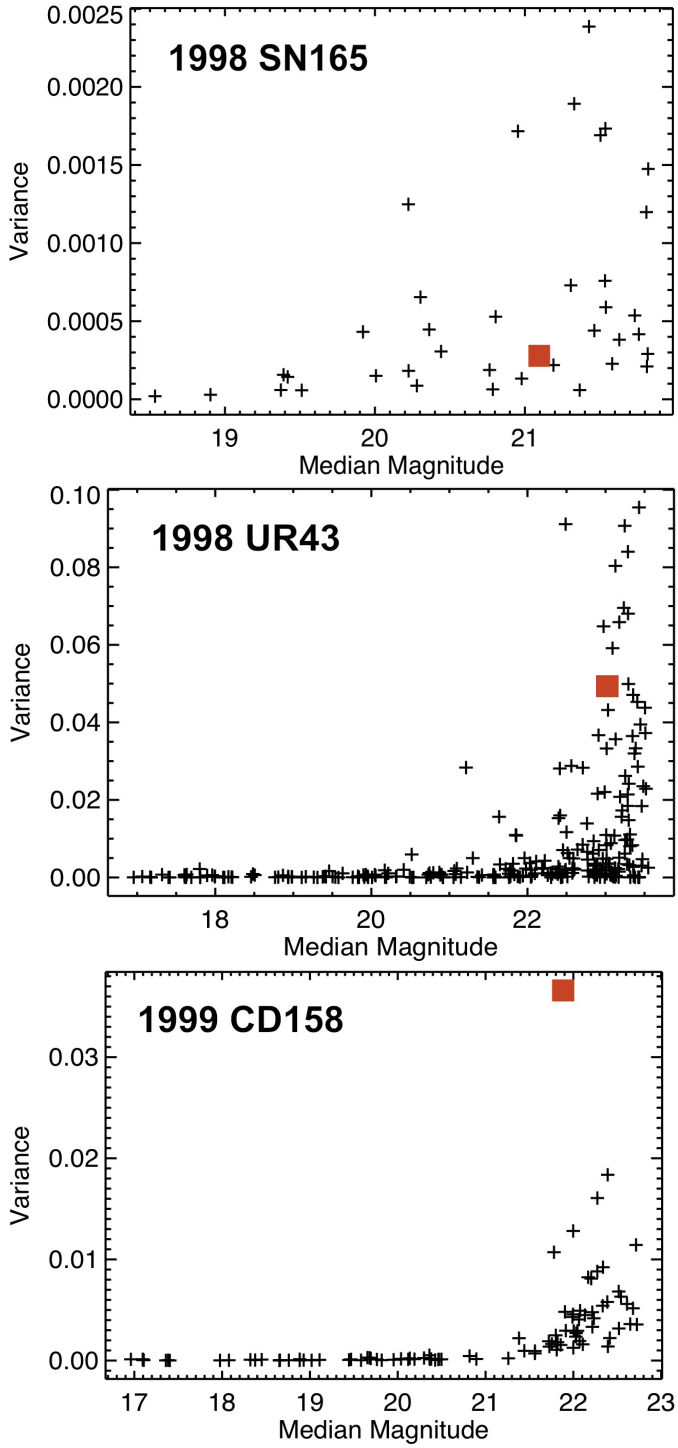

Figure 4.3 Continued

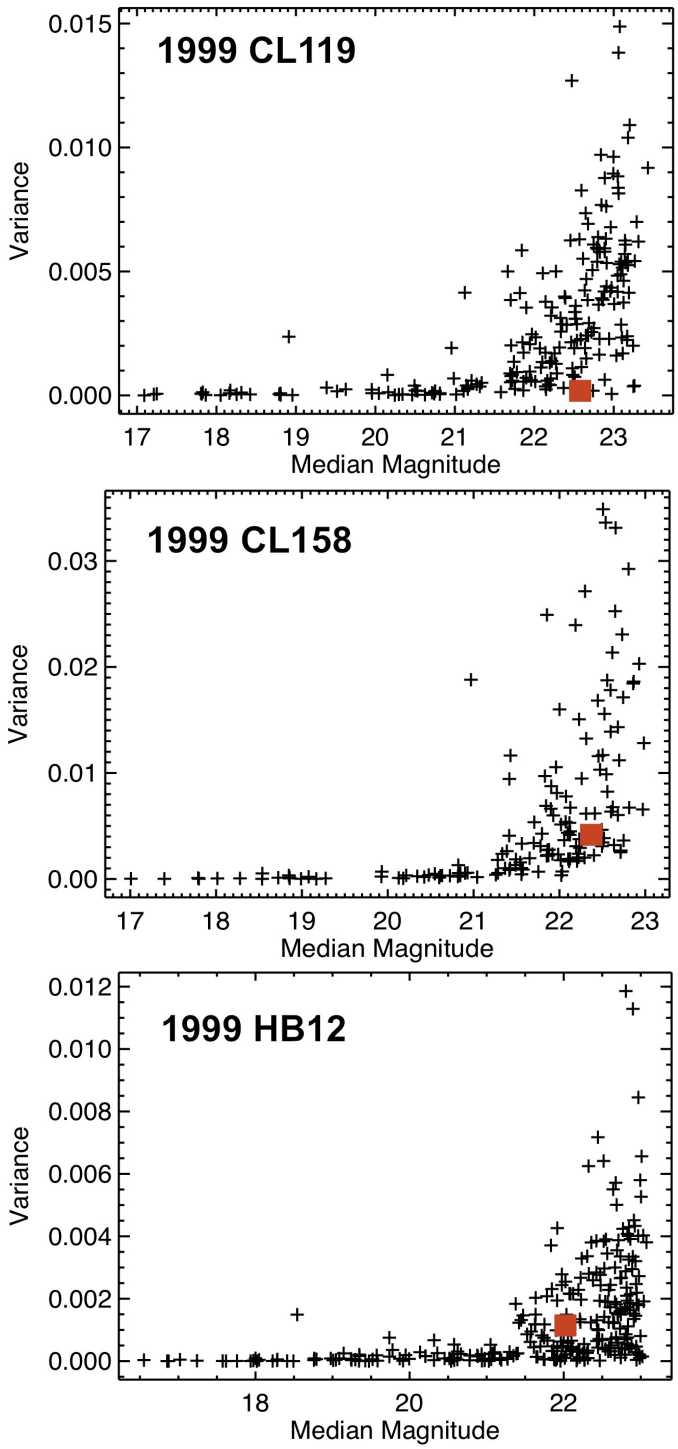

Figure 4.3 Continued

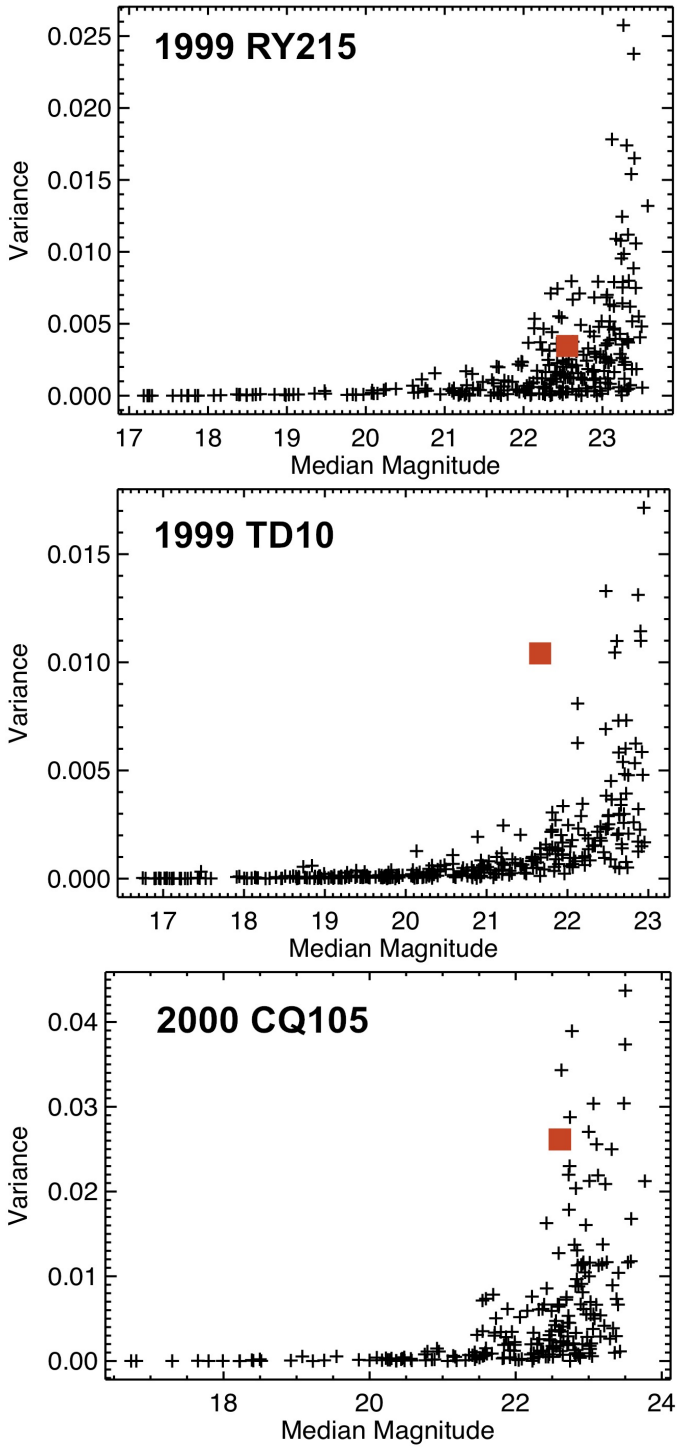

Figure 4.3 Continued

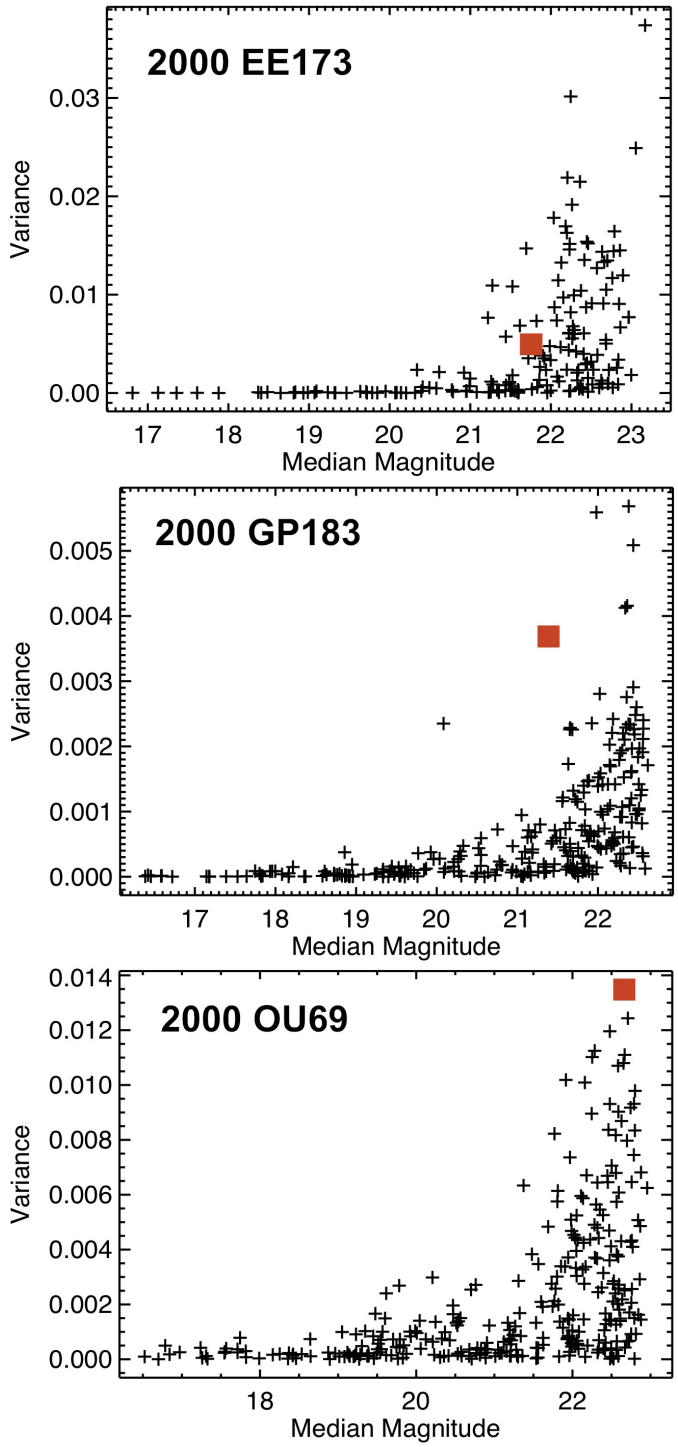

Figure 4.3 Continued

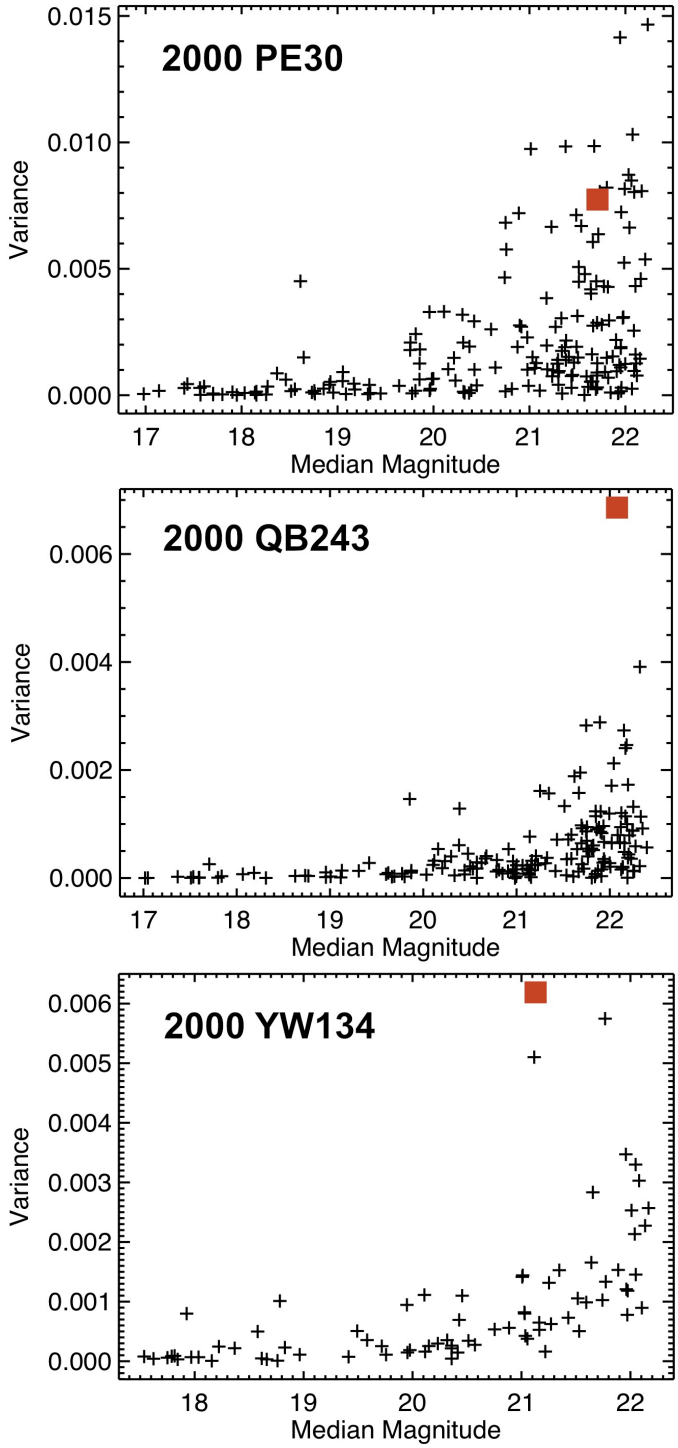

Figure 4.3 Continued

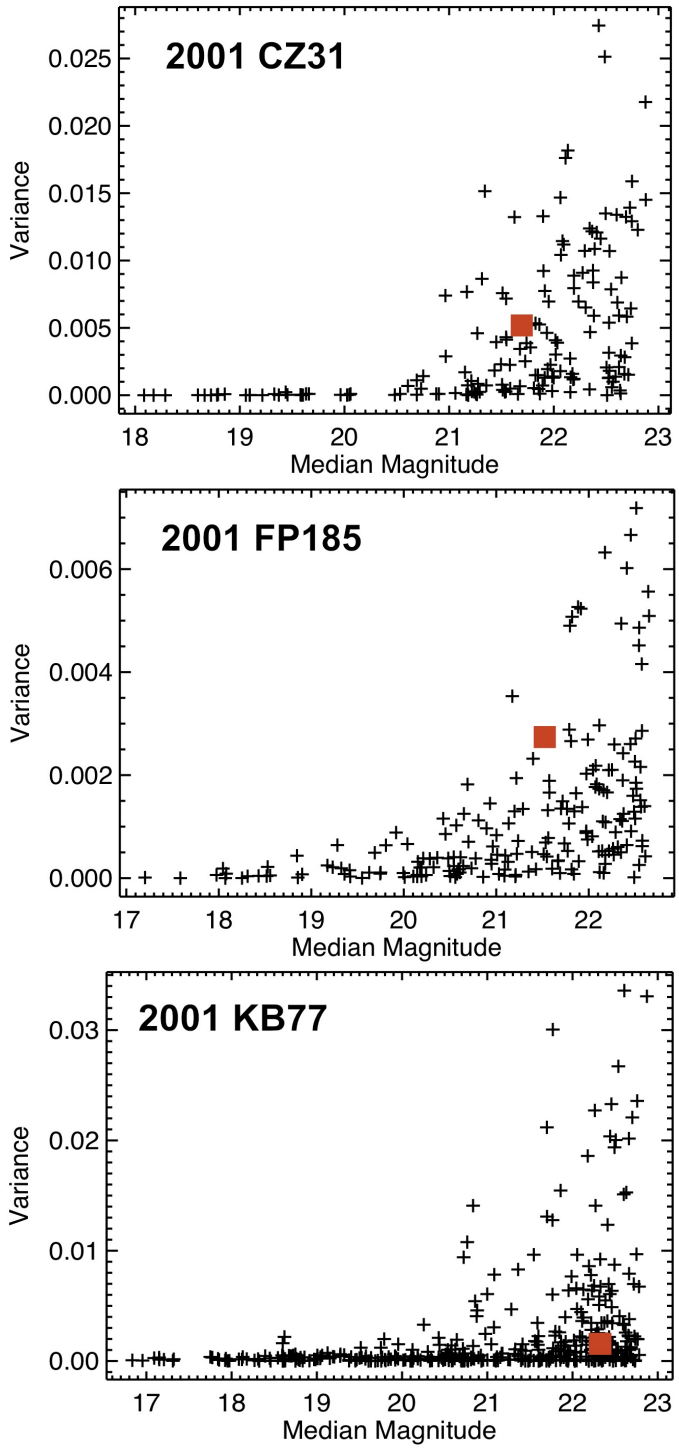

Figure 4.3 Continued

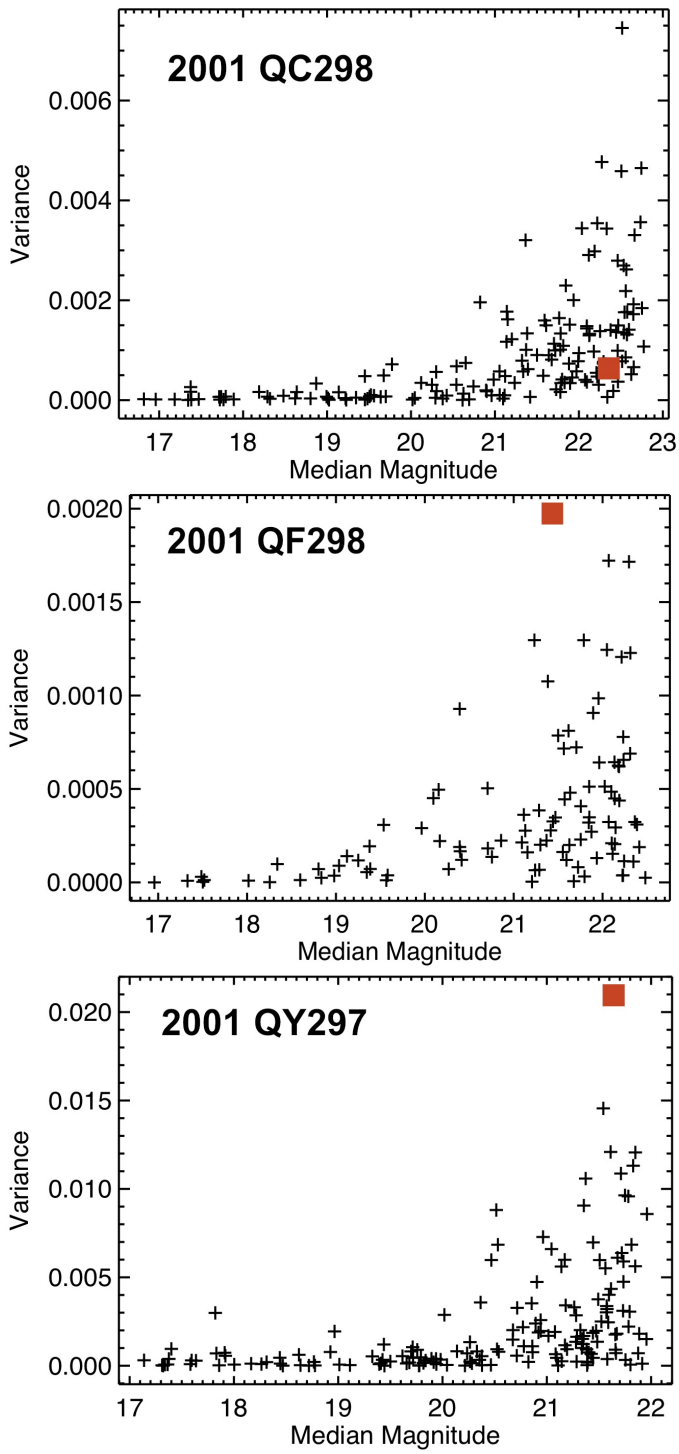

Figure 4.3 Continued

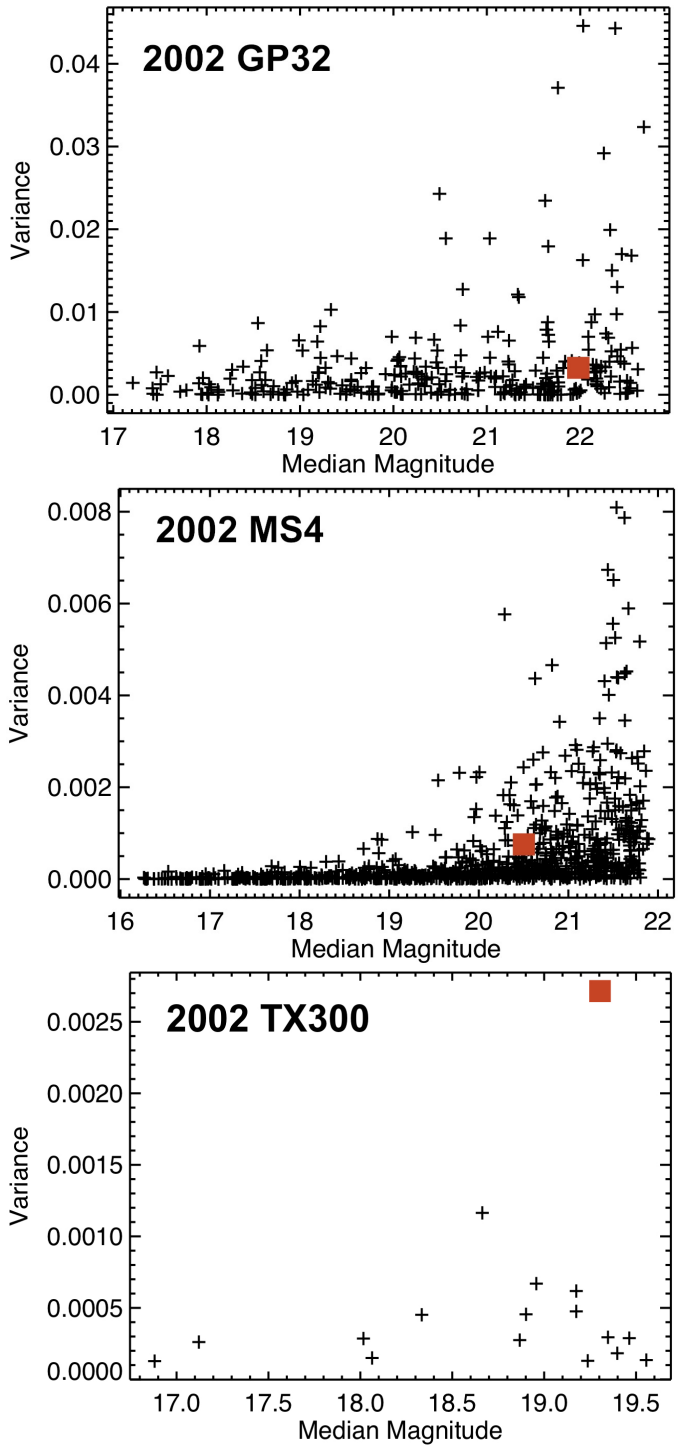

Figure 4.3 Continued

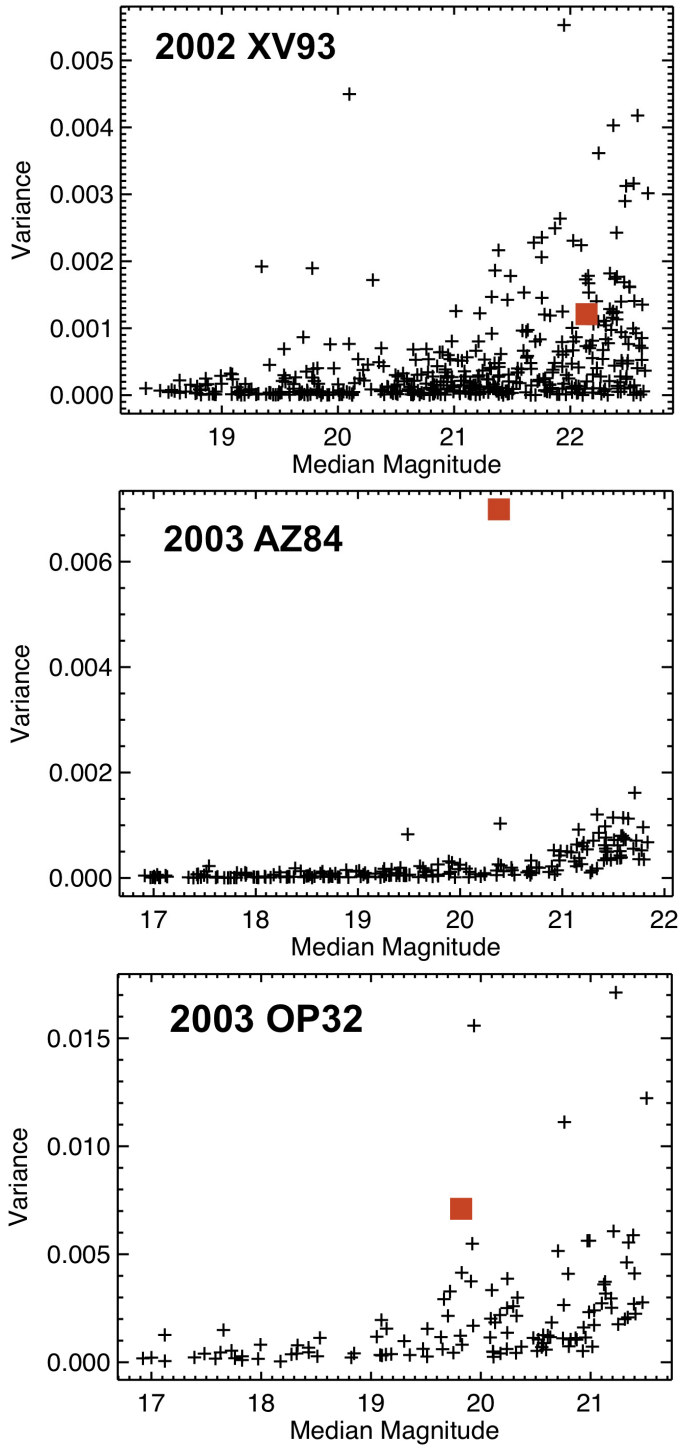

Figure 4.3 Continued

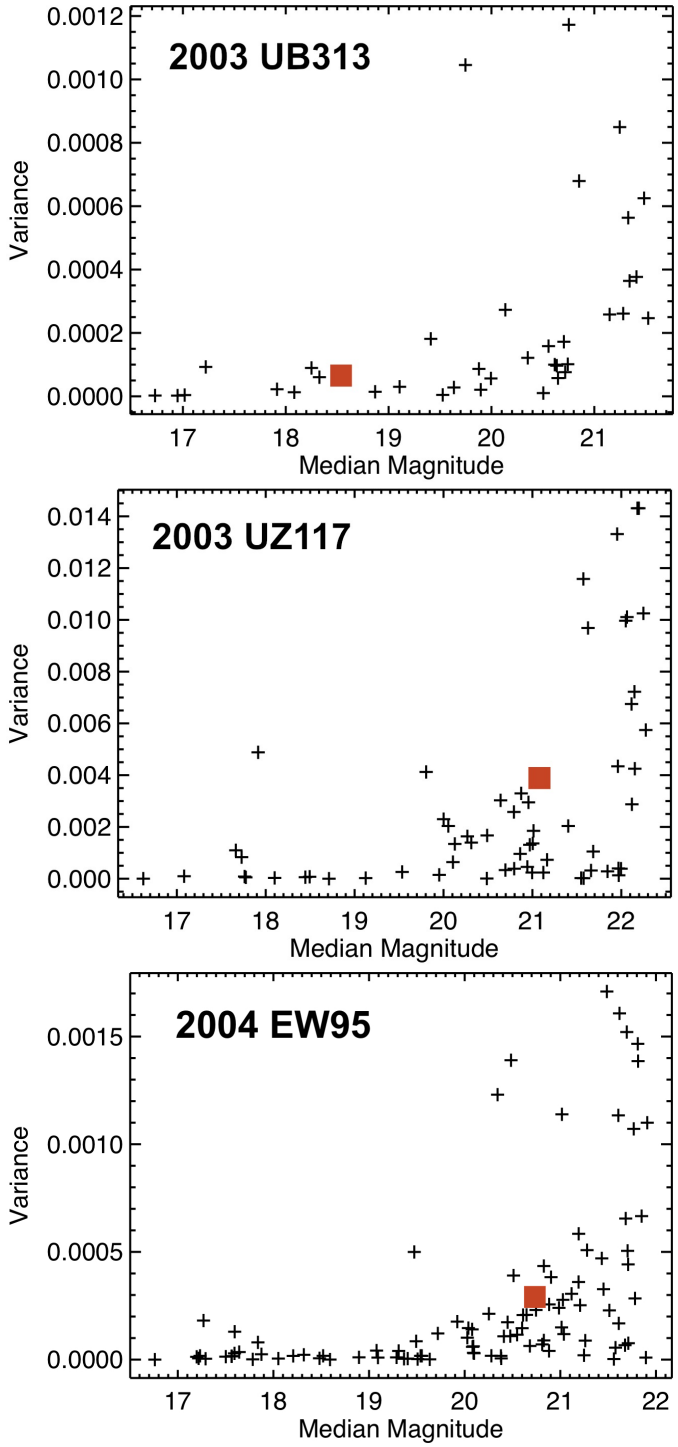

Figure 4.3 Continued

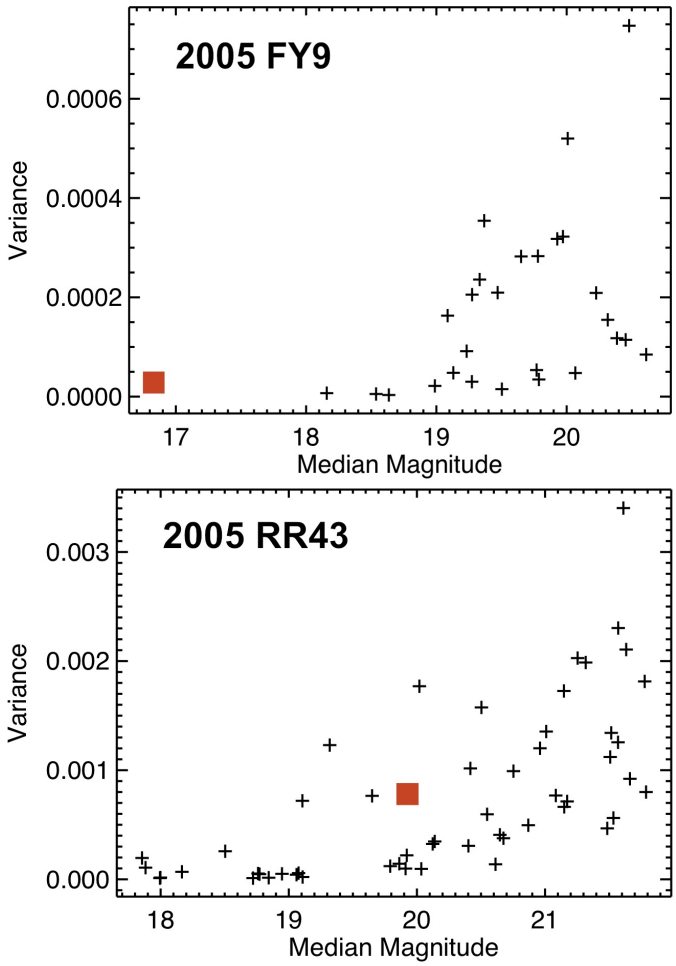

Figure 4.3 Continued

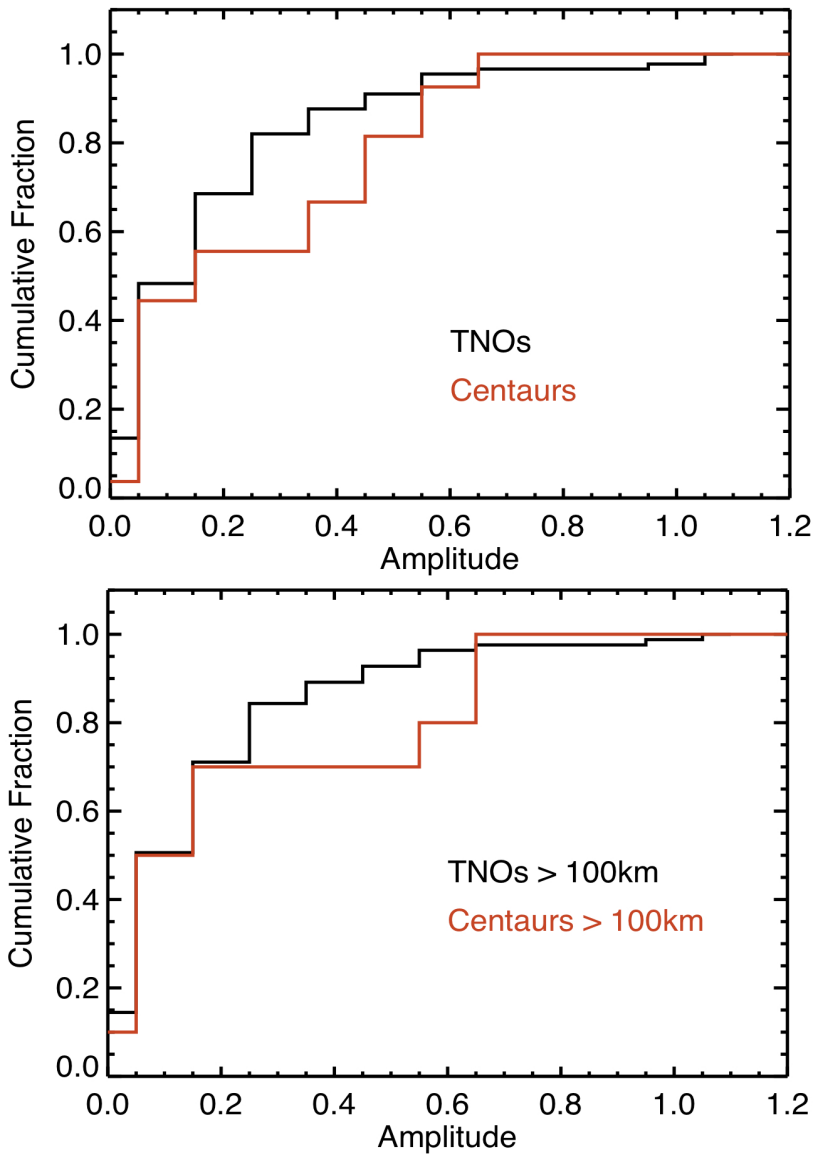

Figure 4.4 Updated cumulative fraction distribution of TNOs compared to Centaurs.

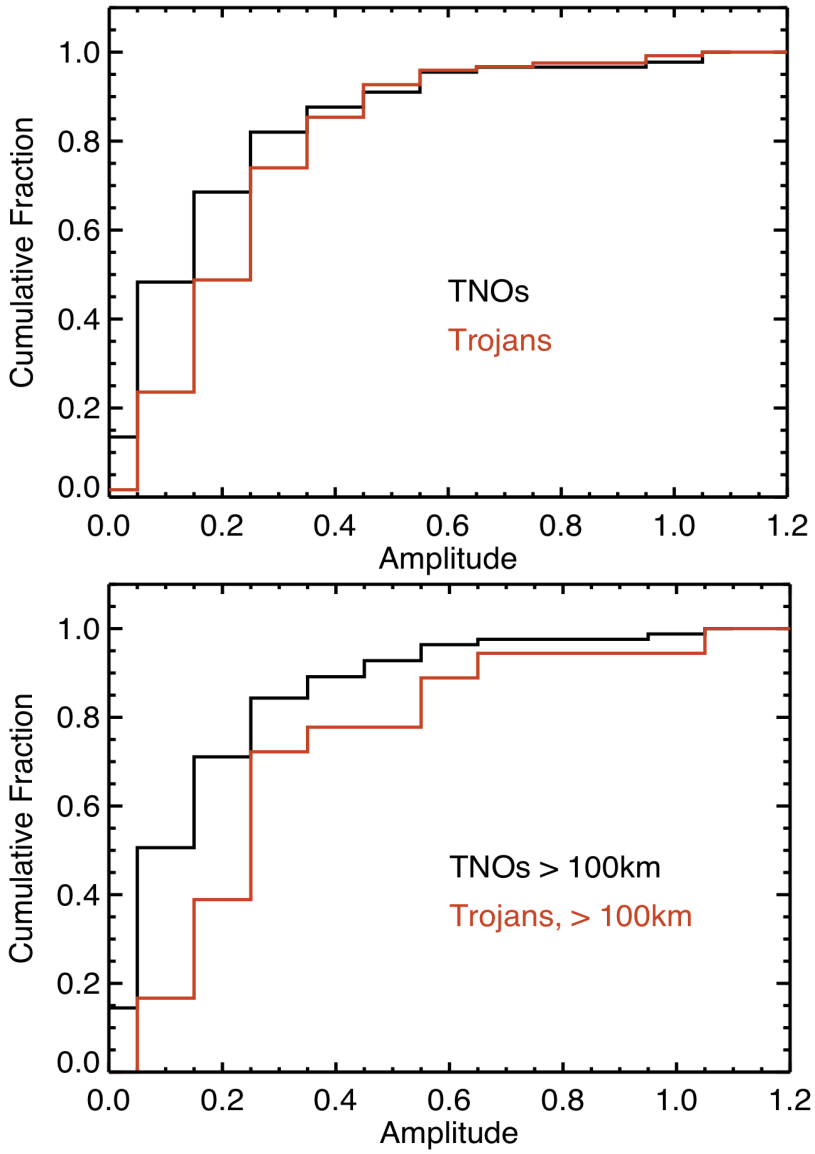

Figure 4.4 Continued

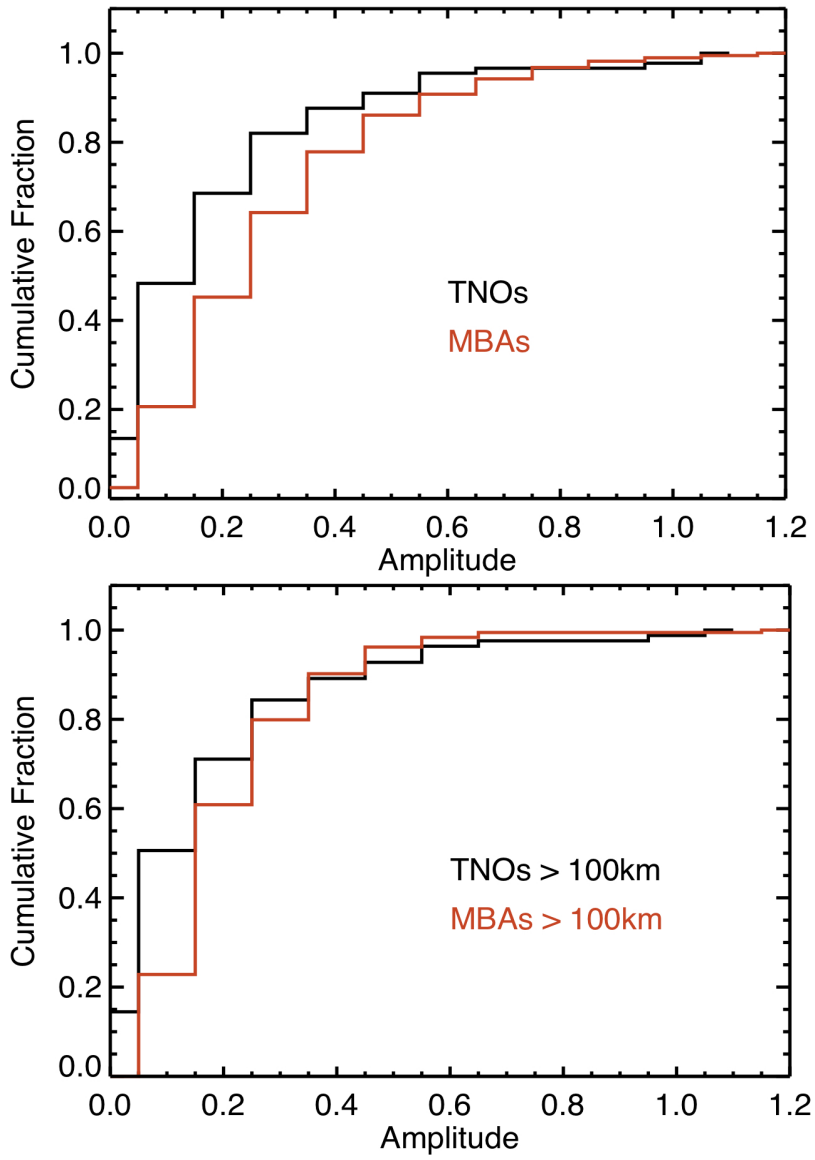

Figure 4.4 Continued

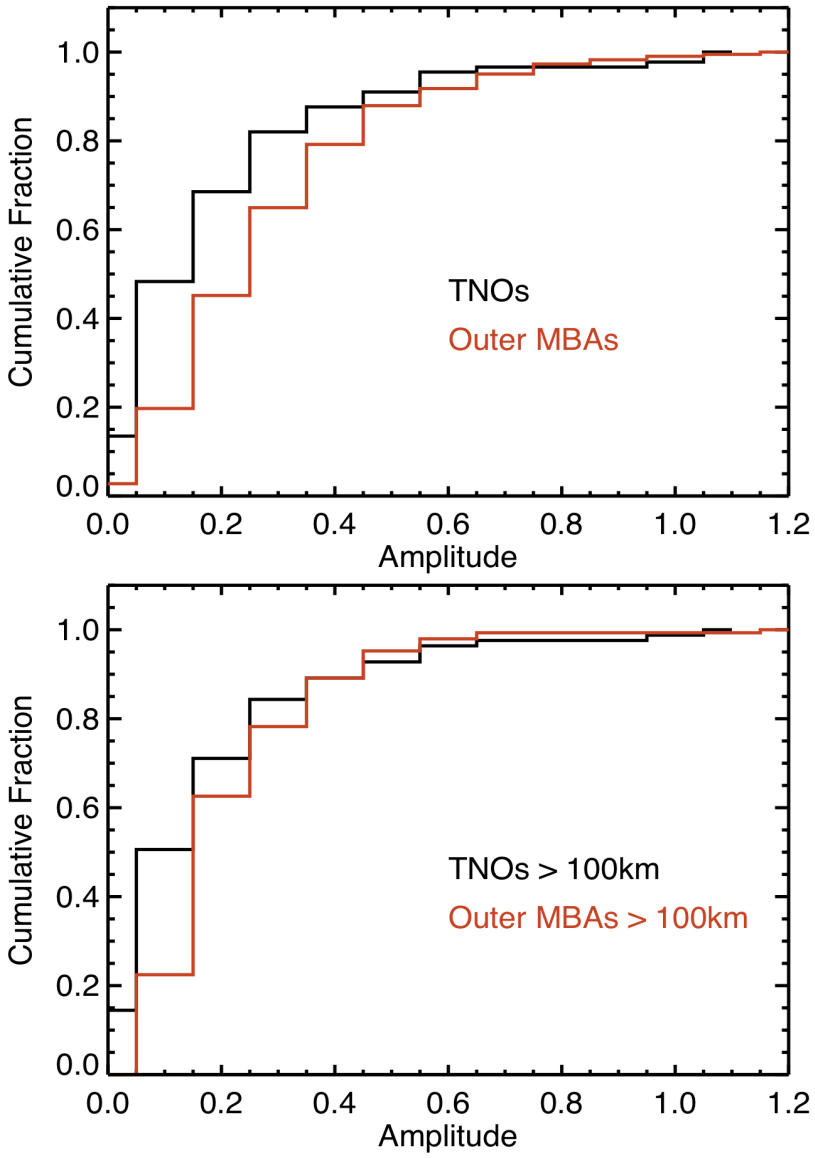

Figure 4.4 Continued

References

Astakhov, S. A., Lee, E. A., & Farrelly, D. 2005, MNRAS, 360, 401

Barucci, M. A., Romon, J., Doressoundiram, A., & Tholen, D. J. 2000, AJ, 120, 496

Bauer, J. M., Meech, K. J., Fernández, Y. R., Pittichova, J., Hainaut, O. R., Boehnhardt, H., & Delsanti, A. C. 2003, *Icarus*, 166, 195

Benecchi, S. D. & Sheppard, S. S. 2013, AJ, 145, 124

Binzel, R. P. & Sauter, L. M. 1992, *Icarus*, 95, 222

Brunetto, R., Barucci, M. A., Dotto, E., & Strazzulla, G. 2006, ApJ, 644, 646

Canup, R. M. 2005, Science, 307, 546

Catullo, V., Zappala, V., Farinella, P., & Paolicchi, P. 1984, A&A, 138, 464

Chandrasekhar, S. 1969, Ellipsoidal figures of equilibrium

Chorney, N. & Kavelaars, J. J. 2004, *Icarus*, 167, 220

Davies, J. K., McBride, N., Ellison, S. L., Green, S. F., & Ballantyne, D. R. 1998, *Icarus*, 134, 213

Delsanti, A. C., Boehnhardt, H., Barrera, L., Meech, K. J., Sekiguchi, T., & Hainaut, O. R. 2001, A&A, 380, 347

DeMeo, F. E., Fornasier, S., Barucci, M. A., Perna, D., Protopapa, S., Alvarez-Candal, A., Delsanti, A., Doressoundiram, A., Merlin, F., & de Bergh, C. 2009, A&A, 493, 283

Doressoundiram, A., Barucci, M. A., Romon, J., & Veillet, C. 2001, *Icarus*, 154, 277

Doressoundiram, A., Peixinho, N., de Bergh, C., Fornasier, S., Thébault, P., Barucci, M. A., & Veillet, C. 2002, AJ, 124, 2279

Doressoundiram, A., Peixinho, N., Doucet, C., Mousis, O., Barucci, M. A., Petit, J. M., & Veillet, C. 2005, *Icarus*, 174, 90

Doressoundiram, A., Peixinho, N., Moullet, A., Fornasier, S., Barucci, M. A., Beuzit, J.-L., & Veillet, C. 2007, AJ, 134, 2186

Dotto, E., Perna, D., Barucci, M. A., Rossi, A., de Bergh, C., Doressoundiram, A., & Fornasier, S. 2008, A&A, 490, 829

Elliot, J. L., Person, M. J., Zuluaga, C. A., Bosh, A. S., Adams, E. R., Brothers, T. C., Gulbis, A. A. S., Levine, S. E., Lockhart, M., Zangari, A. M., Babcock, B. A., Dupré, K., Pasachoff, J. M., Souza, S. P., Rosing, W., Secrest, N., Bright, L., Dunham, E. W., Sheppard, S. S., Kakkala, M., Tilleman, T., Berger, B., Briggs, J. W., Jacobson, G., Valleli, P., Volz, B., Rapoport, S., Hart, R., Brucker, M., Michel, R., Mattingly, A., Zambrano-Marin, L., Meyer, A. W., Wolf, J., Ryan, E. V., Ryan, W. H., Morzinski, K., Grigsby, B., Brimacombe, J., Ragozzine, D., Montano, H. G., & Gilmore, A. 2010, Nature, 465, 897

Farinella, P. & Davis, D. R. 1996, Science, 273, 938

Farnham, T. L. 2001, in Bulletin of the American Astronomical Society, Vol. 33, AAS/Division for Planetary Sciences Meeting Abstracts #33, 1047

Funato, Y., Makino, J., Hut, P., Kokubo, E., & Kinoshita, D. 2004, Nature, 427, 518

Gil-Hutton, R. & Licandro, J. 2001, *Icarus*, 152, 246

Goldreich, P., Lithwick, Y., & Sari, R. 2002, Nature, 420, 643

Hicks, M. D., Simonelli, D. P., & Buratti, B. J. 2005, *Icarus*, 176, 492

Ivanova, V., Borisov, G., & Belskaya, I. 2005, in , 54

Jewitt, D., Peixinho, N., & Hsieh, H. H. 2007, AJ, 134, 2046

Jewitt, D. C. & Luu, J. X. 2001, AJ, 122, 2099

Kaňuchová, Z., Brunetto, R., Melita, M., & Strazzulla, G. 2012, *Icarus*, 221, 12

Kenyon, S. J. & Bromley, B. C. 2004, AJ, 128, 1916

Kern, S. D. 2006, PhD thesis, Massachusetts Institute of Technology

Kern, S. D. & Elliot, J. L. 2006a, *Icarus*, 183, 179

—. 2006b, ApJ, 643, L57

Lacerda, P. & Luu, J. 2006, AJ, 131, 2314

Lee, E. A., Astakhov, S. A., & Farrelly, D. 2007, MNRAS, 379, 229

Leone, G., Paolicchi, P., Farinella, P., & Zappala, V. 1984, A&A, 140, 265

Levison, H. F., Morbidelli, A., Tsiganis, K., Nesvorný, D., & Gomes, R. 2011, AJ, 142, 152

Lim, T. L., Stansberry, J., Müller, T. G., Mueller, M., Lellouch, E., Kiss, C., Santos-Sanz, P., Vilenius, E., Protopapa, S., Moreno, R., Delsanti, A., Duffard, R., Fornasier, S., Groussin, O., Harris, A. W., Henry, F., Horner, J., Lacerda, P., Mommert, M., Ortiz, J. L., Rengel, M., Thirouin, A., Trilling, D., Barucci, A., Crovisier, J., Doressoundiram, A., Dotto, E., Gutiérrez Buenestado, P. J., Hainaut, O., Hartogh, P., Hestroffer, D., Kidger, M., Lara, L., Swinyard, B. M., & Thomas, N. 2010, A&A, 518, L148

Luu, J. X. & Jewitt, D. C. 2002, ARA&A, 40, 63

Magnusson, P. 1991, A&A, 243, 512

Mann, R. K., Jewitt, D., & Lacerda, P. 2007, AJ, 134, 1133

Marzari, F. & Scholl, H. 1998, A&A, 339, 278

Mommert, M., Harris, A. W., Kiss, C., Pál, A., Santos-Sanz, P., Stansberry, J., Delsanti, A., Vilenius, E., Müller, T. G., Peixinho, N., Lellouch, E., Szalai, N., Henry, F., Duffard, R., Fornasier, S., Hartogh, P., Mueller, M., Ortiz, J. L., Protopapa, S., Rengel, M., & Thirouin, A. 2012, A&A, 541, A93

Morbidelli, A., Levison, H. F., Tsiganis, K., & Gomes, R. 2005, Nature, 435, 462

Moroz, L., Baratta, G., Strazzulla, G., Starukhina, L., Dotto, E., Barucci, M. A., Arnold, G., & Distefano, E. 2004, *Icarus*, 170, 214

Mueller, B. E. A., Hergenrother, C. W., Samarasinha, N. H., Campins, H., & McCarthy, D. W. 2004, *Icarus*, 171, 506

Neese, C. 2008, NASA Planetary Data System, 103

Nesvorný, D., Youdin, A. N., & Richardson, D. C. 2010, AJ, 140, 785

Noll, K. S., Grundy, W. M., Chiang, E. I., Margot, J.-L., & Kern, S. D. 2008, Binaries in the Kuiper Belt, ed. M. A. Barucci, H. Boehnhardt, D. P. Cruikshank, A. Morbidelli, & R. Dotson, 345–363

Noll, K. S., Stephens, D., Grundy, W., Tegler, S., Romanishin, W., & Cruikshank, D. 2003, in Bulletin of the American Astronomical Society, Vol. 35, AAS/Division for Planetary Sciences Meeting Abstracts #35, 1016

Ortiz, J. L., Gutiérrez, P. J., Casanova, V., & Sota, A. 2003a, A&A, 407, 1149

Ortiz, J. L., Gutiérrez, P. J., Santos-Sanz, P., Casanova, V., & Sota, A. 2006, A&A, 447, 1131

Ortiz, J. L., Gutiérrez, P. J., Sota, A., Casanova, V., & Teixeira, V. R. 2003b, A&A, 409, L13

Ortiz, J. L., Santos Sanz, P., Gutiérrez, P. J., Duffard, R., & Aceituno, F. J. 2007, A&A, 468, L13

Ortiz, J. L., Sicardy, B., Braga-Ribas, F., Alvarez-Candal, A., Lellouch, E., Duffard, R., Pinilla-Alonso, N., Ivanov, V. D., Littlefair, S. P., Camargo, J. I. B., Assafin, M., Unda-Sanzana, E., Jehin, E., Morales, N., Tancredi, G., Gil-Hutton, R., de La Cueva, I., Colque, J. P., da Silva Neto, D. N., Manfroid, J., Thirouin, A., Gutiérrez, P. J., Lecacheux, J., Gillon, M., Maury, A., Colas, F., Licandro, J., Mueller, T., Jacques, C., Weaver, D., Milone, A., Salvo, R., Bruzzone, S., Organero, F., Behrend, R., Roland, S., Vieira-Martins, R., Widemann, T., Roques, F., Santos-Sanz, P., Hestroffer, D., Dhillon, V. S., Marsh, T. R., Harlingten, C., Bagatin, A. C., Alonso, M. L., Ortiz, M., Colazo, C., Lima, H. J. F., Oliveira, A. S., Kerber, L. O., Smiljanic, R., Pimentel, E., Giacchini, B., Cacella, P., & Emilio, M. 2012, Nature, 491, 566

Ortiz, J. L., Sota, A., Moreno, R., Lellouch, E., Biver, N., Doressoundiram, A., Rousselot, P., Gutiérrez, P. J., Márquez, I., González Delgado, R. M., & Casanova, V. 2004, A&A, 420, 383

Parker, A. H. & Kavelaars, J. J. 2010, *Icarus*, 209, 766

Peixinho, N., Boehnhardt, H., Belskaya, I., Doressoundiram, A., Barucci, M. A., & Delsanti, A. 2004, *Icarus*, 170, 153

Perets, H. B. 2011, ApJ, 727, L3

Perets, H. B. & Naoz, S. 2009, ApJ, 699, L17

Perna, D., Dotto, E., Barucci, A., Rossi, A., de Bergh, C., Doressoundiram, A., & Fornasier, S. 2008, in Bulletin of the American Astronomical Society, Vol. 40, AAS/Division for Planetary Sciences Meeting Abstracts #40, 483

Petit, J.-M. & Mousis, O. 2004, *Icarus*, 168, 409

Porter, S. B. & Grundy, W. M. 2012, *Icarus*, 220, 947

Rabinowitz, D. L., Barkume, K., Brown, M. E., Roe, H., Schwartz, M., Tourtellotte, S., & Trujillo, C. 2006, ApJ, 639, 1238

Rabinowitz, D. L., Schaefer, B. E., Schaefer, M., & Tourtellotte, S. W. 2008, AJ, 136, 1502

Rabinowitz, D. L., Schaefer, B. E., & Tourtellotte, S. W. 2007, AJ, 133, 26

Romanishin, W. & Tegler, S. C. 1999, Nature, 398, 129

Romanishin, W., Tegler, S. C., & Consolmagno, G. J. 2010, AJ, 140, 29

Rousselot, P., Petit, J.-M., Poulet, F., Lacerda, P., & Ortiz, J. 2003, A&A, 407, 1139

Rousselot, P., Petit, J.-M., Poulet, F., & Sergeev, A. 2005, *Icarus*, 176, 478

Santos-Sanz, P., Lellouch, E., Fornasier, S., Kiss, C., Pal, A., Müller, T. G., Vilenius, E., Stansberry, J., Mommert, M., Delsanti, A., Mueller, M., Peixinho, N., Henry, F., Ortiz, J. L., Thirouin, A., Protopapa, S., Duffard, R., Szalai, N., Lim, T., Ejeta, C., Hartogh, P., Harris, A. W., & Rengel, M. 2012, A&A, 541, A92

Santos-Sanz, P., Ortiz, J. L., Barrera, L., & Boehnhardt, H. 2009, A&A, 494, 693

Sheppard, S. S. 2007, AJ, 134, 787

—. 2010, AJ, 139, 1394

Sheppard, S. S. & Jewitt, D. 2004, AJ, 127, 3023

Sheppard, S. S. & Jewitt, D. C. 2002, in ESA Special Publication, Vol. 500, Asteroids, Comets, and Meteors: ACM 2002, ed. B. Warmbein, 21–24

Sheppard, S. S. & Jewitt, D. C. 2003, Earth Moon and Planets, 92, 207

Sheppard, S. S., Ragozzine, D., & Trujillo, C. 2012, AJ, 143, 58

Shoemaker, E. M., Shoemaker, C. S., & Wolfe, R. F. 1989, in Asteroids II, ed. R. P. Binzel, T. Gehrels, & M. S. Matthews, 487–523

Sicardy, B., Ortiz, J. L., Assafin, M., Jehin, E., Maury, A., Lellouch, E., Gil-Hutton, R., Braga-Ribas, F., Colas, F., Lecacheux, J., Roques, F., Santos-Sanz, P., Morales, N., Thirouin, A., Camargo, J. I. B., Vieira-Martins, R., Gillon, M., Manfroid, J., Behrend, R., & Widemann, T. 2011, in EPSC-DPS Joint Meeting 2011, 137

Snodgrass, C., Carry, B., Dumas, C., & Hainaut, O. 2010, A&A, 511, A72

Stansberry, J., Grundy, W., Brown, M., Cruikshank, D., Spencer, J., Trilling, D., & Margot, J.-L. 2008, Physical Properties of Kuiper Belt and Centaur Objects: Constraints from the Spitzer Space Telescope, ed. M. A. Barucci, H. Boehnhardt, D. P. Cruikshank, A. Morbidelli, & R. Dotson, 161–179

Stansberry, J. A., Mueller, T. G., Ortiz, J.-L., Santos-Sanz, P., Vilenius, E., Lellouch, E., & Kiss, C. 2011, in EPSC-DPS Joint Meeting 2011, 1437

Stephens, D. C. & Noll, K. S. 2006, AJ, 131, 1142

Tegler, S. C. & Romanishin, W. 1998, Nature, 392, 49

—. 2000, Nature, 407, 979

—. 2003, *Icarus*, 161, 181

Tegler, S. C., Romanishin, W., & Consolmagno, G. J. 2003, ApJ, 599, L49

Thirouin, A., Ortiz, J. L., Campo Bagatin, A., Pravec, P., Morales, N., Hainaut, O., & Duffard, R. 2012, MNRAS, 424, 3156

Thirouin, A., Ortiz, J. L., Duffard, R., Santos-Sanz, P., Aceituno, F. J., & Morales, N. 2010, A&A, 522, A93

Tholen, D. J. & Buie, M. W. 1997, Bulk Properties of Pluto and Charon, ed. S. A. Stern & D. J. Tholen, 193

Trilling, D. E. & Bernstein, G. M. 2006, AJ, 131, 1149

Trujillo, C. A. & Brown, M. E. 2002, ApJ, 566, L125

Vilenius, E., Kiss, C., Mommert, M., Müller, T., Santos-Sanz, P., Pal, A., Stansberry, J., Mueller, M., Peixinho, N., Fornasier, S., Lellouch, E., Delsanti, A., Thirouin, A., Ortiz, J. L., Duffard, R., Perna, D., Szalai, N., Protopapa, S., Henry, F., Hestroffer, D., Rengel, M., Dotto, E., & Hartogh, P. 2012, A&A, 541, A94

Warner, B. D., Harris, A. W., & Pravec, P. 2009, *Icarus*, 202, 134

Weidenschilling, S. J. 2002, *Icarus*, 160, 212

Chapter 5

Phase Curves

5.1 Introduction

An object's phase curve is its brightness as a function of α, the Sun-object-observer (phase) angle. The typical phase curve has a linear portion at large α (greter than a few degrees) and a non-linear portion with increasing brightening for $\alpha <$ a few degrees. The brightening in the linear portion is caused by geometry (the fraction of the surface illuminated). The increase in α at small phase angles occurs for two reasons: shadow-hiding (SH), and constructively-interfering (coherent) backscatter (CB; *e.g.* Drossart 1993; Poulet et al. 2002). Examining phase curves at different wavelengths helps distinguish between these two causes (Rousselot et al. 2003). By determining the phase curve's shape at different wavelengths, especially within the opposition surge at very small phase angles ($\alpha \lesssim 0.5$), one can constrain properties of the surface materials such as porosity, texture, grain size, and complex refractive index (Rousselot et al. 2005; Belskaya et al. 2008).

The linear portion of the phase function (ϕ) can be written as:

$$\phi(\alpha) = 10^{-\beta\alpha} \quad ,$$

where α is in degrees, and β (in mag/$^\circ$) is the coefficient describing how much an object's magnitude will change with respect to α. The β value is also correlated with an object's

albedo. A more detailed empirical fit was determined by Bowell et al. (1989) to describe the entire phase curve through the $H - G$ standard formalism, where H is the absolute magnitude and G is a coefficient proportional to β (Bowell et al. 1989). This formalism was designed such that $0 \leq G \leq 1$ for all small body surfaces. Values of $G > 1.0$ or $G < 0.0$ indicate either highly anomalous surfaces (to the point of being unphysical) or the failure of this technique to accurately describe the phase angle effect. The β coefficient is the more standard way to convey the phase angle effect for TNO phase curves since it relates directly to targets' magnitudes, so we present it here.

One feature that might be present in an object's phase curve is an increased brightening (*i.e.*, an increase in the slope, so a non-linear regime) toward small phase angles, which is dependent on the surface regolith properties. For example, this opposition surge should be seen on porous objects, and its magnitude is determined by CB (Sheppard & Jewitt 2002). The physical mechanisms that cause an opposition surge are complex and provide unique insights to the surfaces of small bodies. If an opposition surge is observed at very small phase angles ($\alpha \lesssim 0.3°$), then CB is its dominant cause. A surge at larger phase angles ($\alpha < 5°$) is instead attributable to SH (Belskaya & Shevchenko 2000). Belskaya et al. (2006) found that lightcurve amplitudes can vary with observed phase angle on a body with a pronounced opposition surge - a purely equatorial view corresponding to the maximum lightcurve amplitude. They use Varuna's non-flat phase curve to explain a ~ 0.1 magnitude change in the amplitude of its rotational lightcurve when observed from a very low phase angle ($\alpha \lesssim 0.1°$).

The maximum observable solar phase angle is roughly $\alpha = 180/(\pi R)$, where R is the distance to the object in AU. For the closest TNOs in our sample, $R \sim 27$ AU, giving $\alpha_{max} = 2.0°$. Over this range of phase angles, β is difficult to constrain because unless a large opposition surge is present, the phase curve's shallow slope will be sensitive to photometric error and the amplitudes of rotational lightcurves, so decoupling the phase angle effect from rotational modulation requires extensive observational constraints on the rotation signature. The inverse is also true - syncing rotational lightcurves using data taken

over diverse solar phase angles, requires constraining the phase curve to remove brightening independent of the rotational period. The primary motivation for our observational work was to determine rotational lightcurves, so determining the phase curves for our targets was a necessary by-product for comparing our datasets between weeks or months. We note, however, that because TNOs can only be observed over small phase angles, it is not likely that the values presented as β here reflect the slope of the linear portion of the phase curve, since the data are within a typical opposition surge.

We compiled all phase curve measurements for TNOs from the literature (Table 5.1). To date, 41 TNO optical β coefficients have been determined. From this data, a correlation was seen between optical colors and phase coefficient, implying that surface properties of neutral objects differ from those of red objects (Rabinowitz et al. 2008; Schaefer et al. 2009), but this correlation is weak mostly due to narrow α-coverage, poor signal-to-noise, and small number statistics (few neutral TNOs have determined β values). Given the differing colors and likely different dynamical histories amongst the three different dynamical classes (Morbidelli et al. 2008), a correlation between dynamical class and β is theoretically predicted. Here, we report results from phase curve investigation of nine targets observed as part of the CVS in order to assess their effect on the rotational lightcurve of each object.

Table 5.1. Phase coefficients (β) as reported from the literature

Designation	Class[a]	$V-R$	σ_{V-R}	$V-R$ Ref.	β_B	σ_{β_B}	β_V	σ_{β_V}	β_R	σ_{β_R}	β_I	σ_{β_I}	$\beta_{avg.}$[b]	$\sigma_{\beta_{avg.}}$[b]	β Ref.
1995 SM_{55}	Q	0.42	0.02	this work[c]	···	···	···	···	···	···	···	···	0.06	0.03	R08
1996 GQ_{21}	S	0.73	0.04	D07	···	···	···	···	0.14	0.03	···	···	0.14	0.03	S02
1999 DE_9	R	0.58	0.03	T03	0.16	0.03	0.21	0.04	0.18	0.06	0.14	0.03	0.17	0.02	R07;S02
1999 KR_{16}	Q	0.74	0.04	JL01	···	···	···	···	0.14	0.02	···	···	0.14	0.02	S02
1999 OX_3	U	0.69	0.01	TR00	···	···	···	···	0.30	0.03	···	···	0.30	0.03	T12
1999 TC_{36}	P	0.69	0.01	T03	0.26	0.04	0.13	0.05	···	···	0.24	0.06	0.21	0.03	R07
1999 TD_{10}	C	0.51	0.02	D07	···	···	···	···	0.12	0.06	···	···	0.12	0.06	R05
2000 EB_{173}	P	0.53	0.01	D01	···	···	0.16	0.04	0.125	0.009	···	···	0.14	0.02	R07; Sc02
2000 EC_{98}	C	0.47	0.05	B02	···	···	0.22	0.06	0.17	0.02	···	···	0.20	0.03	R05
2000 GN_{171}	P	0.63	0.03	S02	···	···	0.14	0.03	0.14	0.03	0.28	0.03	0.19	0.02	R07;S02
2000 WR_{106}	Q	0.64	0.01	S02	0.26	0.03	0.28	0.05	0.11	0.03	0.20	0.04	0.21	0.02	R07;S02; B06
2001 CZ_{31}	Q	0.5	0.1	S02	···	···	···	···	0.13	0.04	···	···	0.13	0.04	S02
2001 KX_{76}	P	0.61	0.03	D07	0.20	0.04	0.13	0.04	0.20	0.04	0.08	0.07	0.15	0.03	R07; B04
2002 AW_{197}	Q	0.58	0.02	J07	0.04	0.05	0.13	0.04	···	···	0.12	0.05	0.10	0.03	R07
2002 KX_{14}	U	0.61	0.04	D09	···	···	0.16	0.04	0.13	0.06	0.20	0.04	0.16	0.04	R07; BS13
2002 LM_{60}	Q	0.64	0.01	T03	0.06	0.03	0.16	0.03	···	···	0.29	0.04	0.17	0.02	R07
2002 TC_{302}	S	0.64	0.02	S10	···	···	···	···	···	···	···	···	0.12	0.04	R08
2002 TX_{300}	Q	0.33	0.03	this work	-0.01	0.04	0.16	0.05	···	···	0.09	0.06	0.08	0.03	R07
2002 UX_{25}	Q	0.54	0.03	J07	0.13	0.03	0.16	0.03	0.13	0.01	0.13	0.03	0.14	0.01	R07
2002 VE_{95}	P	0.71[d]	0.04	Ba06	0.12	0.03	0.12	0.04	···	···	0.10	0.03	0.12	0.02	R07
2003 AZ_{84}	P	0.4	0.03	D09	···	···	···	···	···	···	···	···	0.06	0.03	R08

Table 5.1—Continued

Designation	Class[a]	$V-R$	σ_{V-R}	$V-R$ Ref.	β_B	σ_{β_B}	β_V	σ_{β_V}	β_R	σ_{β_R}	β_I	σ_{β_I}	$\beta_{avg.}$[b]	$\sigma_{\beta_{avg.}}$[b]	β Ref.
2003 EL_{61}	U	0.37	0.02	J07	0.09	0.01	0.11	0.01	···	···	0.12	0.01	0.105	0.007	R07
2003 OP_{32}	Q	0.39	0.03	this work	···	···	···	···	0.13	0.11	···	···	0.04	0.02	BS13; R08
2003 UB_{313}	S	0.39	0.02	C06	0.00	0.03	0.11	0.02	0.09	0.03	0.14	0.03	0.08	0.02	R07;S07
2003 VB_{12}	S	0.61	0.03	S10	···	···	···	···	0.15	0.03	···	···	0.15	0.03	R07
2004 DW	P	0.37	0.04	d05	0.11	0.02	0.11	0.03	0.26	0.05	0.20	0.03	0.17	0.02	R07;S07
2004 GV_9	Q	0.7	0.1	G01	···	···	···	···	0.18	0.06	···	···	0.13	0.01	R08; S07
2004 TY_{364}	U	···	···	···	0.14	0.04	0.18	0.07	0.19	0.03	0.41	0.06	0.23	0.04	R07; S07
2005 FY_9	Q	0.46	0.02	J07	0.07	0.02	0.05	0.02	···	···	0.05	0.02	0.06	0.01	R07
2005 RM_{43}	S	···	···	···	···	···	···	···	···	···	···	···	0.18	0.02	R08
2005 RR_{43}	Q	···	···	···	···	···	···	···	···	···	···	···	0.01	0.02	R08
2007 JF_{43}	P	···	···	···	···	···	···	···	0.20	0.05	···	···	0.20	0.05	BS13
2007 JH_{43}	P	···	···	···	···	···	···	···	0.20	0.01	···	···	0.20	0.01	BS13
2007 JJ_{43}	Q	···	···	···	···	···	···	···	0.56	0.03	···	···	0.56	0.03	BS13
2008 QY_{40}	S	···	···	···	···	···	···	···	0.4	0.1	···	···	0.4	0.1	BS13
2010 EK_{139}	S	···	···	···	···	···	···	···	0.19	0.06	···	···	0.19	0.06	BS13
2010 EL_{139}	P	···	···	···	···	···	···	···	0.05	0.07	···	···	0.05	0.07	BS13
2010 EP_{65}	R	···	···	···	···	···	···	···	0.11	0.03	···	···	0.11	0.03	BS13
2010 ET_{65}	S	···	···	···	···	···	···	···	0.34	0.02	···	···	0.34	0.02	BS13
2010 FX_{86}	Q	···	···	···	···	···	···	···	0.2	0.1	···	···	0.2	0.1	BS13
2010 WG_9	D	0.52	0.02	R13	···	···	···	···	0.05	0.02	···	···	0.05	0.02	R13

[a]Key to dynamical class: Q = classical, S = scattered disk, R = non-plutino resonator, U = unusual, P = plutino, D = detached

[b]The average β coefficient from those listed in individual filters in this table, and their

[c]Colors from this work (the CVS, Chapter 6) were the median of all those measured, and the error is the mean of all color measurement uncertainties.

[d]The V-R color is inferred from its classification into the RR taxonomic group, and the color uncertainty reported is the uncertainty on the taxonomic group's color.

References. — D07 = Doressoundiram et al. (2007); T03 = Tegler et al. (2003); JL01 = Jewitt & Luu (2001); TR00 = Tegler & Romanishin (2000); D01 = Doressoundiram et al. (2001); B02 = Boehnhardt et al. (2002); J07 = Jewitt et al. (2007); D09 = DeMeo et al. (2009); S10 = Sheppard (2010); Ba06 = Barucci et al. (2006); C06 = Carraro et al. (2006); d05 = de Bergh et al. (2005); G01 = Gil-Hutton & Licandro (2001); R08 = Rabinowitz et al. (2008); S02 = Sheppard & Jewitt (2002); T12 = Thirouin et al. (2012); R07 = Rabinowitz et al. (2007); R05 = Rousselot et al. (2005); B06 = Belskaya et al. (2006); Sc02 = Schaefer et al. (2009); B04 = Boehnhardt et al. (2002); B13 = Benecchi & Sheppard (2013); R13 = Rabinowitz et al. (2013)

5.2 Observations & Analysis

We observed each of the CVS targets over multiple nights. The observational circumstances are summarized in Table 5.2. We plotted the photometry without phase angle correction (but with heliocentric and travel time correction, described in Chapter 6) versus the phase angle at the time of each observation and calculated the β coefficient by fitting a linear least-squares regression.

For the purposes of determining the phase curve, our data generally suffer from two observational setbacks. First, as a whole, our targets were only observed over a limited range of phase angles, where the phase angle effect is essentially overshadowed by the magnitude uncertainty. In order to provide meaningful constraints on the slope of the linear fit, the phase angle range must satisfy $\beta_{max}(\Delta\alpha) > \bar{\sigma}$, where $\bar{\sigma}$ is the mean uncertainty on the magnitudes for the full dataset. The largest β value measured for the V and R filters in the literature is 0.56 ± 0.03 (Table 5.1), and for our data, $\bar{\sigma} = 0.05$, giving $\Delta\alpha \gtrsim 0.1°$. Only five of our nine CVS targets - 2000 YW_{134}, 2001 QF_{298}, 2003 AZ_{84}, 2003 UZ_{117}, and 2004 EW_{95} - achieved at least this α-coverage in their full datasets. Thus, we only show phase curves for these five targets.

Second, the rotational modulation within a night must be adequately sampled to distinguish its signature from the phase angle effect. Delahodde et al. (2001) provide a detailed description of how to effectively remove this modulation in order to determine a phase curve. For a symmetric, double-peaked lightcurve, the full amplitude can be sampled over 1/4 of the rotation, whereas for a single-peaked lightcurve, 1/2 of the lightcurve must be observed to constrain the amplitude. The minimum rotation period previously determined for TNOs is $\sim$ 4 hours (from Table 4.1), so the likely limits to which our data could sample a target's rotation amplitude are $1/4 \times 4$, or $\sim$ 1 hour. All five of our targets with adequate α-coverage achieved this temporal coverage at their most extreme α measurements, but only barely so. Since the phase curve had to be determined in order to phase the data to determine the rotation period, we were not able to assess how well we removed

Table 5.2. Summary of data obtained for the CVS and their observing circumstances.

Designation	Observation date (UT)	Filter	# images	Mean α	Observation span (hrs)[a]
1995 SM_{55}	October 28, 2010	R	6	0.35	2.87
	October 29, 2010	R	5	0.34	2.25
	November 2, 2010	R	4	0.30	2.07
	November 3, 2010	R	2	0.29	0.47
	November 6, 2010	R	7	0.29	2.68
	October 28, 2010	V	6	0.35	2.83
	October 29, 2010	V	5	0.34	2.25
	November 2, 2010	V	5	0.30	2.05
	November 3, 2010	V	3	0.29	1.19
	November 6, 2010	V	7	0.29	2.82
2000 YW_{134}	February 15, 2010	R	9	0.39	5.82
	November 7, 2010	R	3	1.28	1.35
	March 1, 2011	R	9	0.65	6.03
	March 2, 2011	R	5	0.66	2.9
	March 3, 2011	R	2	0.68	0.62
	February 15, 2010	V	9	0.39	4.9
	November 7, 2010	V	3	1.28	1.37
	March 1, 2011	V	9	0.64	6.02
	March 2, 2011	V	6	0.66	3.47
	March 3, 2011	V	5	0.68	4.58
2001 QF_{298}	September 3, 2010	r'	2	0.40	0.52
	September 4, 2010	r'	5	0.37	2.48
	September 5, 2010	r'	5	0.35	4.92
	September 6, 2010	r'	5	0.33	3.5
	October 28, 2010	r'	4	0.83	1.92
	October 29, 2010	r'	3	0.85	1.35
	August 8, 2011	r'	3	0.94	3.05
	September 19, 2011	r'	5	0.16	5.03
	September 23, 2011	r'	7	0.14	6.3
	September 3, 2010	g'	2	0.40	0.45
	September 4, 2010	g'	5	0.37	1.6
	September 5, 2010	g'	5	0.35	4.92

rotational modulation for each target until after the period was determined. In most cases, we instead assumed that the data accumulated within a night was rotationally averaged. We stress that since this was the case for our data, the phase curves we determined may not represent the true phase curves relating to the surface properties. We therefore only use these β coefficients as an approximate way to merge rotational lightcurve data taken over appreciably different α values and not as a way to meaningfully comment on the surface properties of the targets.

Table 5.2—Continued

Designation	Observation date (UT)	Filter	# images	Mean α	Observation span (hrs)[a]
	September 6, 2010	g'	5	0.33	3.5
	October 28, 2010	g'	4	0.83	1.93
	October 29, 2010	g'	3	0.85	1.35
	August 8, 2011	g'	5	0.94	2.97
	September 19, 2011	g'	6	0.16	6.13
	September 23, 2011	g'	7	0.14	6.25
2002 TX_{300}	September 3, 2010	R	10	0.99	4.62
	September 4, 2010	R	13	0.98	2.21
	September 5, 2010	R	14	0.96	3.98
	September 6, 2010	R	20	0.95	5.6
	September 3, 2010	V	10	0.99	4.61
	September 4, 2010	V	13	0.98	0.17
	September 5, 2010	V	13	0.96	3.97
	September 6, 2010	V	20	0.95	5.38
2002 XV_{93}	December 2, 2010	R	4	0.43	2.67
	December 4, 2010	R	13	0.40	4.5
	December 2, 2010	V	5	0.43	4.6
	December 4, 2010	V	12	0.40	4.2
2003 AZ_{84}	February 16, 2012	r'	6	0.66	2.8
	February 24, 2012	r'	9	0.80	5.11
	February 26, 2012	r'	8	0.83	4.74
	February 27, 2012	r'	2	0.85	0.82
	February 28, 2012	r'	7	0.87	4.41
	April 18, 2012	r'	4	1.27	1.41
	February 16, 2012	g'	3	0.66	1.11
	February 24, 2012	g'	8	0.80	5.12
	February 26, 2012	g'	8	0.83	4.65
	February 28, 2012	g'	10	0.87	4.46
	April 18, 2012	g'	2	1.27	1.06
2003 OP_{32}	September 3, 2010	R	11	0.47	6.39
	September 4, 2010	R	12	0.49	2.41
	September 5, 2010	R	8	0.50	3.72

Table 5.2—Continued

Designation	Observation date (UT)	Filter	# images	Mean α	Observation span (hrs)[a]
	September 6, 2010	R	9	0.51	6.61
	September 3, 2010	V	12	0.47	6.35
	September 4, 2010	V	12	0.49	2.4
	September 5, 2010	V	10	0.50	3.88
	September 6, 2010	V	9	0.51	6.6
2003 UZ_{117}	October 14, 2012	R	8	0.90	5.03
	October 15, 2012	R	10	0.88	5.97
	October 19, 2012	R	5	0.80	2.01
	October 20, 2012	R	5	0.78	1.79
	October 14, 2012	V	4	0.90	5.38
	October 15, 2012	V	5	0.88	4.3
	October 19, 2012	V	2	0.80	0.91
	October 20, 2012	V	2	0.78	0.97
2004 EW_{95}	February 28, 2011	R	4	1.60	1.63
	March 1, 2011	R	6	1.58	1.74
	March 31, 2011	R	10	0.68	4.43
	April 22, 2011	R	4	0.14	1.7
	April 25, 2011	R	6	0.24	2.63
	February 24, 2012	R	5	1.77	2.75
	February 26, 2012	R	5	1.73	3.17
	April 17, 2012	R	11	0.22	4.7
	April 18, 2012	R	11	0.19	3.87
	April 27, 2012	R	9	0.24	5.07
	April 28, 2012	R	8	0.27	5.17
	February 28, 2011	V	4	1.60	1.63
	March 31, 2011	V	14	0.68	4.37
	April 22, 2011	V	3	0.14	1.13
	April 25, 2011	V	7	0.24	2.6
	February 24, 2012	V	5	1.77	2.78
	February 26, 2012	V	5	1.73	3.15
	April 17, 2012	V	5	0.22	4.48
	April 18, 2012	V	3	0.19	3.5

Table 5.2—Continued

Designation	Observation date (UT)	Filter	# images	Mean α	Observation span (hrs)[a]
	April 27, 2012	V	5	0.24	5.05
	April 28, 2012	V	4	0.27	5.17

[a]The time difference between the midpoint of the last image taken on the indicated night and the midpoint of the first.

5.3 Results for individual targets

In this section, we present the phase curves for each of the five targets that have sufficient α and temporal coverage - 2000 YW_{134}, 2001 QF_{298}, 2003 AZ_{84}, 2003 UZ_{117}, and 2004 EW_{95}. We discuss their analysis on an individual object basis.

For the TNO 2000 YW_{134}, we took data over $\Delta\alpha = 0.89°$. However, after preliminary lightcurve analysis of data taken on consecutive nights (March 01-03), we found that the data taken on November 07 all corresponded to a lightcurve minimum, which would naturally convey a fainter magnitude than the mean of the lightcurve amplitude and present a bias in determining the β value. Because the November 07 data were driving the fit, we excluded this night and redetermined the linear regression, finding $\beta_V = 0.0 \pm 0.1$ mag/° and $\beta_R = -0.1 \pm 0.1$ mag/°. Both of these values are consistent with a flat phase curve in both filters. Figure 5.1 shows the fit both including and excluding November 07.

We observed 2001 QF_{298} over two years, giving a robust combined dataset over $\Delta\alpha = 0.80°$, with blocks of observations spanning several hours at either end of the observed α distribution. We therefore reason that the data were sufficiently rotationally averaged to determine the slope of the phase curve. We find a relatively high β value that is consistent with being the same between the two filters: $\beta_V = 0.30 \pm 0.04$ and $\beta_R = 0.27 \pm 0.06$ mag/°.

The plutino 2003 AZ_{84} has been previously observed for its phase curve by Rabinowitz et al. (2008), who acquired a combined 67 data points in B, V, and I filters over $\Delta\alpha = 0.92°$ and reported $\beta_{avg} = 0.06 \pm 0.03$ mag/°. Our data span $\Delta\alpha = 0.61°$ and initially gave a shallow phase curve that did not significantly differ between filters (Fig. 5.3, upper). However, very few data were taken at the high end of the observed α range, with only

two g' images and four r' images at $\alpha > 0.9$. Furthermore, preliminary rotation period analysis for 2003 AZ_{84} also showed these data to be located within a rotational lightcurve minimum, which introduced bias into determining the rotationally-averaged magnitude. We therefore eliminated data from this night (April 18) from phase curve analysis. Subsequent redetermination of the linear fit rendered a flat β coefficient with very large uncertainties likely due to the limited number of data points at the small end of the phase distribution and possibly poor rotational averaging (Fig. 5.3, lower). We therefore were unable to significantly constrain 2003 AZ_{84}'s β coefficient to uncertainties useful for removing potential phase angle brightening from the rotational lightcurve. For later lightcurve analysis, we adopted the published $\beta_{avg} = 0.06 \pm 0.03$ for both V and R filters (Rabinowitz et al. 2008).

We observed the Haumea family member 2003 UZ_{117} over a relatively small α-range of $0.12°$, with two clusters of magnitude measurements at $\alpha \sim 0.8°$ and $\alpha \sim 0.9°$. However, as with 2000 YW_{134} and 2003 AZ_{84}, one of the clusters was poorly populated and situated at the lightcurve minima, suggesting poor rotational averaging. Figure 5.4 gives the phase curve over all data. Removing the sparse dataset from analysis would give an adjusted sample spanning only $\Delta\alpha = 0.02$, which is insufficient to constrain the linear fit. Therefore, we could not reliably constrain the β coefficient. Since 2003 UZ_{117}'s phase curve has not been previously explored, we had to assume a β value in later lightcurve analysis. For this, we took the mean β_{avg} for all Haumea family members with measured phase curves (Table 5.1), obtaining a $\beta_{avg} = 0.05$ mag/°. We assumed this value for both the V and R filters.

The last object for which we were able to investigate the phase function was 2004 EW_{95}, which had no published β coefficient. We obtained data for this object over two years and four filters - V and R band data in 2011 and g' and r' band data in 2012. Figure 5.5 shows the phase curves using the complete dataset for each year, giving convincing solutions for both years that are statistically different between filters: $\beta_{g'} = 0.57 \pm 0.03$, $\beta_V = 0.43 \pm 0.03$, $\beta_R = 0.29 \pm 0.02$, and $\beta_{r'} = 0.44 \pm 0.02$ mag/°.

5.4 Summary & Discussion

We obtained photometry on nine objects as part of the CVS, five of which were observed over a wide enough range of solar phase angles to constrain their phase functions. However, for two of these targets, poor magnitude sampling within a cluster of α values crucial to constraining the phase curve caused poor solutions to the slope of the phase curve. Therefore, we were only able to determine phase curves for three TNOs, none of which had previously constrained phase functions. Our results are summarized in Table 5.3.

Table 5.3 Results from our solar phase curve study.

Designation	Class	$V-R$	$\Delta\alpha$ (°)	$\beta_{g'}$	β_V	β_R	$\beta_{r'}$
2000 YW_{134}	S	0.63 ± 0.04	0.29		0.0 ± 0.1	-0.1 ± 0.1	
2001 QF_{298}	P	0.46 ± 0.05	0.80		0.30 ± 0.04	0.27 ± 0.06	
2004 EW_{95}	P	0.40 ± 0.04	1.44		0.43 ± 0.03	0.29 ± 0.02	
2004 EW_{95}	P	0.40 ± 0.04	1.58	0.57 ± 0.03			0.44 ± 0.02

Note. — β values are in units mag/°.

Although its β coefficient has large uncertainties, 2000 YW_{134} is the only optically red TNO whose solar phase curve is consistent with flat, providing evidence against the reported color-β trend (Rabinowitz et al. 2008). We point out, however, that while our data showed optically red colors ($V - R = 0.63 \pm 0.04$), previous color measurements for this object were much more neutral, ranging from $V - R = 0.39 \pm 0.02$ to 0.55 ± 0.03 (Doressoundiram et al. 2007; Jewitt et al. 2007, ,respectively). This suggests that 2000 YW_{134} is a very heterogeneous object, so its placement in the color-β plot is suspect.

In Figure 5.6, we investigated this color-β trend, using β_R and $V-R$ (since they were the most numerous in their respective phase coefficient and color populations). Even excluding the 2000 YW_{134} data point on the grounds of its large uncertainties, minimal phase angle range, and wide range of color measurements, a linear fit to the plotted data rendered a slope of only 0.0 ± 0.1, consistent with no correlation. We speculated that perhaps the correlation

Table 5.4 Comparison between the β_R coefficient of different TNO dynamical classes.

Sample 1	Sample 2	Sample Size 1	Sample Size 2	KS probability
Classicals	Resonators & Plutinos	8	10	0.826
Classicals	Scattered & Detached disk	8	8	0.519
Resonators & Plutinos	Scattered & Detached disk	10	8	0.826

observed by Rabinowitz et al. (2008) was more prominent for the wavelength regime they explored ($V - I$ color and β_{avg}). Our investigation therefore yielded no evidence that neutral TNOs have different surface scattering properties than red TNOs. Surface scattering properties might change if the surface were heavily processed via energetic collisions, so our results combined with previous studies show that neutral TNOs do not show any evidence through their phase curves of being subject to more collisions than red TNOs.

Next, we searched for a trend in phase curve and dynamical class by assessing mutual similarities in the β coefficient. We calculated the Kolmogorov-Smirnov (KS) probability that two samples come from the same distribution and conveyed the results in Table 5.4. All of the KS probabilities for the samples explored give relatively high values, implying similarity. Although our sample size was small, we therefore found no evidence of a correlation between phase curves and dynamical classes of TNOs, suggesting that surface texture and porosity properties of TNOs are independent of dynamical history. However, we reemphasize our points that because we could not ensure removal of the rotational signature and because TNO phase curve observation are likely located within the opposition surge, we cannot specifically comment on the implications of the specific surface properties like texture, porosity, etc. Future work in determining TNO phase curves will require dense lightcurve sampling within a night over several significantly different phase angles, and with magnitude uncertainties less than the expected phase curve brightening in order to ensure adequate removal of the rotational modulation.

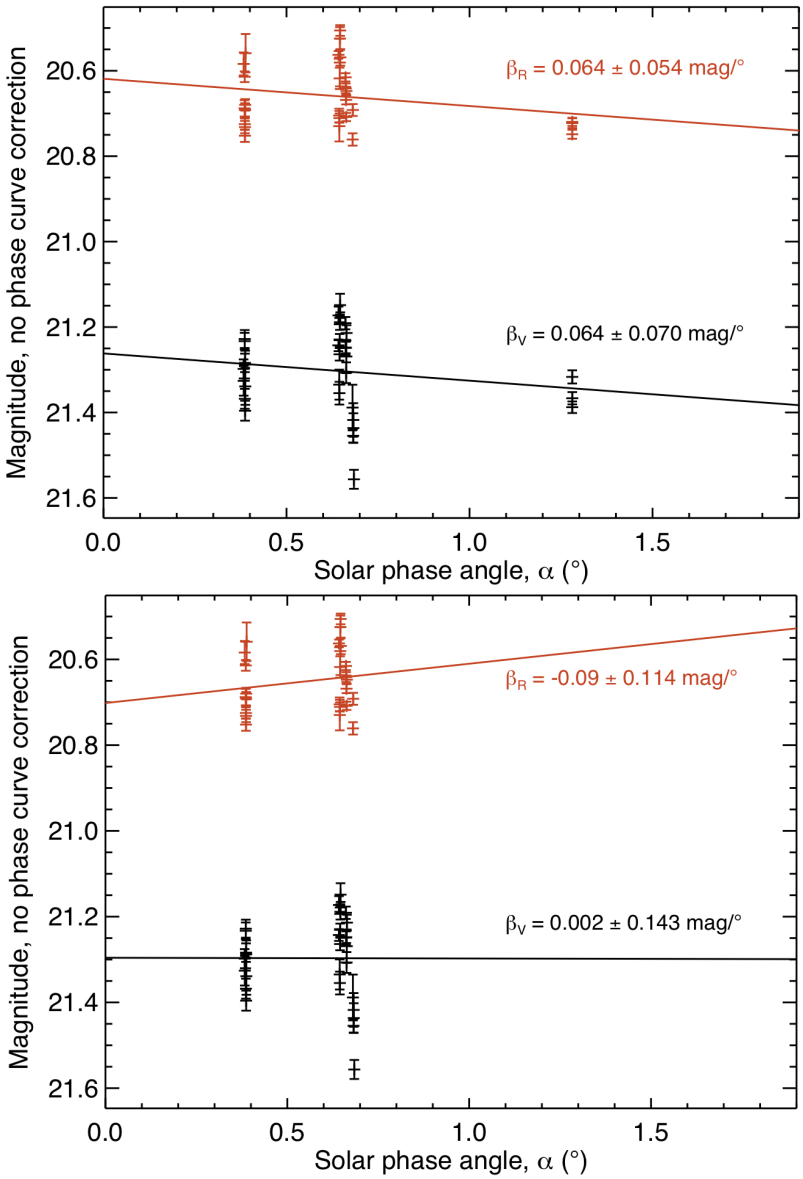

Figure 5.1 Solar phase curve and linear fit to V band (black) and R band (red) data on 2000 YW_{134}. The solid lines represent the linear least-squares regression, and the β value is the slope of this regression. The upper plot is the linear fit to all data, and the lower plot is the fit excluding data taken at $\alpha \sim 1.28$ on November 07, which corresponded to a lightcurve minimum and were therefore not rotationally averaged. The negative phase curve is unphysical, but the measurement itself is consistent with flat when considering the uncertainty in β.

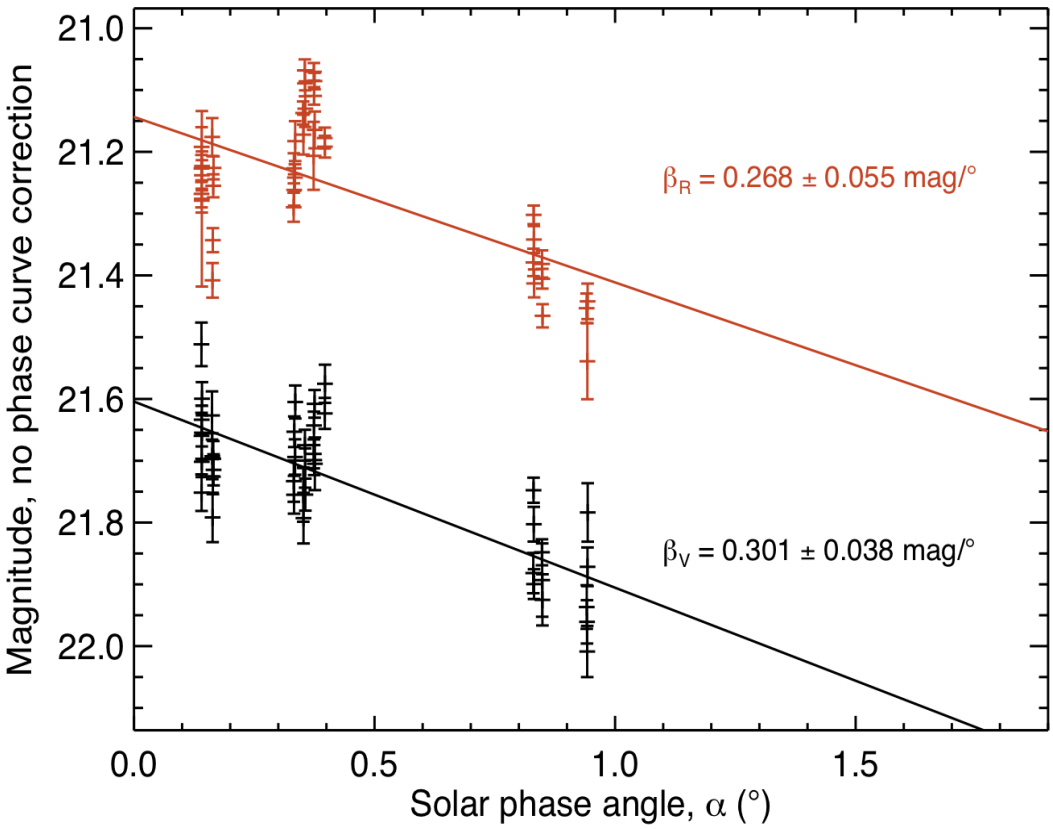

Figure 5.2 Solar phase curve and linear fit to V band (black) and R band (red) data on 2001 QF_{298}. The solid lines represent the linear least-squares regression, and the β value is the slope of this regression.

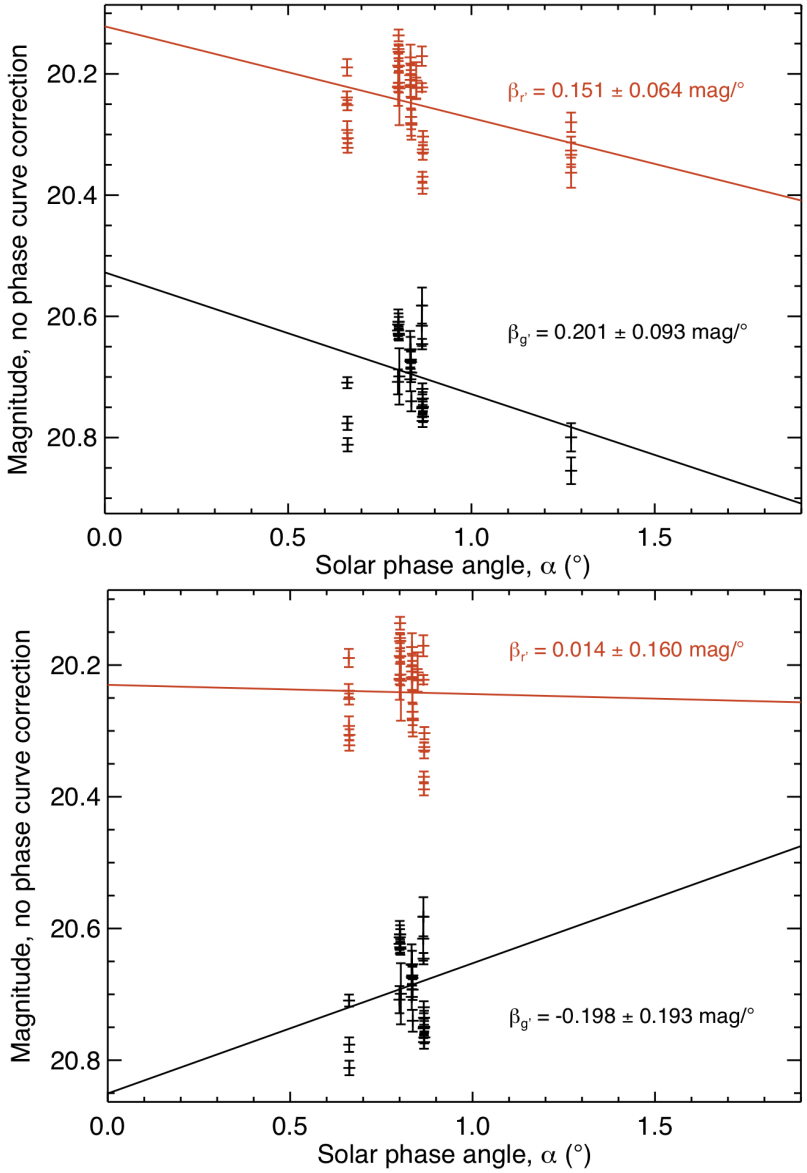

Figure 5.3 Solar phase curve and linear fit to g' band (black) and r' band (red) data on 2003 AZ_{84}. The solid lines represent the linear least-squares regression, and the β value is the slope of this regression. The upper plot gives the fit to all data, and the lower plot is the fit excluding April 18 from analysis, which was not likely to give rotationally-averaged magnitudes. These results show that the phase curve solution for 2003 AZ_{84} is poor (and unphysical in some cases), so we were not able to measure the phase curve for this object.

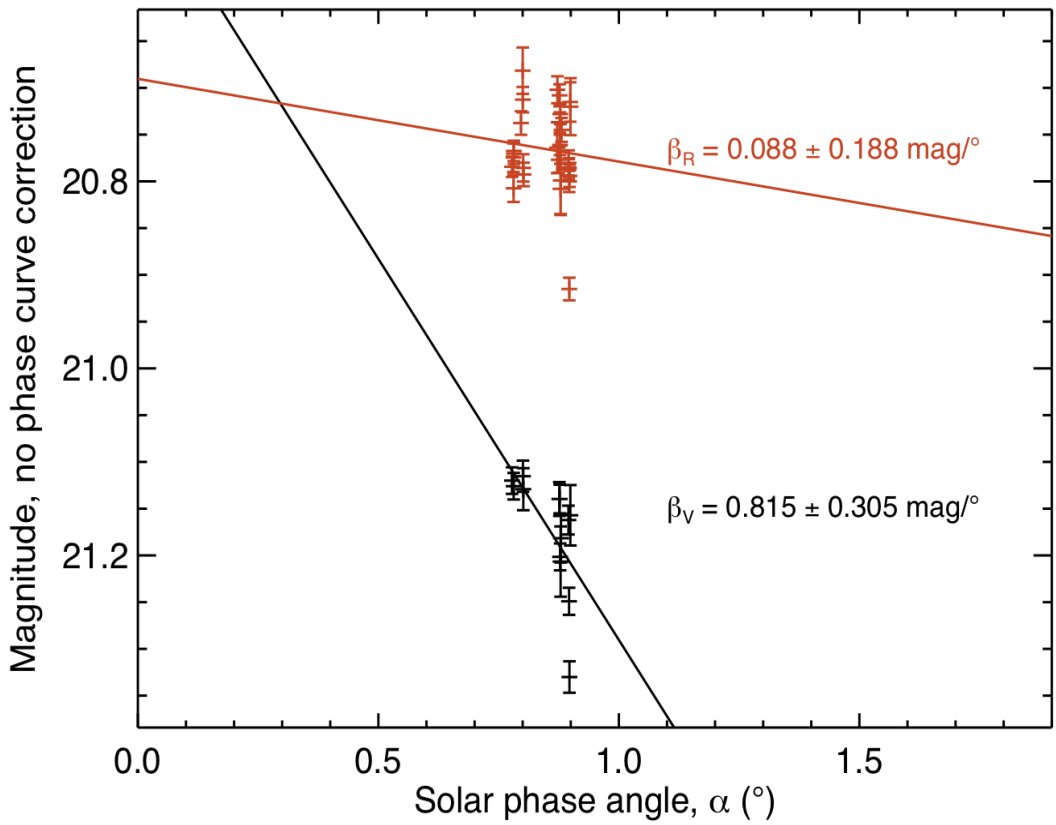

Figure 5.4 Solar phase curve and linear fit to V band (black) and R band (red) data on 2003 UZ_{117}. The solid lines represent the linear least-squares regression, and the β value is the slope of this regression. Such sparsely sampled rotational lightcurves over a very small α range were not likely to produce a convincing phase curve solution, as indicated by the extremely steep slope in the V filter that we consider not representative of the true β value - it is in fact more than twice the steepest phase curve measured for TNOs in the literature.

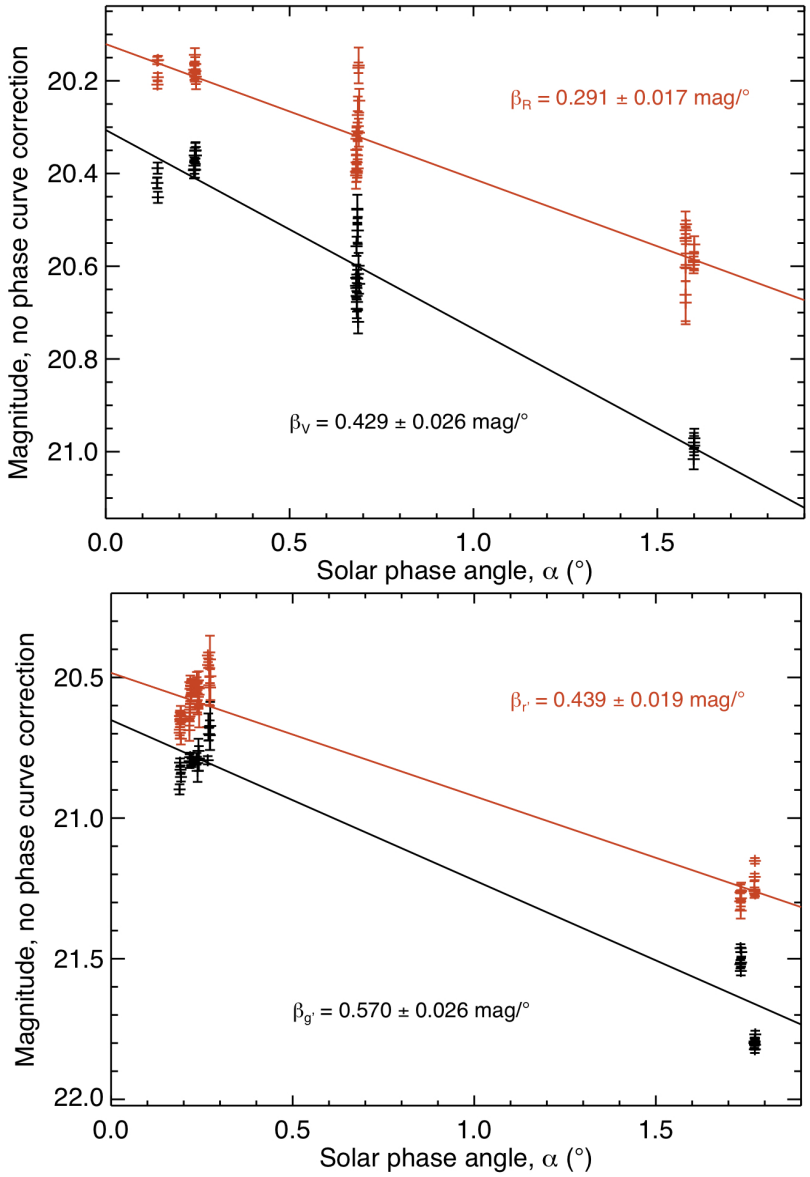

Figure 5.5 Solar phase curve and linear fit to data taken for 2004 EW_{95}. The upper plot gives the 2011 data, with the black line corresponding to the V band and the R band to the red line. The lower plot gives the fits to 2012 data taken in the V filter (black) and R filter (red). The solid lines represent the linear least-squares regression, and the β value is the slope of this regression.

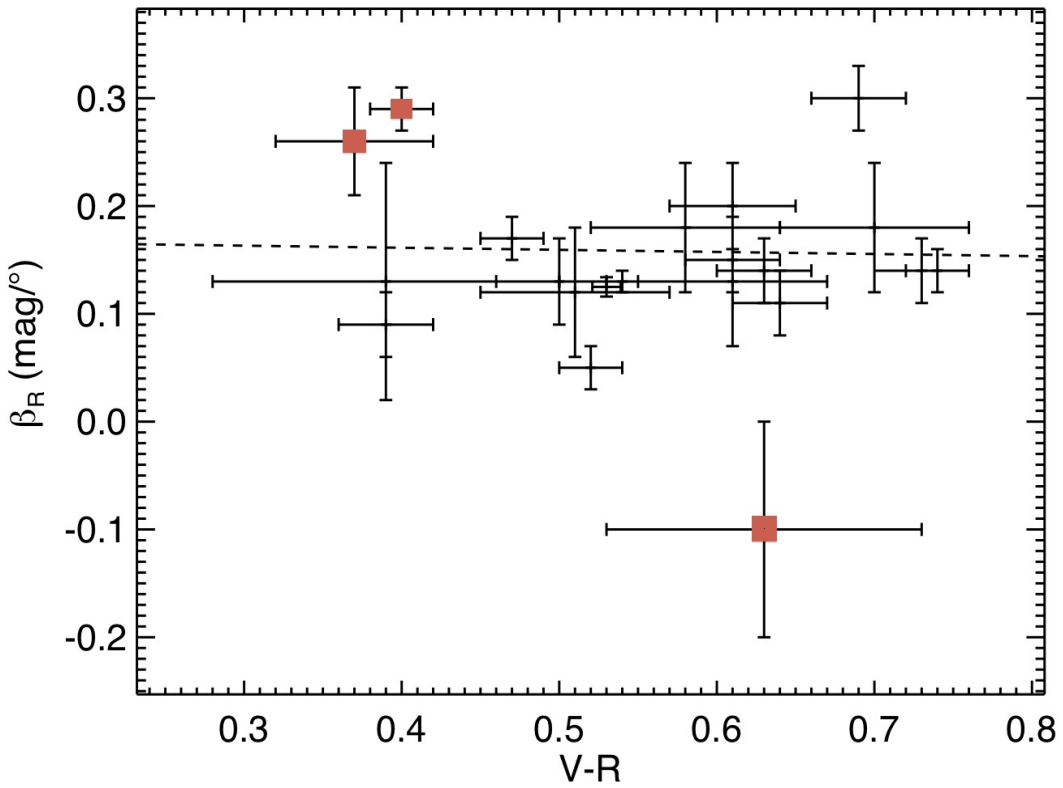

Figure 5.6 $V - R$ color versus β coefficient for the R filter. The anomalously low data point with $\beta_R = -0.1 \pm 0.1$ is 2000 YW_{134}. The dashed line is a linear fit to the data excluding the 2000 YW_{134}data point. Our data are indicated by red filled squares at their centroid.

References

Barucci, M. A., Merlin, F., Dotto, E., Doressoundiram, A., & de Bergh, C. 2006, A&A, 455, 725

Belskaya, I. N., Levasseur-Regourd, A.-C., Shkuratov, Y. G., & Muinonen, K. 2008, Surface Properties of Kuiper Belt Objects and Centaurs from Photometry and Polarimetry, ed. M. A. Barucci, H. Boehnhardt, D. P. Cruikshank, A. Morbidelli, & R. Dotson, 115–127

Belskaya, I. N., Ortiz, J. L., Rousselot, P., Ivanova, V., Borisov, G., Shevchenko, V. G., & Peixinho, N. 2006, *Icarus*, 184, 277

Belskaya, I. N. & Shevchenko, V. G. 2000, *Icarus*, 147, 94

Benecchi, S. D. & Sheppard, S. S. 2013, AJ, 145, 124

Boehnhardt, H., Delsanti, A., Barucci, A., Hainaut, O., Doressoundiram, A., Lazzarin, M., Barrera, L., de Bergh, C., Birkle, K., Dotto, E., Meech, K., Ortiz, J. E., Romon, J., Sekiguchi, T., Thomas, N., Tozzi, G. P., Watanabe, J., & West, R. M. 2002, A&A, 395, 297

Bowell, E., Hapke, B., Domingue, D., Lumme, K., Peltoniemi, J., & Harris, A. W. 1989, in Asteroids II, ed. R. P. Binzel, T. Gehrels, & M. S. Matthews, 524–556

Carraro, G., Maris, M., Bertin, D., & Parisi, M. G. 2006, A&A, 460, L39

de Bergh, C., Delsanti, A., Tozzi, G. P., Dotto, E., Doressoundiram, A., & Barucci, M. A. 2005, A&A, 437, 1115

Delahodde, C. E., Meech, K. J., Hainaut, O. R., & Dotto, E. 2001, A&A, 376, 672

DeMeo, F. E., Fornasier, S., Barucci, M. A., Perna, D., Protopapa, S., Alvarez-Candal, A., Delsanti, A., Doressoundiram, A., Merlin, F., & de Bergh, C. 2009, A&A, 493, 283

Doressoundiram, A., Barucci, M. A., Romon, J., & Veillet, C. 2001, *Icarus*, 154, 277

Doressoundiram, A., Peixinho, N., Moullet, A., Fornasier, S., Barucci, M. A., Beuzit, J.-L., & Veillet, C. 2007, AJ, 134, 2186

Drossart, P. 1993, Planet. Space Sci., 41, 381

Gil-Hutton, R. & Licandro, J. 2001, *Icarus*, 152, 246

Jewitt, D., Peixinho, N., & Hsieh, H. H. 2007, AJ, 134, 2046

Jewitt, D. C. & Luu, J. X. 2001, AJ, 122, 2099

Morbidelli, A., Levison, H. F., & Gomes, R. 2008, The Dynamical Structure of the Kuiper Belt and Its Primordial Origin, ed. M. A. Barucci, H. Boehnhardt, D. P. Cruikshank, A. Morbidelli, & R. Dotson, 275–292

Poulet, F., Cuzzi, J. N., French, R. G., & Dones, L. 2002, *Icarus*, 158, 224

Rabinowitz, D., Schwamb, M. E., Hadjiyska, E., Tourtellotte, S., & Rojo, P. 2013, AJ, 146, 17

Rabinowitz, D. L., Schaefer, B. E., Schaefer, M., & Tourtellotte, S. W. 2008, AJ, 136, 1502

Rabinowitz, D. L., Schaefer, B. E., & Tourtellotte, S. W. 2007, AJ, 133, 26

Rousselot, P., Petit, J.-M., Poulet, F., Lacerda, P., & Ortiz, J. 2003, A&A, 407, 1139

Rousselot, P., Petit, J.-M., Poulet, F., & Sergeev, A. 2005, *Icarus*, 176, 478

Schaefer, B. E., Rabinowitz, D. L., & Tourtellotte, S. W. 2009, AJ, 137, 129

Sheppard, S. S. 2010, AJ, 139, 1394

Sheppard, S. S. & Jewitt, D. C. 2002, AJ, 124, 1757

Tegler, S. C. & Romanishin, W. 2000, Nature, 407, 979

Tegler, S. C., Romanishin, W., & Consolmagno, G. J. 2003, ApJ, 599, L49

Thirouin, A., Ortiz, J. L., Campo Bagatin, A., Pravec, P., Morales, N., Hainaut, O., & Duffard, R. 2012, MNRAS, 424, 3156

Chapter 6

Rotational Lightcurves

6.1 Introduction

Determining rotational lightcurves is a robust way to characterize physical properties of a population. In Chapter 4, we described how sparsely sampling lightcurves allows identification of close or contact binaries and constraints to be set on the shape distribution, which can then be used to infer collisional history. Obtaining densely sampled lightcurves helps determine additional indicators of dynamical and collisional evolution, namely the binary fraction at moderate separations, spin distribution, physical size dimensions, and information on the structure and density. In this chapter, we describe how the data from the Color Variation Survey (CVS) were used to extract these properties.

6.1.1 Estimating shapes

A population's shape distribution is indicative of its collisional history. Further details concerning the implications of amplitudes on solar system evolution models are provided in Section 4.1. Rotating objects can show changes in magnitude attributed to changing projected cross-sections of a non-spherical body. Some brightness variation can be explained by albedo variation, which can account for up to a 25% change in magnitude (Sheppard & Jewitt 2004), but above this limit, either binarity or shape must be the cause of brightness variation.

Small bodies can acquire several different shapes depending on their proximity to other massive bodies, specific angular momentum (the angular momentum per unit mass), and tensile strength, each of which are discussed below. For objects orbiting close to and around a massive body (*i.e.*, satellites of Jovian planets, notably Io), tidal forces may distort the satellite into a prolate shape (Davidsson 2001). Otherwise, objects can take on five different shapes governed by tensile strength and angular momentum (h): prolate spheroids, oblate spheroids, perfect spheres, or irregular fragments. At $h < 0.304$, the equilibrium shape of a rotating body is a Maclaurin (oblate) spheroid, which is rotationally symmetric and so will not exhibit amplitude modulation. Objects with $0.304 < h < 0.390$ will adopt the shape of a Jacobi (triaxial) ellipsoid. Above $h = 0.390$, strengthless bodies are unstable to disruption (Chandrasekhar 1987; Sheppard & Jewitt 2002). Some objects have not been collisionally fractured and are not rotating fast enough to cause shear fracturing so as to distort them into Jacobi ellipsoidal rubble piles, so they retain spherical shapes (Davidsson 2001; Ortiz et al. 2003). Small objects (< 100km in diameter), however, that have undergone disruptive collisions are typically irregularly shaped, rigid fragments.

Because many larger TNOs exhibit brightness variation, they are generally thought to have a Jacobi ellipsoid shape whose axes of lengths $a \geq b \geq c$ (Fig. 6.1) are defined in terms of the photometric range and pole orientation relative to the line of sight (ξ; Binzel et al. 1989):

$$\Delta m = 2.5 \log \left(\frac{a}{b} \right) - 1.25 \log \left(\frac{a^2 \cos^2 \xi + c^2 \sin^2 \xi}{b^2 \cos^2 \xi + c^2 \sin^2 \xi} \right) \quad . \tag{6.1}$$

Equation 6.1 can be simplifed by assuming $\xi = 90°$ to obtain:

$$\Delta m = 2.5 \log \left(\frac{a}{b} \right) \quad . \tag{6.2}$$

Although the spin axis distribution is not observationally constrained for TNOs, it can be inferred. A non-collisionally excited population should typically be oriented with the rotation axis up with respect to the observer's line of sight ($\xi = 90°$) due to the obliquity

dampening (Burns & Safronov 1973). Sheppard et al. (2008) demonstrate that for a collisionally evolved population, pole orientations should be randomized, giving an average ξ of 60° and consequently reducing the observed Δm by a factor of 0.87. Therefore, to obtain the mean axial ratios for population with a significant collisional past, we must divide the calculated ratio by this factor.

If the average absolute magnitude (H) and albedo (p) are known, we can calculate the average diameter of an object using

$$D = \frac{1329 \times 10^{-0.2H}}{\sqrt{p}} \tag{6.3}$$

from Lamy et al. (2004). Using this average diameter calculation in combination with Eq. 6.2 and the 0.87 correction factor, we can estimate the physical dimensions of an object.

6.1.2 The spin period distribution

Determining rotation periods also sets constraints on the dynamical conditions in the Trans-Neptunian belt. A collisionally evolved population is supposed to have a Maxwellian spin period distribution that clusters around the critical period, below which objects will spin apart. Conversely, a non-Maxwellian spin distribution with typically longer rotation periods than the critical period indicates that collisions were not a significant part of the population's history. The widely-cited NICE model of solar system formation includes an episode of chaotic scattering in the outer solar system that implies a high collisional frequency (*e.g.*, Morbidelli et al. 2005) whereas formation models of more gentle planetary migration such as Marzari & Scholl (1998) predict a less collisionally evolved population in the outer solar system. Therefore, by constraining the shape of the spin distribution, we can help distinguish between collisional evolution scenarios inferred by giant planet models. Currently, there are 48 well-determined rotation periods for TNOs, all of which are given in Table 4.1 in Chapter 4.

6.1.3 Determining binary properties through lightcurves

Binaries are particularly diagnostic of the dynamical environment, which gives clues to the major dynamical events in solar system formation such as giant planet migration. Section 4.1 in Chapter 4 reviews the different binary formation models and their competing predictions for the binary fraction as a function of mutual separation.

Very wide binaries (separations $\gtrsim 0.1''$) are visually distinct in high-resolution images such as those from HST, and very close binaries (separations $\lesssim 0.02''$, from Chapter 4) can be identified through large lightcurve amplitudes seen within a night (see Chapter 4). Asynchronous systems with an elongated primary might exhibit two periodicities, one belonging to the brightness change from the binary, and one belonging to the primary's rotation signature; the TNO 2001 QY_{297} is an example of such a system (Grundy et al. 2011). Moderately separated binaries when viewed equatorially manifest as a brightness offset (Δm) on the order of days attributable to the secondary moving behind the primary. The magnitude offset from the binary defines the flux contribution (F) of one of the binary components in the system:

$$\frac{F_s}{F_p} = 10^{0.4\Delta m} - 1 \ , \tag{6.4}$$

where the subscript s indicates the secondary and p indicates the primary. Assuming spherical components, Eq. 6.4 relates to the radius r and albedo p of the components via:

$$\frac{r_s^2\, p_s}{r_p^2\, p_p} = 0^{0.4\Delta m} - 1 \ . \tag{6.5}$$

We can assume that the primary and secondary have similar albedos (*i.e.*, $p_s = p_p$) since they likely formed either in the same region or were a part of a mutual collision. With this assumption, Eq. 6.5 can be simplified to

$$\frac{r_s}{r_p} = \sqrt{10^{0.4\Delta m} - 1} \ . \tag{6.6}$$

We can also use constraints on the synodic period of a binary system (T) to estimate its mutual separation (a). Equating centripetal with gravitational acceleration, we obtain:

$$M_{sys} = \frac{4\pi^2 a^3}{T^2 G} \quad . \tag{6.7}$$

Assuming the two components have the same density, we can substitute density and radius of the components for the system mass in Eq. 6.7 to obtain

$$\frac{\rho}{3}(r_p^3 + r_s^3) = \frac{\pi a^3}{T^2 G} \quad . \tag{6.8}$$

Solving for the component separation:

$$a = \left[\frac{G\rho T^2 r_p^3}{3\pi} \left(1 + \frac{r_s}{r_p} \right) \right]^{1/3} \quad . \tag{6.9}$$

Using Eq.s 6.6 and 6.9, we can therefore constrain the binary component sizes and mutual separations for any identified binary candidates using the measured magnitude offset, estimates of the synodic period from the lightcurve data, and a range of plausible densities and primary radii. The observed binary fraction can then be debiased to determine the true binary fraction.

6.1.4 Material strength & bulk density

The rotation period can also be used constrain the bulk density (ρ) and, in some cases, the material strength (S, in N/m^2) of an object. Density is an important parameter for determining formation conditions and subsequent dynamical history. Objects with low densities are consistent with being more ice-rich and thus having formed beyond condensation lines in the outer solar system. Densities below that of water ice ($\sim$ 1000 kg/m^3) indicate icy and porous objects, likely small so that they do not significantly compress under their own self-gravity. A non-zero tensile strength implies a rigid and

likely primordial structure (Romanishin & Tegler 1999). Davidsson (2001) expressed the minimum spin period (in hours) before breakup as

$$P_{min} = \frac{\pi}{\sqrt{(\frac{1}{3})\pi G\rho + S/\rho r^2}} \quad . \tag{6.10}$$

Objects with no tensile strength (*i.e.*, gravitationally bound rubble piles restructured through collisions) have $S = 0$, so that Eq. 6.10 can be rewritten as

$$P_{min} = \sqrt{\frac{3\pi}{G\rho}} \quad , \tag{6.11}$$

so that if the target is spinning at its critical period, then one can calculate the density.

Davidsson (2001) also define the tensile strength in terms of the density and the diameter at which the structural transition between irregular and spherical objects takes place (D_t):

$$S = 1.29 \times 10^{-9} D_t^2 \rho^2 \quad . \tag{6.12}$$

Constraining the density and D_t from lightcurve data therefore constrains the material strength.

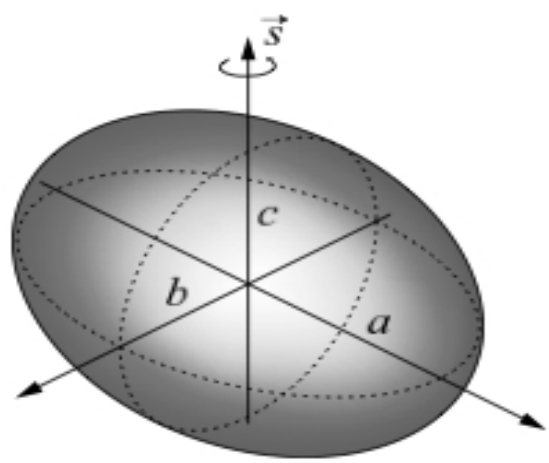

Figure 6.1 Diagram taken from Lacerda & Luu (2003) showing a triaxial ellipsoid rotation about a spin axis vector s, with a as the longest axis and b as the shortest equatorial axis.

6.2 Data acquisition and period determination techniques

Targets for the rotation study were selected based on four traits:

- In order to maximize chances of exploring color variation, only objects with detectable variation (as observed in the BVS) were chosen for follow-up rotation data.
- Objects with the most neutral $V - R$ colors were favored for follow-up over redder objects with comparable brightness variation.
- Brighter (and therefore larger) objects were preferred so as to afford better S/N, thereby allowing better determination of low-amplitude lightcurves.
- At least one object from each of the three major dynamical classes (Classicals, Resonators, and Scattered Disk objects, described in Chapter 1) so as to sample neutral TNOs with a range of possibly different dynamical histories.

Photometry of the BVS was initially done using IRAF's *apphot* task, though this algorithm was later shown to include background contaminants, affecting the accuracy of the calculated magnitudes (described further in Chapter 2). The follow-up targets for rotation were selected and initial CVS observations begun before we discovered the algorithm inaccuracies, so some targets were not as variable as anticipated. For example, 1999 CD_{158} did not show significant variation in the *apphot* results and was therefore not chosen for follow-up, but the tphot results indicated significant high-amplitude variation.

The follow-up sample also contained a number of Haumea family members (remnants of giant catastrophic collision in the outer solar system) and two previously known resolved binary systems. We judged that since there is no reason for large fragments of proto-Haumea and binary components not to have undergone subsequent outgassing and/or impacts, they could still serve as useful test cases to discern between resurfacing mechanisms. The Haumea family targets also make an interesting comparison study of objects that were known to have been involved in a catastrophic collision versus objects that were not likely involved in such

collisions. The final target list for the rotation and color variation study is described in Table 6.1.

Table 6.1 Basic properties of targets chosen for rotational follow-up.

Designation	a (AU)	e	i (°)	Class[a]	Diameter (km)	Diameter Ref.	Comments
1995 SM_{55}	42.03	0.11	27.03	C	250	1	Haumea family
2000 YW_{134}	58.26	0.29	19.78	S	430	2	Known binary
2001 QF_{298}	39.41	0.11	22.36	P	440	3	
2002 TX_{300}	43.41	0.12	25.87	C	340	1,4	Haumea family
2002 XV_{93}	39.55	0.12	13.27	P	860	3	
2003 AZ_{84}	39.64	0.17	13.54	P	350	3	Known binary
2003 OP_{32}	43.13	0.10	27.15	C	320	1	Haumea family
2003 UZ_{117}	44.51	0.14	27.40	C	430	1	Haumea family
2004 EW_{95}	39.32	0.31	29.30	P	190	2	

[a]Key to the dynamical class: C = classical, S = scattered disk objects, P = plutinos

[b]Reference key: 1: Stansberry et al. (2011); 2: Diameter calculated using Eq. 6.3 and an assumed albedo of 0.09 (the mean measured albedo for TNOs (Warner et al. 2009)); 3: Mommert et al. (2012); 4: Elliot et al. (2010)

We chose to measure the colors using the V and R Kron-Cousins filters because they optimized sensitivity and avoided potentially variable spectral features such as deep silicate bands close to the I filter. The $V - R$ optical color is also one of the most commonly measured in the literature, so this filter combination afforded a large comparison color sample. At first, we adopted a $V - R - V - R$ observing cadence, but preliminary analysis of lightcurve patterns proved very difficult to determine or were buried in the noise. We accordingly changed the cadence to deliver more data in one filter (the R filter for sensitivity maximization discussed in Section 4.2 so as to better constrain the rotational lightcurve in this filter, then phase the V filter data to the determined rotation period. The filter cadence adopted for later dates was $R - V - R - R - V - R$.

When possible, we calibrated our data using field star magnitudes reported through data release 9 (the most recent at this time, with typical magnitude uncertainties of $\sim 2 - 3\%$

in g' or r' for $g \sim 23$) of the Sloan Digital Sky Survey (SDSS; Ahn et al. 2012). For fields not calibrated with SDSS, we re-imaged them on photometric nights alongside several Landolt standard stars observed over a wide airmass range ($\sim 1.0 - 2.5$; Landolt 1992). The instrumental magnitudes (m_{inst}) of the Landolt stars were used to calculate the night's extinction coefficients, which can used to calibrate field star magnitudes for images acquired on the same photometric night. We checked the accuracy of the extinction coefficients by using them to correct fields with available SDSS stars and comparing the SDSS-calibrated magnitudes to the Landolt-calibrated magnitudes. In some cases, we found significant offsets between the Landolt-measured and actual zeropoint, which we were able to correct by applying the additional offset to post-Landolt calibrated fields. The source of this offset has not yet been explored.

An object's magnitude can also vary due to changes in the viewing geometry, namely the Sun-target-observer angle (phase angle, α), which changes the amount of shadowing that is observed on a rough and/or porous surface. This phase angle effect provides valuable insights into the surface properties of small bodies and was described and measured for our targets in Chapter 5. Another way the viewing geometry can change is if the object moves closer to the observer (an effective decrease in geocentric distance, Δ) or closer to the Sun in its orbit (a decrease in heliocentric distance, R), which cause brightening in the rotational lightcurve. Phasing data taken at different times over a range of α, Δ, or R requires removing this brightening. Data presented in this chapter have been corrected for phase angle and geocentric distance brightening by applying an offset (C) adapted from Sheppard & Jewitt (2002):

$$C = 5 \ \log \left(\frac{R_2 \Delta_2}{R_1 \Delta_1} \right) - \beta(\alpha_2 - \alpha_1) \quad ,$$

where β is the linear phase angle coefficient (in magnitudes per degree), and the subscript 1 indicates the night to which the data from another night (2) are to be calibrated. A change in R and Δ also changes the amount of time that it takes for light to reach the target

from the Sun and then reflected back to the observer. We obtained the light-time corrected Julian date for each object from its JPL Horizons ephemeris.

To search for periodicity in the lightcurve data, we used the now standard period dispersion minimization (PDM) and the Lomb-Scargle period search techniques (PDM; Lomb 1976; Stellingwerf 1978; Scargle 1982). PDM involves computing the Θ parameter, which is essentially the variance in the data at an array of different rotational phasings divided by the variance in the unphased data, so the period that returns the smallest Θ value is the most likely value. Though no formal confidence limits can be calculated in the PDM method, periods giving $\Theta < 0.2$ are in practice highly significant (Sheppard et al. 2008). The Lomb technique is a least-squares technique similar to Fourier analysis. The main advantages of the Lomb-Scargle method are that it accounts for uneven temporal sampling between data points and it allows for computing formal confidence limits (z; directly corresponding to the significance) via:

$$z = -\ln\left[1 - (I^{\,1/M})\right] \quad , \tag{6.13}$$

where I is the interval at which spectral power z lies (*e.g.*, $I = 0.999$ for 99.9% confidence limits). M is the number of independent periods which can be estimated through

$$M = -6.362 + (1.193N) + (0.00098N^2) \quad ,$$

where N is the number of data points (Scargle 1982). Equation 6.13 can be inverted to compute the confidence interval at a specific z value. We report both PDM and Lomb-Scargle periodograms for each object.

To characterize the significant of color variation with rotation, we first performed Monte Carlo simulations of flat $V - R$ color lightcurves. Flat color lightcurves were constructed by distributing the synthetic data points with the same sample size as the real dataset randomly (the actual magnitude error times a random Gaussian number) about the median measured color. We next produced an RMS distribution comprised of individual RMS measurements

of each synthetic dataset. We then compared the true RMS to the distribution of RMS values of the flat color curves and computed the percentile under which the true data fell within the distribution. Determining the color variation in this way has two main advantages: (i) the simulations use the same error and sample size as the data, and (ii) the result is independent of the rotation period, so if we were unable to determine the rotation period, we could still constrain the degree of color variation. This method of computing color variation relies on having reliable magnitude errors which affects the width of the synthetic RMS distribution. In Chapter 2, we demonstrate why we are confident in our magnitude errors.

6.3 Lightcurve results

We report the results from the period search and use the measured lightcurve properties to estimate physical properties of each target. In cases where evidence of binarity is detected, we also derive constraints on the binary system. All of the data presented in this section were median-smoothed over data taken within an hour.

6.3.1 1995 SM_{55}

Sheppard & Jewitt (2003) observed Haumea family member 1995 SM_{55} to determine its lightcurve and found either a single-peaked 4.04 hour period or double-peaked 8.08 hour period. However, they saw significant scatter in the phased data suggestive of a variable amplitude and/or poor phasing. We obtained 26 V-band and 24 R-band images during five nights spread over nine days. Because our data were acquired over a short time span, all data frames contained field stars observed on more than one night, allowing us to empirically determine the night-to-night offset from common stars.

PDM and Lomb-Scargle periodograms as well as the respective errors on periods were calculated using the PERANSO software[1]. Periodograms calculated using absolute magnitudes gave poor solutions, but better period solutions were achieved by subtracting

[1]Available at http://www.peranso.com/

the mean magnitude from each night to remove intrinsic night-to-night variation possibly due to a secondary, multi-day period. The resultant mean-subtracted periodograms are given for the R filter in Figure 6.2 and the V filter in Figure 6.3. Table 6.2 lists the most significant periods found through both Lomb-Scargle and PDM techniques for both V and R filters using mean-subtracted data.

Table 6.2 The four most prominent rotation periods (in hours) and their respective errors detected through each of the Lomb-Scargle and PDM techniques for mean-subtracted 1995 SM_{55} data. Periods that visually phased well in both filters are given in bold.

Detection Technique	V filter	R filter
Lomb-Scargle	4.8883 ± 0.0307	$\mathbf{3.4336 \pm 0.0120}$
	4.6645 ± 0.0280	4.0256 ± 0.0207
	$\mathbf{4.0349 \pm 0.0209}$	2.9933 ± 0.0114
	$\mathbf{4.8806 \pm 0.0307}$	4.8641 ± 0.0362
PDM	4.5386 ± 0.0331	4.0207 ± 0.0259
	3.8812 ± 0.0291	3.4307 ± 0.0157
	3.8741 ± 0.0362	2.9893 ± 0.0119
	3.3267 ± 0.0267	2.9539 ± 0.0117

We found three single-peaked periods that fit our nightly mean-subtracted data well in both filters: 3.43 $\pm$ 0.01, 4.03 $\pm$ 0.02, and 4.88 $\pm$ 0.03 hours, at 99.1%, 98.3% and 95.0% R filter confidence levels, respectively. The 4.03 hour period has single-day aliases at 3.45 and 4.84 hours (very close to the other two good period fits), whereas the 3.43 hour period aliases are $\sim$ 3.00 and 4.01 hours, the 4.88 hour period are $\sim$ 4.06 and 6.13 hours. Therefore, taking into account the appearance of both single-day aliases as good fits to the data in both filters, we considered the single-peaked 4.03 hour rotation period the most likely of the three prominent solutions for 1995 SM_{55}. It is also possible that the true rotation period of 1995 SM_{55} is in fact double-peaked at $\sim$ 8.07 hours since the timing of the observations were such that 8.07 hours phased identically to 4.03 hours. This finding is consistent with the Sheppard & Jewitt (2003) results. Figures 6.4-6.6 show the nightly mean-subtracted magnitudes in both filters phased to the three prominent periods,

demonstrating the goodness of fit without the nightly offset, and Figure 6.7 shows the data phased to the 4.03 hour period without the nightly offset.

The phased lightcurves gave low and possibly variable amplitudes consistent with the Sheppard & Jewitt (2003) findings. In the V filter data, one night (10/28/10 UT) was particularly variable. A sky composite shifted according to field stars' rates of motion showed no background contaminants close to the target on those nights, and contour plots of the target suggested no deviant pixel behavior within the target PSF. Therefore, we saw no reason to exclude any data from this night and considered this comparably large amplitude intrinsic to 1995 SM_{55}.

If the primary rotation period of 1995 SM_{55} exhibits a variable amplitude, it could have an excited rotation state. Sheppard & Jewitt (2003) argued against 1995 SM_{55} being in an excited state because the damping time for such phenomena in non-binary systems or bodies not recently involved in collisions is short (Burns & Safronov 1973). Harris (1994) derived an approximate expression for the wobble damping timescale for asteroids (τ, in Gyr) as:

$$\tau \sim \frac{T_h^3}{C^3 D} \quad , \tag{6.14}$$

where T_h is the rotation period in hours, C is a constant between 7 and 40 depending on the physical properties of the object, and D is the diameter in kilometers. Using Eq. 6.14, we estimated a damping timescale for 1995 SM_{55} of 4,000 - 800,000 years, suggesting that 1995 SM_{55} is rotating too fast for it to be tumbling unless the collision that caused the Haumea family occurred within the past $\lesssim 800,000$ years. The age of the Haumea family is the subject of much debate and has not yet been determined. Ragozzine & Brown (2007) found through dynamical simulations that the collision that disrupted proto-Haumea must have occurred at least a billion years ago for the fragments to have dissipated to their current orbits. However, Rabinowitz et al. (2008) found that in order for the crystalline water ice bands presently observed on Haumea family surfaces to remain intact under long-term

irradiation that breaks crystalline bonds, the collision must have occurred within the last 100 Myr. If 1995 SM_{55} is indeed in non-principal axis rotation, then it would be consistent with a family formation time much more recent than the scales mentioned in previous studies. Given the low collision rate estimates for the Trans-Neptunian belt, we conclude that it is highly unlikely that 1995 SM_{55} is tumbling (Durda & Stern 2000).

Excluding the anomalously low datapoint in the V filter data from 10/28/10 UT, we calculated the physical dimensions of 1995 SM_{55} from its primary lightcurve amplitude of 0.08 magnitudes in both the V and R bands. Using Eq. 6.2, we calculated a projected axis ratio of $a : b \sim 1.08$, indicating an only slightly non-spherical object. Using the lower limit on the albedo of 1995 SM_{55} from Stansberry et al. (2011), a maximum absolute magnitude of $H_{max} = H + (0.5\Delta m) = 4.8 + 0.04 = 4.95$ (the H value coming from the JPL Horizons small body browser), and Eq. 6.3, we then calculated the diameter corresponding to the lightcurve minima of only the primary to be $\sim$ 230 km. Multiplying this dimension by $a : b$, we find dimensions for 1995 SM_{55} of 230×247 km perpendicular to its spin axis and assuming it was viewed equatorially.

We also calculated the minimum density (such that the object does not spin apart, based on its rotation period) using Eq. 6.11 and the 4.0349 hour period. We found a minimum density of 670 kg/m^3, which is consistent with an icy object (water ice having a density of $\sim$ 1000 kg/m^3) with some degree of porosity, an extremely porous rocky body (rock having densities of $\sim$ 3000 kg/m^3), or a combination of both. A lower limit to the material strength, assuming it was nonzero, was also computed using Eq. 6.12, giving $S_{min} \sim 6 \times 10^6$ N/m^2, which is a couple of orders or magnitude less than pure ice (Davidsson 2001).

Because the change in viewing geometry was negligible, the multi-day brightness variation we saw can only be explained by a binary system. Either the system is asynchronous, with one component rotating at a period of 4.03 or 8.07 hours and the other rotating on a multi-day period, or we viewed an eclipsing event. To investigate the multi-day period, we subtracted the 4.03 hour period and ran the residuals through Lomb-Scargle analysis. We note, however, that because of the significant multi-day offset and

the small range of solar phase angles ($0.29 < \alpha < 0.35$), we were not able to meaningfully constrain the phase coefficient to properly remove artificial brightening due to a change in viewing geometry. We estimated that contribution of the phase angle brightening should be negligible because neutral TNOs tend to have relatively flat phase curves ($\beta \sim 0.1$), meaning that the phase angle brightening $\beta(\Delta\alpha)$ should be ~ 0.006 magnitudes, which is about half of the mean error of the dataset (Rabinowitz et al. 2007). Figure 6.8 shows the R filter residuals as a function of mean Julian date, highlighting the significant variation on the order of days. Figure 6.9 gives the periodogram investigating multi-day periods.

Figure 6.7 shows that several periods are significant to $> 99\%$ confidence, giving an ambiguous solution to the multi-day periodicity. Imaging more than one rotation epoch is necessary to confirm periodicity and break the degeneracy between neighboring rotation periods. However, long rotation periods lend themselves to poor phase and epoch coverage in ground-based observations, yielding several viable brightness patterns, as seen in our results. Therefore, we were not able to unambiguously determine the multi-day rotation period for 1995 SM_{55}.

However, if we were observing a transit, then the radius ratio of the potentially binary system could be constrained via the multi-day amplitude and Eq. 6.6. The maximum offset between nights was 0.11 magnitudes (Fig. 6.8). Using this value, we computed a minimum radius ratio between the secondary and primary of $r_s/r_p \sim 0.33$. If we assume that the two components have the same density, then we can also calculate the mass ratio M_s/M_p since with identical densities, $M \propto r^3$ so that the minimum $M_s/M_p \sim 0.03$.

We also investigated the homogeneity of 1995 SM_{55}'s surface through changes in the measured $V - R$ colors. Figure 6.10 shows the $V - R$ color measurements phased to the 4.0349 hour rotation period, revealing one night (11/06/10 UT) where the data were significantly redder than other nights. Excluding this night, visual inspection of the phased color suggested that one half of 1995 SM_{55} (corresponding to $0.5 < \phi < 1.0$) has more neutral colors than the other. Our Monte Carlo simulations of a flat color distribution for data from all nights gave RMS values below that of the data's color measurements, but only

when including the 11/06/10 UT data (Fig. 6.11). Because the RMS of the full dataset lies well above any of the simulations from flat color curves, we find statistically significant color variation on 1995 SM_{55} on the order of days. Possible color variation excluding data from 11/06/10 is not statistically significant but is well-correlated in phase space. Higher signal-to-noise color measurements are needed to constrain this color variation within a night.

The redder color measurements on 11/06/10 UT are caused by a lower V band magnitude. Therefore, the red night may correspond to a configuration in which a companion travelled behind the primary, dropping the V magnitude, and if the secondary were dark and neutral, then it would not contribute significantly to R band flux, in which case the binary eclipse event would be more noticeable in the V band than the R band. This would suggest a dark, neutral secondary and red primary, with the primary possibly having a heterogeneous surface. If the multi-day variation were caused by a minimum in the secondary's lightcurve rather than an eclipsing event, then that would suggest a heterogeneous secondary. If the separate components have different colors, then it is unlikely that they formed from the same region, favoring the gravitational capture method (Goldreich et al. 2002).

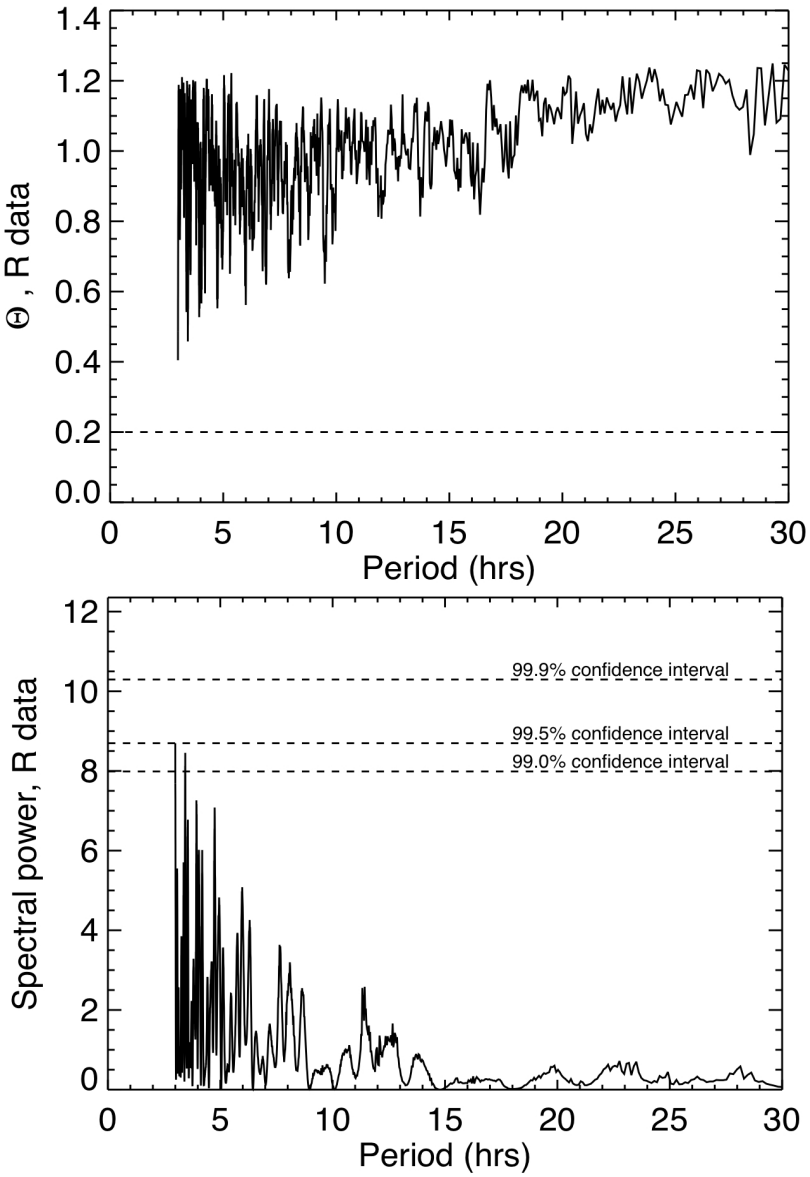

Figure 6.2 Periodograms for mean-subtracted R filter data on 1995 SM_{55}. The upper plot shows the Θ value from the PDM method as a function of rotational periods (solid line) and a dashed line to represent the fiducial value at which Θ becomes highly significant. The lower plot shows the Lomb-Scargle power spectrum as a function of rotation period (solid line) as well as dashed lines at the 99.9% and 99.0% confidence limits. A third dashed line shows the confidence limit corresponding to the maximum spectral power.

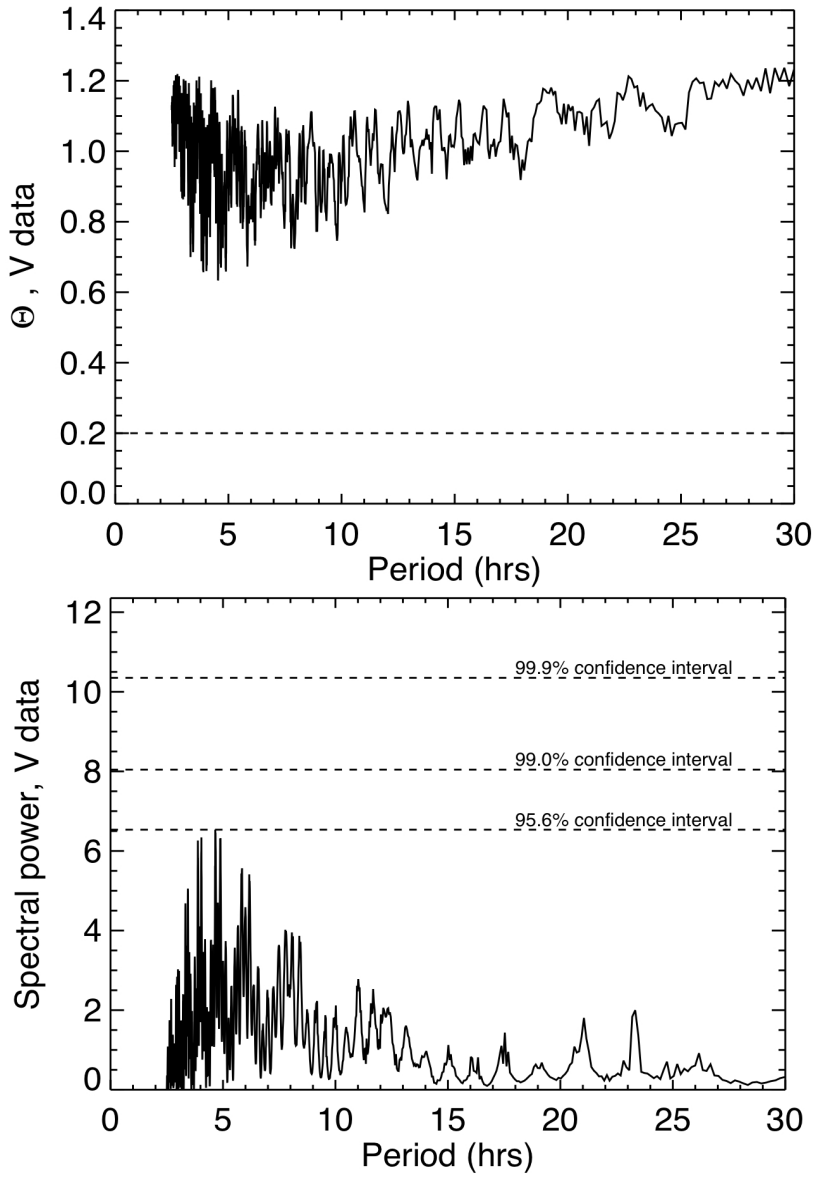

Figure 6.3 Periodograms for mean-subtracted V filter data on 1995 SM_{55}. The upper plot shows the Θ value from the PDM method as a function of rotational periods (solid line) and a dashed line to represent the fiducial value at which Θ becomes highly significant. The lower plot shows the Lomb-Scargle power spectrum as a function of rotation period (solid line) as well as dashed lines at the 99.9% and 99.0% confidence limits. A third dashed line shows the confidence limit corresponding to the maximum spectral power.

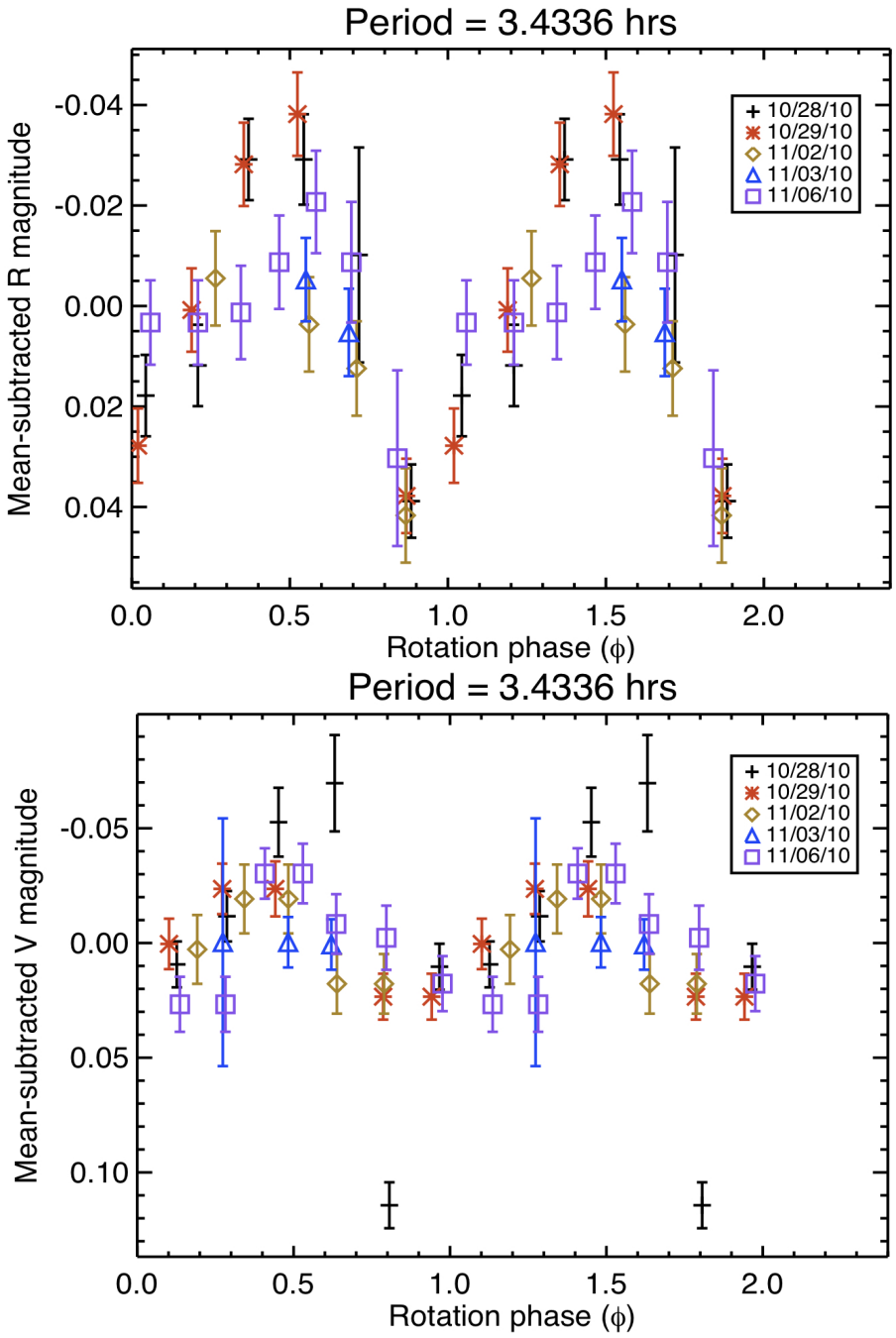

Figure 6.4 R and V filter 1995 SM_{55} data with the per-night mean subtracted phased to 3.4336 hours, which was shown as a prominent period in our analysis. This rotation period is a single-day alias of 4.03 hours, which we argue is the true period.

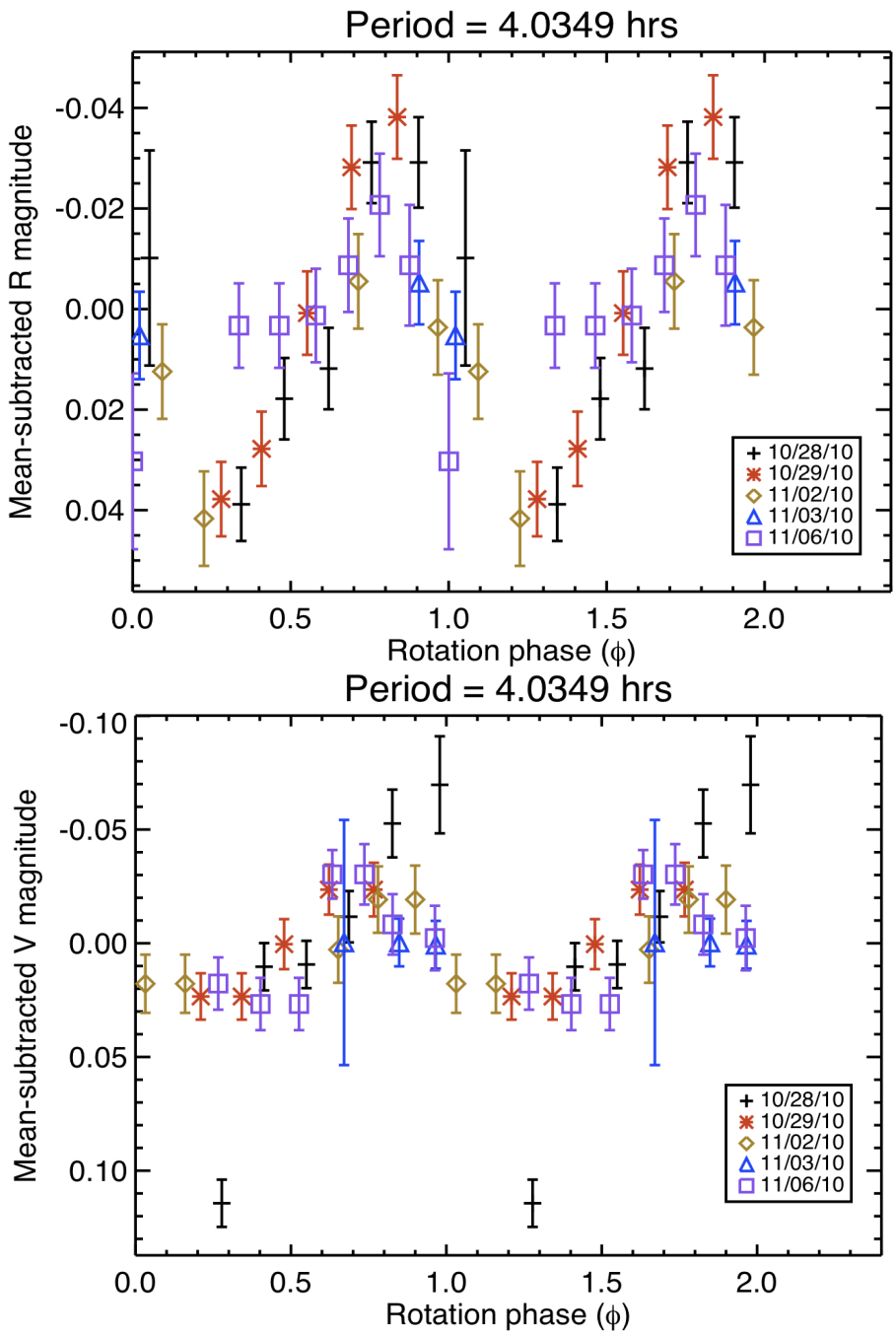

Figure 6.5 R and V filter 1995 SM_{55} data with the per-night mean subtracted phased to 4.0349 hours, which was shown as a prominent period in our analysis and is comparable to previously reported periods for this object (Sheppard & Jewitt 2003). The single-day aliases of this period also appear significant in the data.

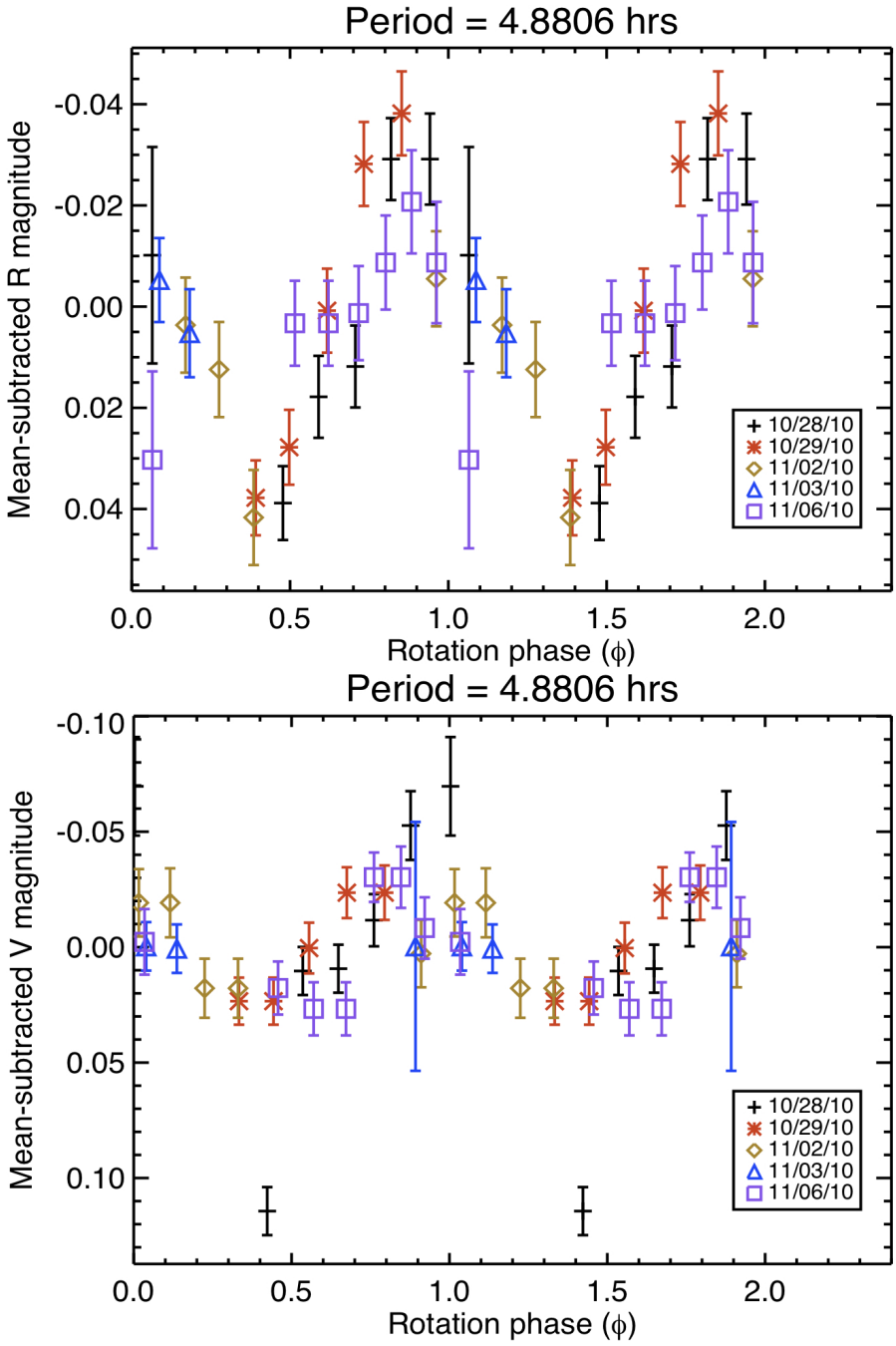

Figure 6.6 R and V filter 1995 SM_{55} data with the per-night mean subtracted phased to 4.8806 hours, which was shown as a prominent period in our analysis. This rotation period is a single-day alias of 4.03 hours, which we argued as the true period.

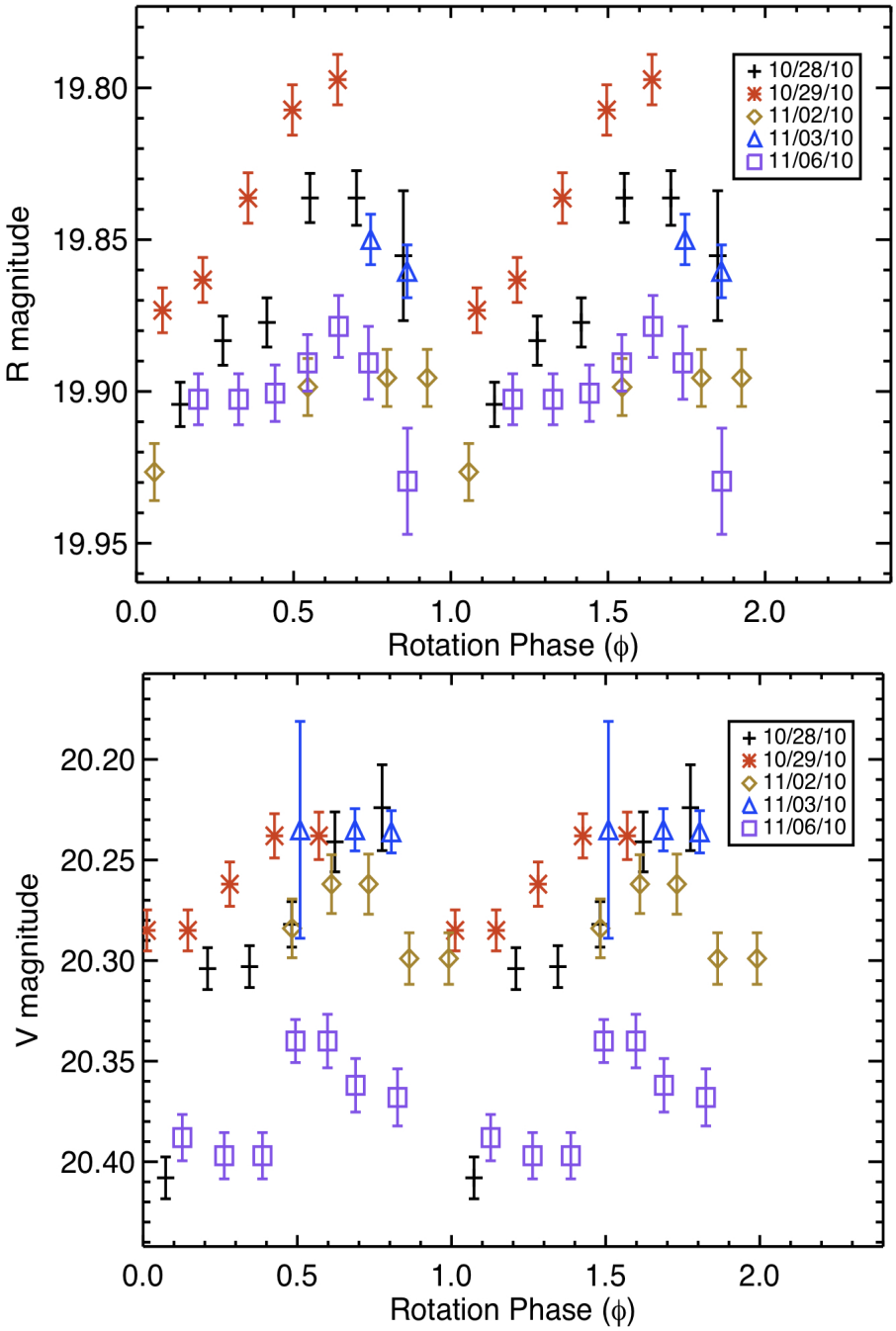

Figure 6.7 R and V filter data for 1995 SM_{55} phased to 4.0349 hours, which we argued was prominent period in our analysis.

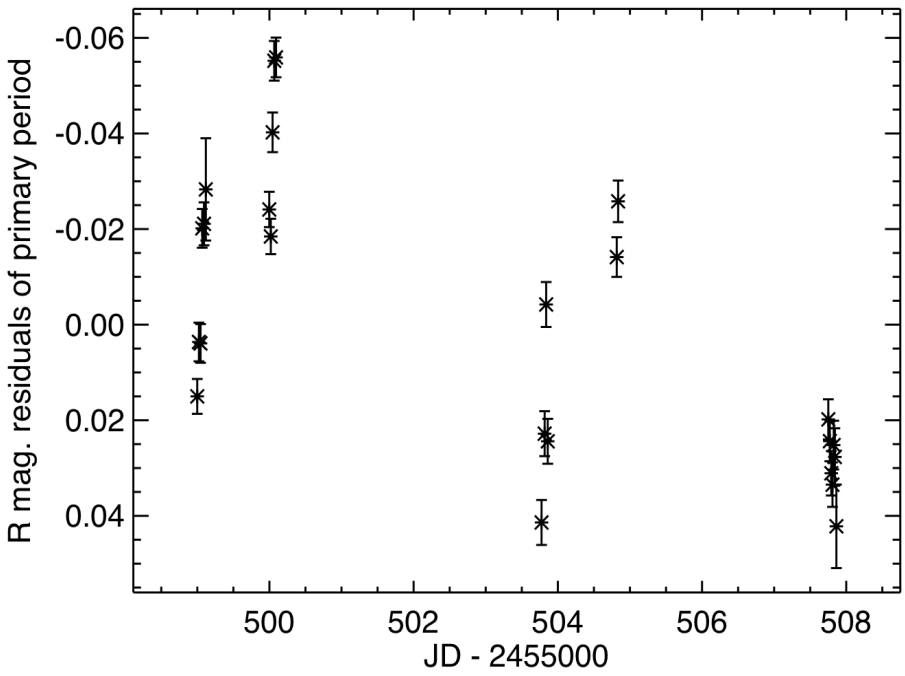

Figure 6.8 R and V filter data for 1995 SM_{55} phased to 4.0349 hours *without* the nightly mean subtracted, which we argued was the prominent period in our analysis.

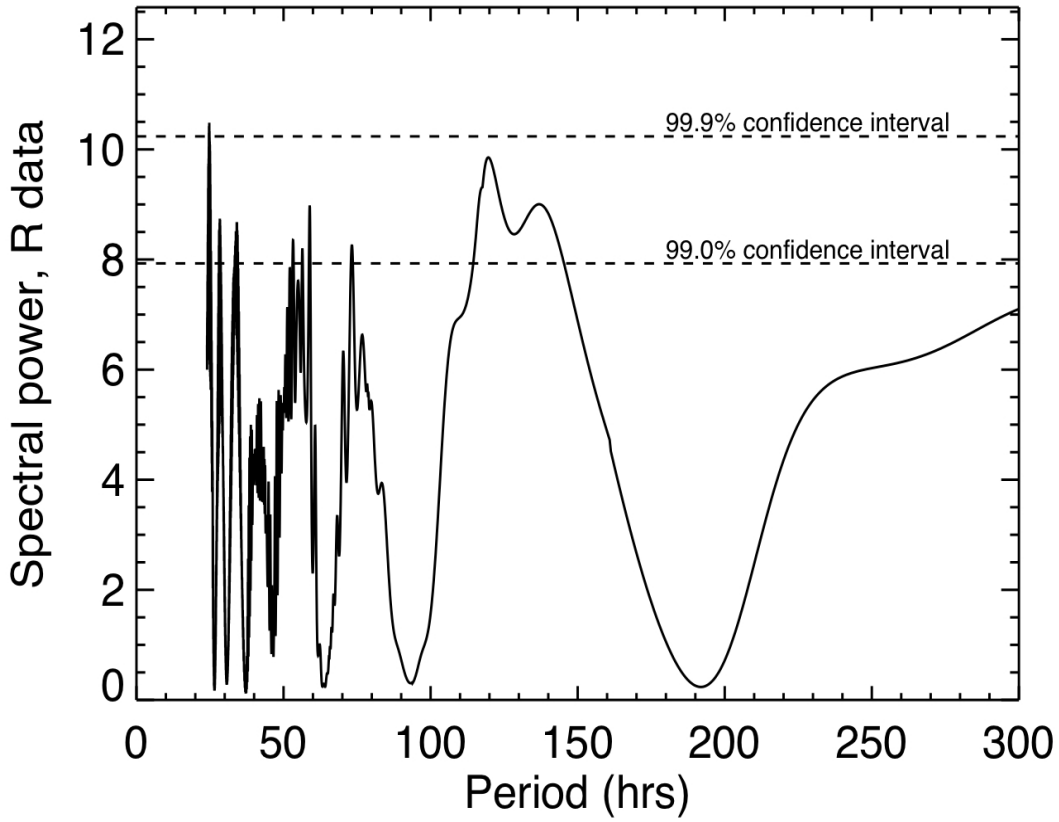

Figure 6.9 The Lomb-Scargle periodogram of the R-band residuals after the 4.03 hour period was subtracted. The plot shows an ambiguous solution giving several viable periods.

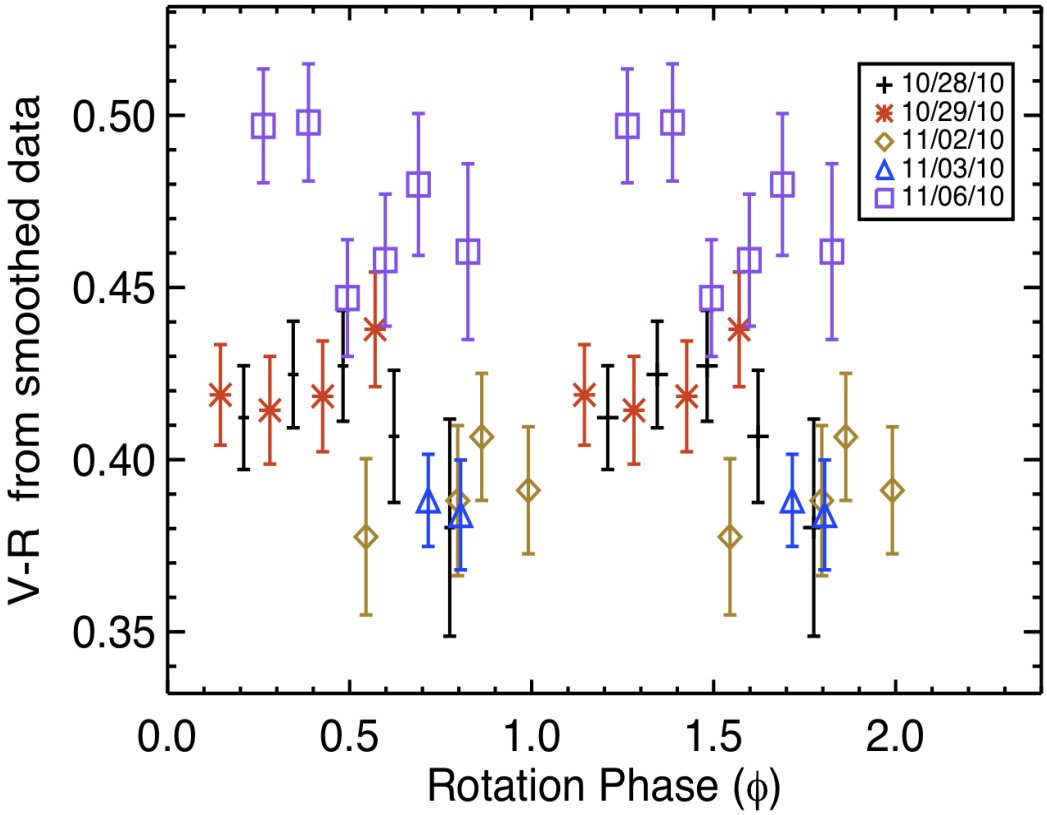

Figure 6.10 $V - R$ color phased to 4.0349 hours for 1995 SM_{55}. Data taken on 11/06/10 UT appear redder than other nights, and excluding this night, there may be correlated color variation, with data at phases $0.5 < \phi < 1.0$ being more neutral than the other half of the surface.

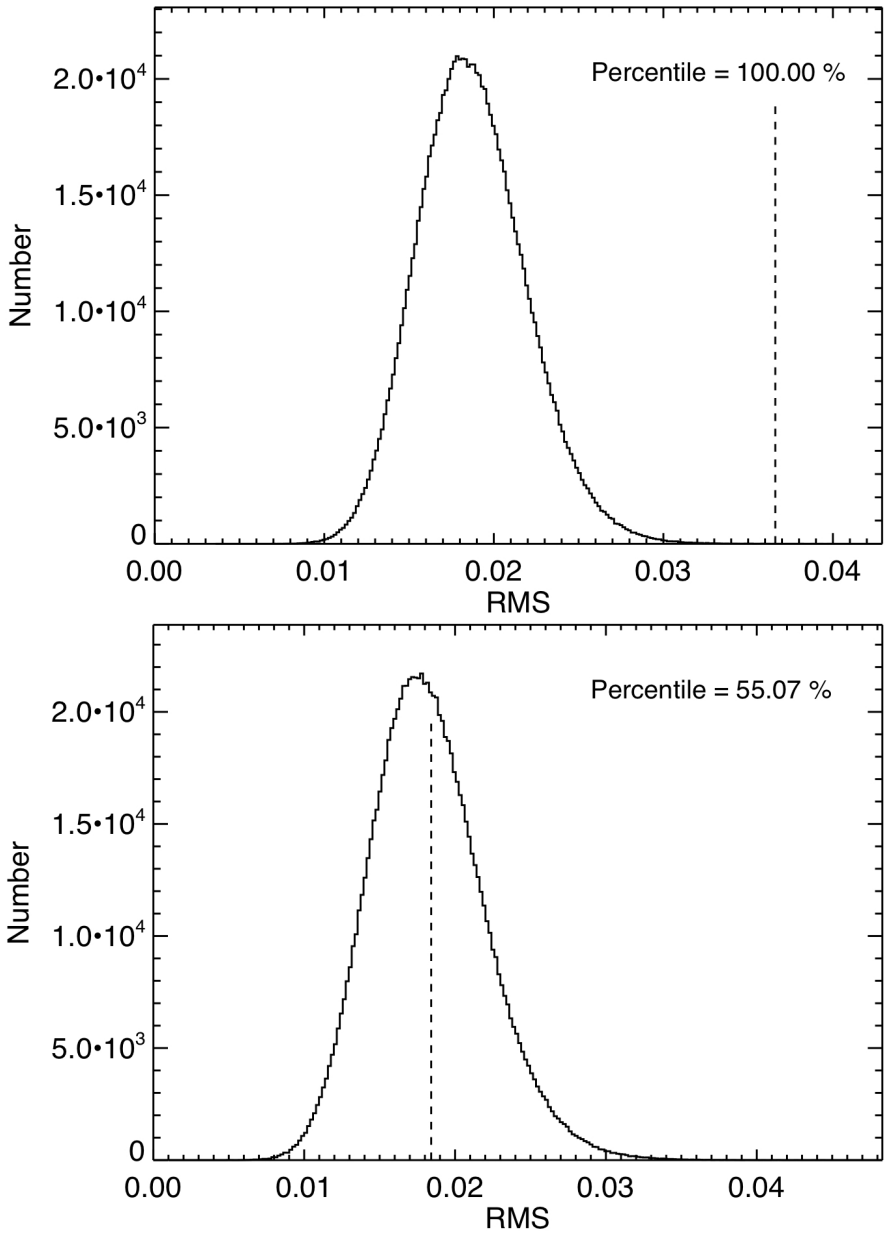

Figure 6.11 Distribution of RMS values for synthetic color curves (solid line) relative to the true RMS of the data (dashed lines). The upper plot shows this distribution including data from all nights while the lower plot excluded data from 11/06/10 UT. The comparison shows that the 1995 SM_{55} data exhibit statistically significant color variation only when including colors measured on 11/06/10 UT.

6.3.2 2000 YW_{134}

The TNO 2000 YW_{134} has been classified as a member of the scattered disk, a resonator, and a detached disk object, depending on the dynamical criteria for membership in each population (Sheppard 2010). The detached disk is a group of TNOs that are thought to have formed in the outer solar system then been dynamically excited into their present eccentric orbits long after the chaotic scattering event that led to the existence of the scattered disk. Emel'Yanenko & Kiseleva (2008) also found weak statistical evidence that 2000 YW_{134} is in 8:3 orbital resonance with Neptune. Therefore, 2000 YW_{134}'s rotation properties may be representative of several populations with different formation locations and dynamical histories.

Stephens & Noll (2006) discovered 2000 YW_{134} to be a binary through direct detection using the *Hubble Space Telescope* and observed a mutual separation of $0.06 \pm 0.01''$, or 1900 ± 300 km. At this angular separation, we were not able to resolve the two components with the University of Hawaii 2.2-meter Tek instrument (0.219 $''$/pixel). The mutual orbit of the 2000 YW_{134} system has not been constrained, so the separation at the time of our observations is unknown. Stephens & Noll (2006) also observed a magnitude difference of 1.3 between the two components in NICMOS's F160W filter, which roughly corresponds to the near-infrared H band. Using Eq. 6.4, we found that assuming the two components have the same $V - H$ and $R - H$ colors, then we should expect to see a magnitude difference of 0.3 between the magnitude of the combined system and the magnitude of only the primary when/if secondary passes behind the primary.

Sheppard & Jewitt (2003) observed 2000 YW_{134} over two nights in the R filter to determine its rotational lightcurve and found that data on one night suggested a ~ 5 hour brightness trend while data from another night was rotationally flat. We obtained 32 V band and 28 R band images on five nights spread over 13 months, with three of the nights being consecutive and thus containing common field stars for calibration. For objects closer to the Sun, the observing geometry may change significantly over this amount of time, meaning rotation data from the individual nights are not comparable. TNOs, however, have such

long orbital periods ($\sim$ 250 years) that their true anomaly changes negligibly within a year. We therefore saw no reason to exclude the 2000 YW_{134} data from the non-consecutive nights in the phased lightcurve. In the V band data, however, as with 1995 SM_{55}, all of the data phased well to the prominent periods apart from one night (03/03/11 UT), which displayed essentially the same brightness pattern but was significantly offset from the other nights. This offset is not attributed to an error in absolute calibration since this was one of the consecutive nights containing field stars observed to be the same magnitude on other nights when the object had brighter magnitudes. Thus, we considered there to be a secondary lightcurve pattern on the order of days that could be attributable to either an eclipsing binary or the superimposed lightcurve signature of a companion rotating with a multi-day spin period (an asynchronous binary). For the V band analysis, we excluded this night in order to investigate only the most prominent period for which we likely had multi-epoch coverage.

Because we were not able to densely sample the lightcurve within a night, we were unable to measure rotationally-averaged magnitudes at each solar phase angle sampled ($0.39 \leq \alpha \leq 1.28$; see Chapter 5). Therefore, although our solar phase curve contained significant scatter which rendered a poorly-constrained β coefficient, the β value measured is consistent with a flat curve ($\beta \sim 0$), which phased well with our results. Figures 6.12 and 6.13 give the PDM- and Lomb-Scargle-generated periodograms for R and V filters, respectively, and Table 6.3 shows the most prominent periods. Visual inspection of the lightcurves phased to the prominent periods yielded two very similar rotation periods that described the data well in both filters – 5.586 ± 0.003 and 5.562 ± 0.003 hours.

The error on these rotation periods are likely underestimated. The error should be roughly represented by the local width of the peak in the periodogram at the rotation period being considered. However, examining data spaced over a large time frame introduces substantial substructure within the local periodogram, which manifests as several small peaks within the broader peak. PERANSO will report only the width of the small peaks rather than the width of the larger peak, which means the final period error is

underestimated in these datasets with large temporal coverage. If the true error in the period is on the order of ~ 0.01 hours (a reasonable estimate after visually inspecting the periodograms), then the two prominent peaks are consistent with being the same. The ~ 4.5 hour rotation period's significance in our data could be explained by the fact that it is approximately a single-day alias of the ~ 5.56 hour rotation period. Figure 6.14 shows the V and R data phased to the 5.562 hour period and highlights the significant offset in the V filter on 03/03/11 UT.

Table 6.3 The four most prominent rotation periods (in hours) and their respective errors detected through each of the Lomb-Scargle and PDM techniques for 2000 YW_{134} data (excluding the 03/03/11 data in the V filter). Periods that visually phased well in both filters for all data are given in bold.

Detection Technique	V filter	R filter
Lomb-Scargle	4.6531 ± 0.0027	5.6098 ± 0.0027
	4.4419 ± 0.0024	5.5963 ± 0.0054
	5.7871 ± 0.0041	5.7118 ± 0.0028
	4.4638 ± 0.0025	6.2627 ± 0.0034
PDM	5.4972 ± 0.0037	$\mathbf{5.5855 \pm 0.0027}$
	4.4638 ± 0.0025	$\mathbf{5.5615 \pm 0.0027}$
	4.4419 ± 0.0024	5.4750 ± 0.0026
	4.4201 ± 0.0048	4.4775 ± 0.0034

The 2000 YW_{134} lightcurve amplitude excluding the V band data from 03/03/11 UT was $\Delta m \sim 0.21$ in V and $\Delta m \sim 0.23$ in R, so we used the average amplitude of 0.22 in computing the minimum axis ratio. The offset due to the possible companion was 0.26 magnitudes, which was consistent with predictions from direct observations (Stephens & Noll 2006). Using Eq. 6.2, we calculated a projected axis ratio of $a : b \sim 1.22$. Taking the H magnitude from Sheppard (2010) and adding $0.5\Delta m$ and the offset due to the possible companion (to isolate the minimum cross-section of just the primary), we also calculated a minimum diameter (corresponding to the projected b axis) of 568 km and giving physical $a : b$ dimensions of $\sim 695 \times 568$ km.

Using a rotation period of 5.5615 hours, we calculated the minimum density with Eq. 6.11 to be ~ 350 kg/m^3, which is roughly 1/3 the density of solid water ice. If material

strength (S) is present, this density value implies that 2000 YW_{134} would have to have $S > 2 \times 10^6$ N/m^2 in order to stay gravitationally bound while rotating at this period.

We attributed the significant offset in the V band data on 03/03/11 to an asynchronous or eclipsing binary. If we assume an eclipsing event was seen, we could constrain the radius ratio between the components. After applying Eq. 6.6, we found that the secondary must have a radius at least half that of the primary, and assuming the same density between the two components, a minimum mass ratio of $\sim 14\%$ of the primary. The offset from the possible eclipsing event we observed is consistent with the magnitude difference observed between the two components via direct detection, suggesting that the system is oriented edge-on (Stephens & Noll 2006).

The final property that we characterize for 2000 YW_{134} is the surface homogeneity through color variation. We found a median color and mean color error of $V - R = 0.63 \pm 0.04$, much redder than previously reported (the most neutral measured being $V - R = 0.39 \pm 0.02$; Doressoundiram et al. 2007), implying that 2000 YW_{134} has non-uniform surface colors. Figure 6.15 shows the phased $V - R$ color lightcurve. Visual inspection suggested correlated variation in the color over rotation phase. The RMS of our 2000 YW_{134} color measurements fell in the 99th percentile of a distribution of simulated flat $V - R$ measurements (Fig. 6.16), indicating that at some rotation phases, 2000 YW_{134} appears moderately red ($V - R \sim 0.55$) and at others it appears to be very red ($V - R \sim 0.73$). The color difference between the companion and the primary could not be constrained since the eclipsing event was only observed in the V filter, so no colors were measured during that time.

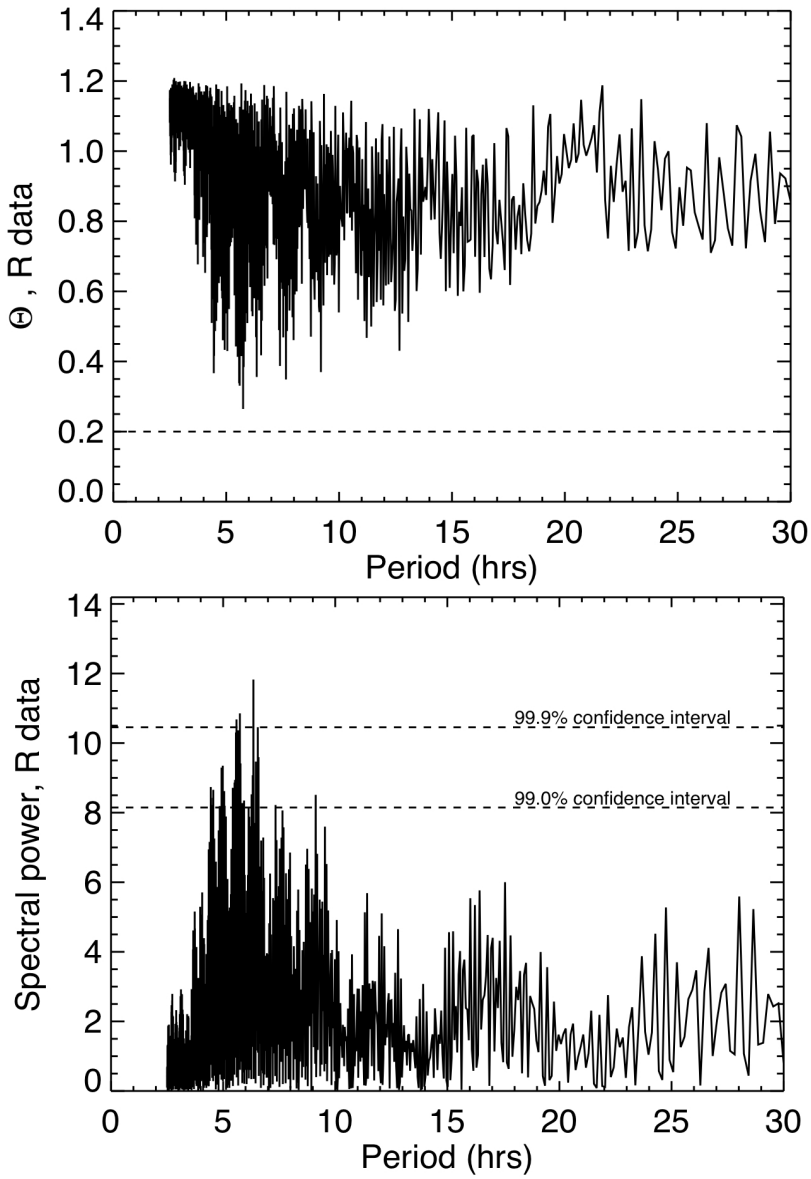

Figure 6.12 Periodograms for all R filter data on 2000 YW_{134}. The upper plot shows the Θ value from the PDM method as a function of rotational periods (solid line) and a dashed line to represent the fiducial value at which Θ becomes highly significant. The lower plot shows the Lomb-Scargle power spectrum as a function of rotation period (solid line) as well as dashed lines at the 99.9% and 99.0% confidence limits. Table 6.3 shows the prominent periods.

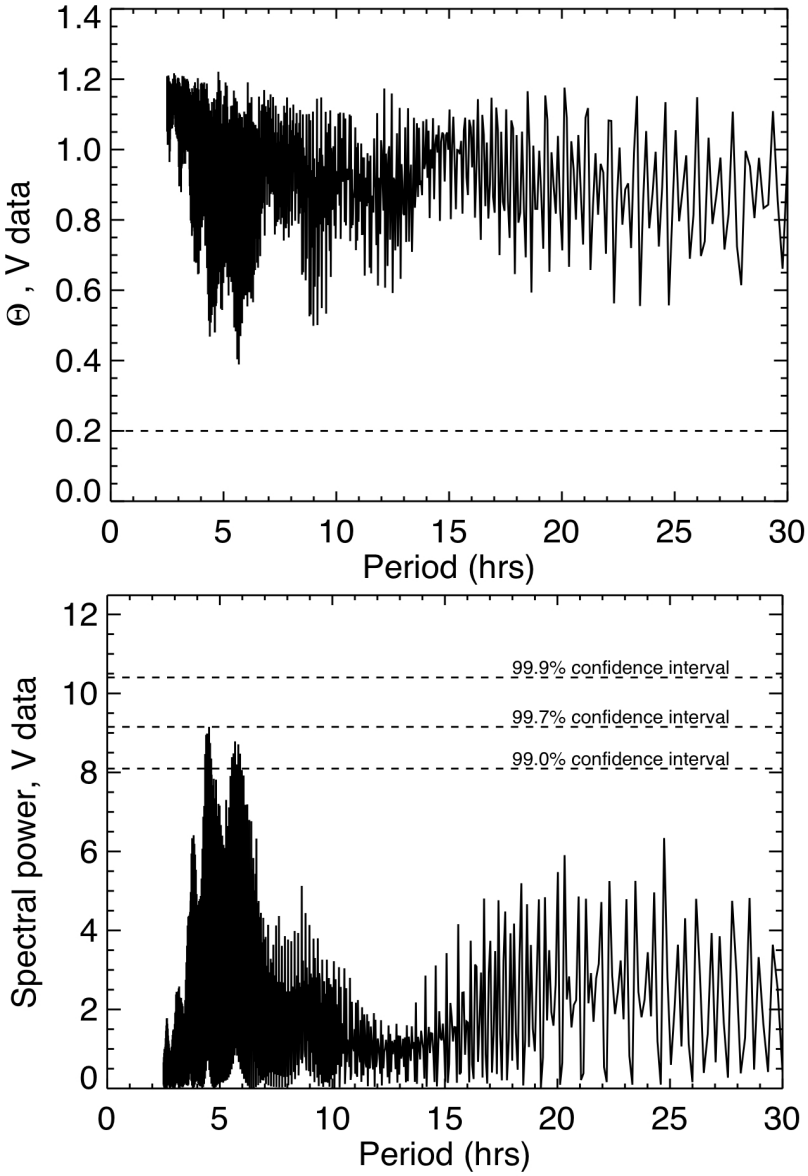

Figure 6.13 Periodograms for V filter data on 2000 YW_{134}, excluding data from 03/03/11 UT. The upper plot shows the Θ value from the PDM method as a function of rotational periods (solid line) and a dashed line to represent the fiducial value at which Θ becomes highly significant. The lower plot shows the Lomb-Scargle power spectrum as a function of rotation period (solid line) as well as dashed lines at the 99.9% and 99.0% confidence limits. A third dashed line shows the confidence level of the peak spectral power. Table 6.3 shows the prominent periods.

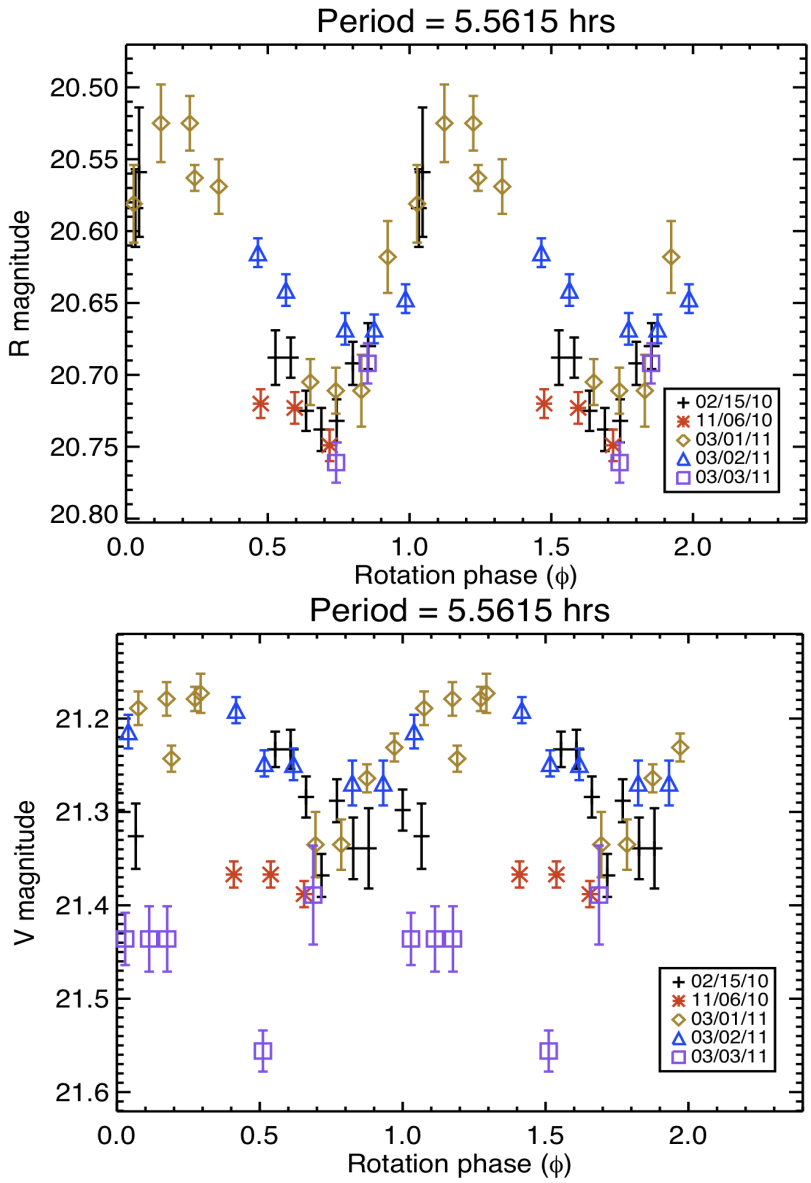

Figure 6.14 Lightcurves of 2000 YW_{134} phased to the rotation period 5.5615 hours for the R band (upper plot) and V band (lower plot). The V data taken on 03/03/11 UT show a significant offset compared to data from the other nights.

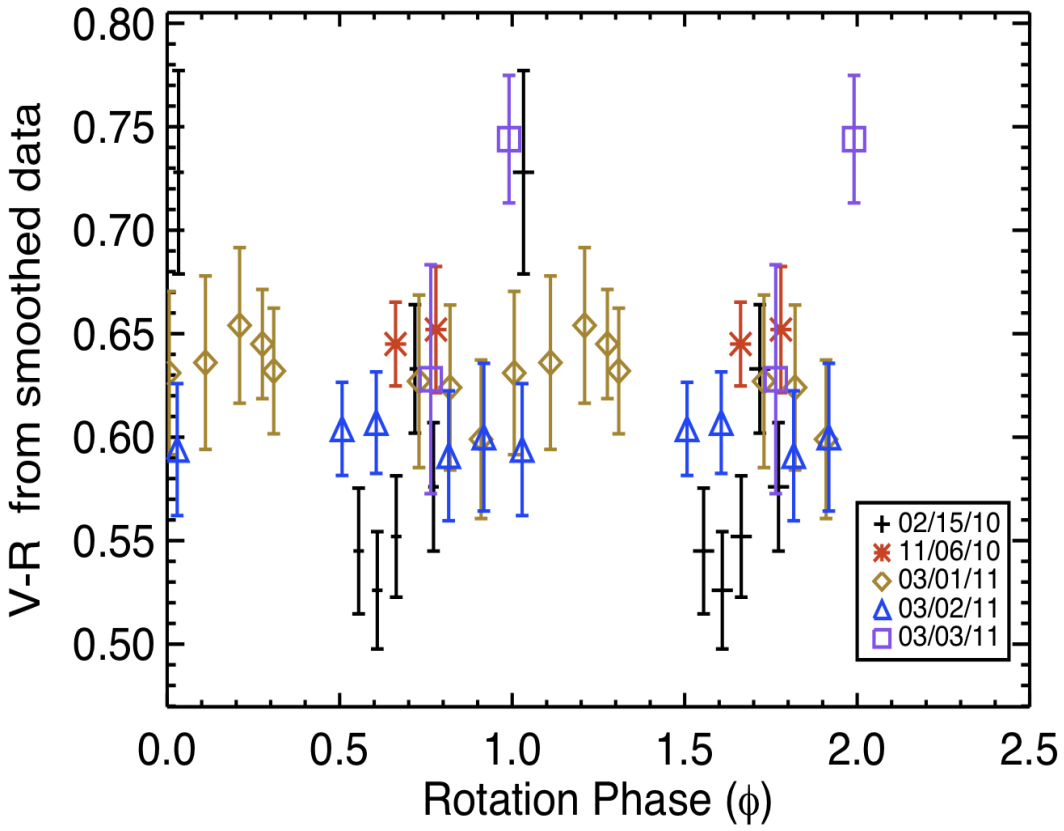

Figure 6.15 $V - R$ color of 2000 YW_{134} as a function of rotation phase for a rotation period of 5.5615 hours. Correlated variation is suggested in the 02/15/10 data, though it is not statistically significant compared to a distribution of simulated flat color curves.

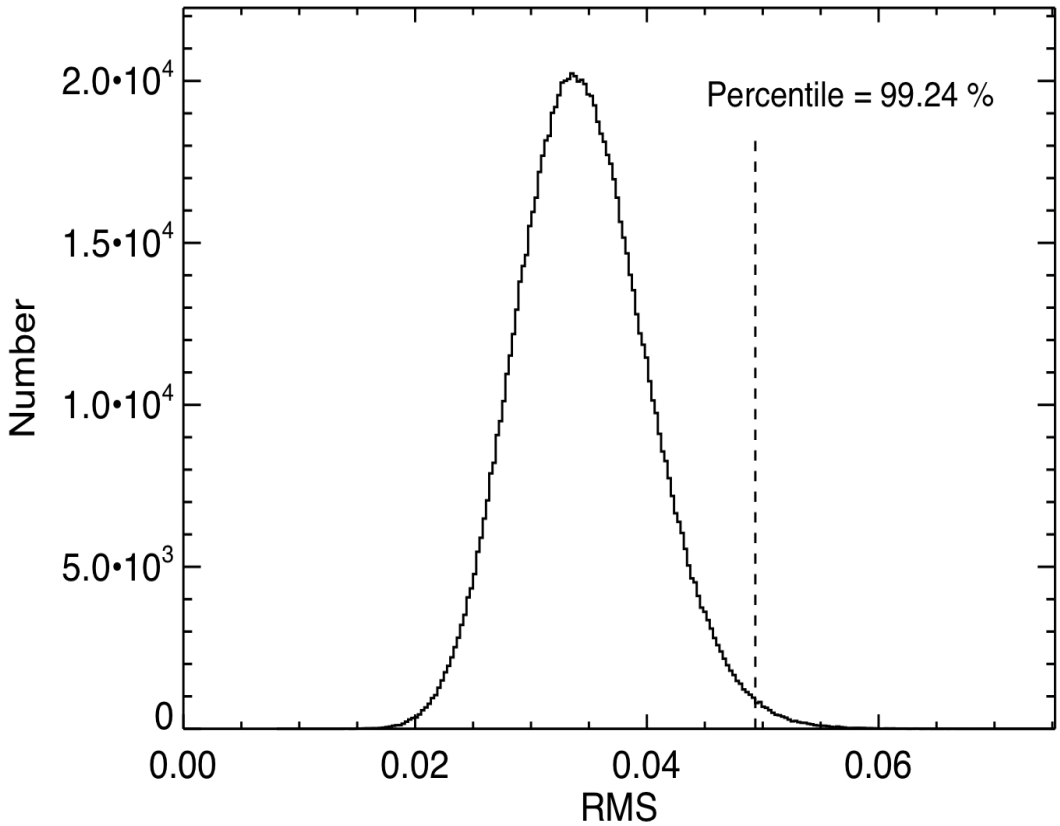

Figure 6.16 Distribution of the RMS of simulated flat $V-R$ datasets (solid line) comparable to 2000 YW_{134}. The dashed line represents the RMS of the 2000 YW_{134} data for all nights.

6.3.3 2001 QF_{298}

The plutino 2001 QF_{298} has been observed for rotation properties before by Sheppard & Jewitt (2003) and Lacerda & Luu (2006), who found variation less than 0.1 magnitudes but were not able to reliably determine the rotation period. Fornasier et al. (2004) took visual spectra of 2001 QF_{298}, detecting a weak absorption feature at $0.7 - 0.8\mu$m which has tentatively been attributed to aqueously altered material. Although this feature has not yet been confirmed through follow-up high signal-to-noise observations, if present, it would imply that 2001 QF_{298} experienced a heating event on its surface such as an impact. Better constraints on the rotation properties through our survey may help determine if this object is collisionally evolved, thereby hinting at the mechanism responsible for potential surface heating.

We observed 2001 QF_{298} on four consecutive nights (September 4-7, 2010 UT), then again on October 28 and 29, 2010 UT. However, the intrinsic faintness of 2001 QF_{298} meant that long exposures were needed to achieve adequate signal-to-noise to investigate color variation. Therefore, over these six nights, we only obtained 24 V filter and 24 R filter images. We removed artificial brightening due to a change in solar phase angle using the phase coefficient measured in Chapter 5. Figures 6.17 and 6.18 give the Lomb-Scargle and PDM periodograms, and Table 6.4 tabulates the prominent periods identified.

Table 6.4 The four most prominent rotation periods (in hours) and their respective errors detected through each of the Lomb-Scargle and PDM techniques for 2001 QF_{298} data.

Detection Technique	V filter	R filter
Lomb-Scargle	14.0684 ± 0445	20.7415 ± 0.0776
	5.4921 ± 0.0068	20.0841 ± 0.0727
	5.4451 ± 0.0133	20.3981 ± 0.0750
	13.7638 ± 0.0426	19.7796 ± 0.0706
PDM	7.5134 ± 0.0127	20.1023 ± 0.1275
	4.4985 ± 0.0091	19.1975 ± 0.0831
	4.4225 ± 0.0088	11.1099 ± 0.0334
	4.1503 ± 0.0232	11.0216 ± 0.0329

Some of the prominent periods in Table 6.4 are single-day aliases of each other. For example, the single day aliases of the ~ 5.5 hour period found in the V filter are 4.5 and 7.1 hours, the 4.5 hour period appearing in the PDM results for the V filter. Aliases of the $14 - hour$ period do not appear in the prominent V filter periods. In the R filter, on the other hand, the ~ 11.1 hour rotation period is an alias of the ~ 20 hour periods given in the R filter periodograms, leaving the R filter periodograms consistent with suggesting only one rotation period in the ~ 20 hour range.

Despite the prominence of the ~ 20 hour period in the R data, none of the periods gave believable lightcurves for all data in both filters. Rotation periods of ~ 20 hours phased best to both filters (rendering confidence levels of $> 99\%$ in the R band), but the scatter in the V band lightcurve phased to this period was still significant (Fig. 6.19). The ~ 11 hour periods that were prominent in the results are a single-day alias of the 20 hour period. Because of its significance in one filter and the prominence of its alias, our data therefore suggests a rotation period at ~ 20 hours, though we do not promote it as the final period solution since higher signal-to-noise observations over full nights are needed to fully investigate a rotation period of this length. Comparing the RMS of the V and R band magnitudes separately to flat lightcurves with the same errors (a process identical to our method of searching for color variation) shows that the data in both filters has statistically significant variation. Thus, brightness variation is assuredly present on 2001 QF_{298}, but it did not manifest a clear rotational pattern. For reference, the data phased to the 20.1023 hour period are given in Figure 6.19.

It is possible that shape is not responsible for the variation seen on 2001 QF_{298}. The scatter in the data may be attributed to tumbling of an elongated or irregularly shaped object. Using Eq. 6.14, for a primary rotation period of 20 hours, the damping timescale for a wobble is $\sim 1 - 250$ Myr. Therefore, if an impact occurred that significantly altered the rotation state, it likely occurred within the last couple hundred Myr. The variation seen in our data can also be attributed to albedo variations (since the observed brightness variation of $\Delta m = 0.23$ is within the range expected for surface variegation; Sheppard &

Jewitt 2004), which may appear as a speckled surface rendering a significant but complex rotation pattern.

In the event that future studies find this variation attributed to an elongated shape on 2001 QF_{298}, we calculated lower limits on the axial ratio and density. From a variation of $\Delta m = 0.23$ (the average of the maximum change in V and R brightnesses) and assuming equatorial viewing, the minimum axis ratio $a : b$ is 1.24 (Eq. 6.2). Using the Mommert et al. (2012) constraints on the diameter of 2001 QF_{298} and this axis ratio, we calculated physical dimensions of 454×367 km. The minimum density from a 20-hour rotation period is ~ 30 kg/m^3, and the corresponding minimum strength is 10^4 N/m^2. These values are not meaningful since they lie far below the range of reasonable bulk densities (~ 500 kg/m^3 for an icy body with 50% porosity up to ~ 3000 kg/m^3 for solid rock) and material strengths (bulk ice measured in laboratory studies has a $S \sim 2 \times 10^6$ N/m^2). Therefore, we were not able to meaningfully constrain the minimum density. Simulations of flat $V - R$ color curves showed significant variation in color (Fig. 6.20). This variation appears well-correlated when phased to the 20.1023 hour rotation period (Fig. 6.21), though as explained above the period itself is ambiguous.

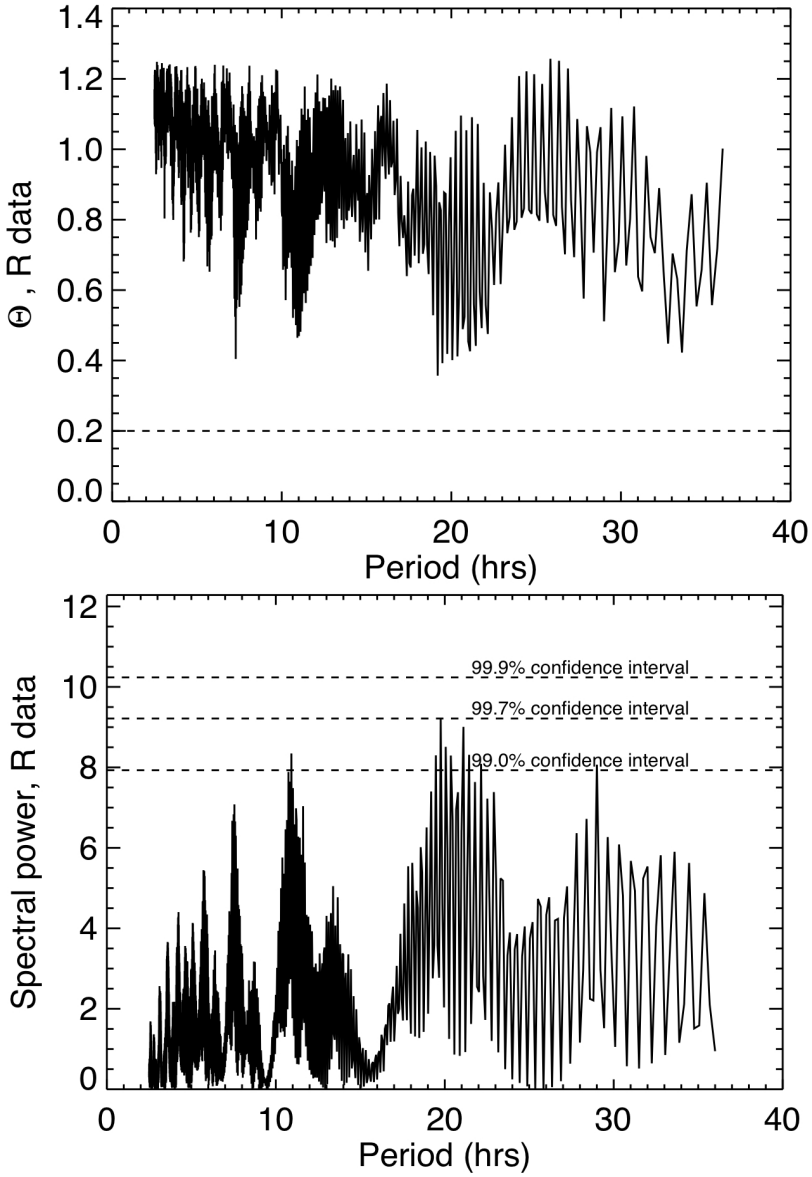

Figure 6.17 Periodograms for all R filter data on 2001 QF_{298}. The upper plot shows the Θ value from the PDM method as a function of rotational periods (solid line) and a dashed line to represent the fiducial value at which Θ becomes highly significant. The lower plot shows the Lomb-Scargle power spectrum as a function of rotation period (solid line) as well as dashed lines at the 99.9% and 99.0% confidence limits. A third dashed line shows the confidence level of the peak spectral power.

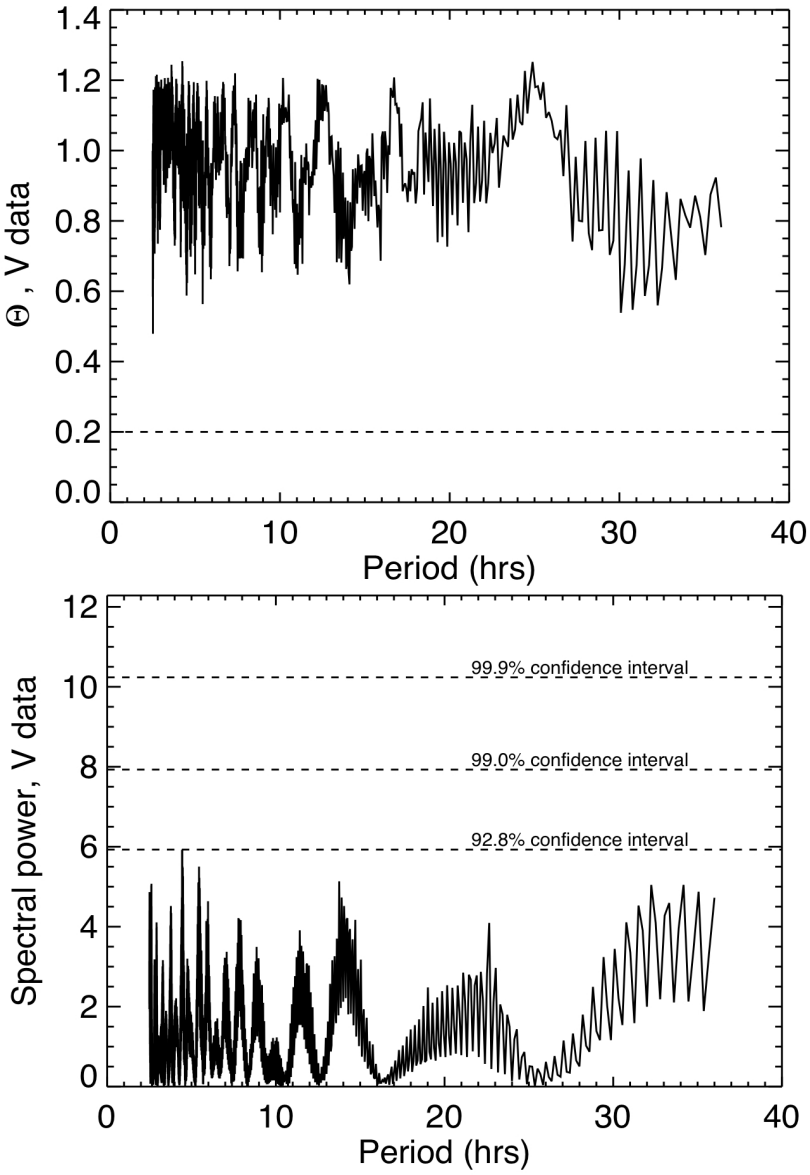

Figure 6.18 Periodograms for V filter data on 2001 QF_{298}. The upper plot shows the Θ value from the PDM method as a function of rotational periods (solid line) and a dashed line to represent the fiducial value at which Θ becomes highly significant. The lower plot shows the Lomb-Scargle power spectrum as a function of rotation period (solid line) as well as dashed lines at the 99.9% and 99.0% confidence limits. A third dashed line shows the confidence level of the peak spectral power.

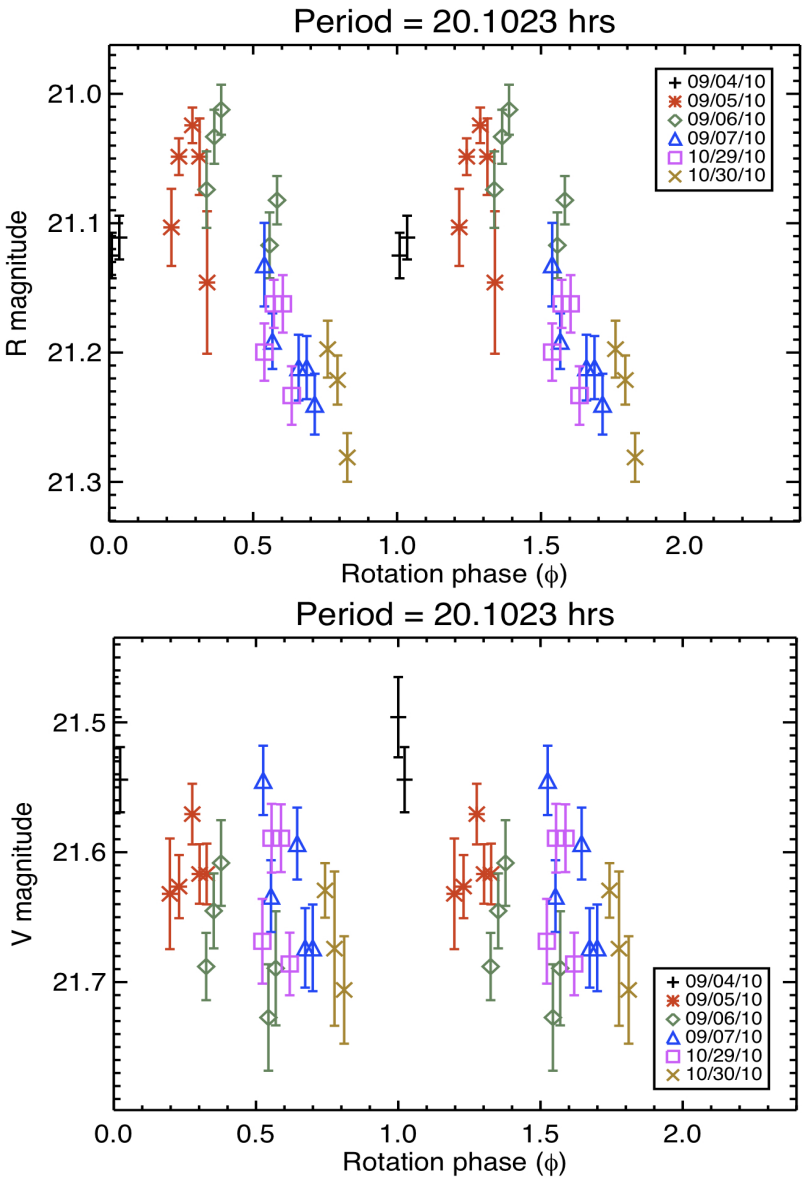

Figure 6.19 Lightcurves of 2001 QF_{298} phased to the rotation period 20.1023 hours for the R band (upper plot) and V band (lower plot).

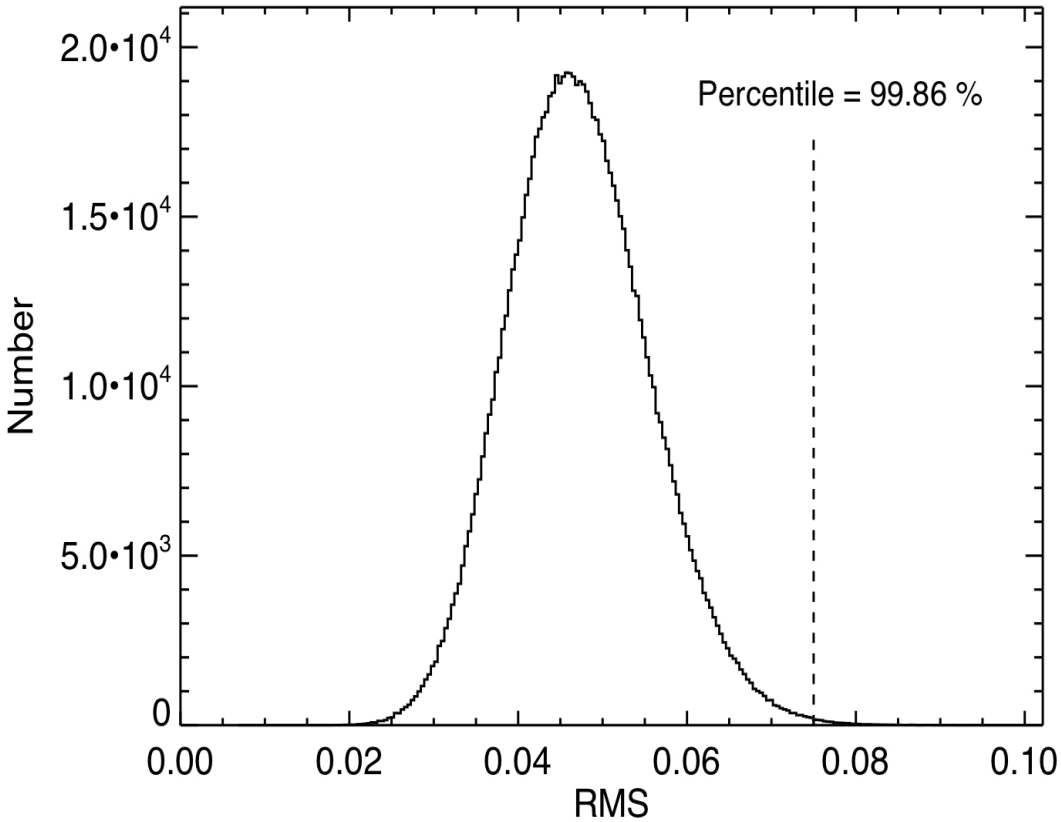

Figure 6.20 Distribution of the RMS of simulated flat $V-R$ datasets (solid line) comparable to 2001 QF_{298}. The dashed line represents the RMS of the 2001 QF_{298} data for all nights.

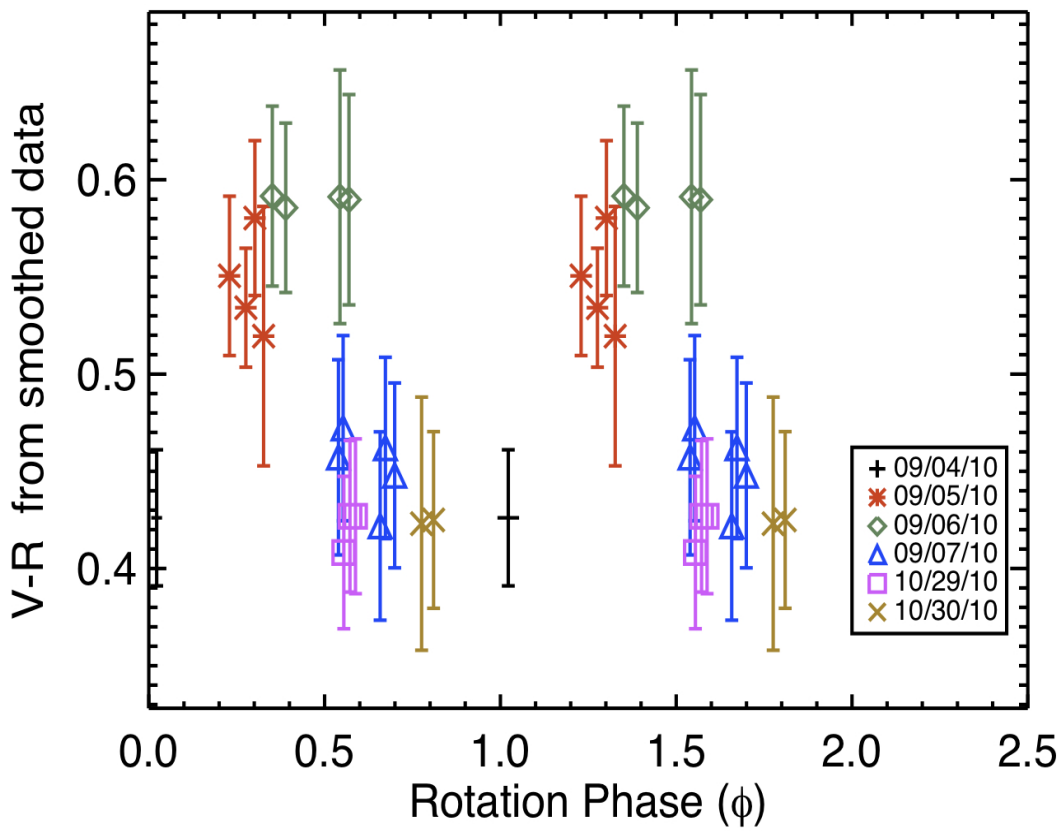

Figure 6.21 $V - R$ color as a function of rotation phase for 2001 QF_{298} phased to a rotation period of 20.1023 hours. Simulations show that this variation is significantly different, indicating heterogeneity. Correlated variation is suggested in the phased colors, but the rotation period itself is not well-determined, so the phasing could be wrong.

6.3.4 2002 TX_{300}

The classical TNO 2002 TX_{300} is the largest known member of the Haumea collisional family apart from Haumea itself. Because of its dynamical significance within the family, its surface properties have been explored in many previous studies. 2002 TX_{300} has one of the highest albedos measured for a solar system object at $p = 0.88^{+0.15}_{-0.06}$, corresponding to a diameter of 290 $\pm$10 km and suggesting a fresh surface (Elliot et al. 2010).

Sheppard & Jewitt (2003) observed 2002 TX_{300} in the R filter and found a rotation period of 8.12 ± 0.08 or 12.10 ± 0.08 hours (one being the true value and the other its alias), although the phased data showed significant scatter, rendering the solution uncertain. Ortiz et al. (2004) also observed 2002 TX_{300} in order to constrain its rotation period and found a single-peaked period of 7.89 ± 0.03 hours, although the phased lightcurve is very noisy. As part of a large-scale observing campaign, Thirouin et al. (2010) and Thirouin et al. (2012) found a rotation period of 8.15 hours (no reported period error), although again, the periodicity is buried in substantial noise, leaving the phasing unconvincing.

We observed 2002 TX_{300} over four consecutive nights (September 4-7, 2010 UT), obtaining a total of 56 V and 59 R filter images over all nights. We could not measure the phase function because the phase angle effectively did not change ($\Delta\alpha \sim 0.04°$) meaning the associated phase angle brightening should be negligible (< 0.005 magnitudes). Figures 6.22 and 6.23 show the resultant periodograms generated via PDM and Lomb-Scargle methods, and the prominent periods are given in Table 6.5.

The only rotation period that phased well to our data was 14.26 ± 0.07 hours (Fig. 6.24). This period, however, is slightly suspicious because it phases the data such that there is almost no overlap in phase space between nights, which would naturally render a low Θ value. Therefore, the 14.26 hour period may only be significant because it isolates the separate nights. This period is also inconsistent with all other period determined for 2002 TX_{300}, implying that perhaps 2002 TX_{300} is in a complex rotation state, with one rotation appearing more significant in one study while the configuration of the spin axes during another study instead highlights a different period. Although such a situation is

Table 6.5 The four most prominent rotation periods (in hours) and their respective errors detected through each of the Lomb-Scargle and PDM techniques for 2002 TX_{300} data. The only rotation period that phased well in both filters is shown in bold-type text.

Detection Technique	V filter	R filter
Lomb-Scargle	7.0574 ± 0.6527	14.3624 ± 0.1674
	7.0957 ± 0.6359	14.4314 ± 0.1463
	5.4570 ± 0.8127	$\mathbf{14.2601 \pm 0.0682}$
	7.1188 ± 0.7378	14.5245 ± 0.1239
PDM	7.0727 ± 1.3527	14.6122 ± 0.1987
	5.4525 ± 0.3162	9.0198 ± 0.1363
	5.4299 ± 0.3943	8.9724 ± 0.1396
	5.4164 ± 0.4254	8.9383 ± 0.1748

difficult to envision, we quantitatively explored the possibility of a wobble in 2002 TX_{300}'s rotation state. Assuming the 14.26 hour period is correct and using Eq. 6.14 and the diameter calculated from Elliot et al. (2010), we found that the maximum damping time for wobbles for this object is $\sim$ 30 Myr, which is consistent with the Haumea family being young.

Assuming that 2002 TX_{300}'s brightness variation is caused by an elongated shape, our observed amplitude of $\Delta m = 0.15$ would correspond to a minimum axis ratio of $\sim$ 1.15. If the diameter of 290 $\pm$10 km calculated from the Elliot et al. (2010) occultation event is considered the average projected diameter of the ellipsoid, then limiting dimensions of 2002 TX_{300} are 270 $\times$ 311 km. The minimum density and strength, assuming the 14.26 hour period is correct, are quite low (55 kg/m^3 and 40,000 N/m^2), meaning that again, our lower limits are essentially meaningless.

The $V - R$ colors measured for 2002 TX_{300} phased to the 14.26 hour period appear to show trending (Fig. 6.25). However, our simulations of a flat distribution of measured $V - R$ colors for 2002 TX_{300} show that the variation seen is not statistically significant, so we cannot conclude heterogeneity. More data at higher signal-to-noise are needed to investigate these potential albedo variations.

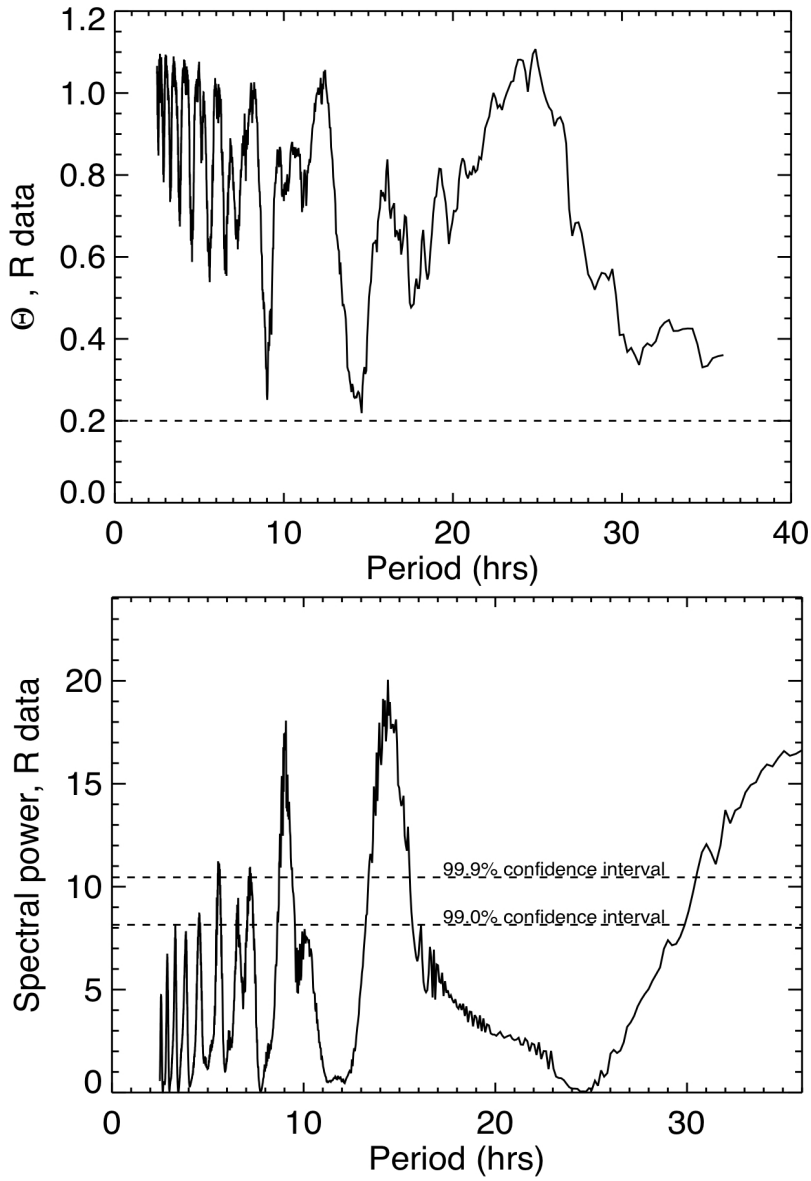

Figure 6.22 Periodograms for all R filter data on 2002 TX_{300}. The upper plot shows the Θ value from the PDM method as a function of rotational periods (solid line) and a dashed line to represent the fiducial value at which Θ becomes highly significant. The lower plot shows the Lomb-Scargle power spectrum as a function of rotation period (solid line) as well as dashed lines at the 99.9% and 99.0% confidence limits.

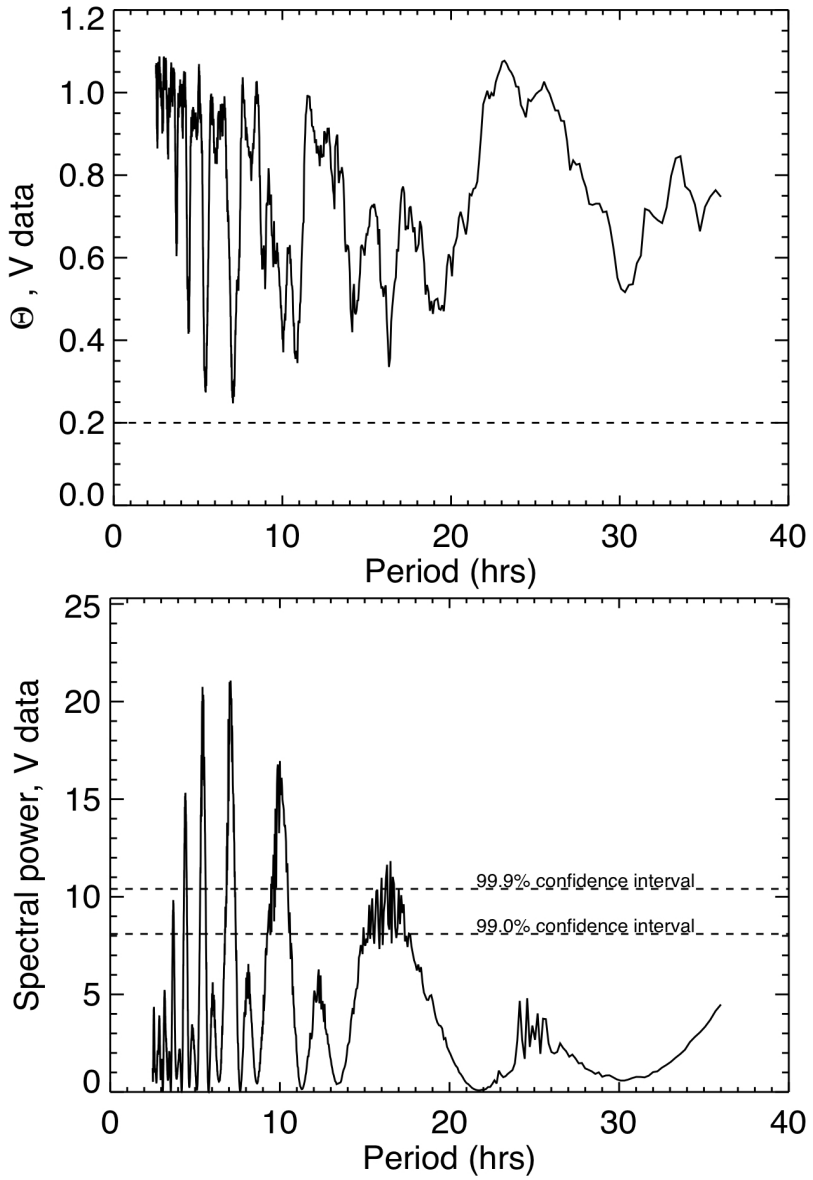

Figure 6.23 Periodograms for V filter data on 2002 TX_{300}. The upper plot shows the Θ value from the PDM method as a function of rotational periods (solid line) and a dashed line to represent the fiducial value at which Θ becomes highly significant. The lower plot shows the Lomb-Scargle power spectrum as a function of rotation period (solid line) as well as dashed lines at the 99.9% and 99.0% confidence limits.

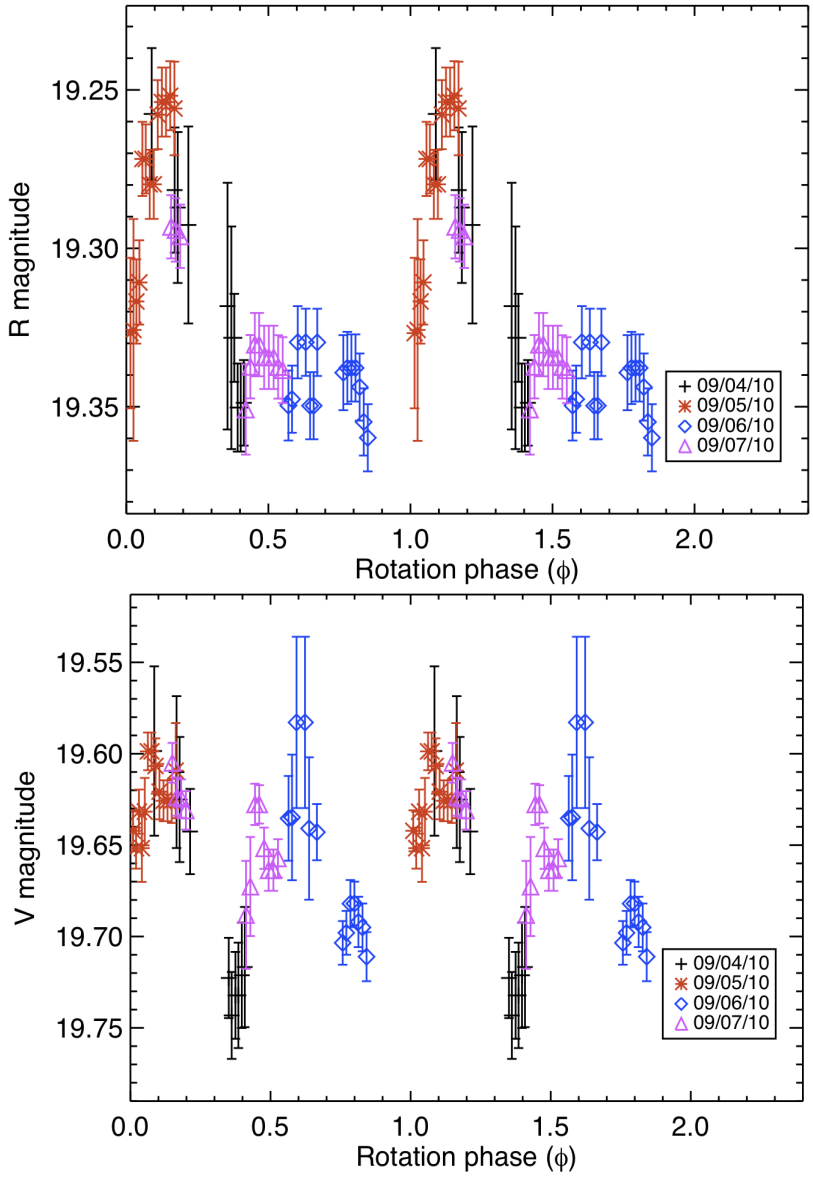

Figure 6.24 Lightcurves of 2002 TX_{300} phased to the 14.2601 hour rotation period for the R band (upper plot) and V band (lower plot).

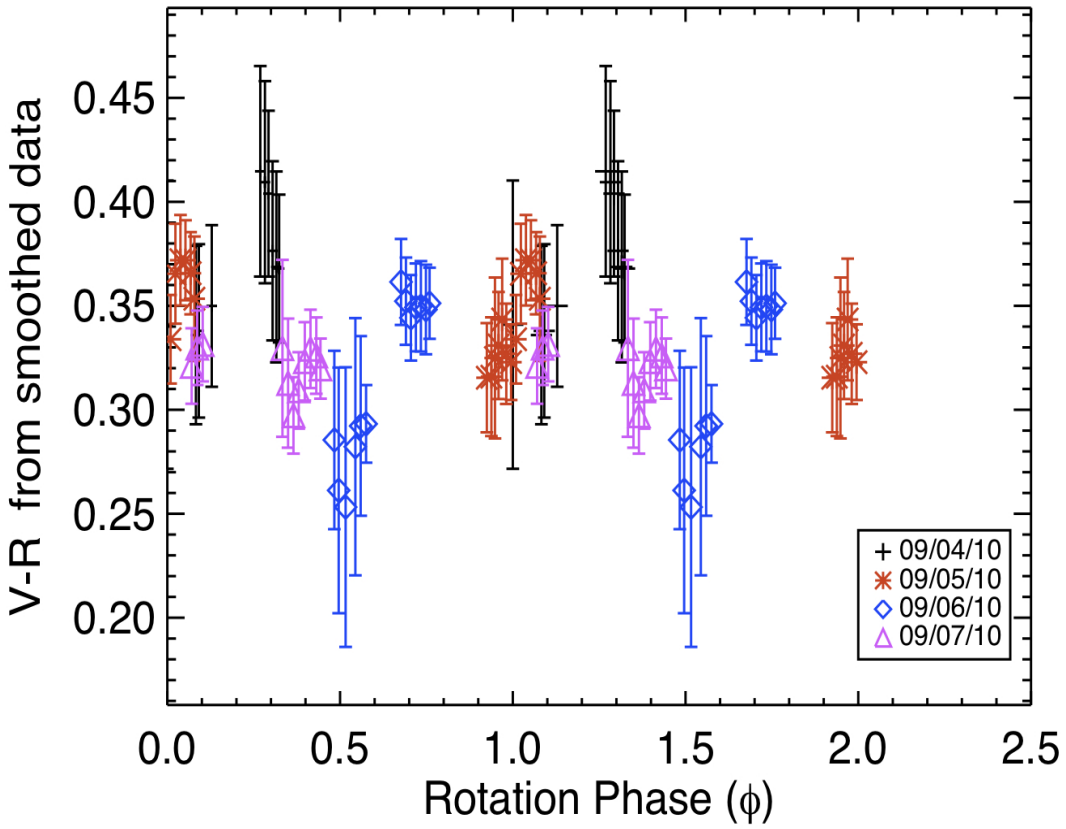

Figure 6.25 $V - R$ color of 2002 TX_{300} as a function of rotation phase for a rotation period of 14.2601 hours. Visual inspection suggests a color-rotation trend.

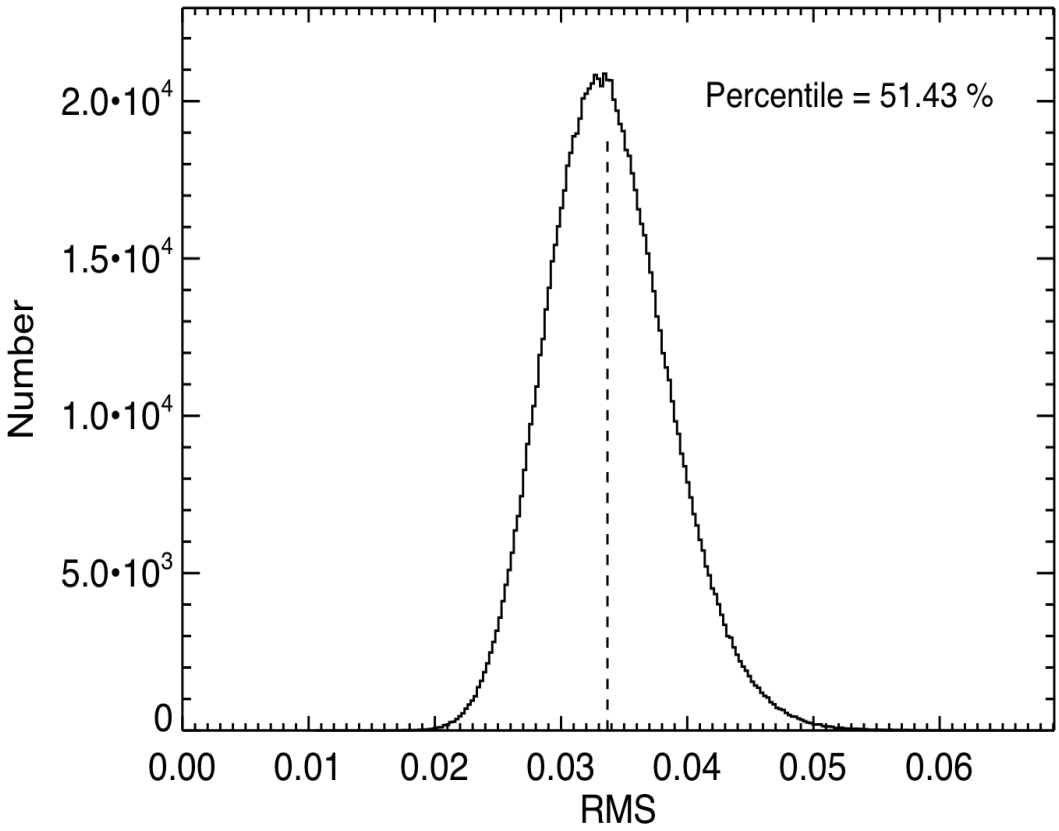

Figure 6.26 Distribution of the RMS of simulated flat $V-R$ datasets (solid line) comparable to 2002 TX_{300}. The dashed line represents the RMS of the 2002 TX_{300} data for all nights.

6.3.5 2002 XV_{93}

The plutino 2002 XV_{93} has never been investigated for rotation properties. We observed this object on two nights (12/02/10 and 12/04/10 UT). On each of these nights, we were only able to obtain a small number of useful images (17 per filter for both nights) due to high winds introducing significant jitter that rendered about half of the frames too trailed for accurate photometry. Consequently, we did not have enough data to get a good estimate of the rotation rate.

Manual adjustment of the data showed that the data phase well to a single-peaked period of $\sim$ 5 hours (Fig. 6.27), though a double-peaked period at 10 hours is equally possible. The minimum lightcurve amplitude of $\Delta m = 0.13$ in the R band corresponds to a minimum axis ratio of $a : b \sim 1.13$. Using the diameter estimates from Mommert et al. (2012) as the mean projected diameter, this axis ratio corresponds to minimum dimensions of $\sim 584 \times 517$ km. If the $\sim$ 5 hour period is real, then 2002 XV_{93} would require a density greater than ~ 500 kg/m^3 not to spin apart (Eq. 6.11). Also, if tensile strength is present on 2002 XV_{93}, it would have to be greater than $\sim 3 \times 10^6$ N/m^2 (Eq. 6.12).

We detected no significant lightcurve offset like that seen in 1995 SM_{55} and 2000 YW_{134}. Figure 6.28 shows the $V - R$ color phased to a 5 hour rotation period. Our simulations of flat color curves show that the variation is not significant (Fig. 6.29). More data at higher signal-to-noise are needed to determine 2002 XV_{93}'s lightcurve and investigate whether the night-to-night offset represents a secondary period consistent with a binary.

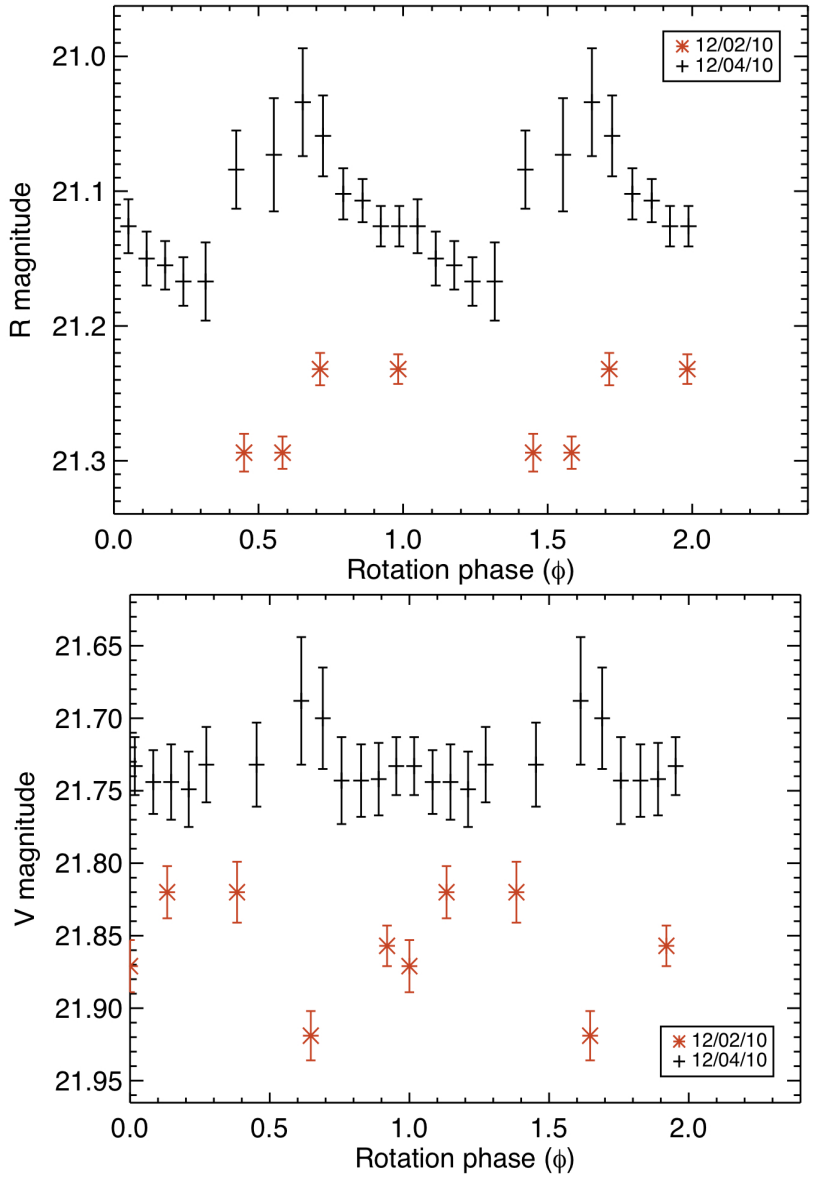

Figure 6.27 Lightcurves of 2002 XV_{93} phased to a 5.0 hour rotation period for the R band (upper plot) and V band (lower plot). This phasing was suggested from visual inspection, not from PDM or Lomb-Scargle analysis. The data were too few to reliably determine a rotation period for this object.

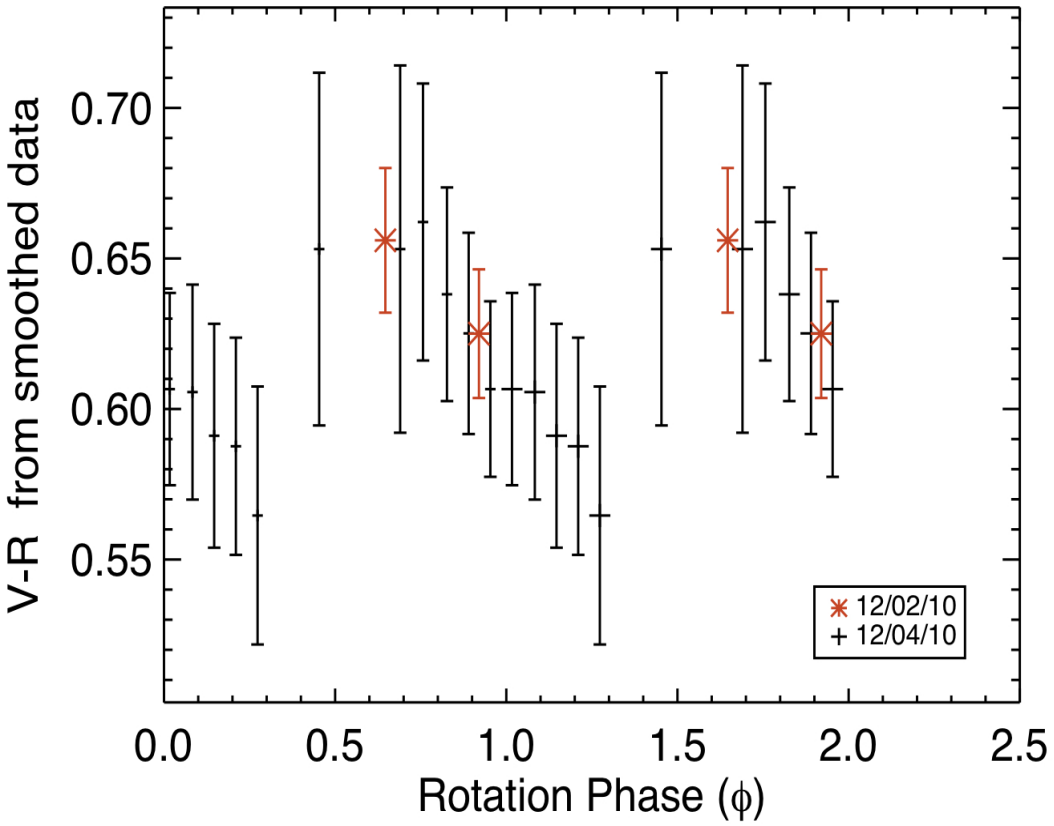

Figure 6.28 $V - R$ color as a function of rotation phase for 2002 XV_{93} phased to a rotation period of 5.0 hours. Visual inspection suggests a color-rotation trend.

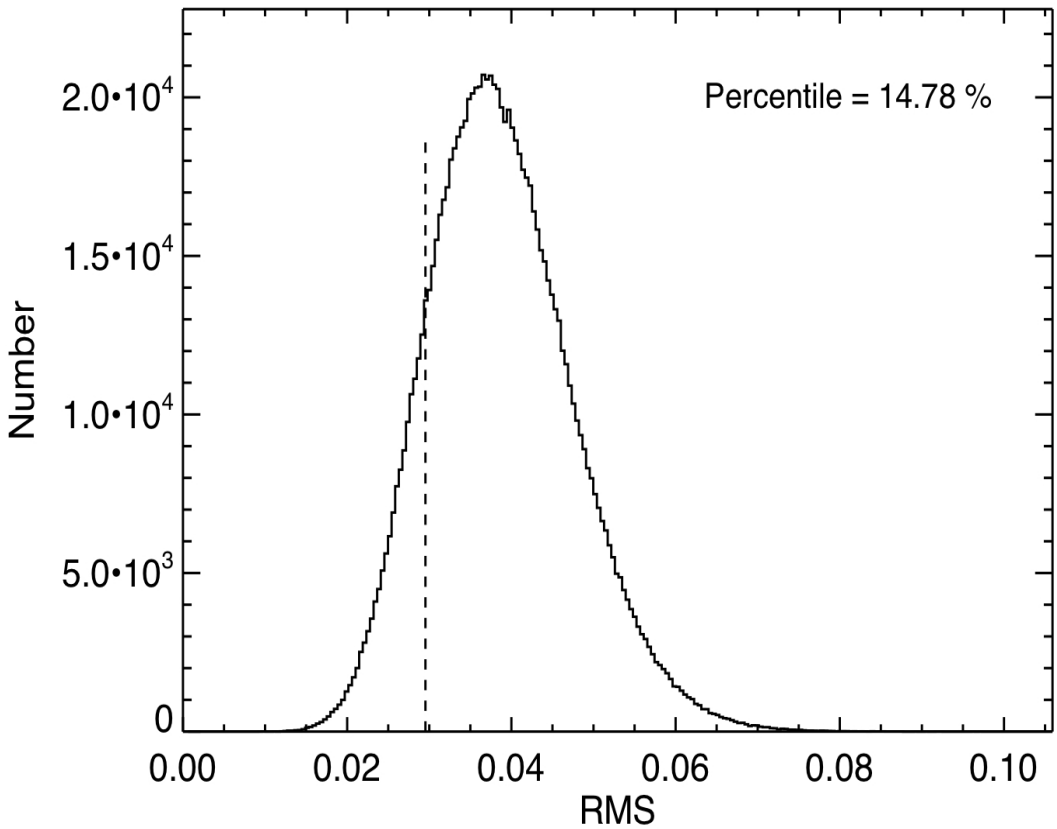

Figure 6.29 Distribution of the RMS of simulated flat $V-R$ datasets (solid line) comparable to 2002 XV_{93}. The dashed line represents the RMS of the 2002 XV_{93} data for all nights.

6.3.6 2003 AZ_{84}

Many independent groups have observed the plutino 2003 AZ_{84} to determine its rotation properties. Sheppard & Jewitt (2003) found a well-defined single-peaked 6.71 ± 0.05 hour or double-peaked 13.42 ± 0.1 hour rotation period. Ortiz et al. (2006) found an ambiguous solution of 5.28 ± 0.01 or 6.76 ± 0.01 hours with significant scatter about the phased lightcurves. Thirouin et al. (2010) determined a rotation period of 6.79 hours (no reported period error), though the phased lightcurve amplitude was on the order of the scatter about the lightcurve. Thus, while previous studies tend to favor a rotation period of ~ 6.8 hours, their solutions in most cases are dominated by noise. Brown & Suer (2007) discovered a companion to 2003 AZ_{84} 5.0 magnitudes fainter than the primary (a mass ratio of $\sim 0.1\%$) at a relatively large separation $0.22 \pm 0.01''$ using the F606W filter (roughly the V filter) onboard the *Hubble Space Telescope*'s High Resolution Camera. Assuming similar densities of the two objects, a binary system with this mass ratio observed as a transit would only produce an offset of 0.01 magnitudes, which is less than our mean error for this dataset of 0.02.

Size calculations from occultations and albedo measurements are inconclusive. Albedo measurements from the *Spitzer Space Telescope* and *Herschel Space Observatory* on three separate occasions rendered diameters of 533^{+25}_{-24}, 727^{+62}_{-66}, and 896 ± 55 km (Stansberry et al. 2008; Müller et al. 2010; Mommert et al. 2012). Size estimates from two occultation events also gave lower limits to 2003 AZ_{84}'s diameter of 573 ± 21 and 663 ± 50 km (Braga-Ribas et al. 2011; Braga Ribas et al. 2012). These diverse size calculations suggest that 2003 AZ_{84} is highly elongated and/or its companion is much larger and more massive than inferred from Brown & Suer (2007), thereby complicating the thermal lightcurve and producing a larger magnitude offset if eclipsing.

We observed 2003 AZ_{84} on six nights spread over two months in 2012 (February 16, 24, and 26-28, and April 18 UT), acquiring a total of 29 g' and 32 r' images in the full dataset. Sufficient data were acquired during the February 24-28 observing nights to constrain the rotation period, so to avoid severe aliasing problems presented by analyzing widely-spaced

data, we excluded the Feb 16 and April 18 runs from the period search. PDM and Lomb-Scargle periodograms fit to the February 24-28 2012 data are shown in Figures 6.30 and 6.31, with the most prominent periods conveyed in Table 6.6.

Table 6.6 The four most prominent rotation periods (in hours) and their respective errors detected through each of the Lomb-Scargle and PDM techniques for the 2003 AZ_{84} data used to calculate the periodograms. Periods that visually phased well in both filters for the full dataset are given in bold.

Detection Technique	g' filter	r' filter
Lomb-Scargle	$\mathbf{9.2575 \pm 0.1981}$	$\mathbf{11.3926 \pm 0.3256}$
	9.2356 ± 0.2118	$\mathbf{11.4118 \pm 0.3267}$
	$\mathbf{9.2796 \pm 0.2359}$	11.4600 ± 0.3779
	9.2137 ± 0.2326	11.3544 ± 0.3710
PDM	9.1855 ± 0.2615	11.3369 ± 0.3153
	7.7035 ± 0.1989	11.2062 ± 0.4869
	6.6891 ± 0.1499	7.7024 ± 0.1878
	6.6444 ± 0.1701	7.6790 ± 0.2100

Our results showed two viable periods for both filters: $\sim$ 9.3 and 11.4 hours. The 6.7 hour period found by previous works was also recovered in our analysis, though it was not as significant as other periods and increases the scatter about the phased lightcurve. Figure 6.32 shows our data phased to the $\sim$ 6.7 hour period while Figures 6.33 and 6.34 show the data phased to the $\sim$ 9.3 and 11.4 hour periods, demonstrating the reduction in scatter in the phased lightcurve at these longer periods. Our data fit both the 9.3 and 11.4 hour periods similarly well. The shorter-period single-day alias of a 9.3 hour rotation period is 6.7 hours, and the shorter single-day alias of 11.4 hours is 7.7 hours. Both of these periods and their aliases are statistically prominent, therefore we could not statistically discern between them.

Examining the $g' - r'$ color curve phased to these two periods (Fig. 6.35) offered additional clues as to the 2003 AZ_{84}'s true rotation period. The scatter in color was reduced by phasing to the 11.4 hour rotation period, although the errors on the color measurements are still too large to make this claim with significance. On the other hand, the prominence of its single-day alias in the previous work suggests that $\sim$ 9.3 hours is

the true rotation period. Therefore, because of the presence of both periods aliases and the lack of significant distinction in the color curve, we could not rule either out the $\sim$ 9.3 or $\sim$ 11.4 hour rotation period and thus found an ambiguous rotation solution. The longer of these two periods conveys minimum density and strength estimates of 85 kg/m^3 and $\sim$ 9000 N/m^2, respectively, so low that they are not meaningful constraints. Our simulations of a statistically flat color measurement distribution revealed no significant variation with rotation, suggesting no more than $\sim$ 15% color variation across the surface (Fig. 6.36). Higher signal-to-noise color measurements over the full rotation phase are needed to determine color variation.

An interesting feature of the 2003 AZ$_{84}$ lightcurve in either of the two possible rotation periods favored in this study is a slightly variable amplitude. At the 9.3 hour phasing, the data from 02/26/12 UT appear to dip below the peak and the 02/28/12 UT data (and one data point from 04/18/12 UT) are $\sim$ 0.1 magnitudes fainter than the general lightcurve shape. This effect is preserved in the 11.4 hour phasing.

As with 1995 SM$_{55}$ and 2000 YW$_{134}$, we investigated one of four possible explanations for this variable amplitude, the first being that 2003 AZ$_{84}$ is spinning on multiple axes (tumbling). Using the full range of diameter estimates given at the beginning of this section as well as both periods, we used Eq. 6.14 to calculate a maximum damping time for a wobble of $\sim$ 8000 years, which is very short on typical collisional timescales, so it is highly unlikely that 2003 AZ$_{84}$ is a tumbler. The fainter portions of the data may also correspond to a transit event of the primary eclipsing the secondary. However, at the secondary's large distance from the primary (0.22$''$, or several thousands of kilometers), the orbital period would be very long and a transit event would therefore be short and rare. We therefore reasoned that it is unlikely that we observed a transit given the properties of the binary observed by Brown & Suer (2007).

If 2003 AZ$_{84}$ were in fact a multiple system, then an additional, larger companion at a smaller mutual separation than the directly detected companion would have a higher transit probability and/or greater effect on the amplitude. There are several known multiples in

the Trans-Neptunian belt (*e.g.*, Pluto, Haumea, 1999 TC_{36}), but their frequency relative to two-component systems is not known. The presence of a third body on a tighter orbit in the 2003 AZ_{84} system may also explain the ambiguity in the diameter estimates, with the projected surface area near the center of mass depending on the system orientation and elongation of the separate components. Lastly, 2003 AZ_{84} could be an asynchronous binary with differing rotation periods of the components causing a variable observed amplitude for the system. The last two explanations were the most likely, and both use binarity (or multiplicity) to explain the offset/amplitude variation.

The multi-day offset observed is between 0.03 and 0.08 magnitudes depending upon the period to which the data is phased. If 2003 AZ_{84} were in fact a multiple system with another, closer component transiting the primary, then constraints can be set on the mass ratio between the two close components with a minimum mass ratio range of $\sim 0.5 - 2.0\%$.

We detected a lightcurve amplitude for 2003 AZ_{84} (excluding the data points that appear slightly fainter due to binarity) of $\Delta m = 0.12$ in both filters, corresponding to a minimum axis ratio of $a : b \sim 1.12$. Applying this ratio to the average diameter estimate, the minimum physical dimensions of 2003 AZ_{84} are $\sim 641 \times 718$ km. This range encompasses three of the five diameter estimates, suggesting that most of the ambiguity in the diameter estimates can be attributed to different projections of an elongated object. We expect that the true axis ratio cannot be much larger than inferred through our data since our data appear to cover the extent of the brightness variation. Therefore, the diameter estimates that cannot be explained by elongation are likely due to a different intrinsic feature of 2003 AZ_{84} such as smaller projected surface area of the multiple components' configurations.

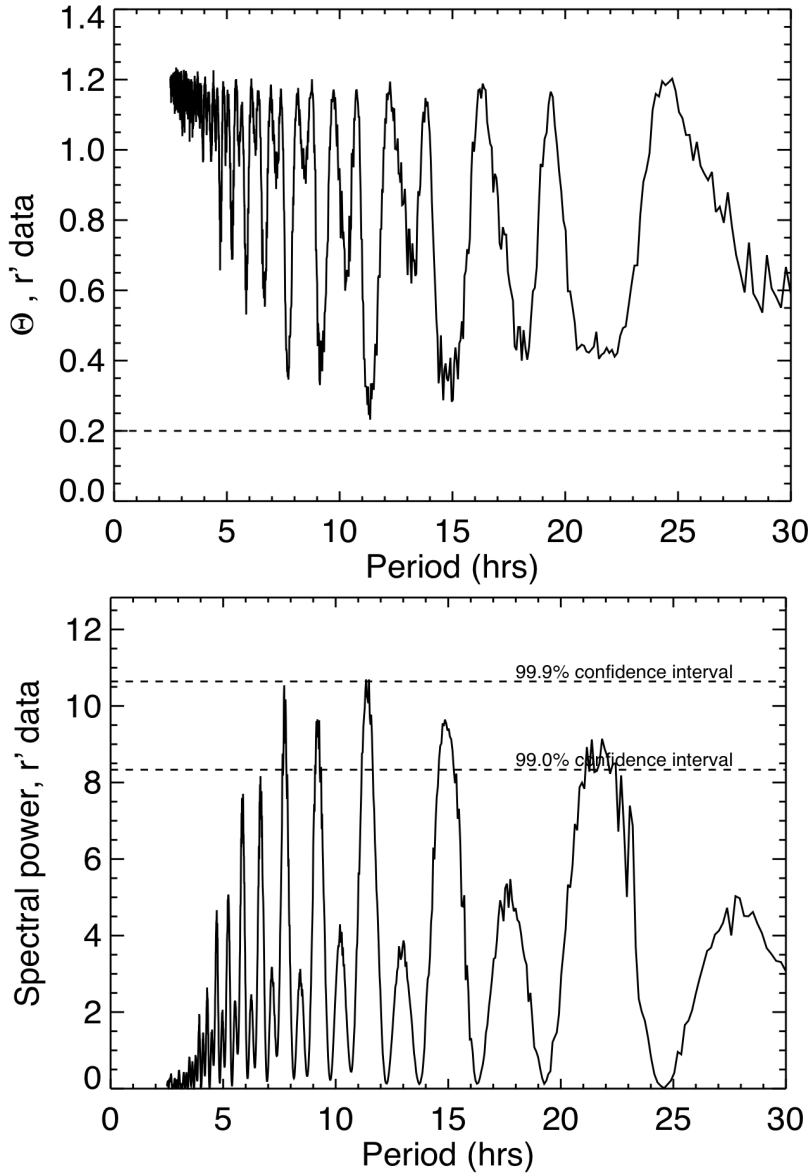

Figure 6.30 Periodograms for r' filter data on 2003 AZ_{84} excluding data from 02/16/12 and 04/18/12 UT. The upper plot shows the Θ value from the PDM method as a function of rotational periods (solid line) and a dashed line to represent the fiducial value at which Θ becomes highly significant. The lower plot shows the Lomb-Scargle power spectrum as a function of rotation period (solid line) as well as dashed lines at the 99.9% and 99.0% confidence limits.

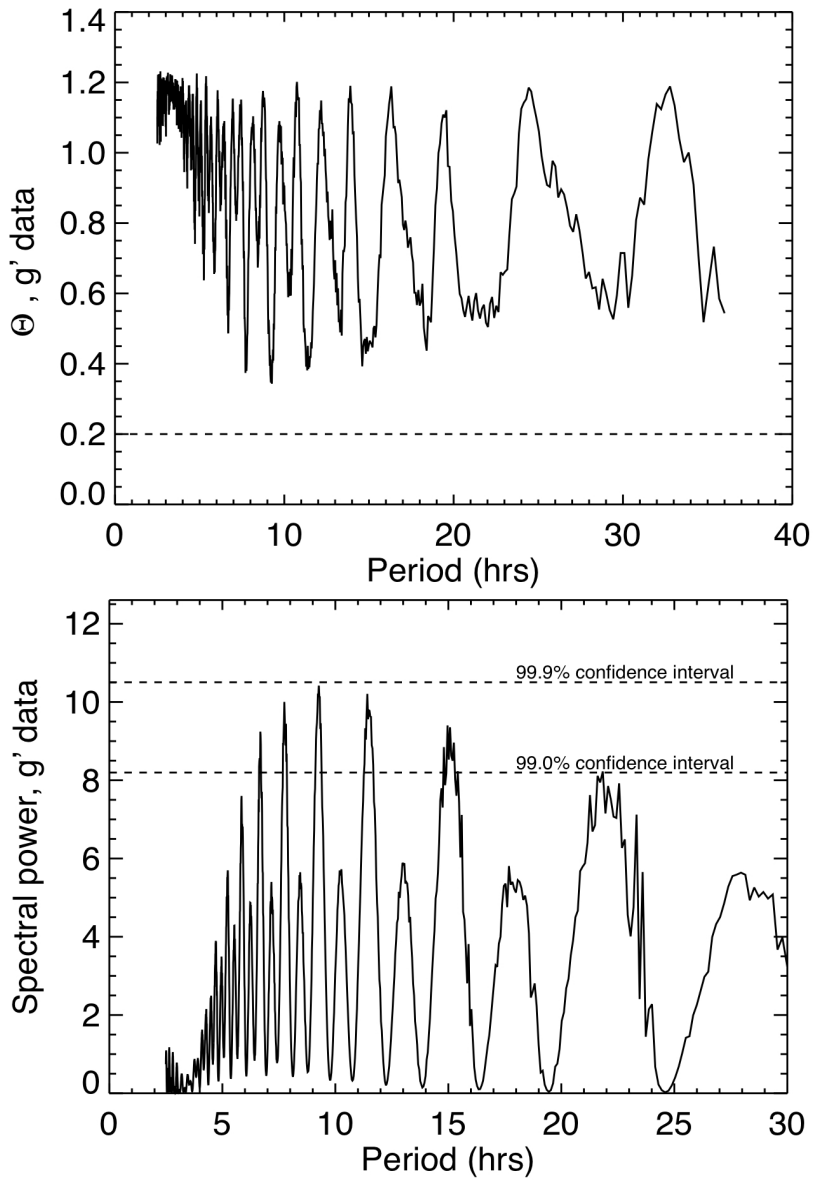

Figure 6.31 Periodograms for g' filter data on 2003 AZ_{84} excluding data from 02/16/12 and 04/18/12 UT. The upper plot shows the Θ value from the PDM method as a function of rotational periods (solid line) and a dashed line to represent the fiducial value at which Θ becomes highly significant. The lower plot shows the Lomb-Scargle power spectrum as a function of rotation period (solid line) as well as dashed lines at the 99.9% and 99.0% confidence limits.

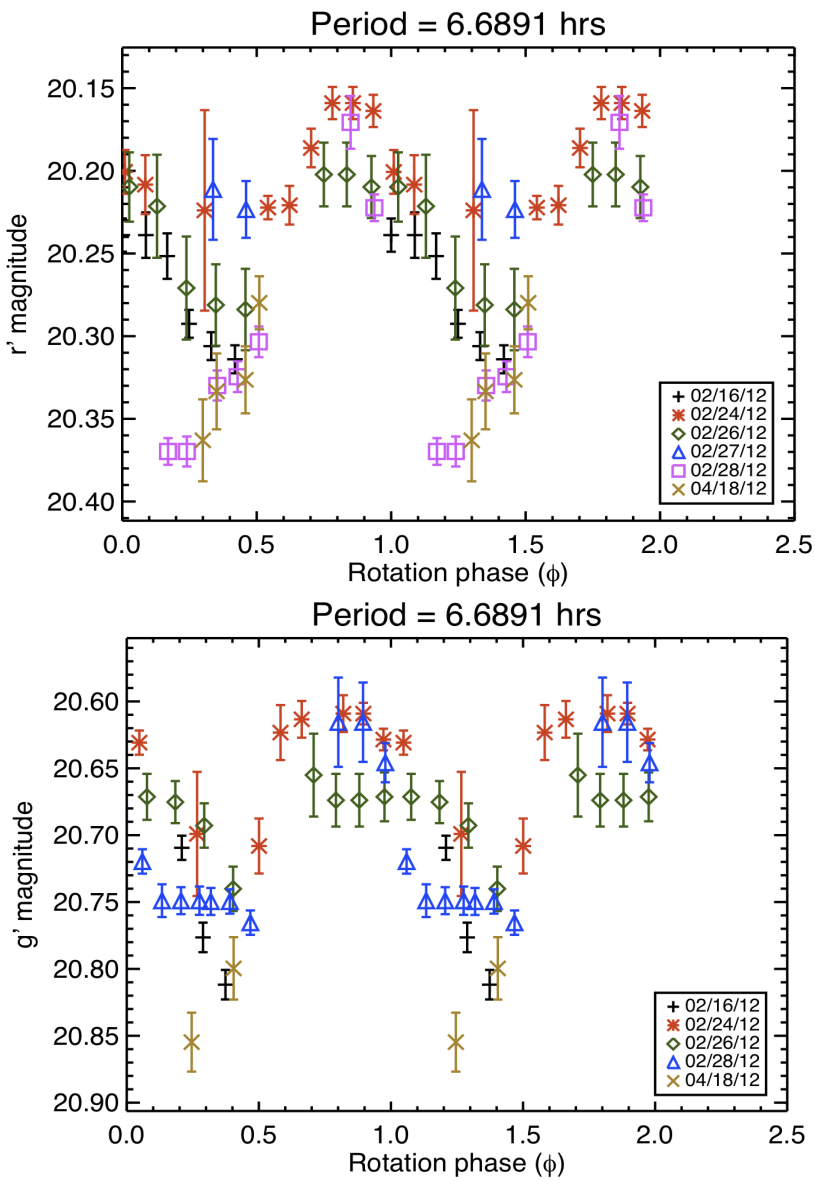

Figure 6.32 Lightcurves of 2003 AZ_{84} phased to the previously published rotation period that manifested with weak relative significance in our data - 6.7 hours - for the r' band (upper plot) and g' band (lower plot).

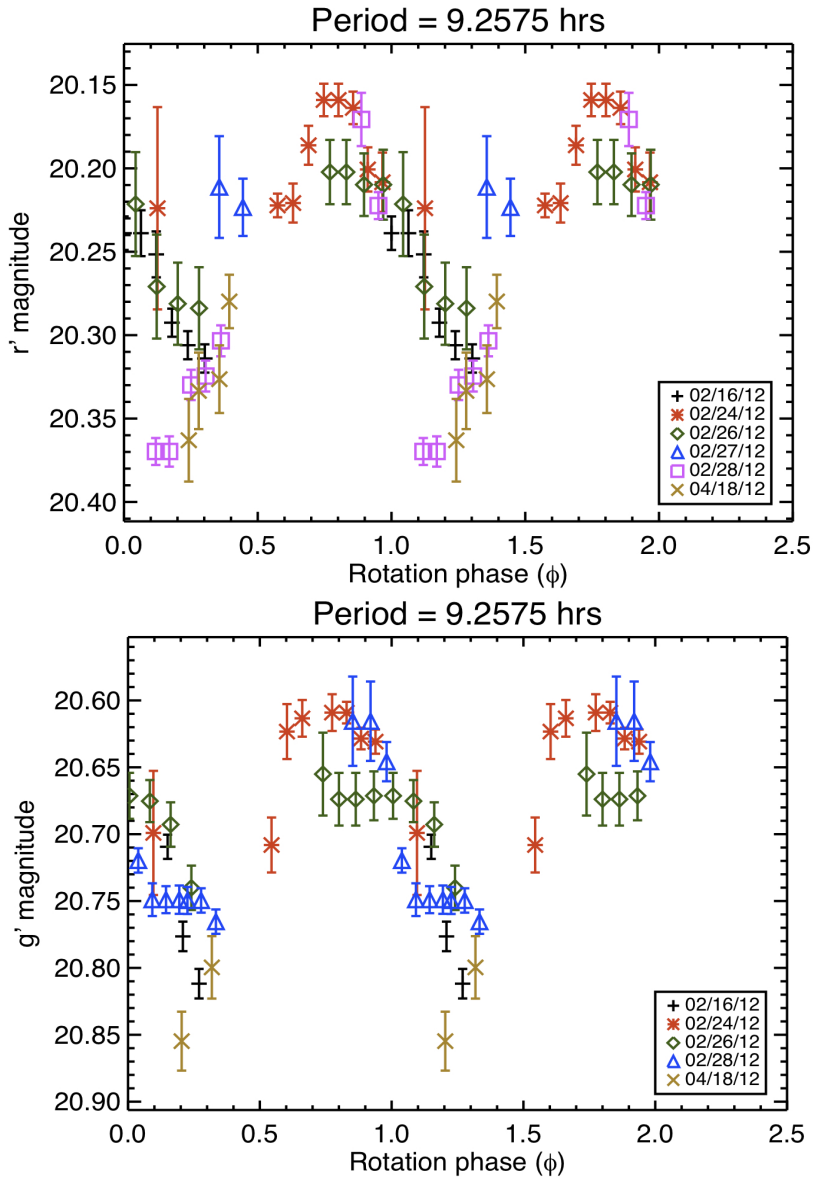

Figure 6.33 Lightcurves of 2003 AZ_{84} phased to one of the viable solutions given through periodograms - $\sim$ 9.3 hours - for the r' band (upper plot) and g' band (lower plot).

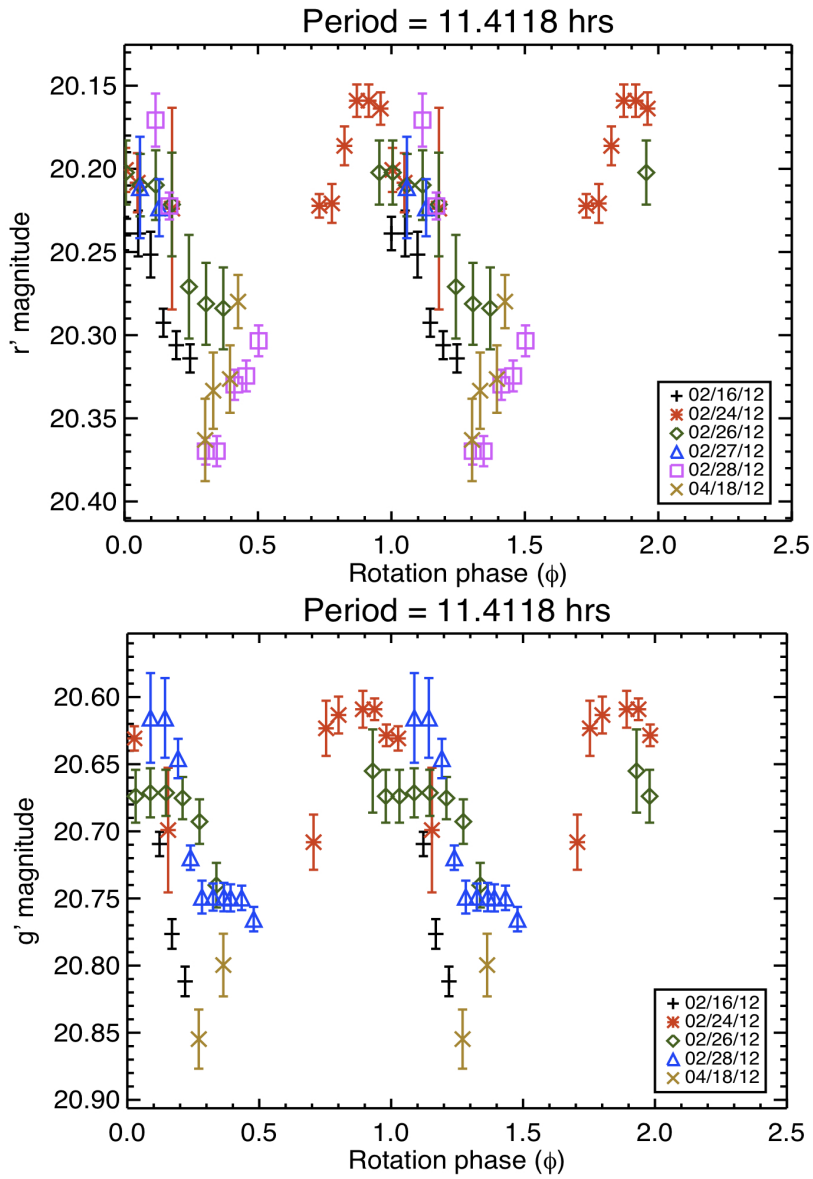

Figure 6.34 Lightcurves of 2003 AZ_{84} phased to one of the viable solutions given through periodograms - $\sim$ 11.4 hours - for the r' band (upper plot) and g' band (lower plot).

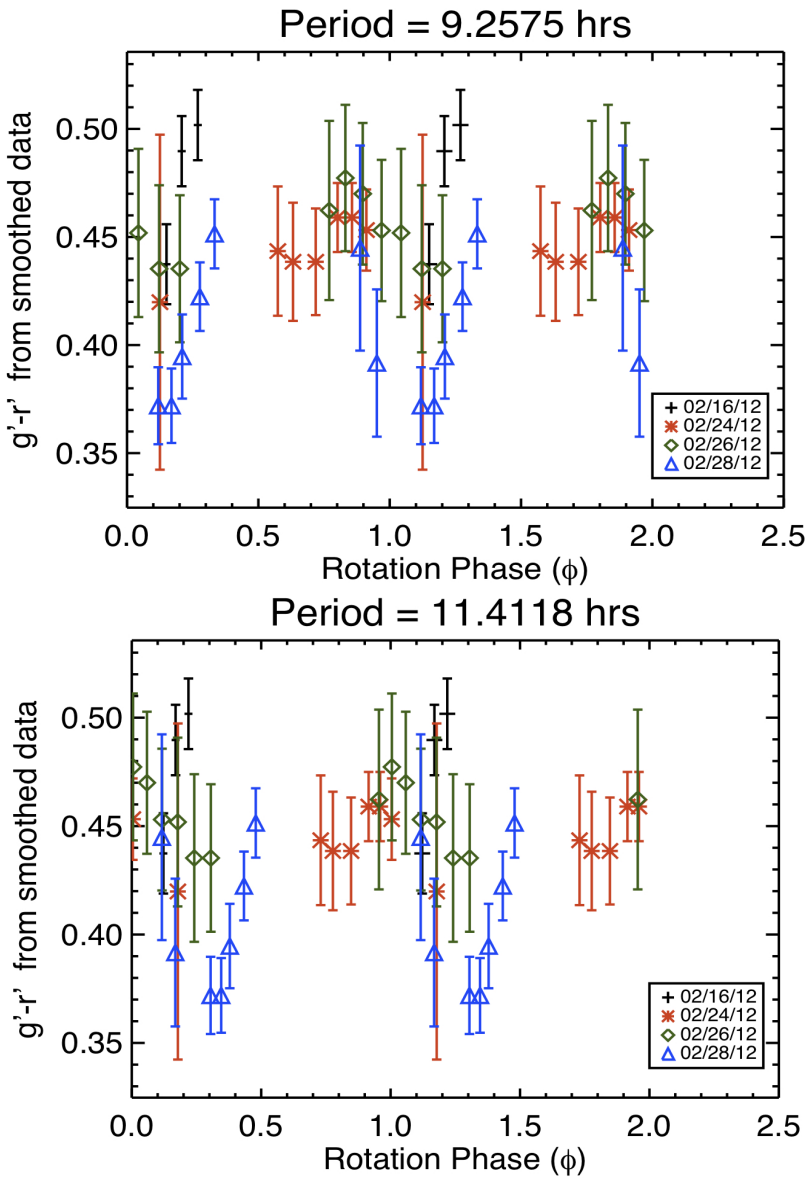

Figure 6.35 The $g' - r'$ measurements phased to the 9.3 hour (upper plot) and 11.4 hour (lower plot) rotation periods. The 11.4 hour phasing appears to incur less scatter.

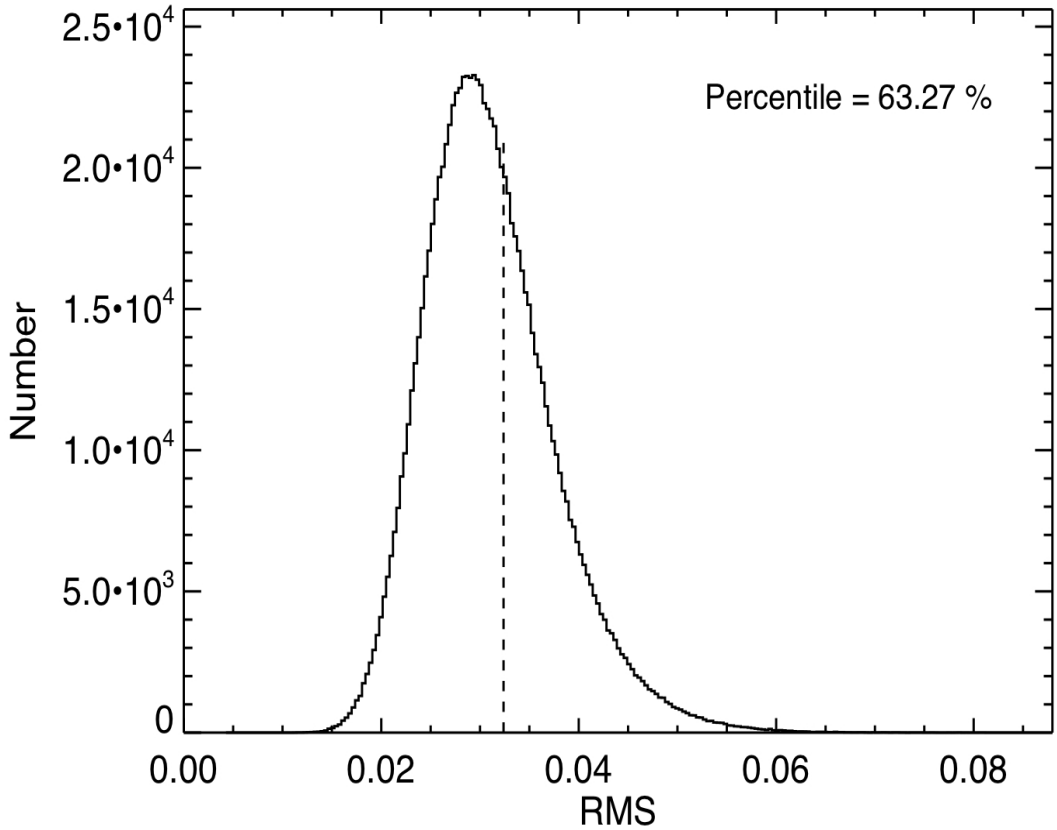

Figure 6.36 Distribution of the RMS of simulated flat $g' - r'$ datasets (solid line) comparable to 2003 AZ_{84}. The dashed line represents the RMS of the 2003 AZ_{84} data for all nights.

6.3.7 2003 OP_{32}

The Haumea family member 2003 OP_{32} dynamically belongs to the classical TNO subpopulation. Its rotation properties have been the subject of three separate observational campaigns. Rabinowitz et al. (2008) obtained data spread over four months, measured a solar phase curve coefficient for calibration between nights, and found a single-peaked 4.854 ± 0.003 hour period and photometric range of ~ 0.27 magnitudes using the phase angle-corrected data. Thirouin et al. (2010) obtained images of 2003 OP_{32} over two months and fit their data best to a 4.05 hour period (no period uncertainty reported) and amplitude of 0.13 ± 0.01 magnitudes. Lastly, Benecchi & Sheppard (2013) observed 2003 OP_{32} over one month and found a single-peaked 4.85 hour rotation period (double-peaked 9.71 hour; errors in period not reported) consistent with Rabinowitz et al. (2008) and an amplitude of 0.18 ± 0.01 comparable to Thirouin et al. (2010). Of the three studies, the Benecchi & Sheppard (2013) lightcurve gives the least amount of scatter because the mean error is comparably small, thereby providing the most convincing period fit. However, the overall inconsistent amplitudes are peculiar and may suggest variable amplitude.

We obtained 43 V band and 41 R band images over four consecutive nights (September 04-07, 2010 UT), providing an advantage over previous work by essentially eliminating uncertainty in the phase coefficient in determining the night-to-night offsets. Figures 6.37 and 6.38 show the resultant periodograms for the full dataset in each filter, and the most prominent periods are given in Table 6.7. Our statistical analysis clearly favored a short rotation period of ~ 2.40 or ~ 2.66 hours. Figures 6.39 and 6.40 show the lightcurves phased to these two solutions. One of the single-day aliases of the 2.40 hour period is 2.66 hours, and vice versa. Therefore, the prominent periods rendered in our analysis are all consistent with being the same period, either 2.40 or 2.66 hours, with one phasing representing the true spin period and the other being its alias. If one of these two values is correct, then 2003 OP_{32} would be the fastest known rotator in the outer solar system.

The phased lightcurves show interesting amplitude features. The data from 09/05/10 UT show a significantly higher amplitude than the other nights in both filters, corresponding

Table 6.7 The four most prominent rotation periods (in hours) and their respective errors detected through each of the Lomb-Scargle and PDM techniques for the full 2003 OP_{32} dataset. Periods that visually phased well in both filters are given in bold.

Detection Technique	V filter	R filter
Lomb-Scargle	2.6614 ± 0.0263	2.4112 ± 0.0269
	2.6553 ± 0.0200	2.6740 ± 0.0299
	2.3944 ± 0.0163	$\mathbf{2.4036 \pm 0.0306}$
	2.3993 ± 0.0201	$\mathbf{2.4074 \pm 0.0281}$
PDM	$\mathbf{2.6582 \pm 0.0275}$	2.6751 ± 0.0383
	2.6519 ± 0.0305	$\mathbf{2.6642 \pm 0.0543}$
	2.6435 ± 0.0398	$\mathbf{2.4031 \pm 0.0353}$
	2.6341 ± 0.0582	$\mathbf{2.4001 \pm 0.0382}$

to an overall dimming at the lightcurve minimum for a duration of $\sim$ 1.5 hours. Most notably for the 2.40 hour phasing, the V band data from 09/04/10 UT also appear ~ 0.05 magnitudes brighter than the other nights at the same ϕ. Using Eq. 6.14, the longer of our two rotation period estimates, and an upper limit to the diameter from Stansberry et al. (2011), the maximum damping time for 2003 OP_{32} to have a complex rotation state is $\sim 130,000$ years, which is remarkably short compared to the collisional timescale of $\gtrsim 70$ Myr for a ~ 100 km object (Durda & Stern 2000).

Instead, the presence of a brightening and dimming event on the order of days and independent of the primary rotation period suggests that 2003 OP_{32} is an asynchronous binary, with the brighter night (09/04/10 UT) corresponding to a configuration in which the longer-period lightcurve of a second component is at a maximum and the dimmer night (09/05/10 UT) corresponds to the longer period minimum. It is possible that the multi-day offset we observed was not found in previous studies because it was disguised as a phase angle effect, which is negligible in our data. We therefore recommend that future lightcurve data be taken at as low a phase angle as possible (*i.e.*, at opposition) and sampling over multiple consecutive nights for the full night to ensure adequate rotation phase coverage and thus good lightcurve determination during the potentially short-duration opposition.

Because the data from 09/04/10 UT appear more distinctly offset in the V band, color variation on the secondary is suggested. Figure 6.42 shows the $V-R$ colors phased to both of the prominent periods in our observations. Some correlated trending is visually noticeable, especially within the data from 09/05/10 UT. The data from 09/04/10 UT also are more neutral than the data from the other nights. However, color variation is not statistically supported when considering the full dataset, with the RMS of the data being comparable to simulated flat color curves (Fig 6.43). We suspect this insignificance arose from the large errors on the data from 09/05/10 UT, which introduced scatter in the RMS calculation that was larger in scale than the color variation itself. After removing the 09/05/10 UT data from the simulations and the RMS calculation of the actual data, we did find statistically significant color variation. Because the data from 09/04/10 UT are therefore significantly more neutral than the data taken on 09/06/10 and 09/07/10 UT, the color variation must be on the order of days and thus correspond to surface heterogeneity on the secondary, or that the secondary is a different color than the primary.

The 2.40 hour rotation period is roughly half the period reported in Benecchi & Sheppard (2013) and is not its alias. Both the 2.40 hour lightcurve in our data and the 4.85 hour lightcurve in Benecchi & Sheppard (2013) are single-peaked, so a 4.85 hour period cannot be the double-peaked rendition of the 2.40 hour period. Our data therefore suggest a rotation period distinct from previous studies. We explored phasing our data to 4.85 hours to investigate how well they could be described by the published periods (Fig. 6.41). This longer period does not appear to phase well with the data, with the first two nights in our series exhibiting significant deviation from the single-peaked lightcurve trend suggested by the last two nights. Therefore, our rotation period results are inconsistent with those published. We also suggest that the data taken for previous studies may have been confused by the secondary rotation with the net effect of it appearing to phase well to a different rotation period.

We used the photometric range of the observations that did not give evidence of a secondary rotation period to isolate the Δm corresponding to the primary rotation,

finding $\Delta m = 0.22 \pm 0.03$. Then using Eq. 6.2, we calculated a minimum axis ratio of $a : b = 1.22$. Stansberry et al. (2011) estimated the upper limit on 2003 OP_{32}'s size via albedo measurements as $D \lesssim 350$ km. Assuming this value to be the mean diameter of the primary, we estimated the equatorial dimensions of 2003 OP_{32} to be 315×389 km. We estimated the secondary amplitude from the maximum offset between brighter and dimmer nights after subtracting the 2.4036 hour period, obtaining $\Delta m \sim 0.1$ in both filters, which corresponds to a mass ratio of 3% if the system were eclipsing.

The fast rotation period that we found sets meaningful lower limits on the bulk density assuming tensile strength to be negligible (Eq. 6.11), giving $\rho \gtrsim 1900$ kg/m^3. Spectra of 2003 OP_{32} revealed a high fraction of water ice ($\gtrsim 70\%$) consistent with the rest of the Haumea family (Barkume et al. 2008; Brown et al. 2007). However, water ice has a density of ~ 1000 kg/m^3. Our density limits suggest that although the surface of 2003 OP_{32} appears to be nearly pure water ice, its interior must have a significant rock fraction. If we assume that 2003 OP_{32} has negligible porosity and is only composed of rock and ice, then the bulk density (ρ) can be approximated as a linear combination of the densities of rock (ρ_r) and ice (ρ_i):

$$\rho = f_i \rho_i + (1 - f_i)\rho_r \quad , \tag{6.15}$$

where f_i is the fraction of the body's mass contained in ice. Using our lower estimate of $\rho = 1900$ and the values, $\rho_r \sim 3000$ and $\rho_i \sim 1000$ kg/m^3, we calculated that no more than 55% of 2003 OP_{32}'s mass exists in the form of water ice.

Because it is much smaller and therefore less massive than present-day Haumea, 2003 OP_{32} is thought to be a fragment of the outer layer(s) of pre-collisional (or proto-) Haumea. Our minimum rock fraction estimate is not consistent with 2003 OP_{32} coming from part of a pure ice layer on proto-Haumea, as assumed by some previous observational and theoretical studies of the Haumea family (*e.g.*, Brown et al. 2007; Snodgrass et al. 2010). Instead, our results imply that there must have been an appreciable amount of rock in these layers,

perhaps in the form of a rock/ice crust suggested by the thermal models of Desch et al. (2009). If this rock/ice crust was present on proto-Haumea overlying an icy mantle, then that would indicate that partial differentiation within TNOs was possible and should be common on objects of comparable size.

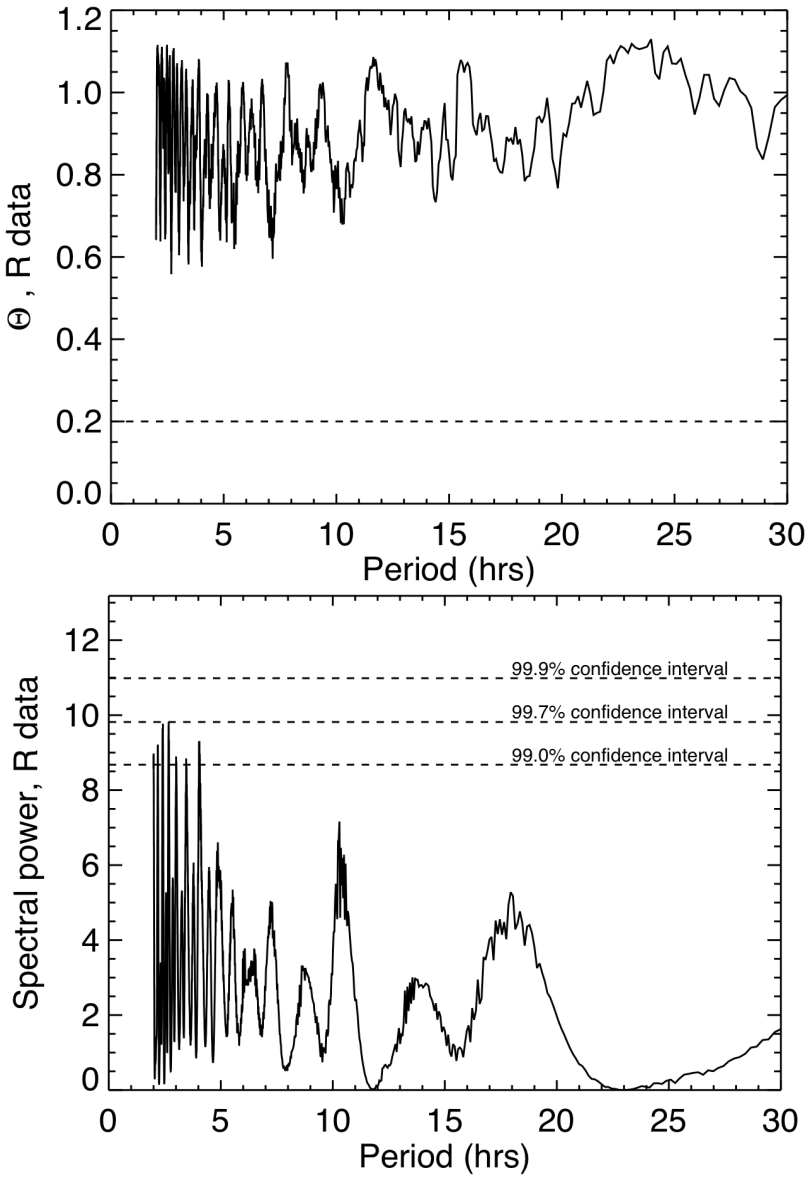

Figure 6.37 Periodograms for R filter data on 2003 OP_{32}. The upper plot shows the Θ value from the PDM method as a function of rotational periods (solid line) and a dashed line to represent the fiducial value at which Θ becomes highly significant. The lower plot shows the Lomb-Scargle power spectrum as a function of rotation period (solid line) as well as dashed lines at the 99.9% and 99.0% confidence limits. A third dashed line shows the confidence limit corresponding to the maximum spectral power.

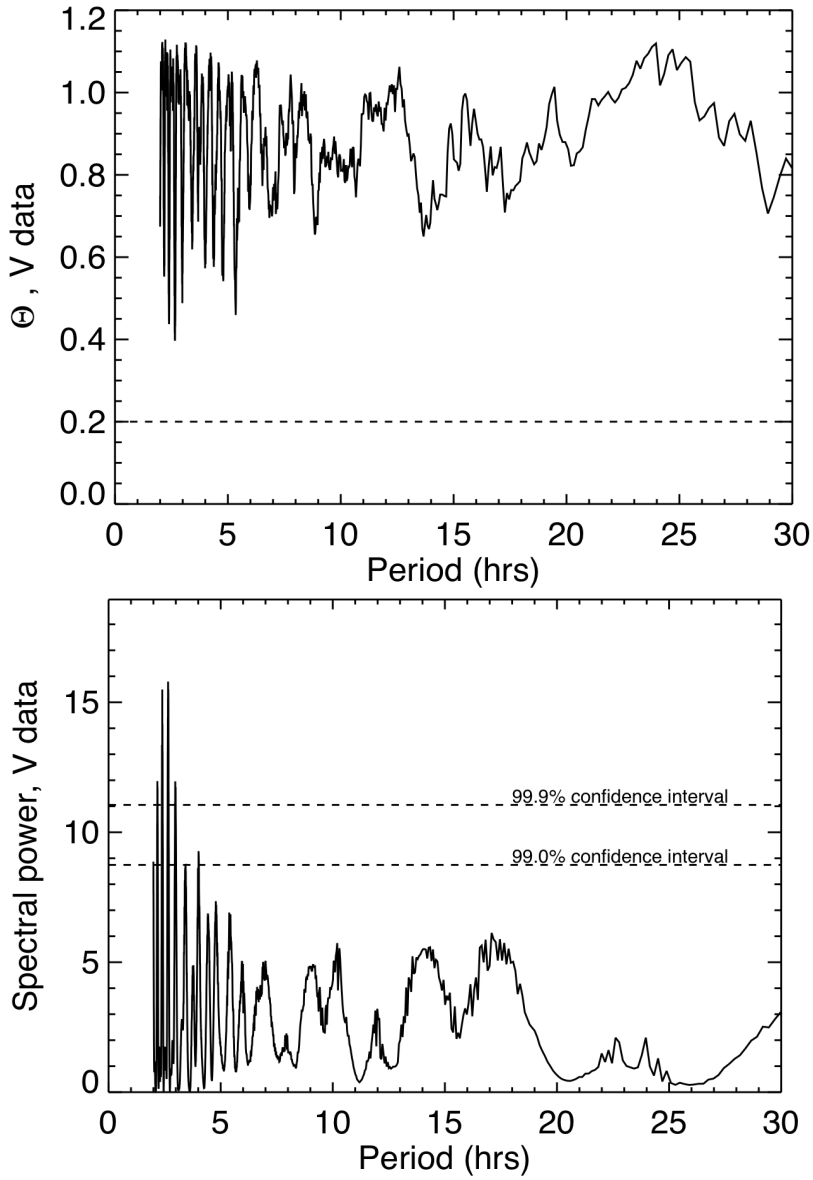

Figure 6.38 Periodograms for V filter data on 2003 OP_{32}. The upper plot shows the Θ value from the PDM method as a function of rotational periods (solid line) and a dashed line to represent the fiducial value at which Θ becomes highly significant. The lower plot shows the Lomb-Scargle power spectrum as a function of rotation period (solid line) as well as dashed lines at the 99.9% and 99.0% confidence limits.

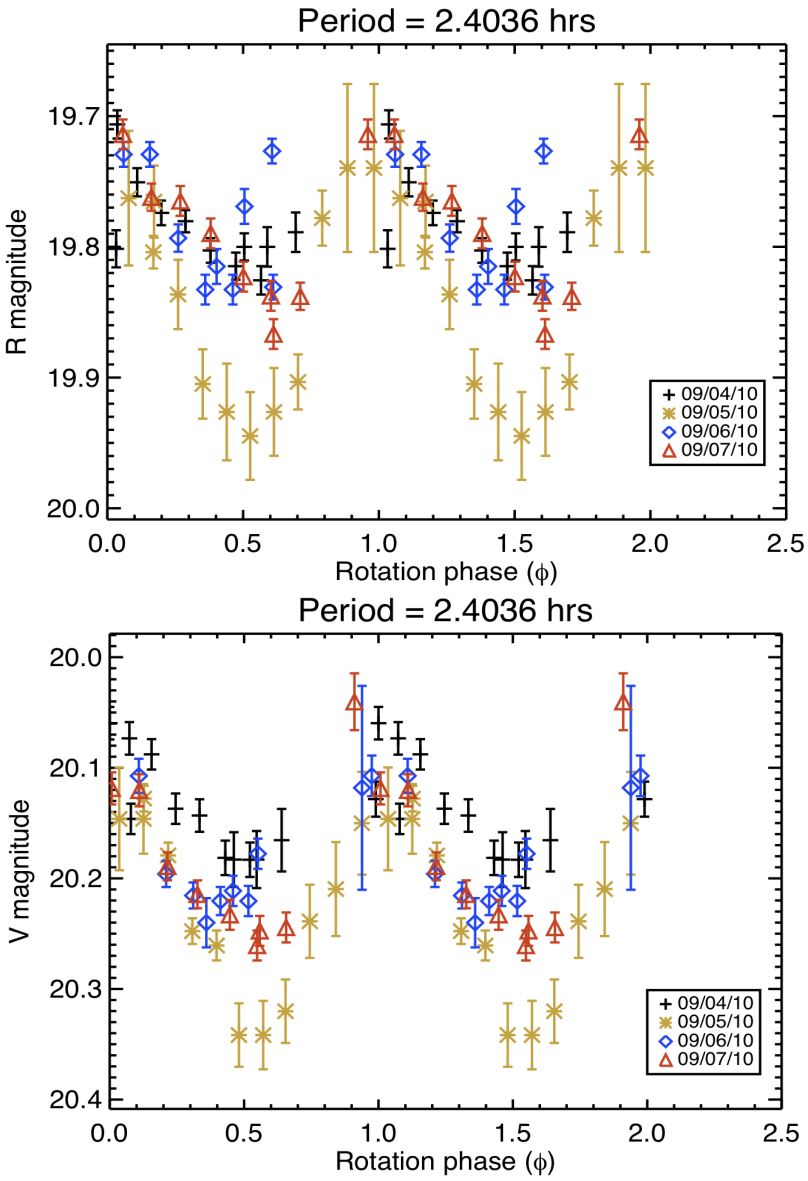

Figure 6.39 Lightcurves of 2003 OP_{32} phased to one of the viable solutions given through periodograms - ~ 2.40 hours - for the R band (upper plot) and V band (lower plot).

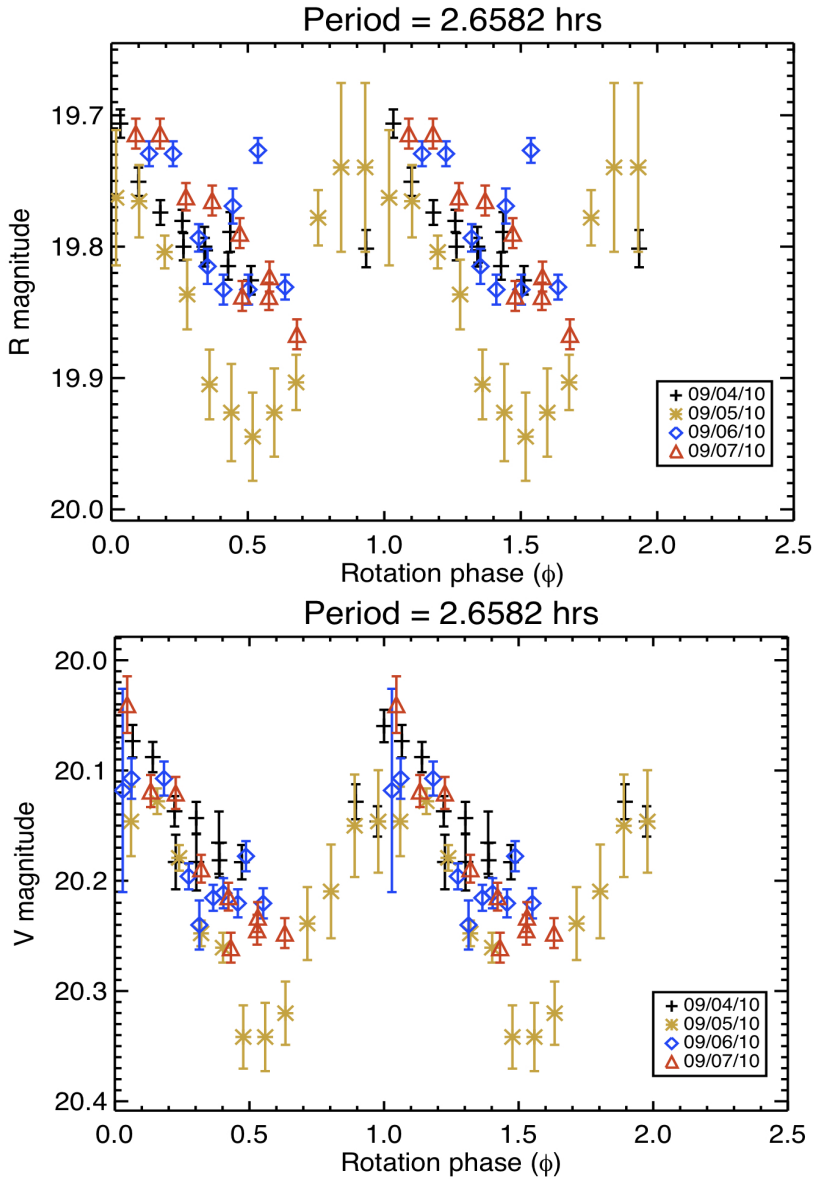

Figure 6.40 Lightcurves of 2003 OP_{32} phased to one of the viable solutions given through periodograms - $\sim$ 2.66 hours - for the R band (upper plot) and V band (lower plot).

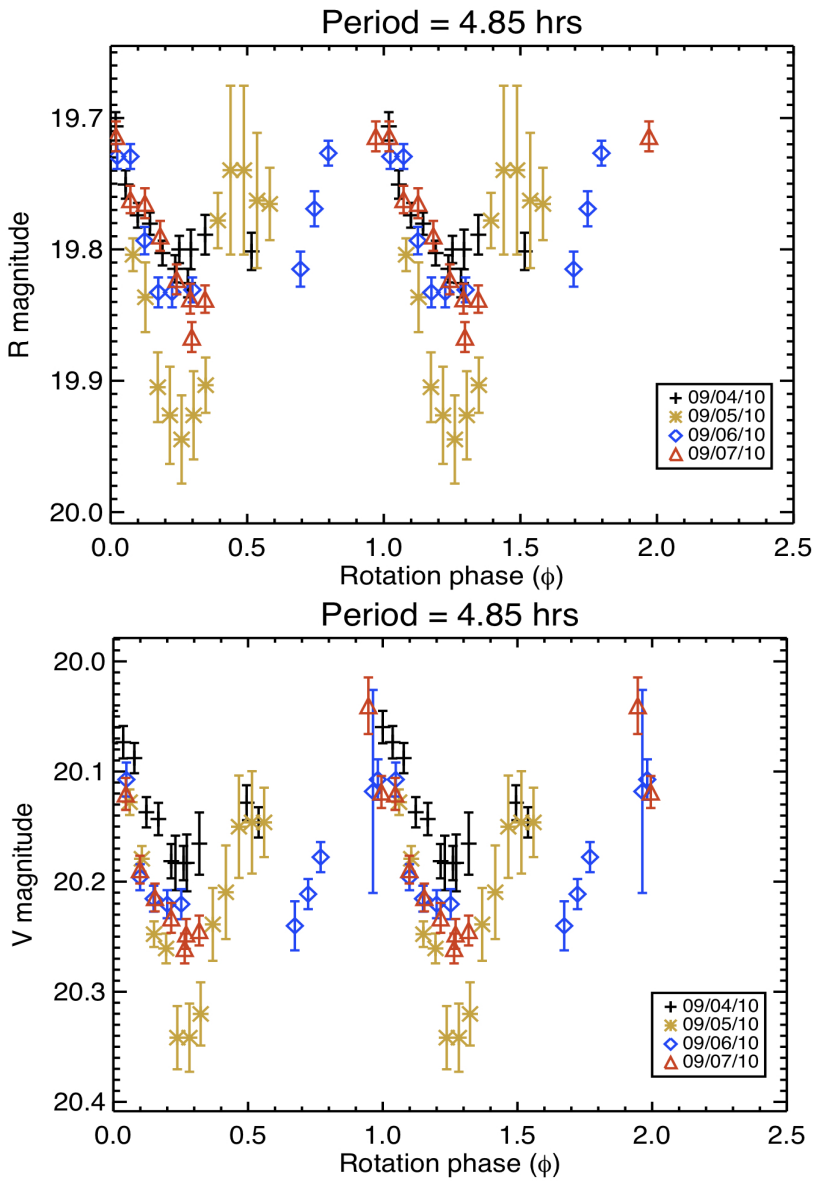

Figure 6.41 Lightcurves of 2003 OP_{32} phased to twice the prominent $\sim$ 2.4 hour period - 4.81 hours - for the R band (upper plot) and V band (lower plot). This period is consistent with previously published periods.

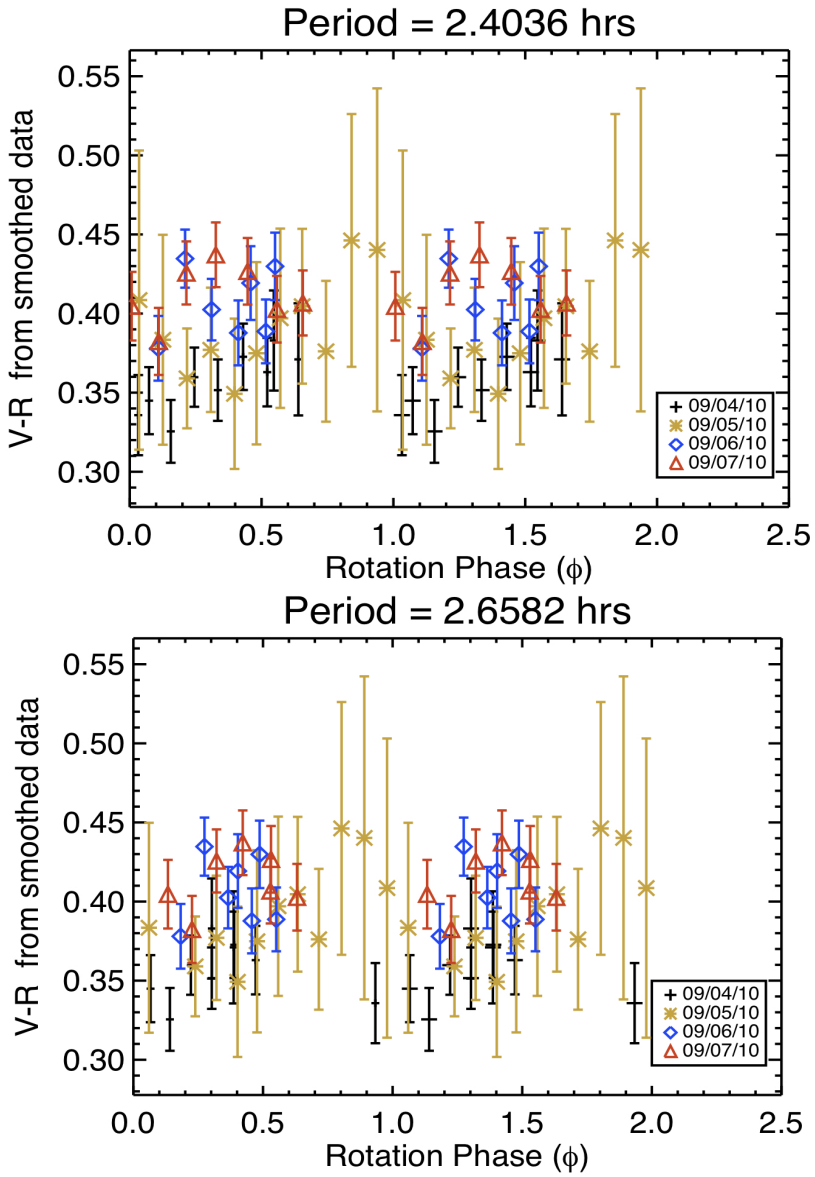

Figure 6.42 The $V-R$ measurements for 2003 OP_{32} phased to the 2.4036 hour (upper plot) and 2.6582 hour (lower plot) rotation periods. Data from 09/05/10 UT have much larger error bars than the other nights, and data from 09/04/10 UT all appear more neutral than data from either 09/06/10 or 09/07/10 UT.

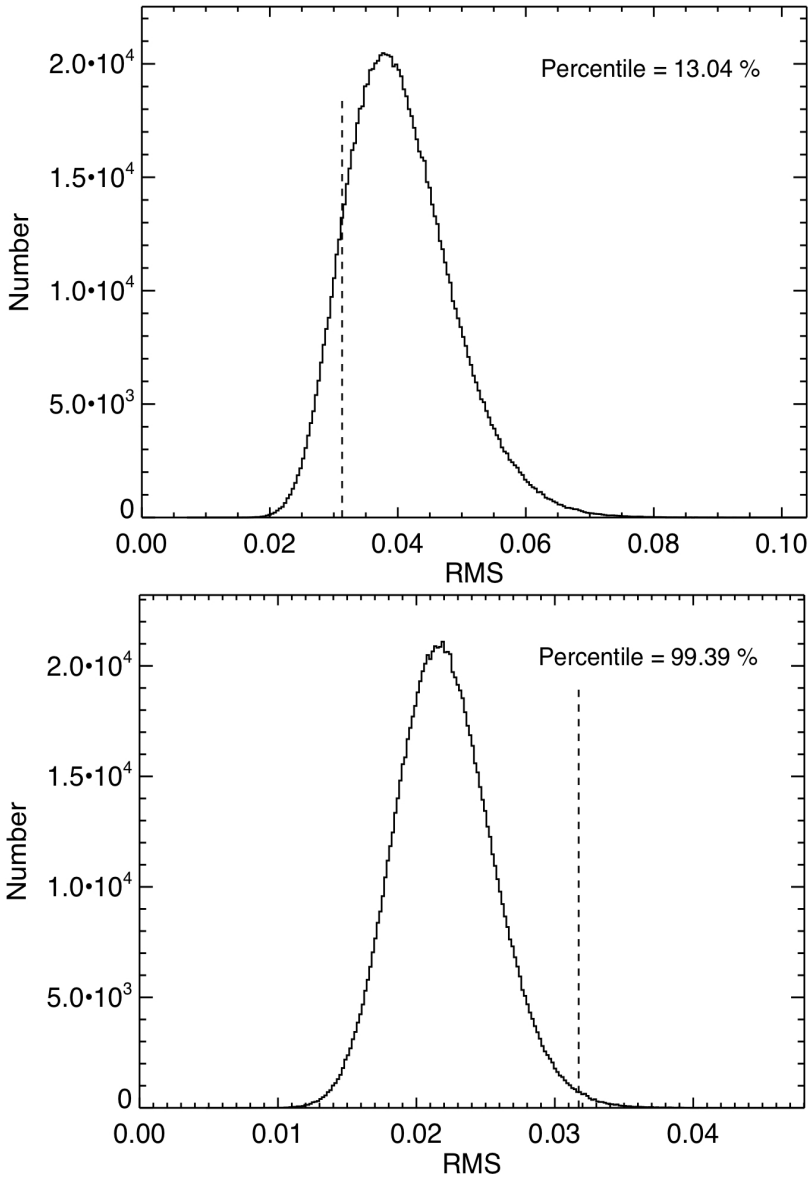

Figure 6.43 Distribution of the RMS of simulated flat $V-R$ datasets (solid line) comparable to 2003 OP_{32} for the full dataset (upper plot) and after excluding data from 09/05/10 UT, which had much larger mean errors (lower plot). The dashed line represents the RMS of the 2003 OP_{32} data in each scenario.

6.3.8 2003 UZ_{117}

The classical TNO 2003 UZ_{117} is the last and smallest member of the Haumea family presented in this work (Stansberry et al. 2011). The rotation properties of this object have not been constrained apart from one study. Perna et al. (2008) observed 2003 UZ_{117} on two nights and did not find a unique spin solution, although they did remark that their data seemed to phase well to ~ 6 hours. We observed 2003 UZ_{117} on a total of four nights spaced over one week (October 14-15, 19-20, 2012 UT), obtaining a total of 13 V filter and 28 R filter images. The prominent periods from PDM and Lomb-Scargle periodograms (Figs. 6.44 and 6.45) using the full dataset are tabulated in Table 6.8. None of these periods provided a convincing fit to the data in both filters, giving significant shifts between datasets.

Table 6.8 The four most prominent rotation periods (in hours) and their respective errors detected through each of the Lomb-Scargle and PDM techniques for the full 2003 UZ_{117} dataset. None of the prominent periods in this scenario phased well to both filters.

Detection Technique	V filter	R filter
Lomb-Scargle	7.8906 ± 0.1013	6.9599 ± 0.0832
	7.8617 ± 0.0862	6.9408 ± 0.0891
	5.9411 ± 0.0574	9.7238 ± 0.1500
	11.6332 ± 0.2201	6.9792 ± 0.1159
PDM	5.9832 ± 0.1215	6.9349 ± 0.0845
	5.9711 ± 0.1089	6.8846 ± 0.1778
	5.9172 ± 0.1010	5.4232 ± 0.0724
	4.7835 ± 0.0582	5.4026 ± 0.0787

However, we manually adjusted the spin period and noticed that the data generally fit a ~ 5.6 hour period well when excluding one night, 10/20/12 UT, which was comparably fainter than the general trend suggested by the other data. We therefore reran only the R band data (which was more numerous and thereby provided a better opportunity to constrain the rotation period) through PDM and Lomb-Scargle period search routines, the results of which are given in Table 6.9 and shown in Figure 6.46.

We found that all of the single-peaked periods at ~ 5.68 hours phased well apart from the data from 10/20/12 UT, which are offset by ~ 0.07 magnitudes at their greatest difference

Table 6.9 The four most prominent 2003 UZ_{117} rotation periods (in hours) and their respective errors detected through each of the Lomb-Scargle and PDM techniques for the only the R filter excluding 10/20/12 UT data. Periods that visually phased well in both filters are given in bold.

Detection Technique	R filter
Lomb-Scargle	$\mathbf{5.6975 \pm 0.0700}$
	$\mathbf{5.7099 \pm 0.0703}$
	$\mathbf{5.6852 \pm 0.0861}$
	$\mathbf{5.7306 \pm 0.0917}$
PDM	$\mathbf{5.6907 \pm 0.0939}$
	$\mathbf{5.6695 \pm 0.1144}$
	4.6000 ± 0.0781
	3.8819 ± 0.0497

(Figs. 6.47). If the true rotation period was $\sim$ 5.68 hours and this offset was therefore intrinsic to 2003 UZ_{117}, then we would have another instance where an asynchronous or transiting companion was needed to explain the observed lightcurve. While exploring the lightcurve via manual adjustments, although it did not appear as one of the four most prominent periods in these analyses, a 10.75 hour period was also found to fit the data well as a double-peaked period with no multi-day offsets (Fig. 6.48). Because our data were described well by both the $\sim$ 5.68 hour and 10.75 hour period, only one of which suggests a multi-day offset indicative of a companion, we could not unambiguously conclude that 2003 UZ_{117} showed evidence of binarity.

We observed a $\Delta m = 0.12 \pm 0.03$. in the R filter. The amplitude in the V filter was poorly constrained because of the small sample size (only 13 data points). From the R band amplitude and the maximum diameter estimates from Brown et al. (2007) as the average diameter, we calculated a lower limits to the equatorial dimensions of 236×265 km. Assuming the most pessimistic circumstances for inferring the minimum density and tensile strength (*i.e.*, the longest of the two plausible rotation periods in this study), we calculated a very low minimum density of 94 kg/m^3 and minimum strength of 10,000 N/m^2.

Figure 6.49 shows the $V-R$ colors phased to both periods, revealing a sinusoidal trend in for the 10.75 hour phasing. We investigated the significance of this color trend through our

null color variation simulations. Because there were very few V filter data taken, our color measurement sample was small. In simulating a null sample for a small, randomized sample, the RMS will typically be overestimated because the mean is more poorly represented and therefore more variant. Therefore, it is not surprising that although clear trending is inferred visually in the 10.75 hour period, it is not highly significant, existing in the 94th percentile relative to the null sample.

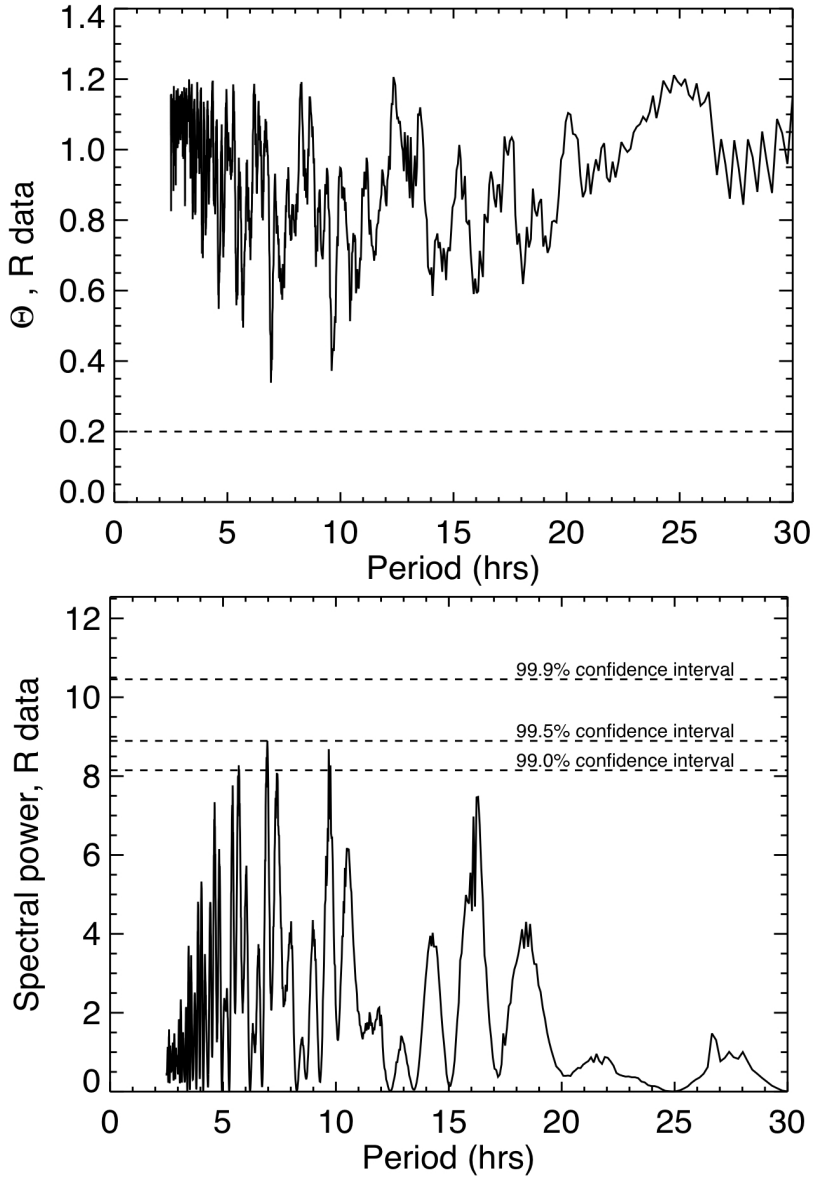

Figure 6.44 Periodograms for all R filter data on 2003 UZ_{117}. The upper plot shows the Θ value from the PDM method as a function of rotational periods (solid line) and a dashed line to represent the fiducial value at which Θ becomes highly significant. The lower plot shows the Lomb-Scargle power spectrum as a function of rotation period (solid line) as well as dashed lines at the 99.9% and 99.0% confidence limits. A third dashed line shows the confidence limit corresponding to the maximum spectral power.

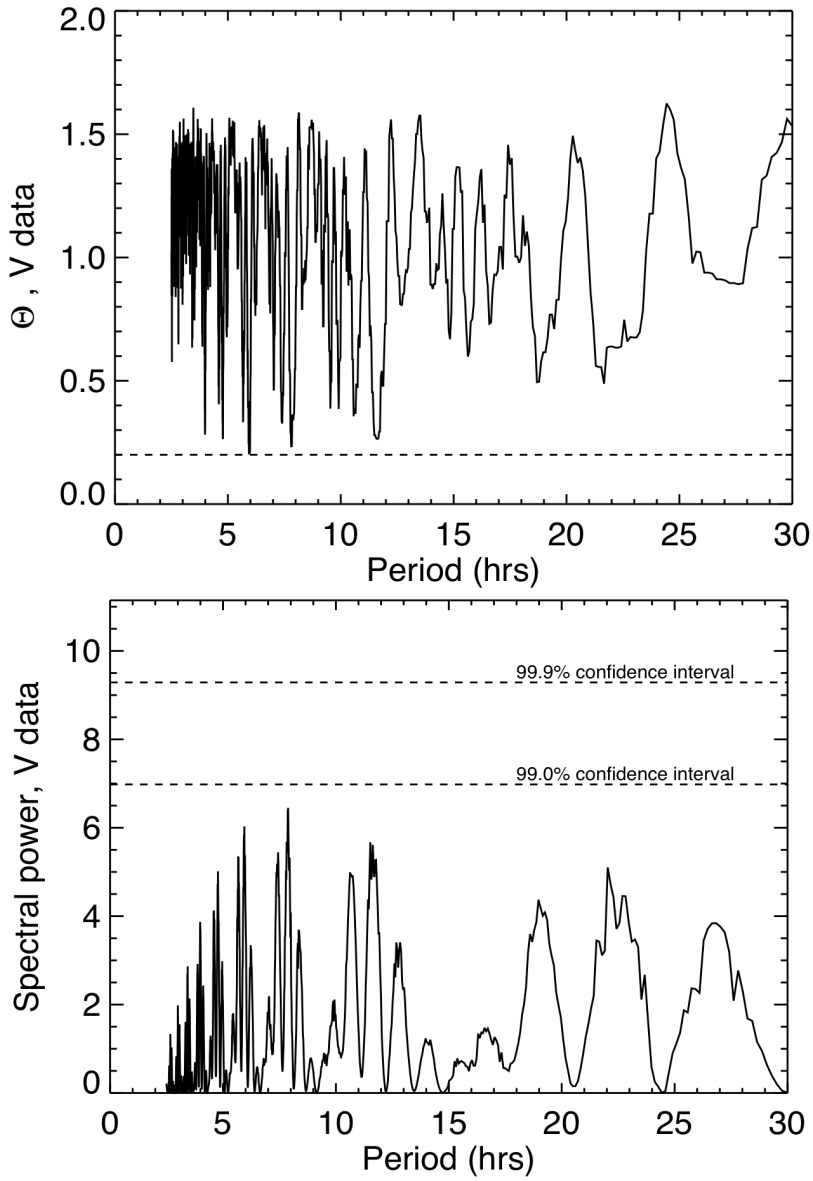

Figure 6.45 Periodograms for all V filter data on 2003 UZ_{117}. The upper plot shows the Θ value from the PDM method as a function of rotational periods (solid line) and a dashed line to represent the fiducial value at which Θ becomes highly significant. The lower plot shows the Lomb-Scargle power spectrum as a function of rotation period (solid line) as well as dashed lines at the 99.9% and 99.0% confidence limits.

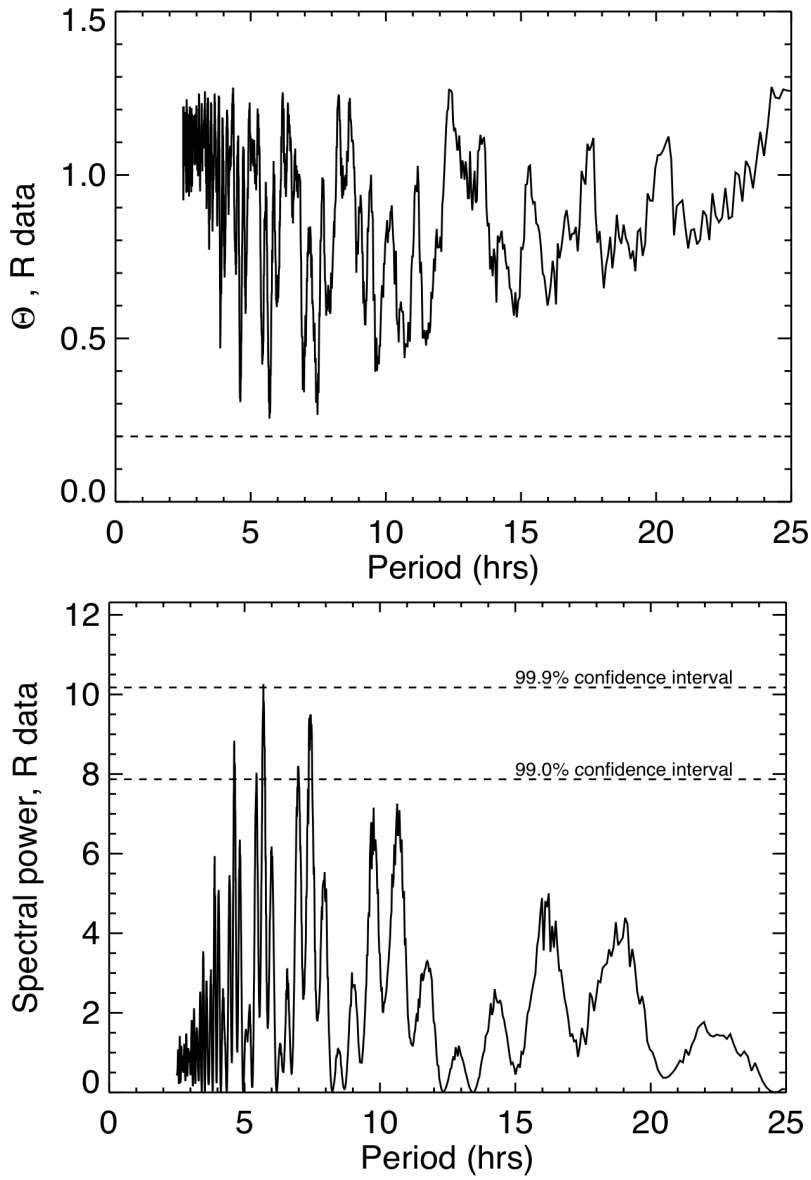

Figure 6.46 Periodograms for all R filter data on 2003 UZ_{117}. The upper plot shows the Θ value from the PDM method as a function of rotational periods (solid line) and a dashed line to represent the fiducial value at which Θ becomes highly significant. The lower plot shows the Lomb-Scargle power spectrum as a function of rotation period (solid line) as well as dashed lines at the 99.9% and 99.0% confidence limits. A third dashed line shows the confidence limit corresponding to the maximum spectral power.

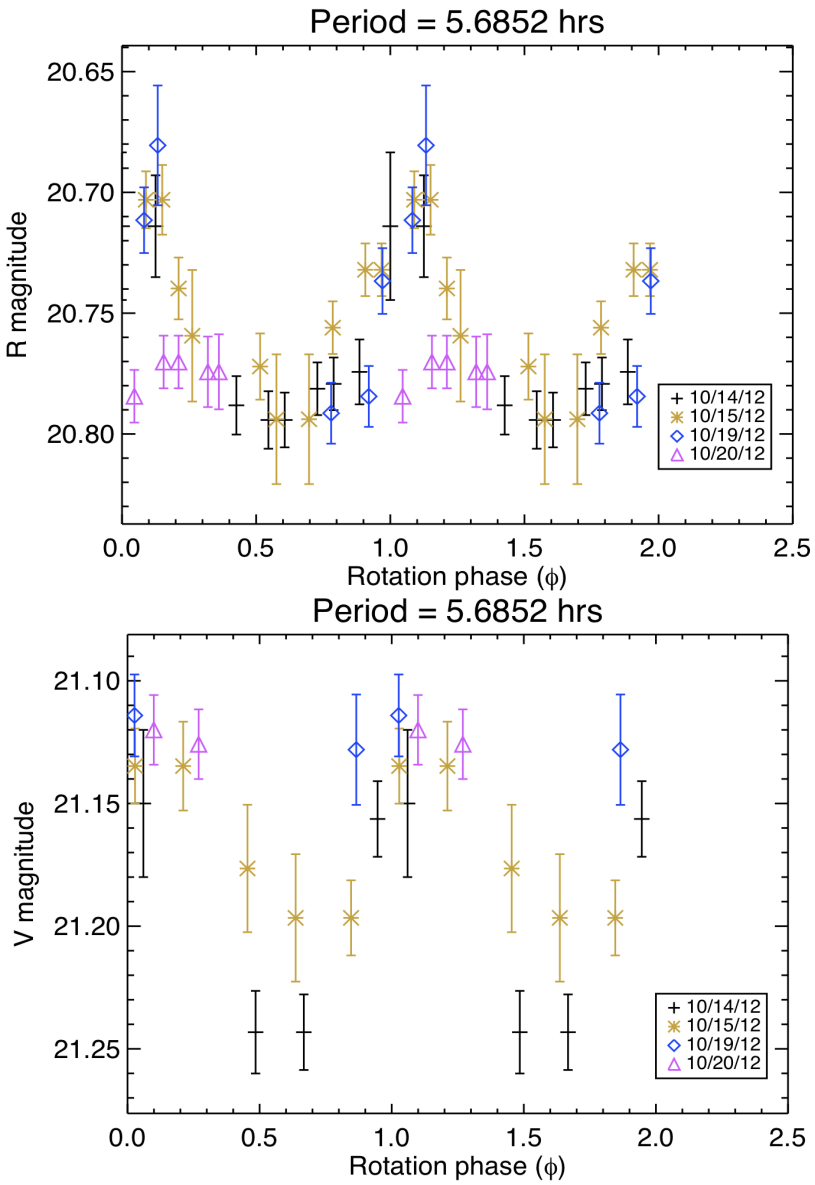

Figure 6.47 Lightcurves of 2003 UZ_{117} phased to 5.6852 hours - the preferred solution given through periodograms constructed without data from 10/20/12 UT. The upper plot is the R band the lower plot is the V band.

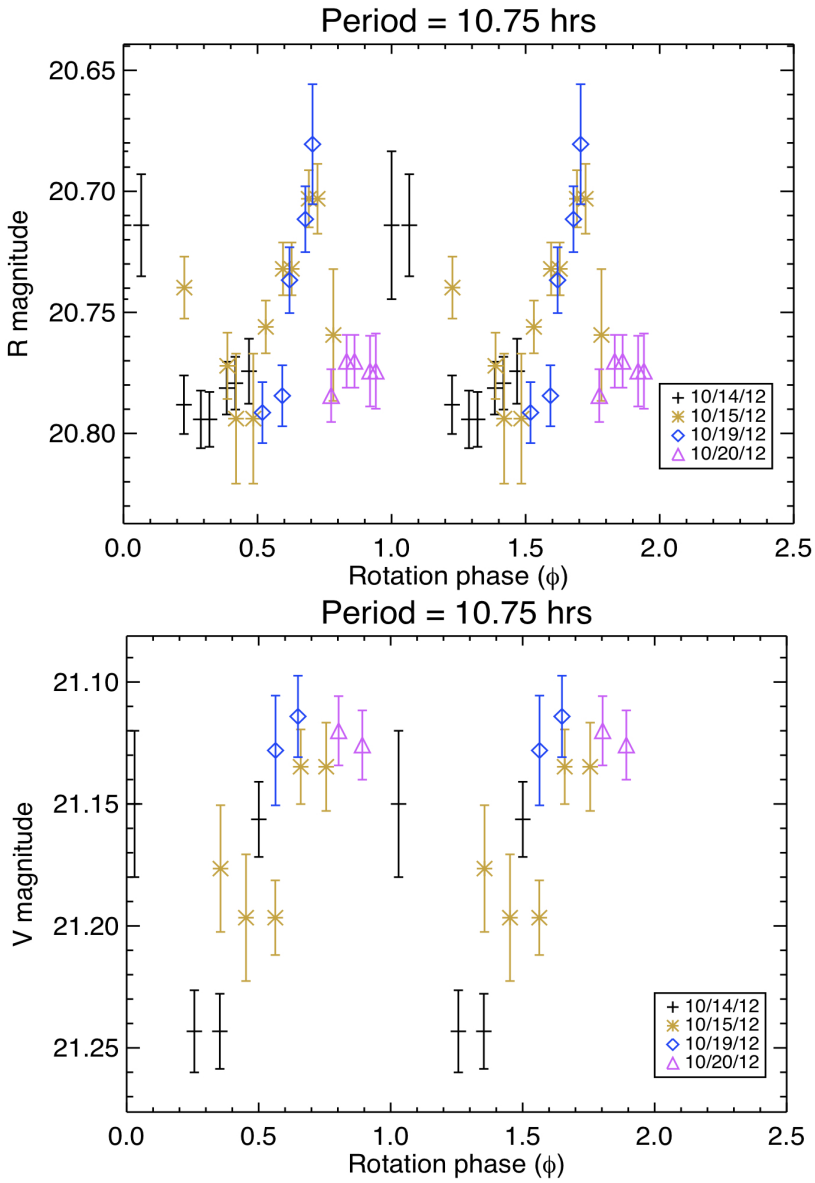

Figure 6.48 Lightcurves of 2003 UZ_{117} phased to 10.75 hours - which was recognized as a good fit to the data during manual phasing. The upper plot is the R band the lower plot is the V band.

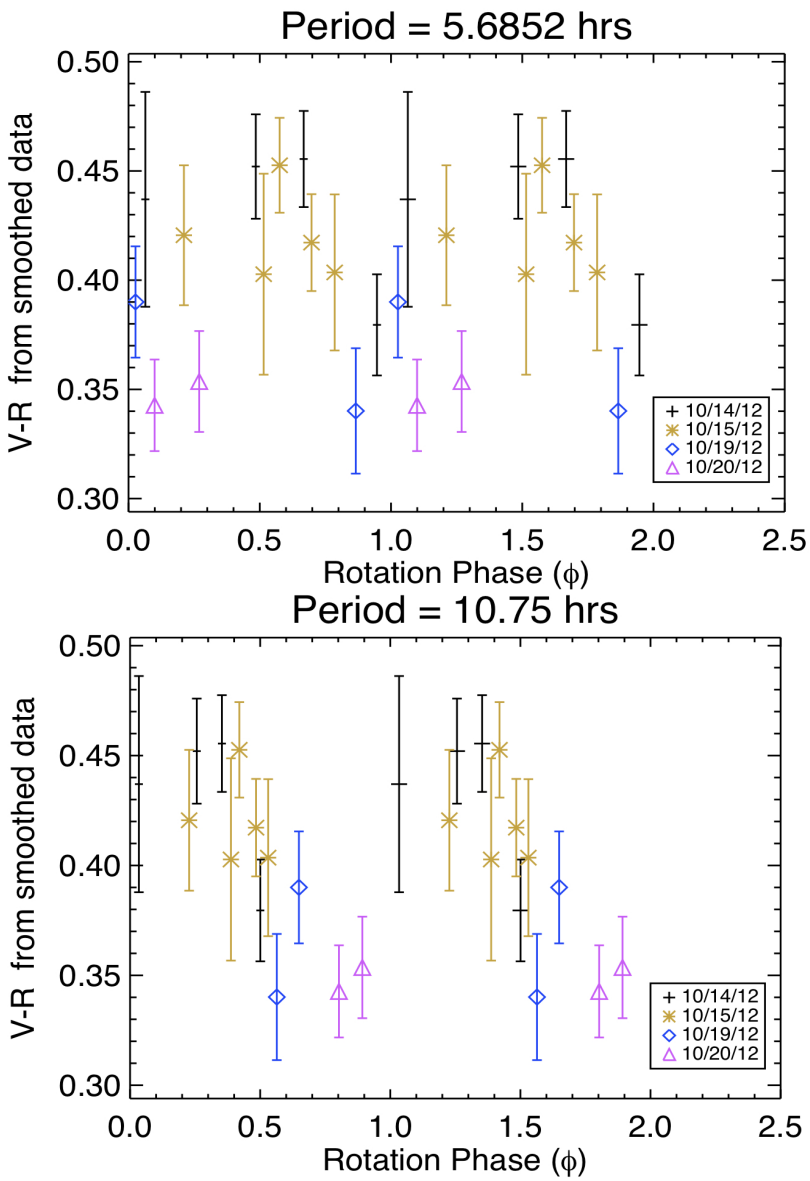

Figure 6.49 The $V - R$ measurements for 2003 UZ_{117} phased to the 5.6852 hour (upper plot) and 10.75 hour (lower plot) rotation periods.

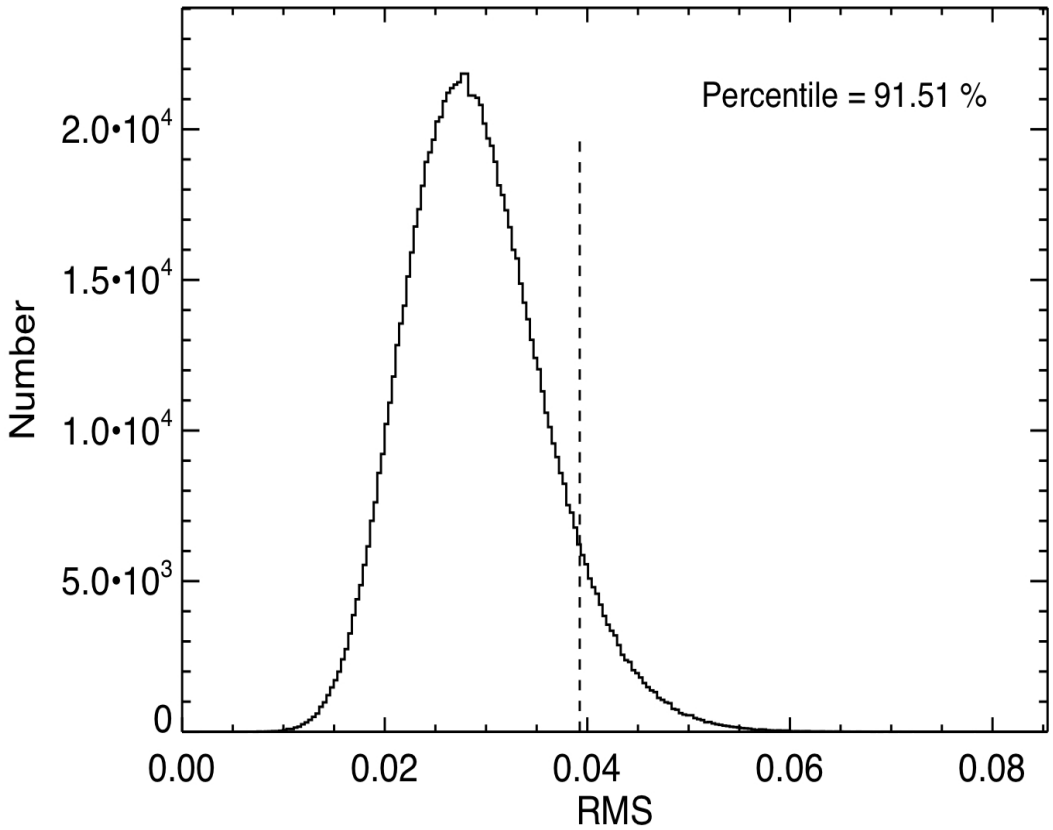

Figure 6.50 Distribution of the RMS of simulated flat $V-R$ datasets (solid line) comparable to 2003 UZ_{117} for the full dataset. The dashed line represents the RMS of the 2003 UZ_{117} data in each scenario.

6.3.9 2004 EW_{95}

The plutino 2004 EW_{95} is poorly constrained through observations, with no rotational properties (or even limits) yet published. We acquired data on 11 nights over two years: 31 V and 39 R filter images during 5 nights in 2011 (February 28, March 1 & 31, and April 22 & 25 UT) and 27 g' and 49 r' images during 6 nights in 2012 (February 24 & 26 and April 17, 18, 27, and 28 UT). We analyzed the two years separately to avoid severe aliasing problems.

Figures 6.51-6.54 show the results for our period search techniques for both filters and both years of data. The prominent periods are given in Tables 6.10 and 6.11. The periodograms suggest several viable solutions to the rotation period, but none of them provided a convincing fit to all of the data in each filter and each year. We ran Monte Carlo simulations of flat lightcurves with the same sample size and errors as the data and found that the magnitudes for each data set (each year and filter) showed significant variation. Our data gave photometric ranges of $\Delta m_V = 0.21 \pm 0.03$, $\Delta m_R = 0.24 \pm 0.06$, $\Delta m_{g'} = 0.31 \pm 0.01$, and $\Delta m_{r'} = 0.31 \pm 0.02$. Therefore, brightness variation is significant on 2004 EW_{95}, but we could not constrain its pattern in this search.

Table 6.10 The four most prominent 2004 EW_{95} rotation periods (in hours) and their respective errors detected through each of the Lomb-Scargle and PDM techniques for the V and R filters data taken in 2011. None of the periods listed fit the data well in both filters.

Detection Technique	V filter	R filter
Lomb-Scargle	12.3518 ± 0.0414	6.3942 ± 0.0111
	8.2564 ± 0.0185	8.7256 ± 0.0207
	9.2745 ± 0.0233	8.8301 ± 0.0423
	15.1432 ± 0.1248	9.3927 ± 0.0479
PDM	34.0069 ± 0.6276	6.7453 ± 0.0247
	7.3507 ± 0.0147	4.9115 ± 0.0131
	6.1386 ± 0.0102	4.1958 ± 0.0096
	6.0779 ± 0.0201	4.1439 ± 0.0140

Table 6.11 The four most prominent 2004 EW_{95} rotation periods (in hours) and their respective errors detected through each of the Lomb-Scargle and PDM techniques for the g' and r' filters data taken in 2012. None of the periods listed fit the data well in both filters.

Detection Technique	g' filter	r' filter
Lomb-Scargle	31.6892 ± 0.2058	20.7673 ± 0.1767
	28.0471 ± 0.1612	19.1386 ± 0.0751
	32.3187 ± 0.2140	28.3732 ± 0.1648
	36.1486 ± 0.2677	20.4197 ± 0.1707
PDM	32.3187 ± 0.2140	20.7673 ± 0.1767
	31.4847 ± 0.4096	20.4197 ± 0.4282
	28.0471 ± 0.1615	19.1386 ± 0.1501
	19.2898 ± 0.0763	18.8430 ± 0.1455

We explored the possibility that we could not constrain the lightcurve because 2004 EW_{95}, was a tumbler (Harris 1994). Using Eq. 6.14, we found that 2004 EW_{95}, could be tumbling if it possessed a very long rotation period (> 70 hours), so that the damping timescale of a wobble would on the order of the time since collisions were frequent in the Trans-Neptunian belt (*i.e.*, roughly the age of the solar system). A period this long is not impossible, but it is very difficult to constrain from the ground, especially in this dataset where we were only able to observe 2004 EW_{95} for a few hours each night. To determine a long rotation period, we would need dense and prolonged sampling of the lightcurve each night for at least three consecutive nights (to achieve full rotation phase coverage). It is equally possible that 2004 EW_{95} has a complex lightcurve due to binarity, but we could not infer a companion from this dataset because we could not distinguish its rotational signature. Thus, 2004 EW_{95} can either be a tumbler, an elongated object with a long rotation period, or a binary.

Without knowing the lightcurve, we can only set limits on the full photometric range for computing the axis ratio. The amplitude constraint we measured for 2004 EW_{95} is the highest of the CVS targets, with the maximum $\Delta m = 31 \pm 0.01$, giving an axis ratio of $a : b \sim 1.33$. We use diameter estimates from an assumed albedo value (the median for all

neutral TNOs) and the H magnitude from the JPL small body browser to calculate the minimum equatorial dimensions 200×266 km.

Because we measured no rotation period, we could not constrain the bulk density or tensile strength. We could, however, investigate color variation. Figure 6.55 gives the RMS distribution for flat Monte Carlo simulated colors for both the 2011 and the 2012 data. Data from both years show significant color variation, indicating a heterogeneous surface.

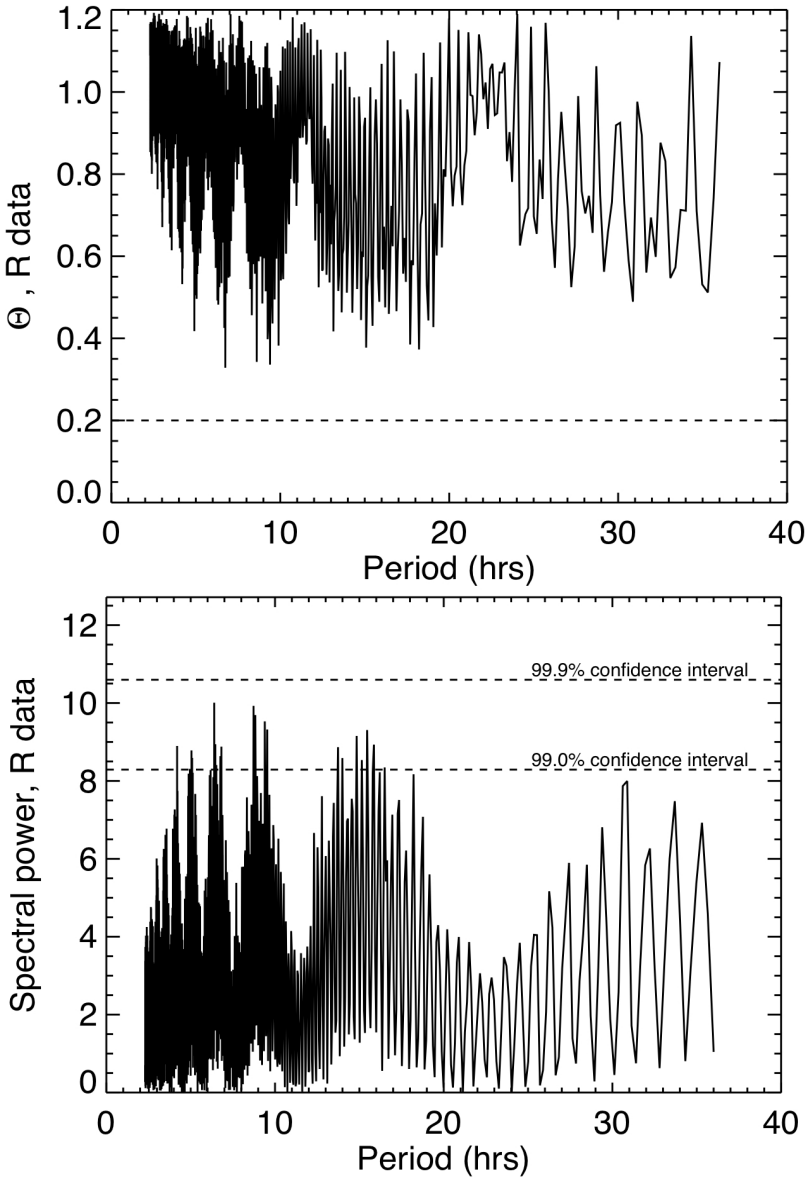

Figure 6.51 Periodograms for 2011 R filter data on 2004 EW_{95}. The upper plot shows the Θ value from the PDM method as a function of rotational periods (solid line) and a dashed line to represent the fiducial value at which Θ becomes highly significant. The lower plot shows the Lomb-Scargle power spectrum as a function of rotation period (solid line) as well as dashed lines at the 99.9% and 99.0% confidence limits.

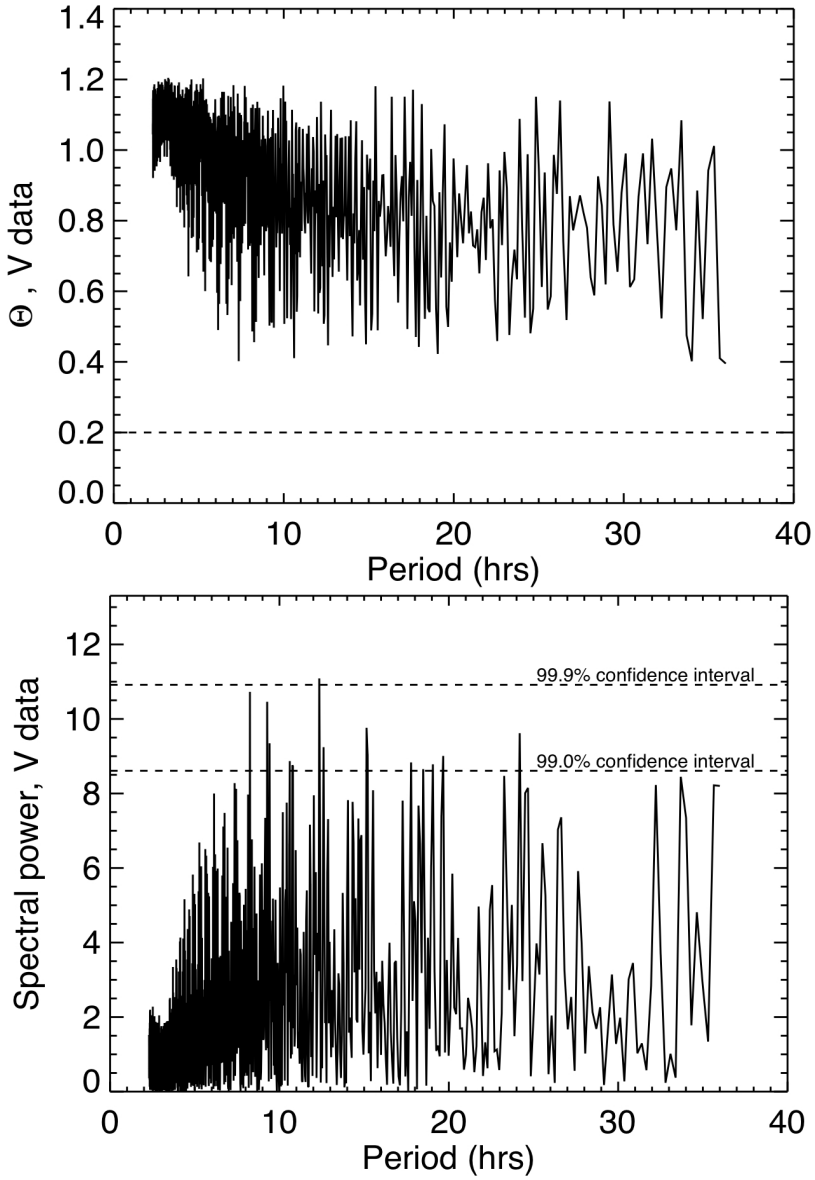

Figure 6.52 Periodograms for 2011 V filter data on 2004 EW_{95}. The upper plot shows the Θ value from the PDM method as a function of rotational periods (solid line) and a dashed line to represent the fiducial value at which Θ becomes highly significant. The lower plot shows the Lomb-Scargle power spectrum as a function of rotation period (solid line) as well as dashed lines at the 99.9% and 99.0% confidence limits.

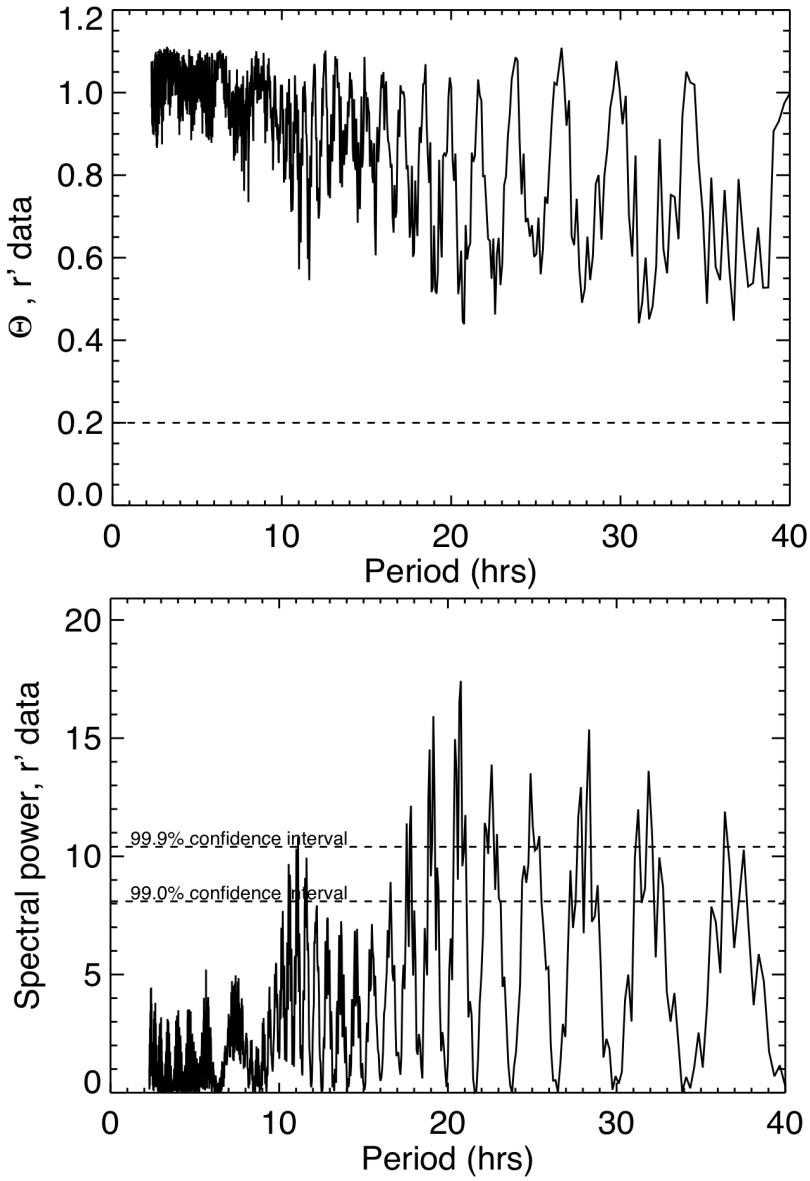

Figure 6.53 Periodograms for 2012 r° filter data on 2004 EW_{95}. The upper plot shows the Θ value from the PDM method as a function of rotational periods (solid line) and a dashed line to represent the fiducial value at which Θ becomes highly significant. The lower plot shows the Lomb-Scargle power spectrum as a function of rotation period (solid line) as well as dashed lines at the 99.9% and 99.0% confidence limits.

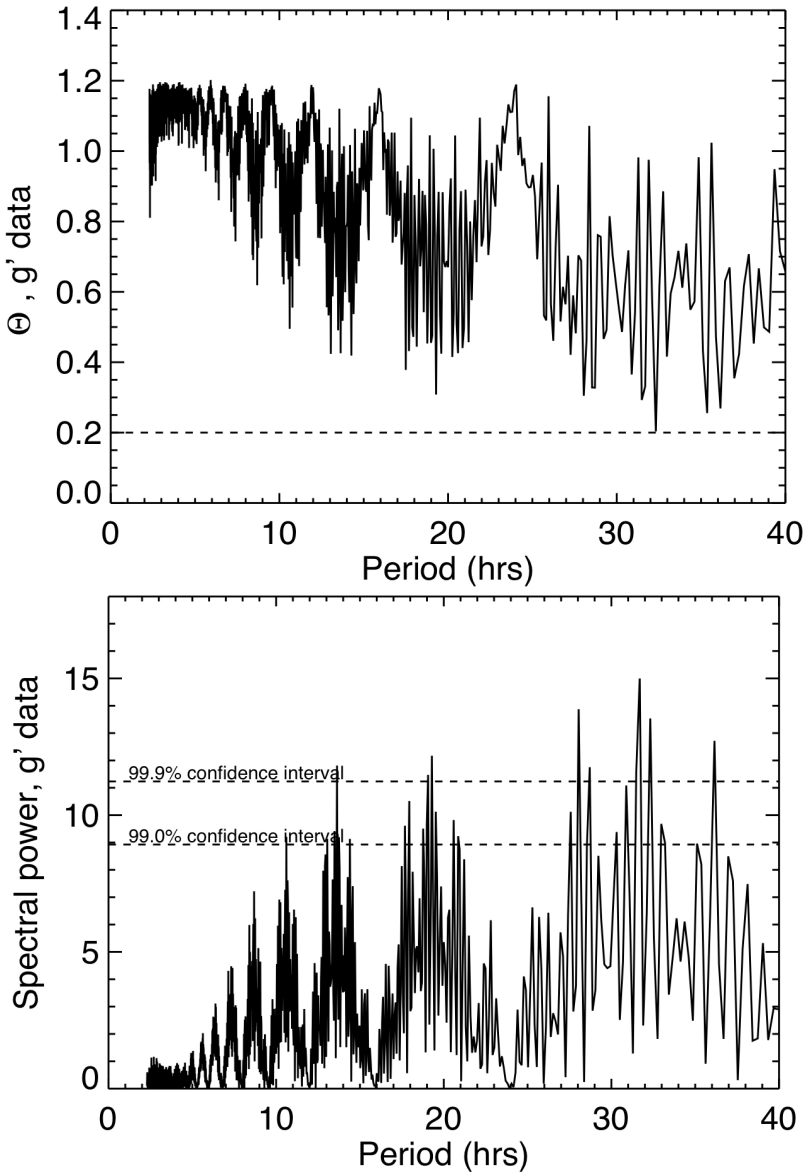

Figure 6.54 Periodograms for 2012 g° filter data on 2004 EW_{95}. The upper plot shows the Θ value from the PDM method as a function of rotational periods (solid line) and a dashed line to represent the fiducial value at which Θ becomes highly significant. The lower plot shows the Lomb-Scargle power spectrum as a function of rotation period (solid line) as well as dashed lines at the 99.9% and 99.0% confidence limits.

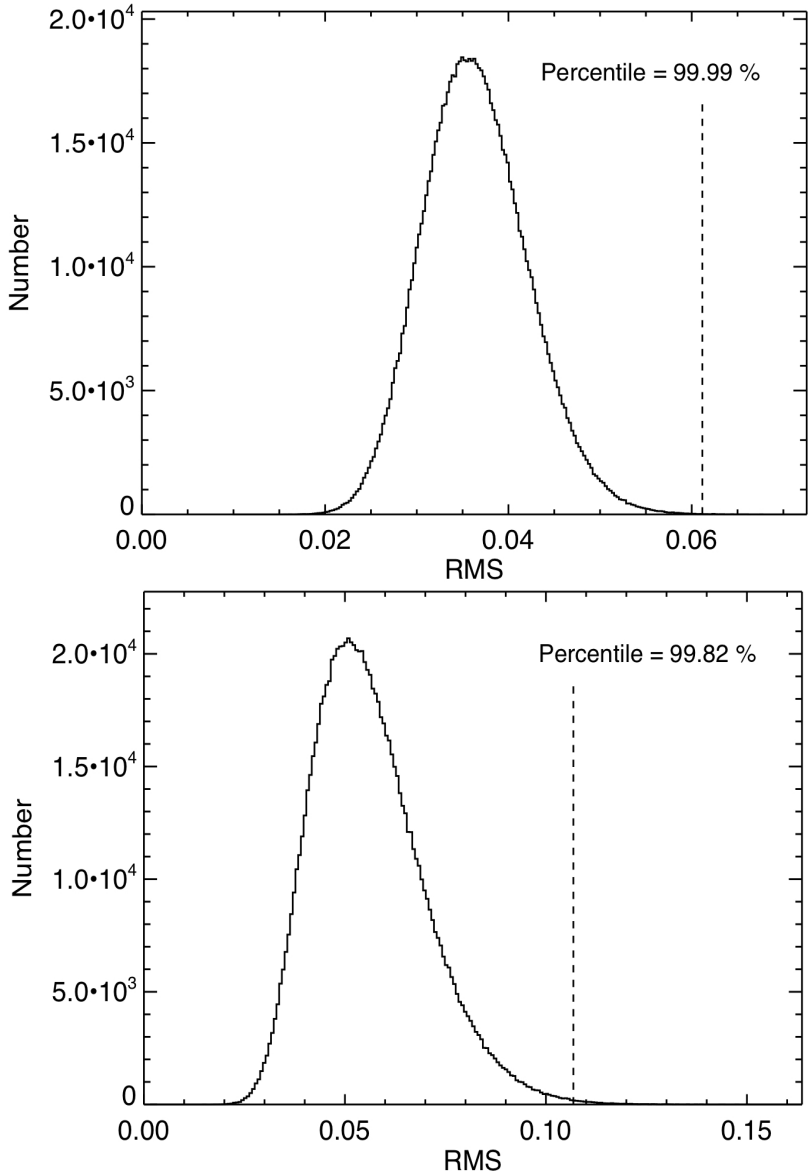

Figure 6.55 Distribution of the RMS of simulated flat color measurements (solid line) with uncertainties comparable to 2004 EW_{95} for the 2011 $V - R$ full dataset (upper plot) and the 2012 $g' - r'$ full dataset (lower plot). The dashed line represents the RMS of the 2004 EW_{95} data in each scenario.

6.4 Calculating the binary fraction at moderate separations

Table 6.12. Summary of the rotation properties determined in this study.

Designation	Single-peaked Period (hrs)	Double-peaked Period (hrs)	Δm[a]	$a:b$	Dimensions (km)	Δm_{bin}[b]	M_s/M_p	ρ_{min} (kg/m^3)	S_{min} (N/m^2)	Color[c] Variaton?
1995 SM_{55}	4.03	8.07	0.08	1.08	230×247	0.11	0.03	669	6×10^6	secondary
2000 YW_{134}	5.56	11.12	0.22	1.22	568×695	0.26	0.14	352	2×10^6	primary
2001 QF_{298}	~ 20	~ 40	0.23	1.24	454×367	···	···	~ 30	1×10^4	primary
2002 TX_{300}	···	14.26	0.15	1.15	270×311	···	···	~ 55	4×10^4	none
2002 XV_{93}	~ 5?	~ 10?	0.13	1.13	517×584	···	···	···	···	none
2003 AZ_{84}	9.3 or 11.4	18.5 or 22.8	0.12	1.12	641×718	0.03-0.08	0.005-0.02	85	9×10^4	none
2003 OP_{32}	2.40 or 2.66	4.81 or 5.32	0.22	1.22	315×389	0.1	0.03	1900	5×10^7	secondary
2003 UZ_{117}	5.68	10.75	0.12	1.12	236×265	···	···	94	1×10^4	none
2004 EW_{95}	···	···	0.31	1.33	200×266	···	···	···	···	primary or secondary

[a]The change in magnitude excluding multi-day variation.

[b]The change in magnitude seen on a multi-day timescale and attributed to a binary companion.

[c]A comment on whether or not the objects showed significant color variation and, if so, whether its presence corresponded to heterogeneity in the primary rotation period or a secondary multi-day period.

Table 6.12 summarizes the observational findings of the CVS, showing many instances of binarity detected. The fraction of neutral binaries at separations to which we were sensitive in the CVS (f) is expressed as:

$$f = \frac{n}{\epsilon\, N} \quad , \tag{6.16}$$

where n is the number of binaries detected in our sample of N objects, and ϵ is the survey's efficiency at detecting a companion. We found evidence of binarity in four of our nine targets: 1995 SM_{55}, 2000 YW_{134}, 2003 AZ_{84}, and 2003 OP_{32}. In calculating the binary fraction, we must define our sample. If we restrict the sample to neutral TNOs (irrespective of their dynamical class), we must exclude 2000 YW_{134}, which was shown to have optically red colors in our data over the full length of the rotation phase. We must also exclude 2004 EW_{95} because we were not able to constrain its lightcurve and therefore its binarity. Therefore, out of a refined sample of $N = 7$ neutral TNO lightcurves, we inferred binarity in $n = 3$ of them.

The survey efficiency can be defined in two ways depending on the nature of the binary system being considered. If we assume that all of the binary evidence in our survey came from eclipsing events, then ϵ is the probability of detecting a transit. If however, the lightcurve features that suggested binarity in our sample came from asynchronous binaries, then ϵ is the probability of detecting variation in the lightcurve of a secondary component. We explored both of these circumstances and calculated a neutral binary fraction from this study.

6.4.1 Calculating the binary fraction assuming eclipsing systems

The following method of computing the binary fraction from eclipsing events assumes that the data points are independent and therefore does not take into account the cadence of the observations relative to the binary's synodic period. Incorporating the observing cadence into the computation will require another set of simulations overlapping the timing of the

dataset onto the simulated binary lightcurve at an array of binary rotation phasings. These simulations will be part of future work we intend to carry out on constraining the TNO binary fraction through lightcurve observations.

To detect an eclipse event, we must obtain at least two data points during the eclipse event (to guard against spurious detections) and at least two data points outside of the eclipse. The ϵ term can therefore be represented as the probability of 2 eclipse event detections amongst a sample of N data points times the probability of 2 non-eclipse event detections in the same sample. The issue of whether or not a data point lies within an eclipse is a scenario best described by binomial statistics, where only one of two outcomes (a "positive" and "negative") are possible. In our case, a positive event is the data point being within the eclipse. The binomial probability (P_B) of having x positive events given a total number of X events and a likelihood of positive event randomly occurring (q) is notated as $P_B(x; X, q)$. Therefore, we can write ϵ as:

$$\epsilon = P_B(2; X, q) \times P_B(2; X, 1 - q) \quad . \tag{6.17}$$

We took X to be the average number of data points in the datasets obtained in both filters (since detecting an eclipse is essentially independent of the filter used), giving $X = 63$. The q term is the probability of observing a transit, which is also the fraction of the mutual orbit in which a transit causes a magnitude difference greater than the detection limits (Δm_{lim}). Our detection sensitivity was the mean photometric error in all of the full datasets, or $\Delta m_{lim} = 0.05$.

We determined the q parameter by simulating transits within binary lightcurves with different orbital configurations and mass ratios using software that we developed. We simulated a uniform range of mass ratios and main orbital elements (semimajor axis, eccentricity, inclination, and longitude of the ascending node). In actuality, the distributions of these parameters are poorly constrained. Full mutual orbital elements have only been determined for 12 Trans-Neptunian binaries, which is too small of a sample size to

statistically represent all outer solar system binaries (*e.g.*, Grundy et al. 2011; Sheppard et al. 2012).

However, some limits can be assumed from the literature for the mass ratio distribution. Noll et al. (2008) demonstrated that even after considering the observational bias toward detecting high mass ratio systems, the difference in magnitude between Trans-Neptunian binaries tends to be less than 1, especially after excluding the largest and thus most anomalous TNOs (Pluto, Eris, Haumea, etc.). A magnitude difference of 1.0 between the primary and secondary corresponds to a mass ratio greater than 0.25 (with the standard assumptions of common albedos and spherical components). Porter & Grundy (2012) also found that the effects of the Kozai mechanism and tidal dissipation combined on Trans-Neptunian binaries tends to produce tight, circularized orbits, with eccentricities $\lesssim 0.1$. If we impose these limits in mass ratio and eccentricity, our simulations show that $q = 0.03$. With $X = 63$ and $q = 0.03$, we used Eq. 6.17 to calculate $\epsilon = 51\%$. Feeding this result into Eq. 6.16, we obtained a binary fraction $f = 84\%$.

The uncertainty in f is dominated by the number of binary detections n. If we assume that the number of binaries we detected was perfectly representative of the true binary fraction, then it follows that every time we observe the same number of neutral of TNOs, we will always detect the same number of binaries. In truth, if our survey were repeated with the same sample size in some arbitrarily large number of trials, we could construct a distribution of n values. This distribution would be defined by Poisson statistics, meaning its peak location (λ) would correspond to the most likely value of n, and the width of the distribution (σ) would be $\sqrt{\lambda}$.

The uncertainty in n thus corresponds to the λ values such that the 1-σ bounds are equal to n. In other words, the lower and upper statistical bounds on n are equal to λ such that $\lambda \pm \sqrt{\lambda} = n$. In our case, $n = 3$, giving lower and upper bounds of 1.697 and 5.303, respectively. Substituting these bounds for n in Eq. 6.16, we got $f = 0.48$ and 1.49, respectively. Therefore, our debiased binary fraction for neutral TNOs is $f = 0.84^{+0.65}_{-0.36}$, with the large uncertainties stemming from a low N value. The upper bounds on f are

unphysical (giving a binary fraction greater than one), so we were only able to meaningfully constrain its lower limits. We conclude that if our positive detections came of mutual eclipses, $f > 0.48$ for neutral TNOs.

6.4.2 Calculating the binary fraction assuming asynchronous systems

Considering instead the possibility that the binary lightcurve features we observed were attributed to observing an asynchronous binary, the ϵ term becomes:

$$\epsilon = P_d \times P_m \times P_e \quad ,$$

where P_d is the probability that the two components will be visually distinct (*i.e.*, not eclipsing) so as to observe the rotations of the two separate components simultaneously, P_m is the probability that the secondary's rotation period will be less than the span of the observations, and P_e is the probability that the secondary will be elongated so as to produce a detectable rotation signature.

It follows that $P_d = 1-q$, or 0.97, as determined in the previous section. Determining P_m requires making assumptions about the spin distribution of TNOs. While longer rotation periods are difficult to detect observationally, the current spin distribution suggests a mean period of $\sim$ 13 hours, with the tail of the distribution (excluding Pluto, which has a rotation period of $\sim$ 153 hours) appears to be on the order of a couple days. Because all of our observations spanned longer times than this, we took $P_m = 1.0$. Objects in binary systems are subject to mutual tidal distortion, which stretches them in the direction of the companion (Chandrasekhar 1987). The amount of distortion depends upon many parameters including the separation between the two bodies and their mass ratio. We used Eq. 6.2 to estimate the elongation required by the secondary in order to produce variation great than our detection sensitivity of 0.05 magnitudes, finding that $a : b$ must be $\gtrsim 1.05$ to have detectable variation. This distortion has not been quantified for moderately separated systems with periods on the order of days, so we had to assume that all secondaries have

axial ratios greater than 1.05 or at least albedo variations greater than 5%, leaving $P_e = 1$. Therefore, we took ϵ to be 0.97.

Feeding this value into Eq. 6.16 then taking the bounds on $n = 3$ as described in the previous section, we calculated $f = 0.43^{+33}_{-19}$. The 1σ upper bounds on the binary fraction from assuming asynchronous systems is thereby meaningfully constrained. However, the 1σ lower bounds are much lower than those calculated by assuming eclipsing events. Since we cannot yet distinguish between which of these two lightcurve explanations (eclipsing or asynchronous binaries) are dominant in our data, the more extreme of the two lower limits must be adopted in the final binary fraction calculation. We therefore conclude that the 1σ neutral binary fraction for the moderate separations to which we were sensitive is $f > 0.24$.

6.4.3 Determining the mutual separation sensitivity

In the CVS, we were sensitive to binaries with eclipsing events. The minimum separation to which we were sensitive corresponded to the shortest synodic period detectable on a multi-day timespan, *i.e.*, with the binary's maximum observed at the end of one night and the transit observed at the beginning of the next, or a mutual orbital period of 28 hours. Using Eq. 6.9, a minimum primary radius of 100 km (comparable to our data), a density of 1000 kg/m^3, and a radius ratio of 1/3 (also consistent with our minimum radius ratio), we find that the minimum physical separation to which we were sensitive was 600 km, or $\theta = 0.02''$.

The maximum separation to which we were sensitive corresponded to the longest synodic period detectable within the timespan in which the data were taken. For an eclipsing binary system, a transit happens twice per orbital period. Therefore, the longest synodic period to which we were sensitive was twice the span of the observations (dt). We furthermore limited dt to include only observation sets that were separated by no more than a few days so that the likelihood of observing a transit was not overwhelmingly compromised by large gaps between nights. The dt value differed between datasets, giving an average dt of ~ 13 days.

Using Eq. 6.9 and the estimated parameters above, we calculated the maximum observable binary separation to be ~ 1700 km, or $\sim 0.06''$.

Combining this result with the lower limits on the binary fraction, we conclude that $\gtrsim 24\%$ (the 1σ limits) of neutral TNOs must be in binary systems with mutual separations of $0.04 \pm 0.02''$.

6.5 Summary of observed rotation properties & Discussion

Through the CVS, we were able to determine two new TNO lightcurves (2003 UZ_{117} and 2000 YW_{134}), revise a further four (2003 AZ_{84}, 2003 OP_{32}, 2002 TX_{300}, and 1995 SM_{55}), and constrain two (2001 QF_{298} and 2002 XV_{93}). Our data for 2004 EW_{95} did not render a convincing periodicity. From these lightcurves, we were able to determine a number of physical properties of the targets. Table 6.12 summarizes the observed properties that we determined.

Previous studies found weak evidence that smaller outer solar system objects are faster rotators and are consequently a collisionally evolved population, though this may only be true for Centaurs (Thirouin et al. 2010). Figure 6.56 shows the updated plot of size versus rotation period. No clear trend is observed, suggesting that smaller TNOs do not have preferentially faster rotation periods indicative of having been part of a collisional event.

Figure 6.57 shows the updated spin distribution for all TNOs, with an mean period of 13.0 hours. We calculated the Kolmogorov-Smirnov probability that two samples come from the same distribution (thereby assessing common origins) for the spin distributions of red versus neutral TNOs and between TNOs and several other major small body populations (Table 6.13). Our results show that TNOs have a spin distribution dissimilar from most other small body populations, with the mean periods of the Centaur, Jupiter Trojan (hereafter, Trojan), and Main belt asteroid spin distributions being $\sim$ 9, 25, and 17 hours, respectively.

The most dissimilarity is seen between TNOs and Trojans, which if real, would have important implications on solar system formation models. The NICE model of planetary migration explains the origin of Trojans as being implanted from the Trans-Neptunian region during an episode of chaotic scattering that started when Jupiter and Saturn reached their 2:1 orbital resonance, sending Neptune plunging into the outer solar system (*e.g.*, Morbidelli et al. 2005). Solar system formation models that instead employ a gentler migration of the giant planets and gravitational capture of Trojans suggest that TNOs and Trojans do not

have to share a common dynamical history (Marzari & Scholl 1998). Since our results suggest that TNOs and Trojans have not undergone the same dynamical history, the gentle planetary migration model is favored.

However, subsequent dynamical evolution, which was likely weak for the newly depleted TNO region but could have been more significant for Trojans, may have caused further and different changes to the spin distributions. Also, owing to their large geocentric distances, there is a known bias against detecting longer period rotators, especially for fainter targets like those in the distant outer solar system. Thus, statistical tendency of TNOs to have shorter periods than Trojans and Main belt asteroids may be partially due to an observational bias. A survey sensitive to long period rotators in the outer solar system would significantly assist in the establishment of this similarity between spin distributions of small body populations.

Table 6.13 Comparison between spin distributions of red vs. neutral TNOs and between spin distributions of TNOs and other major small populations, including Centaurs, Trojans, and Main belt asteroids.

Sample 1	Sample 2	Sample Size 1	Sample Size 2	KS probability
Neutral TNOs	Red TNOs	14	18	0.814
TNOs	Centaurs	51	16	0.112
TNOs	Trojans	51	117	0.005
TNOs	Main belt asteroids	51	2132	0.090
TNOs	Outer Main belt asteroids	51	1148	0.321

If collisions were responsible for the color diversity amongst TNOs, then we should see a difference in the spin distributions between colors, with the resurfaced population having shorter rotation periods clustered at the critical period ($\sim$ 3.3 hours for a solid body of ice). However, our statistical comparison between red and neutral TNO spin distributions, though sparsely populated, suggests that the two groups have similar rotation periods and therefore a common dynamical history, an outcome not supported by the collisional resurfacing mechanism as the explanation for the color diversity seen in TNOs.

None of the TNOs observed in this work were rotationally flat, but their sizes are larger than the limit of a rigid, elongated fragment ($\sim$ 100 km), implying that all neutral TNOs are rotationally distorted rubble piles (*e.g.*, Farinella & Davis 1996). If all neutral TNOs are rubble piles, then tensile strength is essentially negligible and our minimum strength estimates are not important. Most of the minimum density estimates we obtained were too low to meaningfully constrain the density. Only estimates with $\rho_{min} \gtrsim 500$ kg/m^3 were capable of constraining the mass fraction of rock/ice, which we only achieved for two objects, 2003 OP_{32} and 1995 SM_{55}. Our density limits on 2003 OP_{32} correspond to a rock fraction of at least 45%, although 2003 OP_{32}'s surface is dominated by nearly pure water ice absorptions. Therefore, much of the interior of 2003 OP_{32} must be rock, with possible differentiation to explain the disparity between the density implied by the surface ice fraction and the density required for 2003 OP_{32} not to spin apart. The minimum density for 1995 SM_{55} could be representative of an entirely icy or mixed rock/ice object with $\gtrsim$ 30% porosity.

If the binary signatures in our lightcurves come from observing an eclipsing event, then the mass ratios inferred are quite low, implying a typical mass ratio less than one. Compared to the binary detection techniques previously used (direct detection or sparse sampling for identification of tight, large amplitude binaries), ours is the most sensitive to smaller mass ratios (Noll et al. 2008).

Four of our targets showed lightcurve features that we attributed to having at least one companion. However, one of these targets was found to have optically red colors, so after excluding it from analysis, we calculated a 1-σ lower bound on the binary fraction for neutral TNOs of 24%. Figure 6.58 (an updated version of Fig. 4.1) shows the binary fraction for TNOs as a function of mutual separation for both our work (including the BVS result) and published direct imaging surveys. Since our spin distribution analysis suggests that neutral and red TNOs have a common dynamical history, there is no reason to assume that their binary fractions at the mutual separations to which we were sensitive will be

different. Therefore, we can assume that our binary fraction calculation is applicable to all TNOs.

In this Chapter, we will not compare how consistent our BVS and CVS binary fractions are with each other, instead deferring that discussion to Chapter 7, the Summary for the dissertation work as a whole. Figure 6.58 suggests a turnover in the binary fraction at $0.02 < \theta('') < 0.04$, which is consistent with one of two scenarios. First, there may have been two binary formation mechanisms at work simultaneously in the primordial Trans-Neptunian belt (one producing more tight binaries and one producing more wide binaries) such that the observed binary fractions follow a superposition of these two models. In this case, the only model that yet predicts a higher fraction of tight binaries is the Goldreich et al. (2002) model of dynamical friction later refined by Astakhov et al. (2005) and Lee et al. (2007), so it must have been significant.

The second scenario to explain the observed binary fraction is that one binary formation model was at work while subsequent evolution mechanisms preferentially depleted binaries that the model tended to form. For example, if the Goldreich et al. (2002) formation scenario were dominant, then a mechanism to deplete tight binaries (not yet proposed in the literature) during subsequent dynamical evolution must have been present. Given how well the Goldreich et al. (2002) model fits the data at wider separations, we suggest that it must at least partially explain the observed distribution of binary fractions as a function of component separation.

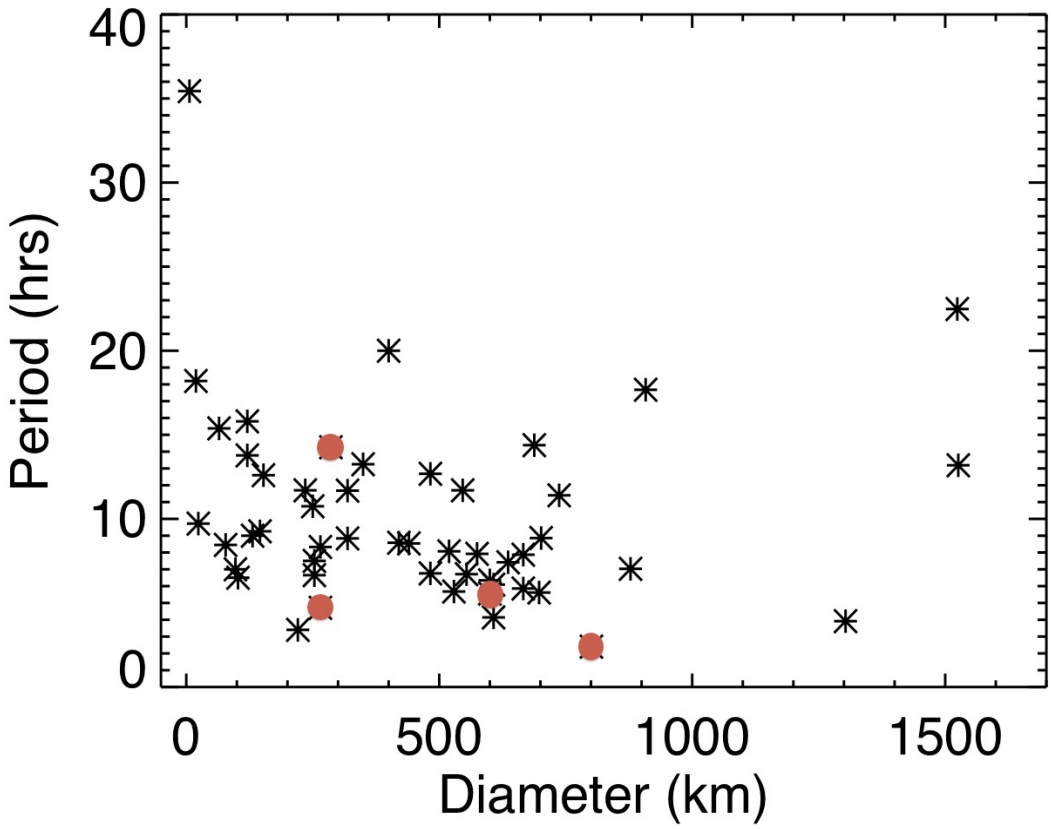

Figure 6.56 Spin period in hours versus Diameter in kilometers for all TNOs. The diameter estimates come from Table 4.1, and the rotation periods plotted are updated to include our results. Objects added from our survey are indicated by red circles.

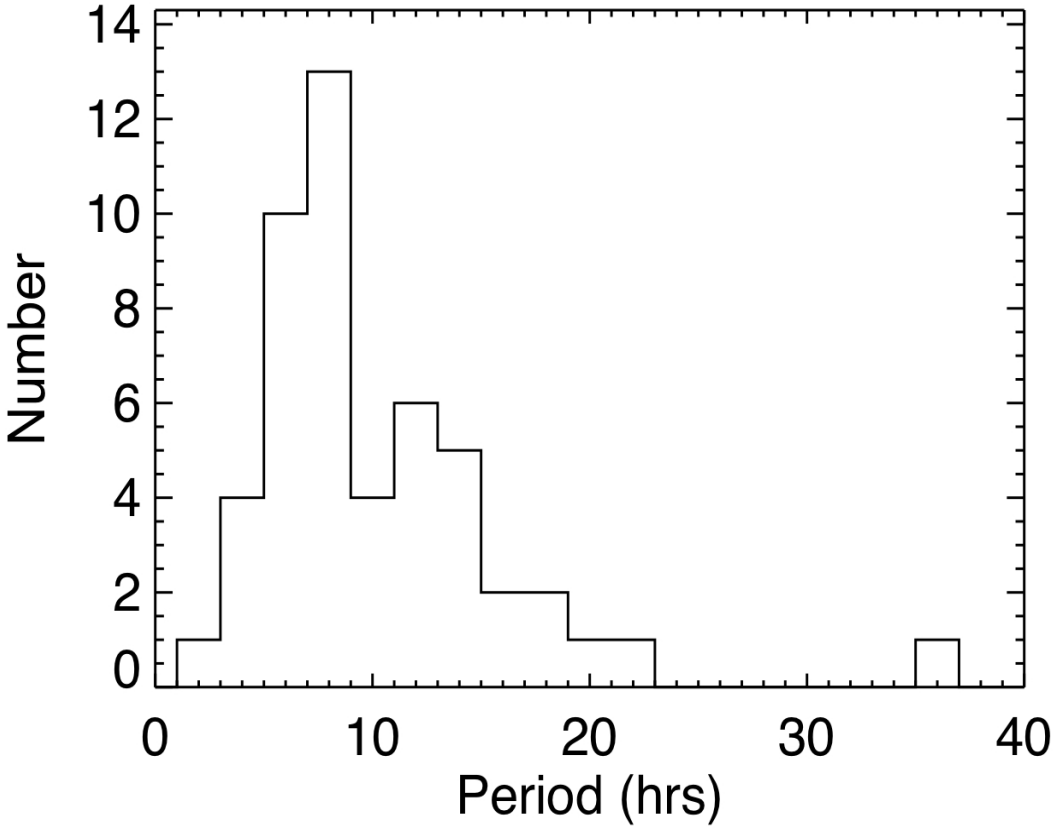

Figure 6.57 Updated spin distribution for all TNOs, including periods determined in this work.

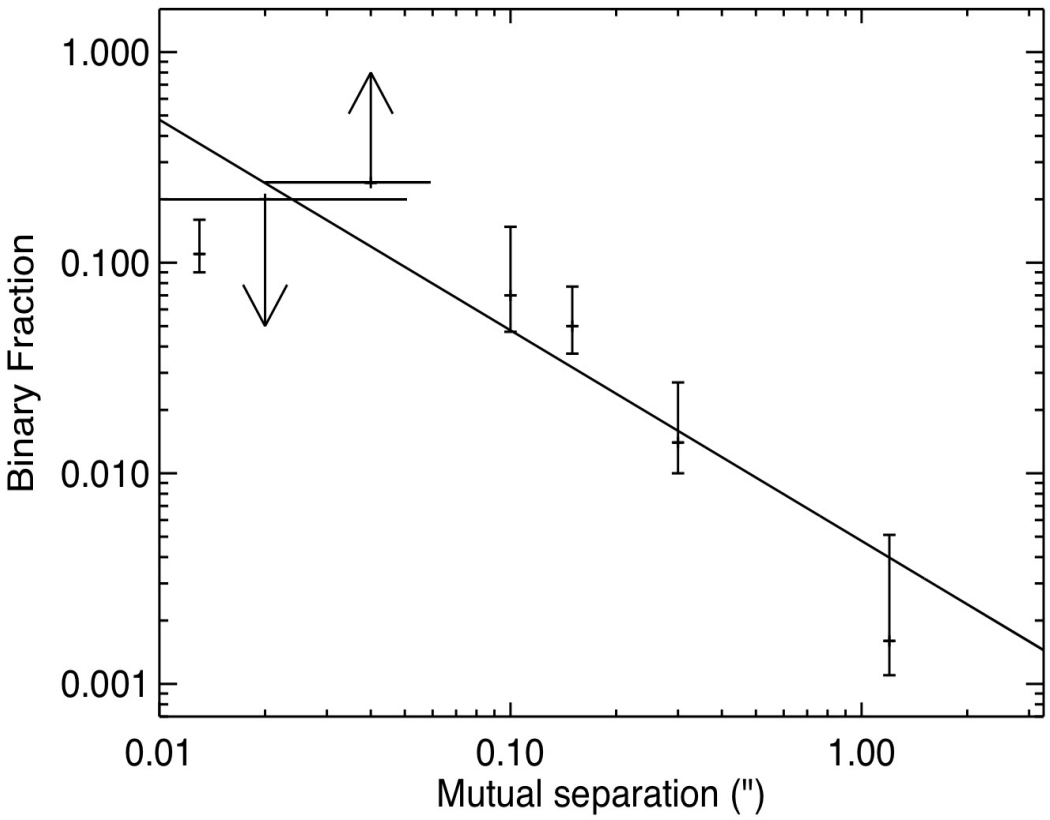

Figure 6.58 Figure 2 from Kern & Elliot (2006) updated to include our 1σ limits. The solid line represents the general trend predicted by the Goldreich et al. (2002) binary formation model.

References

Ahn, C. P., Alexandroff, R., Allende Prieto, C., Anderson, S. F., Anderton, T., Andrews, B. H., Aubourg, É., Bailey, S., Balbinot, E., Barnes, R., & et al. 2012, ApJS, 203, 21

Astakhov, S. A., Lee, E. A., & Farrelly, D. 2005, MNRAS, 360, 401

Barkume, K. M., Brown, M. E., & Schaller, E. L. 2008, AJ, 135, 55

Benecchi, S. D. & Sheppard, S. S. 2013, AJ, 145, 124

Binzel, R. P., Farinella, P., Zappala, V., & Cellino, A. 1989, in Asteroids II, ed. R. P. Binzel, T. Gehrels, & M. S. Matthews, 416–441

Braga-Ribas, F., Sicardy, B., Colas, F., Lecacheux, J., Maury, A., Ortiz, J. L., Morales, N., de, I., Jehin, E., Manfroid, J., Gillon, M., Assafin, M., Vieira-Martins, R., Camargo, J. I. B., & Harlinten, C. 2011, Central Bureau Electronic Telegrams, 2675, 1

Braga Ribas, F., Sicardy, B., Ortiz, J. L., Duffard, R., Camargo, J. I. B., Lecacheux, J., Colas, F., Vachier, F., Tanga, P., Sposetti, S., Brosch, N., Kaspi, S., Manulis, I., Baug, T., Chandrasekhar, T., Ganesh, S., Jain, J., Mohan, V., Sharma, A., Garcia-Lozano, R., Klotz, A., Frappa, E., Jehin, E., Assafin, M., Vieira Martins, R., Behrend, R., Roques, F., Widemann, T., Morales, N., Thirouin, A., Mahasena, P., Benkhaldoun, Z., Daassou, A., Rinner, C., & Ofek, E. O. 2012, in AAS/Division for Planetary Sciences Meeting Abstracts, Vol. 44, AAS/Division for Planetary Sciences Meeting Abstracts, 402.01

Brown, M. E., Barkume, K. M., Ragozzine, D., & Schaller, E. L. 2007, Nature, 446, 294

Brown, M. E. & Suer, T.-A. 2007, IAU Circ., 8812, 1

Burns, J. A. & Safronov, V. S. 1973, MNRAS, 165, 403

Chandrasekhar, S. 1987, Ellipsoidal figures of equilibrium

Davidsson, B. J. R. 2001, *Icarus*, 149, 375

Desch, S. J., Cook, J. C., Doggett, T. C., & Porter, S. B. 2009, *Icarus*, 202, 694

Doressoundiram, A., Peixinho, N., Moullet, A., Fornasier, S., Barucci, M. A., Beuzit, J.-L., & Veillet, C. 2007, AJ, 134, 2186

Durda, D. D. & Stern, S. A. 2000, *Icarus*, 145, 220

Elliot, J. L., Person, M. J., Zuluaga, C. A., Bosh, A. S., Adams, E. R., Brothers, T. C., Gulbis, A. A. S., Levine, S. E., Lockhart, M., Zangari, A. M., Babcock, B. A., Dupré, K., Pasachoff, J. M., Souza, S. P., Rosing, W., Secrest, N., Bright, L., Dunham, E. W., Sheppard, S. S., Kakkala, M., Tilleman, T., Berger, B., Briggs, J. W., Jacobson, G., Valleli, P., Volz, B., Rapoport, S., Hart, R., Brucker, M., Michel, R., Mattingly, A., Zambrano-Marin, L., Meyer, A. W., Wolf, J., Ryan, E. V., Ryan, W. H., Morzinski, K., Grigsby, B., Brimacombe, J., Ragozzine, D., Montano, H. G., & Gilmore, A. 2010, Nature, 465, 897

Emel'Yanenko, V. V. & Kiseleva, E. L. 2008, Astronomy Letters, 34, 271

Farinella, P. & Davis, D. R. 1996, Science, 273, 938

Fornasier, S., Doressoundiram, A., Tozzi, G. P., Barucci, M. A., Boehnhardt, H., de Bergh, C., Delsanti, A., Davies, J., & Dotto, E. 2004, A&A, 421, 353

Goldreich, P., Lithwick, Y., & Sari, R. 2002, Nature, 420, 643

Grundy, W. M., Noll, K. S., Nimmo, F., Roe, H. G., Buie, M. W., Porter, S. B., Benecchi, S. D., Stephens, D. C., Levison, H. F., & Stansberry, J. A. 2011, *Icarus*, 213, 678

Harris, A. W. 1994, *Icarus*, 107, 209

Kern, S. D. & Elliot, J. L. 2006, ApJ, 643, L57

Lacerda, P. & Luu, J. 2003, *Icarus*, 161, 174

—. 2006, AJ, 131, 2314

Lamy, P. L., Toth, I., Fernandez, Y. R., & Weaver, H. A. 2004, The sizes, shapes, albedos, and colors of cometary nuclei, ed. M. C. Festou, H. U. Keller, & H. A. Weaver, 223–264

Landolt, A. U. 1992, AJ, 104, 340

Lee, E. A., Astakhov, S. A., & Farrelly, D. 2007, MNRAS, 379, 229

Lomb, N. R. 1976, Ap&SS, 39, 447

Marzari, F. & Scholl, H. 1998, A&A, 339, 278

Mommert, M., Harris, A. W., Kiss, C., Pál, A., Santos-Sanz, P., Stansberry, J., Delsanti, A., Vilenius, E., Müller, T. G., Peixinho, N., Lellouch, E., Szalai, N., Henry, F., Duffard, R., Fornasier, S., Hartogh, P., Mueller, M., Ortiz, J. L., Protopapa, S., Rengel, M., & Thirouin, A. 2012, A&A, 541, A93

Morbidelli, A., Levison, H. F., Tsiganis, K., & Gomes, R. 2005, Nature, 435, 462

Müller, T. G., Lellouch, E., Stansberry, J., Kiss, C., Santos-Sanz, P., Vilenius, E., Protopapa, S., Moreno, R., Mueller, M., Delsanti, A., Duffard, R., Fornasier, S., Groussin, O., Harris, A. W., Henry, F., Horner, J., Lacerda, P., Lim, T., Mommert, M., Ortiz, J. L., Rengel, M., Thirouin, A., Trilling, D., Barucci, A., Crovisier, J., Doressoundiram, A., Dotto, E., Gutiérrez, P. J., Hainaut, O. R., Hartogh, P., Hestroffer, D., Kidger, M., Lara, L., Swinyard, B., & Thomas, N. 2010, A&A, 518, L146

Noll, K. S., Grundy, W. M., Chiang, E. I., Margot, J.-L., & Kern, S. D. 2008, Binaries in the Kuiper Belt, ed. M. A. Barucci, H. Boehnhardt, D. P. Cruikshank, A. Morbidelli, & R. Dotson, 345–363

Ortiz, J. L., Gutiérrez, P. J., Casanova, V., & Sota, A. 2003, A&A, 407, 1149

Ortiz, J. L., Gutiérrez, P. J., Santos-Sanz, P., Casanova, V., & Sota, A. 2006, A&A, 447, 1131

Ortiz, J. L., Sota, A., Moreno, R., Lellouch, E., Biver, N., Doressoundiram, A., Rousselot, P., Gutiérrez, P. J., Márquez, I., González Delgado, R. M., & Casanova, V. 2004, A&A, 420, 383

Perna, D., Dotto, E., Barucci, A., Rossi, A., de Bergh, C., Doressoundiram, A., & Fornasier, S. 2008, in Bulletin of the American Astronomical Society, Vol. 40, AAS/Division for Planetary Sciences Meeting Abstracts #40, 483

Porter, S. B. & Grundy, W. M. 2012, *Icarus*, 220, 947

Rabinowitz, D. L., Schaefer, B. E., Schaefer, M., & Tourtellotte, S. W. 2008, AJ, 136, 1502

Rabinowitz, D. L., Schaefer, B. E., & Tourtellotte, S. W. 2007, AJ, 133, 26

Ragozzine, D. & Brown, M. E. 2007, AJ, 134, 2160

Romanishin, W. & Tegler, S. C. 1999, Nature, 398, 129

Scargle, J. D. 1982, ApJ, 263, 835

Sheppard, S. S. 2010, AJ, 139, 1394

Sheppard, S. S. & Jewitt, D. 2004, AJ, 127, 3023

Sheppard, S. S. & Jewitt, D. C. 2002, in ESA Special Publication, Vol. 500, Asteroids, Comets, and Meteors: ACM 2002, ed. B. Warmbein, 21–24

Sheppard, S. S. & Jewitt, D. C. 2003, Earth Moon and Planets, 92, 207

Sheppard, S. S., Lacerda, P., & Ortiz, J. L. 2008, Photometric Lightcurves of Transneptunian Objects and Centaurs: Rotations, Shapes, and Densities, ed. M. A. Barucci, H. Boehnhardt, D. P. Cruikshank, A. Morbidelli, & R. Dotson, 129–142

Sheppard, S. S., Ragozzine, D., & Trujillo, C. 2012, AJ, 143, 58

Snodgrass, C., Carry, B., Dumas, C., & Hainaut, O. 2010, A&A, 511, A72

Stansberry, J., Grundy, W., Brown, M., Cruikshank, D., Spencer, J., Trilling, D., & Margot, J.-L. 2008, Physical Properties of Kuiper Belt and Centaur Objects: Constraints from the Spitzer Space Telescope, ed. M. A. Barucci, H. Boehnhardt, D. P. Cruikshank, A. Morbidelli, & R. Dotson, 161–179

Stansberry, J. A., Mueller, T. G., Ortiz, J.-L., Santos-Sanz, P., Vilenius, E., Lellouch, E., & Kiss, C. 2011, in EPSC-DPS Joint Meeting 2011, 1437

Stellingwerf, R. F. 1978, ApJ, 224, 953

Stephens, D. C. & Noll, K. S. 2006, AJ, 131, 1142

Thirouin, A., Ortiz, J. L., Campo Bagatin, A., Pravec, P., Morales, N., Hainaut, O., & Duffard, R. 2012, MNRAS, 424, 3156

Thirouin, A., Ortiz, J. L., Duffard, R., Santos-Sanz, P., Aceituno, F. J., & Morales, N. 2010, A&A, 522, A93

Warner, B. D., Harris, A. W., & Pravec, P. 2009, *Icarus*, 202, 134

Chapter 7

Summary

We sought to constrain the collisional and dynamical history of neutral TNOs by characterizing their rotational lightcurves and surface properties. Toward this end, we conducted a large observing campaign using the University of Hawaii 2.2-meter Telescope, during which we collected 80 nights of optical photometry data divided into two surveys. The first survey was the Brightness Variation Survey (BVS) - designed to sparsely sample lightcurves of neutral TNOs to search for objects with detectable brightness variation. Those showing significant variation were then selected for follow-up as part of the Color Variation Survey (CVS), during which time we densely sampled the lightcurves of nine neutral TNOs in two optical bandpasses (V and R when possible, and g' and r' otherwise) in order to determine both their rotation properties and color variation with rotation. Some of the CVS targets were observed over a range of solar phase angles, in order to remove brightness variations caused by phase effects. Consequently, we were able to constrain their phase functions.

In Chapter 2, we explored the publicly available and most widely-used photometry algorithms for maximizing signal-to-noise of faint moving targets. We demonstrated that the tphot software outperforms all others in accuracy and precision, so we adopted its use in all photometry measurements reported in later chapters. We also found that although standard aperture photometry through IRAF's "PHOT" was sensitive to background contamination

within the aperture, the PSF-fitting routine within IRAF'S "DAOPHOT" produced the next-best results in both accuracy and precision.

The main results of the BVS are summarized as follows:

- We constrained the lightcurve amplitudes of 38 neutral TNOs, finding that combined with previous studies, the amplitude distribution for neutral TNOs is not statistically different from that of red TNOs, though only 20 red TNOs have sampled lightcurves. This result suggests that the mechanisms that would alter their physical shapes (*i.e.*, collisions) affected the red and neutral TNOs similarly, thus providing evidence against collisional resurfacing being responsible for an object having neutral colors.

- We found no evidence for a size-amplitude correlation, which further refutes the idea that collisions, which would produce numerous small, irregularly shaped fragments, were common in the Trans-Neptunian region.

- Because we did not detect any tight binaries (which have a distinctly large photometric range), we placed upper limits of $< 12 - 20\%$ on the fraction of neutral TNOs that are in tight binary systems corresponding to mutual separations $\sim 0.02^{+0.03}_{-0.02}''$ and for mass ratios greater than 0.6.

- Our derived tight binary fraction is consistent with the turnover in the binary fraction as a function of separation presented in Kern & Elliot (2006). We suggest this turnover may exist because of a combination of simultaneously functioning formation mechanisms - one that preferentially forms tighter binaries (Goldreich et al. 2002), and another that more efficiently forms wide binaries (Weidenschilling 2002; Funato et al. 2004; Nesvorný et al. 2010).

- Because our amplitude distribution does not suggest TNOs to be collisionally evolved, we suggest that active formation mechanisms did not involve collisions, which would eliminate the Weidenschilling (2002) and Funato et al. (2004) binary formation models.

We were able to constrain the solar phase curves for three CVS targets with no previously existing phase function data – 2000 YW_{134}, 2001 QF_{298}, and 2004 EW_{95}. We determined the following results:

- We measured red colors for 2000 YW_{134} of $V - R = 0.63 \pm 0.04$, contrary to previous color measurements which were as neutral as $V - R = 0.39 \pm 0.02$ for this object (Doressoundiram et al. 2007). We also measured a flat phase curve (slope $\beta = 0$) for 2000 YW_{134}, making it the only red TNO with a flat phase curve and thereby inconsistent with color-phase coefficient correlation previously observed by Rabinowitz et al. (2008), who found that phase coefficients increase with redness. The two other objects for which we determined linear phase coefficients were neutral and did not give flat phase curves ($\beta_V = 0.30 \pm 0.04$ mag/° for 2001 QF_{298} and $\beta_V = 0.43 \pm 0.03$ mag/° for 2004 EW_{95}), providing further evidence against this correlation and thus suggesting that neutral TNOs do not have different surface properties than red TNOs (at least that can be determined from the within the opposition surge).

- After assessing common origins between phase coefficient and TNO dynamical class by calculating their Kolmogorov-Smirnov probability, we found no difference between surfaces of different dynamical classes, though the sample size was very small (≤ 10) for each population.

After correcting for phase angle brightening quantified in the phase curve chapter, we determined rotational lightcurve properties for nine targets as part of the CVS. Our main conclusions are:

- Combining our results with the literature, we found no size-spin rate correlation, contrary to Thirouin et al. (2010), who only found weak support for this trend. Absence of this correlation is evidence against TNOs being a collisionally evolved population since small objects should have faster rotation periods in a population that experienced a significant collisional history.

- Neutral and red TNOs appear to share the same spin distribution, implying a common dynamical past and further refuting the theory that neutral TNOs acquired their colors via higher instances of collisions that remove red surface material.

- We also found no evidence of similarity between the spin distributions of TNOs and other major populations of small bodies in the solar system (MBAs, Trojans, Centaurs), implying different origins.

- We determined a single-peaked rotation period of 2.40 hours for Haumea family member 2003 OP_{32} - faster than any other measured in the outer solar system. From this period, we calculated minimum density limits of 1900 kg/m^3 for 2003 OP_{32}, corresponding to a minimum rock fraction of 45%, most of which should be subsurface since previous publications show a surface of nearly pure water ice. This rock fraction is consistent with a substantial portion of rock existing in the outer layers of proto-Haumea, which supports the Desch et al. (2009) thermal models that bodies of proto-Haumea's size partially differentiated into a thick rock/ice crust overlying an ice mantle and rocky core.

- We detected surface heterogeneity via color variation in five of our targets, suggesting that these objects were subject to either an outgassing event or collisional excavation.

- Lightcurves of four of the targets showed multi-day offsets from the rotation signature that we attributed to asynchronous or eclipsing binary systems. We explored the possibility that these objects were in a complex rotation state, tumbling about multiple axes and confusing their lightcurves with secondary rotation periods, but found generally short damping timescales for such wobbles relative to the age of these objects. Of these four binary detections, one of them was the Haumea family member 1995 SM_{55}, making it the first evidence for a binary within a collisional family in the outer solar system.

- Based on the CVS results, we calculated the debiased binary fraction for neutral TNOs to be $> 24\%$ at 1σ for mutual separations of $\sim 0.04 \pm 0.02''$. Combined with published surveys, this binary fraction is consistent with an increase in binary fraction toward smaller separations - a trend initially suggested by the Goldreich et al. (2002) model of formation through dynamical friction.

Combining the results from the BVS, phase curve determination, and CVS, we found that the surface and rotation properties of neutral and red TNOs are statistically indistinguishable, thereby refuting collisional resurfacing as being responsible for an object's neutral colors. Instead, neutral TNOs may have formed in a different location, thereby acquiring intrinsically different compositions and space weathering patterns (Brown et al. 2011). It is also possible that cometary-like outgassing events have occurred and re-coated the surface with fresh, neutral material. We speculate that outgassing may better explain the observed surface heterogeneity through jets of outgassed material, whereas intrinsically different compositions for an isolated, non-interacting object are expected to produce homogeneous colors.

Combining our binary fraction results from the BVS and CVS with literature values, we also found that our data are consistent with a turnover in the binary fraction at separations in the range $0.02 < \theta < 0.04$. We note that the two separate ranges of θ to which we were sensitive overlap, giving a lower limit in one (the CVS) that is higher than the upper limit in the other (the BVS). This would at first suggest that our data are not consistent with each other. However, we point out that in determining the BVS binary fraction, we were only sensitive to binary systems with mass ratios > 0.6, whereas with the CVS we were able to detect systems with much smaller mass ratios ($\gtrsim 0.03$), naturally giving rise to a higher binary fraction estimate in the CVS. If the distribution of mass ratios within Trans-Neptunian binary systems were known, we could extrapolate our results from the CVS to have them be applicable to same mass ratios detectable by the BVS.

For example, if it was found that Trans-Neptunian binaries exhibit a uniform mass ratio distribution, then 40% of binary systems would have mass ratios greater than 0.6. Only in

this example, we assume that the CVS was sensitive to detecting systems of any mass ratio. Adjusting the binary fraction determined in the CVS ($> 24\%$) to describe the same sample as the binary fraction to which the BVS was sensitive, we would then obtain a CVS binary fraction lower limit for mass ratios $\gtrsim 0.6$ of $0.24 \times 0.4 \sim 0.1$, or 10%. A binary fraction of $> 10\%$ at $\theta = 0.04 \pm 0.02$ would be in agreement with the BVS results of $< 12 - 20\%$ at $\theta = 0.02^{+0.03}_{-0.02}$. Thus, adjusting the CVS binary fraction to be applicable to systems with mass ratios > 0.6 could remove the apparent inconsistency in our results, if the mass ratio distribution were known.

Our combined BVS and CVS binary fraction limits are consistent with the turnover highlighted in Kern & Elliot (2006). We suggest that this turnover is due to two different binary formation mechanisms that do not invoke collisions simultaneously at work in the Trans-Neptunian belt, perhaps the Goldreich et al. (2002) model of dynamical friction and the Nesvorný et al. (2010) model of gravitational collapse. Our other evidence from updated amplitude and spin distributions supports the idea that TNOs are generally not a collisionally evolved population, thus providing evidence that they experienced perhaps a gentler dynamical history than suggested by the NICE model (*e.g.*, Morbidelli et al. 2005).

References

Brown, M. E., Schaller, E. L., & Fraser, W. C. 2011, ApJ, 739, L60

Desch, S. J., Cook, J. C., Doggett, T. C., & Porter, S. B. 2009, *Icarus*, 202, 694

Doressoundiram, A., Peixinho, N., Moullet, A., Fornasier, S., Barucci, M. A., Beuzit, J.-L., & Veillet, C. 2007, AJ, 134, 2186

Funato, Y., Makino, J., Hut, P., Kokubo, E., & Kinoshita, D. 2004, Nature, 427, 518

Goldreich, P., Lithwick, Y., & Sari, R. 2002, Nature, 420, 643

Kern, S. D. & Elliot, J. L. 2006, ApJ, 643, L57

Morbidelli, A., Levison, H. F., Tsiganis, K., & Gomes, R. 2005, Nature, 435, 462

Nesvorný, D., Youdin, A. N., & Richardson, D. C. 2010, AJ, 140, 785

Rabinowitz, D. L., Schaefer, B. E., Schaefer, M., & Tourtellotte, S. W. 2008, AJ, 136, 1502

Thirouin, A., Ortiz, J. L., Duffard, R., Santos-Sanz, P., Aceituno, F. J., & Morales, N. 2010, A&A, 522, A93

Weidenschilling, S. J. 2002, *Icarus*, 160, 212

Chapter 8

Future Plans

8.1 Rotation properties of Trojans and Hildas

In the next couple of months, I will be starting a postdoctoral position working on several different projects. I will use archival WISE data to study the rotation properties small bodies in the inner solar system, with particular emphasis on the Jupiter Trojans and Hilda asteroids. Jupiter Trojans (hereafter, Trojans), which occupy the L4 and L5 equilibrium Lagrange points of Jupiter's orbit and Hildas, which lie in 3:2 orbital resonance with Jupiter inward of the Trojans, are particularly indicative of planetary migration patterns since their capture and physical state (size, structure, volatile fraction, etc.) must be explained by dynamical evolution models. Early models of minimal planetary migration necessitate that Trojans were dynamically captured from the giant planet region of the solar system (Shoemaker et al. 1989; Marzari & Scholl 1998). In this case, Trojans would be the only small body population that formed in that area, providing a unique window into this region of the solar nebula.

The more recent and widely cited "Nice" model of solar system formation instead suggests that the giant planets underwent significant migration, scattering planetesimals violently and chaotically (*e.g.*, Morbidelli et al. 2005; Levison et al. 2011). In the Nice model, Trojans were injected from the outer solar system, thus providing the closest observable proxy to the faint outer solar system objects. Understanding the nature and composition

of distant, primitive outer solar system bodies is complicated by their intrinsic faintness, so if the much closer Trojans did indeed originate from this population, investigating Trojan properties would allow the outer parts of the solar nebula to be more easily probed by proxy. A more recent version of the Nice model suggests that if Neptune or Uranus traversed one of the Trojan clouds during migration, asymmetric scatterings and collisions would have taken place, producing dissimilar clouds (Nesvorný et al. 2013).

In each of these three solar system formation scenarios, Trojans would acquire different rotation properties diagnostic of their different formation locations and/or collisional evolution. Because of their unique dynamical state, Trojans are one of the only small body classes that offer a way to test these formation scenarios. Similar to my dissertation work, my postdoctoral work will be focused on determining the close/contact binary fraction of Trojans and Hildas by searching for large lightcurve amplitudes. I will also be able to better examine long-period rotators through the continuous $\sim$ 36-hour observational coverage achieved by the WISE spacecraft.

8.2 Black Sheep in the Haumea family

I have also been an active part of a search for additional, darker members of the Haumea TNO collisional family, a project that has tremendous potential for informing planetary scientists about the interiors of TNOs. Models of TNO interiors by Desch et al. (2009) predict that even small (radius 600 km) TNOs with cometary abundances of ammonia should contain substantial subsurface liquid—there may be more liquid in the Trans-Neptunian belt today than in Earth's oceans. The persistence of subsurface liquid is thanks in part to the presence of thick (50-100 km), undifferentiated rock/ice crusts, which should be common to TNOs because their surfaces are too cold, and their ice too viscous, to overturn. Testing these predictions is imperative but astronomical observations cannot probe TNO interiors, with one exception. Haumea is a large, differentiated TNO that was stripped of its ice mantle during an impact, and fragments of the ice mantle form a collisional

family in the outer solar system. Interior models from Desch et al. (2009) predict that this family should also contain an equal number of fragments from the undifferentiated crust. These darker members (the "black sheep") are not identified as family members, in part because individually they resemble ordinary TNOs. To date, we have obtained observations of more than a dozen black sheep candidates to search for clustering in color-color space and identify crustal fragments among TNOs with orbital elements similar to Haumea's. Over the next several months, I will reduce and analyze these data, then prepare the results for publication.

8.3 Other planned work

Another major part of my professional plan is submitting the dissertation work presented in this document for publication. I envision at least three papers within this body of work, one concerning the BVS and its implications for the amplitude distribution and tight binary fraction, another on the results of the rotation period search and updated spin distribution for the CVS results, and lastly, an article on the constraints to the binary fraction from objects identified as binary in the CVS. Given the ambiguity surrounding the implications of the phase curves measured, we have not yet decided whether or not the results from the phase curve study merit independent publication, or rather just being incorporated into the analysis of the CVS data.

Outside of research, I am eager to participate in more education and public outreach events. I have enjoyed being a part of the events run by the IfA and UHNAI and look forward to taking on a more active roll in their design and implementation and to honing my skills as an educator.

References

Desch, S. J., Cook, J. C., Doggett, T. C., & Porter, S. B. 2009, *Icarus*, 202, 694

Levison, H. F., Morbidelli, A., Tsiganis, K., Nesvorný, D., & Gomes, R. 2011, AJ, 142, 152

Marzari, F. & Scholl, H. 1998, A&A, 339, 278

Morbidelli, A., Levison, H. F., Tsiganis, K., & Gomes, R. 2005, Nature, 435, 462

Nesvorný, D., Vokrouhlický, D., & Morbidelli, A. 2013, ApJ, 768, 45

Shoemaker, E. M., Shoemaker, C. S., & Wolfe, R. F. 1989, in Asteroids II, ed. R. P. Binzel, T. Gehrels, & M. S. Matthews, 487–523